Report #3077
COO-3158-63

AN ATOM PROBE FIELD ION MICROSCOPE STUDY OF THE RANGE AND DIFFUSIVITY OF HELIUM IN TUNGSTEN

by

Alfred Wagner

Prepared for

THE U.S. DEPARTMENT OF ENERGY UNDER

CONTRACT NO. EY-76-S-02-3158. *000

Ph.D. Thesis
August 1978

Research Group:
Prof. D. N. Seidman
MSE

DISCLAIMER

ACKNOWLEDGEMENTS

The author wishes to thank his advisor, Professor David N. Seidman for his assistance, guidance and encouragement. He would also like to thank Professors J. M. Blakely and H. H. Johnson who served as members of his special committee. The essential contribution of the author's coworkers, Dr. Thomas M. Hall and Dr. Arnold S. Berger is gratefully acknowledged. The assistance of Mr. Robert Whitmarsh, Mrs. Karen Pratt and Mr. Anthony Barbarro is appreciated. Special thanks go to Dr. Sidney S. Brenner for supplying the plans for the goniometer stage, to Professor John Moteff for supplying the neutron irradiated specimen of the Mo-1.0 at.% Ti alloy, to John Walter for supplying the Metglas 2826 specimens and to Louis K. Mansur for supplying the low swelling stainless steel (LS1A).

This work was supported by the United States Department of Energy. Additional support was received from the National Science Foundation through the use of the technical facilities of the Materials Science Center at Cornell University. The author also wishes to thank International Business Machines Corporation for financial support in the form of a fellowship.

TABLE OF CONTENTS

LIST OF FIGURES

LIST OF TABLES

AN ATOM-PROBE FIELD-ION MICROSCOPE STUDY OF THE RANGE AND DIFFUSIVITY OF HELIUM IN TUNGSTEN

Alfred Wagner, Ph.D.
Cornell University 1978

A time-of-flight (TOF) atom-probe field-ion microscope (FIM) specifically designed for the study of defects in metals is described. This atom probe features (1) a variable-magnification internal image-intensification system based on a channel electron multiplier array for viewing the FIM image; (2) a liquid-helium-cooled goniometer stage which allows the specimen to be maintained at a temperature anywhere in the range of 13 to 450K; (3) a low-energy (< 3 KeV) gas ion gun for in-situ irradiations; (4) an ultra-high vacuum ($\sim 2 \cdot 10^{-10}$ torr) chamber to minimize specimen contamination; (5) a high-vacuum ($\sim 1 \cdot 10^{-6}$ torr) specimen-exchange device; (6) a Chevron ion detector; and (7) an eight-channel digital timer with $\pm$ 10 nsec resolution for measuring the TOF's of the pulsed-field evaporated ions.

The entire process of applying the evaporation pulse to the specimen, measuring the dc and pulse voltages and analysing the TOF data is controlled by a Nova 1220 computer. Data in the form of a histogram of the number of events versus the mass-to-charge ratio are displayed on a Tektronix graphics terminal. An extensive set of computer programs to test and operate the atom-probe FIM has also been developed. With this automated system 600 TOF min^{-1} can be recorded and analyzed.

Performance tests of the instrument demonstrated that (1) the seven isotopes of molybdenum and the five isotopes of tungsten can be clearly resolved; and (2) the concentration and spatial distribution

of all constitutents present at levels greater than 0.05 at.% in a W-25 at.% Re, Mo-1.0 at.% Ti, Mo-1.0 at.% Ti-0.08 at.% Zr (TZM), a low swelling stainless steel (LS1A) and a metallic glass (Metglas 2826) can be measured.

The effect of the rate of field evaporation on the quantitative atom probe analysis of a Mo-1.0 at.% Ti alloy and a Mo-1.0 at.% Ti-0.08 at.% Zr alloy was investigated. As the field evaporation rate increased the measured Ti concentration was found to also increase. A simple qualitative model was proposed to explain the observation.

The spatial distribution of titanium in a fast neutron irradiated Mo-1.0 at.% Ti alloy has been investigated. No evidence of Ti segregation to the voids was detected nor has any evidence of significant resolution of Ti from the TiC precipitates been detected. A small amount of segregation of carbon to a void was detected.

The existence of an isolated, immobile, interstitial helium atom in tungsten was demonstrated. In addition, the range of low energy (300 and 475 eV) helium ions in tungsten was directly measured and the diffusivity of interstitial helium atoms in tungsten was determined. A mean range and standard deviation of 40 ± 4 A and 20 to 36 A respectively for 300 eV helium ions and 56 ± 6 A and 35 to 43 A respectively for 475 eV helium ions on tungsten was determined. The interstitial helium atoms became mobile in tungsten in the temperature range of 90 to 110 K. A simple model of the diffusion process yielded a migration energy for the diffusion of interstitial helium atoms in tungsten of 0.24 to 0.32 eV. An upper limit to the reflection coefficient for 300 eV helium on tungsten was found to be 0.89 while the upper limit for 475 eV helium on tungsten was found to be 0.85.

1. INTRODUCTION

The effect of energetic particle irradiation on the properties of materials has been the subject of considerable scientific investigation. The major practical objective of this research has been the developement of materials which are suitable for use in the fast breeder reactor and the controlled thermonuclear reactor (CTR). However, the study of radiation effects also provides fundamental information on the properties of defects in materials. This information has a significant impact in a number of areas that are not directly related to energy technology, for example diffusion, mechanical properties and semiconductor device technology.

The fundamental studies of radiation effects in metals have been increasingly concerned with processes that occur on the atomic scale. While computer calculations have provided valuable theoretical information, there has been a lack of direct experimental techniques capable of providing both structural and chemical information on the atomic scale. The only direct experimental technique which has been employed in the study of atomic scale processes in irradiated metals is the field ion microscope (FIM). The developement of the atom probe FIM by Muller and co-workers[1-6] represented a major extension to the capability of the FIM.[7]

The atom probe combines a FIM with a unique time-of-flight (TOF) mass spectrometer which can chemically identify individual atoms. Employing the atom probe, the three dimensional microstructure of a specimen can be viewed on an atomic scale and correlated with a simultaneous chemical analysis. Thus the atom probe is capable of

imaging lattice defects such as vacancies,[8,9] self interstitial atoms (SIAs),[10] dislocations,[11] grain boundaries[12] and voids,[13] and can also chemically identify individual atoms which were associated with these lattice defects.

Since the first publication concerning the atom probe by Muller et. al.,[1] a number of other instruments have been reported in the literature and also described at field emission symposia.[14-27] The major metallurigical applications of the atom probe have been: (1) a study of the early stages of precipitation in the Fe-Cu system[28,29] and in an Fe-3 at.% Mo alloy;[30] (2) an analysis of precipitates in iron and steels;[31,32] and (3) an investigation of chromium depletion near the surface of a 410 stainless steel In addition, Muller and Tsong[6] and Panitz[34] have written review articles which deal primarily with the physics of the atom probe. In the present work, an atom probe FIM specifically designed for the study of defects in metals has been constructed and applied to two problems in the area of radiation effects in metals.

The physical principles involved in the operation of the atom probe are described in section 1.1. The main features of the present atom probe are outlined in section 1.2 while a detailed description of the design and construction of the instrument is presented in sections 2 through 4. The most unique technical feature of this atom probe involved the developement of a computer controlled data acquisition system. In addition to providing on-line data analysis, the system has permitted rapid accumulation of large quantities of data which was an essential aspect of the experiments presented in this work. In section 5, several performance tests are

presented which clearly demonstrate the ability of the instrument to examine a wide variety of pure metals and alloys. The type of information which can be obtained with an atom probe is also demonstrated and the various forms of presenting the data are described. The spatial distribution of the alloying elements in several unirradiated alloys which exhibit different void swelling characteristics is also presented.

A potential source of error in quantitative atom probe analysis is discussed in section 6 and several examples which demonstrate the nature and magnitude of the errors are presented.

The application of the atom probe to the study of the fundamental behavior of helium in tungsten is described in section 7. This subject is of interest to the field of radiation effects due to the crucial role which helium plays in the nucleation and stabilization of voids in materials that have been irradiated in the fast breeder reactor and due to the problem of helium blister formation in the CTR. Tungsten was chosen for this investigation since it is amenable to field-ion microscopy and because the most thorough experimental and theoretical work on helium in the bcc metals has employed tungsten as the prototype. By utilizing the structural and chemical information which can be obtained with the atom probe, the existence of an isolated, immobile, interstitial helium atom in tungsten has been demonstrated and an approximate migration energy for interstitial helium diffusion in tungsten has been determined. In addition the range profile of low-energy helium ions (300 and 475 eV He^+) in tungsten has been measured. The results were compared with the current theoretical predictions.

The swelling properties of fast neutron irradiated metals are strongly dependent on alloy composition. Although numerous mechanisms have been proposed to explain this effect, there has been essentially no definitive experimental work in which a mechanism has been identified. This is not surprising in view of the complexity of the swelling problem. The majority of the proposed mechanisms rely on either a pronounced segregation of the solute to sinks for point defects, for example dislocations and voids, or are based on the solute remaining in solid solution. In section 8 the nature and extent of the solute redistribution in a fast neutron irradiated Mo-1.0 at.% Ti alloy is presented. This alloy exhibits an enhanced swelling compared to pure molybdenum when both materials are irradiated under identical conditions. The objective of the present experiment was to interpret the results in terms of the proposed mechanisms for the effect of alloying on swelling.

1.1 Physical Principles of the TOF Atom Probe FIM

A highly schematic diagram illustrating the main features of a TOF atom probe FIM is shown in Fig. 1. The FIM specimen is typically a wire ~ 0.15 mm in diameter and ~ 10 mm in length. Before inserting the specimen into the FIM, it is etched or electropolished to a fine point that may have an initial radius of curvature (R_t) of only 50 to 100 A. The specimen is maintained at a positive potential with respect to a grounded imaging system and an imaging gas which is typically helium or neon is admitted into the FIM to a

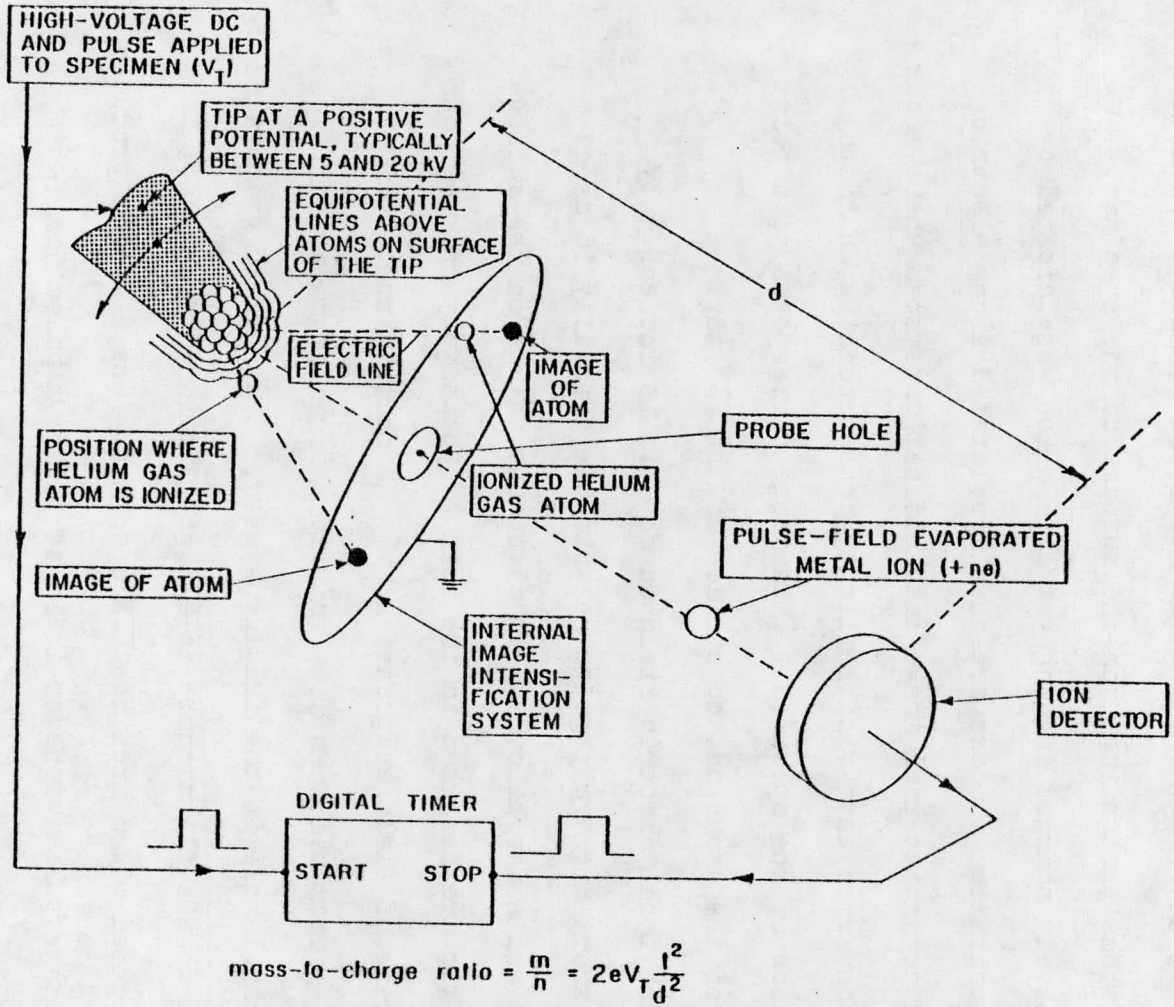

Figure 1. A highly schematic diagram illustrating the principle of the time-of-flight atom-probe field-ion microscope.

pressure of $\sim 10^{-5}$ torr*. Since the tip of the specimen has a small R_t, a local electric field of several volts per angstrom can be obtained by applying a positive potential to the specimen which is in the range of 5 to 20 kV. As a result of this high local electric field the imaging gas atoms are field ionized[35] over individual atoms protruding from the surface of the specimen. These positively charged imaging gas ions which were created by the field ionization process are then accelerated along electric field lines to an internal image intensification system where their energy is converted into visible light, thus producing an image of the surface of the specimen. This image corresponds to a point projection of the atoms on the surface of the FIM tip.

When the local electric field on the tip is increased by applying a short high voltage pulse which is typically 10 nsec in duration and a few kilovolts in magnitude, atoms on the surface of the FIM tip are desorbed in the form of positively charged ions by the process of field evaporation.[36] A certain number of the pulse field-evaporated ions have trajectories which take them through a small hole in the imaging system. These field evaporated ions travel down a flight tube to a high gain ($\sim 10^7$) detector which is located $\sim$ 2 m from the FIM specimen. The detector produces a small voltage pulse whenever it is struck by a pulse field-evaporated ion. These ions are chemically identified by determining

---

* All pressures reported in this text are gauge pressures.

their mass-to-charge ratio (m/n). The time interval between the application of the field evaporation pulse and the voltage pulse produced by the detector is measured by a digital timer.[37] The value of (m/n) of the pulse field-evaporated ion is then deduced by equating the potential energy of the ion to its kinetic energy from the equation

$$neV_t = \frac{1}{2} mv^2 \qquad (1)$$

where n is the charge state of the ion, e is the electron charge, V_t is the effective total voltage (the sum of the dc imaging voltage and the pulse voltage) applied to the specimen, m is the mass of the ion and v is the terminal velocity of the ion. The quantity v is given by (d/t) where d is the flight distance and t is the TOF of the ion under the assumption that the terminal velocity of the ion is reached in a time $\ll$ t and a distance $\ll$ d. These assumptions are valid for a value of d $\gtrsim$ 1 m since the ions approach their terminal velocity within a few tip radii ($\sim$ 1 μm). The value of (m/n) is then given by

$$\frac{m}{n} = 2eV_t t^2/d^2. \qquad (2)$$

Equation 2 is basically the expression which was employed to determine the value of (m/n) for each pulse field-ev aporated ion. In section 3.4 it is shown that this equation must be modified slightly to determine (m/n) to a high degree of accuracy.

1.2 Special Features of the Cornell TOF Atom Probe

A number of unique features were incorporated in the design of the Cornell atom probe which made it ideally suited for the study of materials science problems. A schematic diagram illustrating the basic components and configuration of this atom probe is shown in Fig. 2. The entire FIM was contained in a stainless steel ultra-high vacuum (UHV) system which minimized contamination of the specimen under examination. The FIM specimen was mounted on a goniometer stage with two axes of rotation so that any region on the surface of the tip could be projected over the probe hole for chemical analysis. This goniometer stage was cooled by liquid helium which improved the quality of the FIM image and also allowed the diffusivity of point defects such as interstitial helium atoms (see section 7) to be varied. The FIM specimen was inserted into the microscope via a high-vacuum specimen exchange device which allowed specimens to be exchanged without bringing the entire FIM up to atmospheric pressure. An ion gun was constructed which permitted <u>in-situ</u> irradiation of the specimen with any low-energy (< 10 KeV) gas ion, for example H^+, He^+, Ne^+, Ar^+ or Xe^+. The FIM image was produced on an internal image intensification system consisting of a channel electron multiplier array (CEMA) and a phosphor screen. The magnification of the FIM image was varied by an areal factor of ~ 64 by moving the entire internal image intensification system relative to the FIM specimen. The FIM image was recorded on 1000 foot rolls of 35 mm film employing an Automax ciné camera.

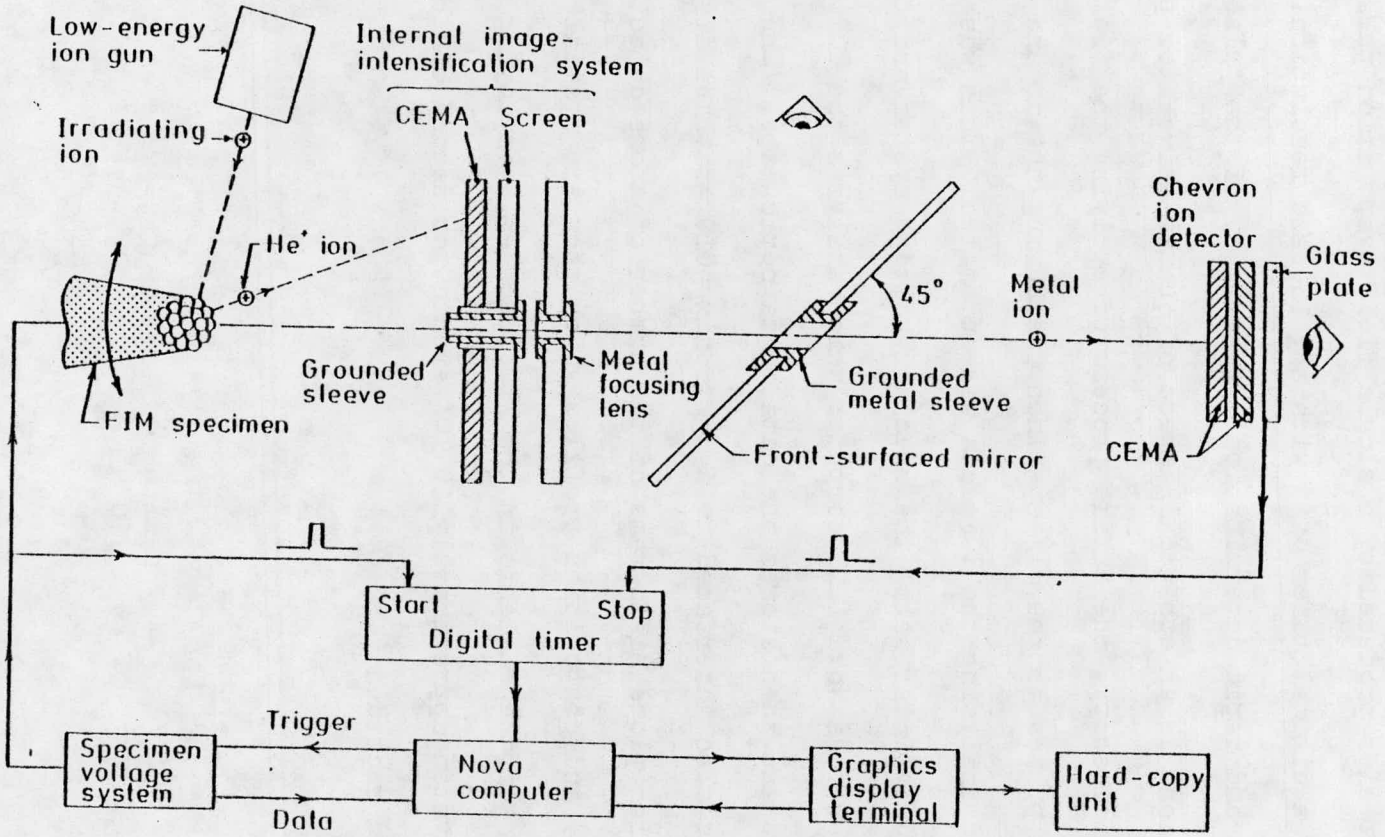

Figure 2. The TOF atom-probe FIM. Shown at the top of the figure are the internal elements of the atom probe including the FIM specimen, the internal image-intensification system, the focusing lens, the 45° viewing mirror, the Chevron ion detector and the low-energy ion gun for performing in-situ irradiations. The digital timer and specimen voltage system shown in the lower part of the figure are operated automatically by a Nova 1220 minicomputer interfaced to a Tektronix 4010 graphics display terminal and a 4610 hardcopy unit so that data can be plotted on-line during the course of an experiment.

The pulse field-evaporated ions were detected by two CEMAs arranged in the Chevron configuration.[38] The TOF of up to eight different species produced by a single field evaporation pulse were measured by a digital timer [37] with a ± 10 nsec resolution. Since an accurate and rapid determination of the (m/n) of the pulsed field-evaporated ions is an essential aspect of quantitative atom probe field ion microscopy, the entire process of applying the field evaporation pulses to the FIM specimen, measuring the dc and pulse voltages and analysing the TOF data was automated. This was accomplished by interfacing the specimen voltage system and the digital timer to a Nova 1220 computer which analyzes the TOF and voltage data and then stores the data on magnetic tape. The computer was also interfaced to a Tektronix 4010 graphics display terminal which plots histograms of the number of atoms detected versus (m/n) and composition profiles which show the spatial distribution of the elements in the FIM specimen. Employing this automated system approximately 10 TOF events per second can be analyzed and recorded.

2. FIELD-ION MICROSCOPE SYSTEM

This section contains a description of the components of the TOF atom-probe FIM that were primarily employed to obtain a visible image of the FIM specimen.

2.1 Internal Image Intensification System and Focusing Lens

A diagram illustrating the details of the internal image intensification system, focusing lens, viewing mirror and Chevron ion detector is presented in Fig. 3. The tip of the FIM specimen is shown facing a Gallileo 75 mm diameter channel electron multiplier array (CEMA). The internal image intensification system consisted of the CEMA and a phosphor coated glass screen. The screen was made by first coating a glass disk with a transparent and conducting layer of tin oxide and then laying the disk horizontally in a petri dish containing a sufficient quantity of distilled water to cover the glass disk. A suspension of Sylvania P-14 phosphor in a dilute solution of potassium silicate in water was then agitated and poured into the petri dish. The phosphor was allowed to precipitate and settle onto the glass disk for approximately 1 hr. The excess water was drained with a syringe and then the screen was baked at 180 C for 3 hr.[39] This process yielded a uniform screen which did not flake or peel under normal handling conditions.

The probe tube and lens arrangement shown in Fig. 3 was the result of numerous trial-and-error attempts at obtaining a configuration that would efficiently collect the pulse field-evaporated

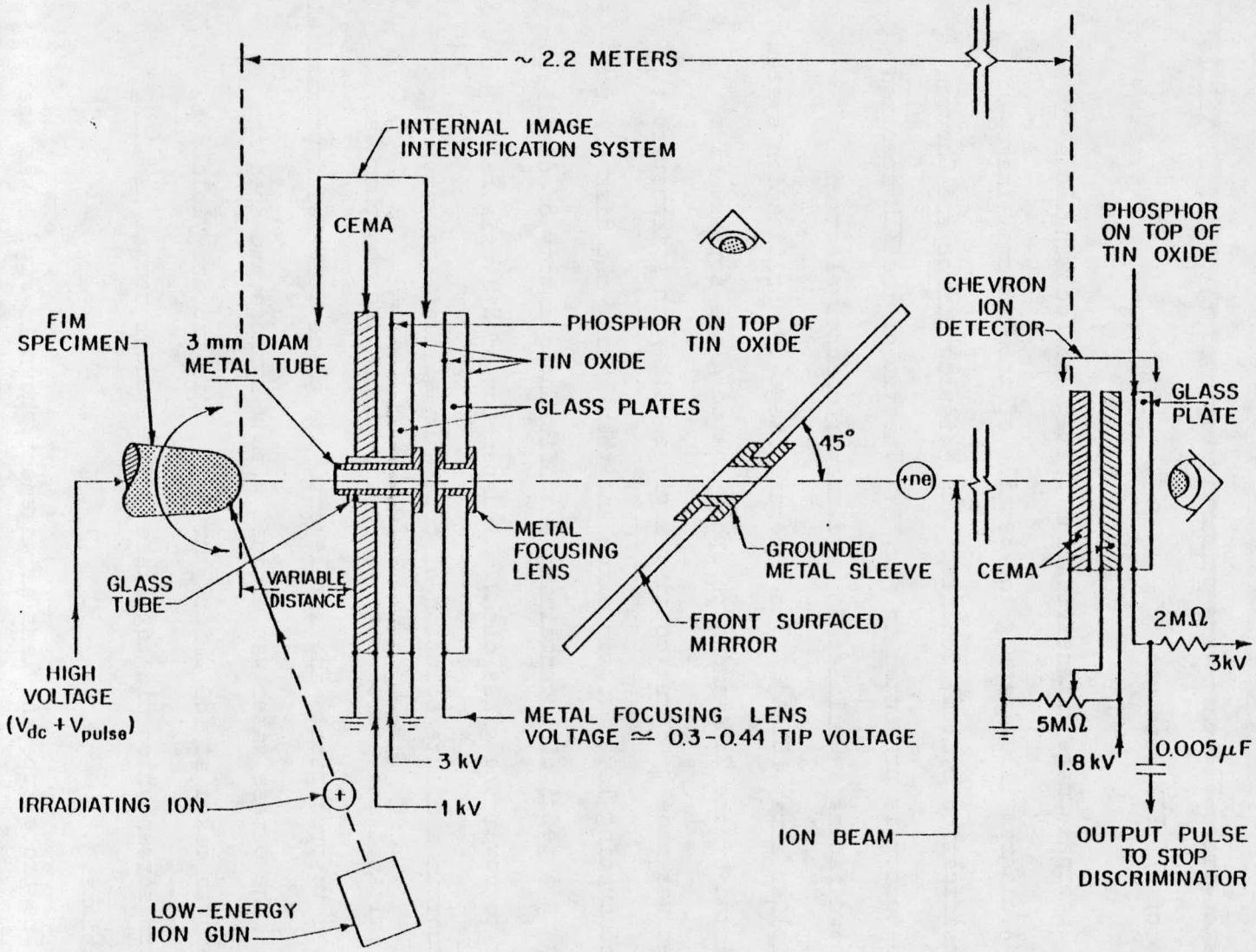

Figure 3. A detailed schematic of the internal elements of the atom probe.

ions and focus them onto the Chevron ion detector. As indicated in Fig. 3 the internal image intensification system had a 3 mm diameter hole through its center. A grounded probe tube was inserted through this hole which electrostatically shielded the ion beam from the back of the CEMA and the front of the screen which were maintained at 1 and 3 kV respectively. The probe tube consisted of a stainless steel tube whose walls were thinned to ~ 25 μm by electropolishing. The grounded stainless steel tube was electrically insulated from the CEMA and the front of the glass screen by a glass tube with ~ 50 μm thick walls. This insulating tube was thinned from stock Pyrex glass tubing using hydrofluoric acid. The outer diameter was decreased by dipping the tube in the acid and the inner diameter was increased by squirting the acid through the tube until the desired dimensions were obtained. A 50 μm diameter stainless steel wire was spot welded to the back of the probe tube and clamped under tension so that the probe tube could not move. The back side of the glass screen was given a separate coating of tin oxide which was electrically isolated from the phosphor screen and which was maintained at ground potential. This grounded coating ensured that the ion beam was electrostatically shielded from the CEMA and screen potentials and prevented electrostatic charging of the glass.

Immediately behind the image intensification system was a focusing lens in the form of a stainless steel bushing which passed through a glass plate coated on both sides with tin oxide. A beryllium-copper coil spring and a small washer spot-welded onto the side of the bushing facing away from the specimen retained the bushing

in a fixed position. This lens was maintained at a voltage which was proportional to the dc voltage applied to the specimen (see section 3.1 for a description of the voltage control system). The constant of proportionality required to focus the ions onto the Chevron ion detector varied between 0.30 and 0.55 as the distance from the specimen to the image intensification system was varied between 100 and 12 mm respectively.

The production of a well focused beam of ions at the detector was critically dependent on the alignment of the probe tube and focusing lens. The focusing lens was aligned with the probe tube by sighting through them and adjusting the position of the focusing lens until no eccentricity was visible. This procedure allowed the ion beam to be focused to a spot ~ 1 mm in diameter on the Chevron ion detector at the downstream end of the flight tube.

A front surfaced glass mirror containing a 10 mm diameter hole through its center was placed behind the focusing lens at an angle of 45 degrees with respect to the flight path (see Fig. 3). This mirror allowed the image of the specimen which was produced by the image intensification system to be viewed without obstructing the flight path. The hole through the mirror was lined with a grounded stainless steel sleeve which prevented charged particles from accumulating on the exposed glass surfaces.

The entire assembly consisting of the image intensification system, focusing lens and viewing mirror was attached to two UHV metal bellows arranged so that the distance from the tip of the specimen to the front surface of the image intensification system

was continously variable. When the image intensification system was translated toward the specimen the magnification of the FIM image decreased and hence the magnitude of the area on the surface of the specimen which was projected over the probe hole increased. Thus by varying the distance between the specimen and the image intensification system, the size of the chemically analyzed region on the surface of the specimen was varied. Since the tip-to-image intensification system distance can be varied from ~ 12 to 100 mm, a lineal magnification change of ~ 8x and an areal magnification change of ~ 64x was obtainable.

2.2 Helium Cooled Goniometer Stage

A liquid helium cooled goniometer stage was constructed with the following features: (1) the specimen could be cooled to cryogenic temperatures to improve the quality and resolution of the FIM image and also to change the diffusivity of point defects; (2) the specimen could be rotated about two orthogonal axes which intersect at the tip of the specimen so that any desired region on the surface of the specimen could be projected over the probe hole for chemical analysis; and (3) the goniometer stage could be translated in three mutually orthogonal directions to facilitate alignment of the tip with respect to the probe hole and the low energy ion gun described in section 2.4.

A cutaway view of the goniometer stage is shown in Fig. 4. The FIM specimen was mounted in a copper specimen holder that was removed when one specimen was exchanged for another. This copper

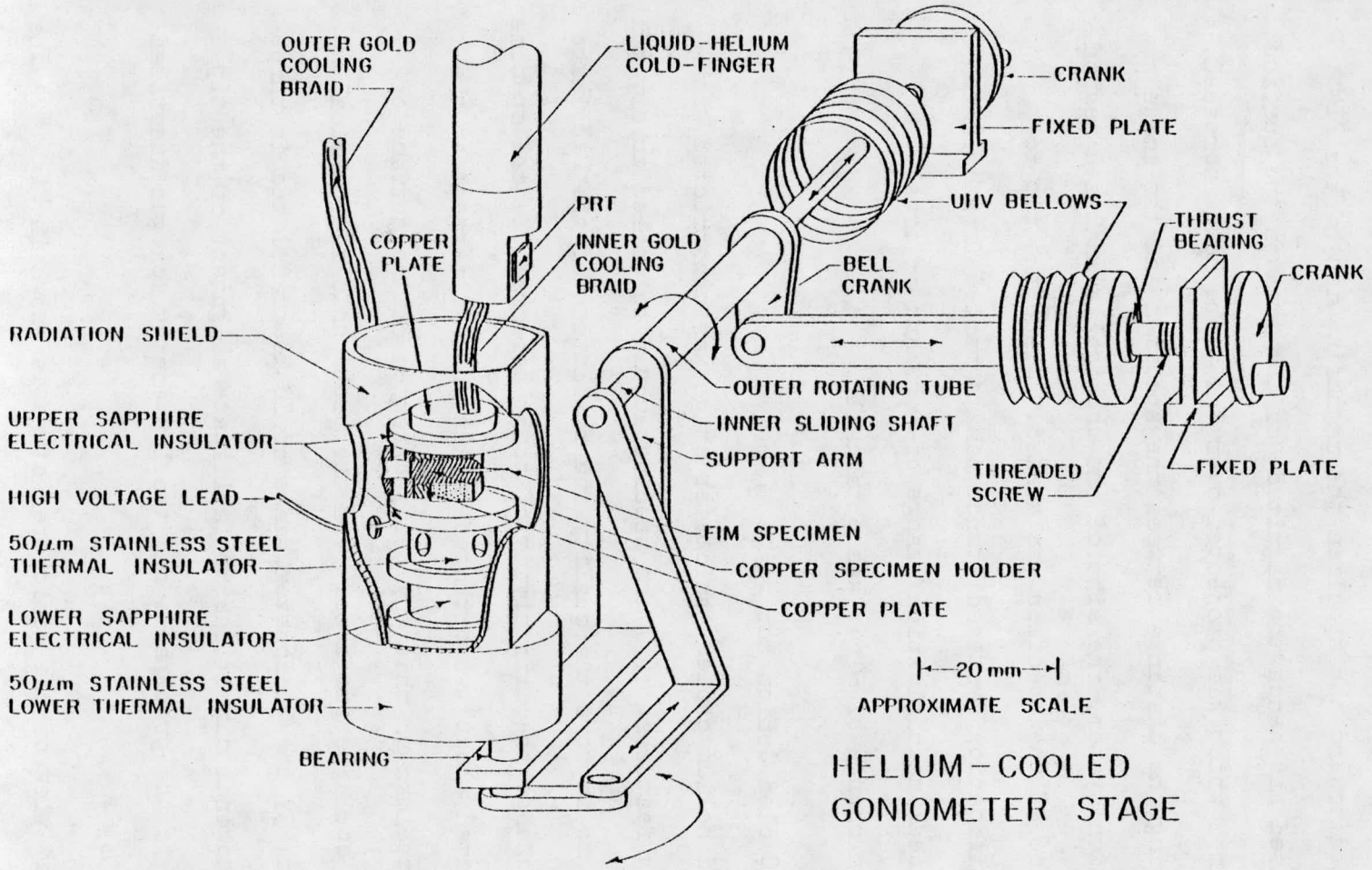

Figure 4. A schematic diagram of the goniometer stage which allows the FIM specimen to be rotated about two mutually orthogonal axes. The liquid-helium cryostat is connected to the specimen via a flexible gold braid. The copper radiation shield surrounding the specimen mount is cooled by a second gold braid which is also connected to the cryostat.

specimen holder was threaded into a copper plate which was bolted onto the back of the upper sapphire electrical insulator. A cooling braid was formed from approximately 50 strands of 0.3 mm diameter pure gold wire which were clamped at each end with a copper plate. The upper end of this braid was clamped to the lower end of the cold finger while the lower end of the braid was clamped to the upper sapphire insulator.

The cold finger, which was similar to the one described by Seidman et. al.,[40] consisted of essentially two heat exchangers as shown in Fig. 5. The bottom of the cold finger contained a hollow copper rod with a bored hole that served as a liquid helium reservoir. The walls of this rod were extended upward 50 mm around the outer vacuum jacket of the liquid helium transfer tube. The cold exhaust gas from the boiling liquid helium was forced between the vacuum jacket and the copper tube and consequently cooled the copper rod at the bottom of the cold finger. This feature was found to be crucial in the initial cool down when most of the liquid helium boiled before reaching the end of the cold finger and all of the cooling was performed by the cold helium gas.

Approximately 150 mm from the bottom of the cold finger was a second copper tube ~ 100 mm in length which surrounded the vacuum jacket of the transfer tube. This copper tube served as a heat exchanger for cooling the radiation shields which surrounded the cold finger. The lower end of the radiation shield was connected by a second gold braid to the radiation shield surrounding the goniometer stage.

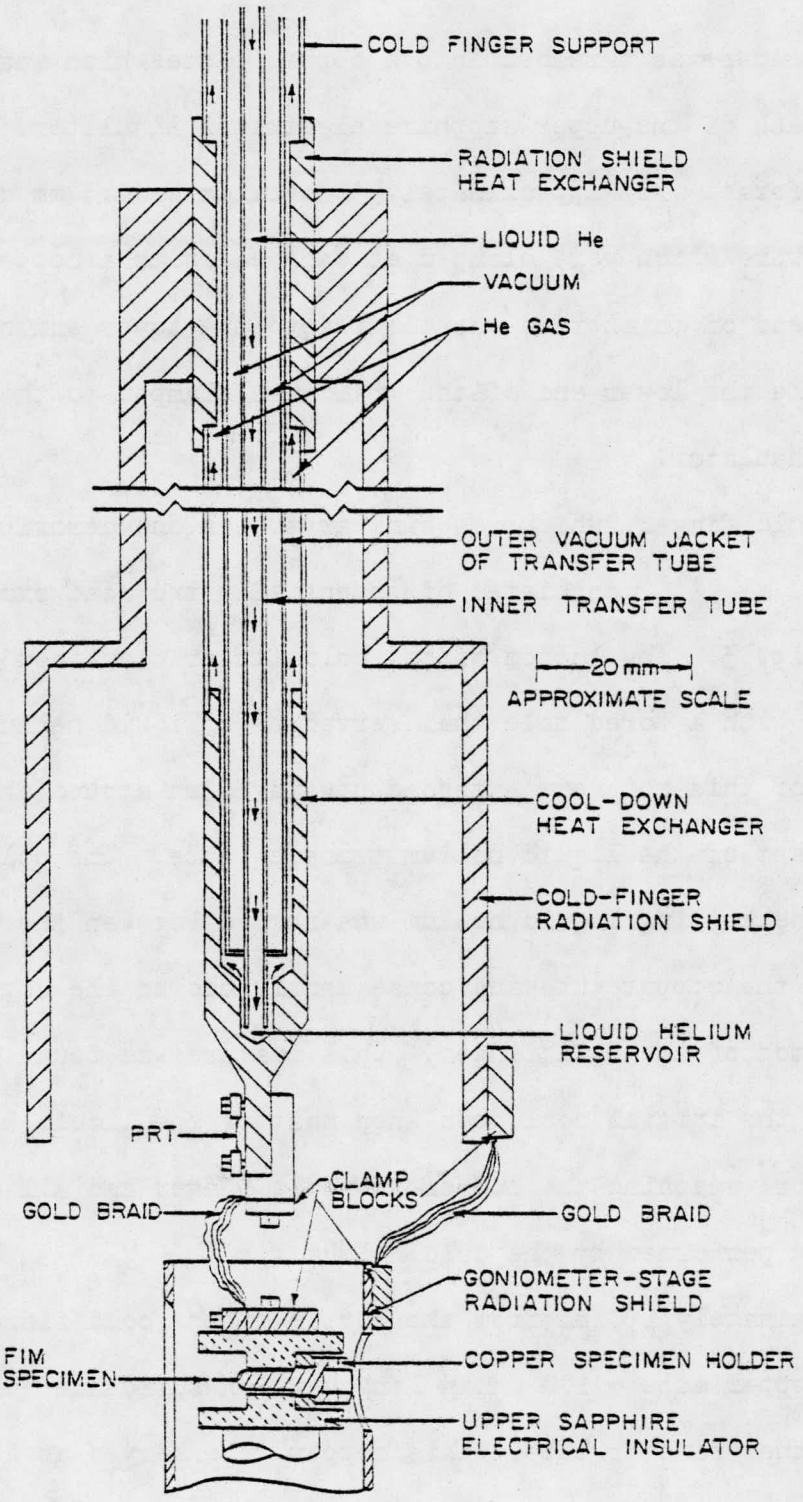

Figure 5. A cut-away view of the liquid-helium cold-finger. The FIM specimen is cooled by both the liquid helium and the cold helium gas. The radiation shields are cooled by the helium exhaust gas.

The upper sapphire electrical insulator of the goniometer stage was thermally isolated from the lower part of the cryostat by a 12 mm diameter stainless steel tube with a 50 μm wall thichness as shown in Fig. 4. Beneath this was the lower sapphire electrical insulator (similar to the upper sapphire insulator) which was capable of supporting an optional high-voltage pulse ring. This ring, which is not shown in the figure, was able to be pulsed negative with respect to the specimen when desired.[14] In addition, a copper plate supported from the top of the upper sapphire insulator and extending down in front of the specimen has also been omitted from the figure. This plate had a 0.250 inch diameter hole in-line with the specimen and served as a defining aperture for the low-energy gas ions employed to irradiate the specimen. By defining the irradiated area, accurate measurement of the flux and hence the fluence of the irradiating ions was obtained. This plate was clamped between the upper sapphire insulator and the copper plate at the end of the gold cooling braid and thus was maintained at ground potential and at the specimen temperature. In assembling the cryostat, 50 μm thick gold gaskets were inserted between all clamped heat-conducting surfaces such as the copper plates on top of the upper sapphire electrical insulator.

The cooling ability of the helium-cooled goniometer stage was tested by mounting platinum resistance thermometers (PRT) on the top of the upper sapphire insulator and on the bottom of the cold finger. In addition, iron-constantan thermocouples were attached to the copper specimen holder and the radiation shields

which surrounded the cold finger and the goniometer stage. The results of these tests showed that the specimen was cooled to 30 K within ~ 20 minutes and to 13 K within ~ 1 hr at a liquid helium consumption rate of approximately 1.7 liquid liters per hour. At temperatures greater than ~ 50 K the consumption decreases to less than 0.5 liter hr^{-1}. The thermal gradient across the inner cooling braid (see Fig. 4) was a function of the specimen temperature and total cooling time but was typically between 7 and 12 K under normal operating conditions. Within the accuracy of the measurements[40], the specimen was at the same temperature as the bottom end of the inner cooling braid. The radiation shields were found to cool more slowly than the inner specimen support but reached 100 to 150 K within approximately 1 hr. In routine operation, the specimen temperature was measured by the PRT located on the top of the upper sapphire insulator; this PRT is not indicated in Figs. 4 and 5.

The goniometer supporting the specimen mount was adapted from plans supplied by Dr. S. S. Brenner of U. S. Steel Corporation. This goniometer provided rotation of the specimen about two orthogonal axes which intersected at the tip of the specimen. Ultra-high vacuum conditions were maintained through the use of two linear-motion stainless steel bellows. As shown in Fig. 4, the entire specimen mount was supported on an arm at the end of a hollow rotating tube. This tube-arm assembly was rotated about a horizontal axis by a bell crank coupled to the inside of one of the bellows seals. The outside of this bellows seal was moved in and out by

a crank and lead screw threaded through a fixed plate.

Motion about the vertical axis was provided by a bearing at the lower end of the support arm. The lower support shaft which passed through this bearing was turned by a crank that was linked to the inner sliding shaft. This shaft passed through the outer rotating tube and was coupled to the inside of a second bellows assembly. The two bellows assemblies were connected to the vacuum system via two of a total of three ports machined into a stainless steel block. This block was mounted on three machinist's slides and was connected to the vacuum system through a third bellows seal so that the entire goniometer stage could be translated in three mutually orthogonal directions. The motion provided by the three external machinist's slide was essential for the initial alignment of the specimen with the probe tube and the ion gun and for making small corrections to the alignment during an experiment.

The goniometer stage provided precise and reproducible rotation of the specimen and allowed any region of the specimen's surface to be projected over the probe hole in the internal image intensification system. Due to the compact design of the goniometer stage, the lateral position of the tip varied by less than 1 mm when the tip was rotated through its full arc.

2.3 Low-Energy Gas Ion Gun

A simple low-energy gas ion gun[41-44] was constructed for irradiating FIM specimens <u>in-situ</u>. A schematic diagram of the ion gun is shown in Fig. 6. The ion gun was designed so that the plasma

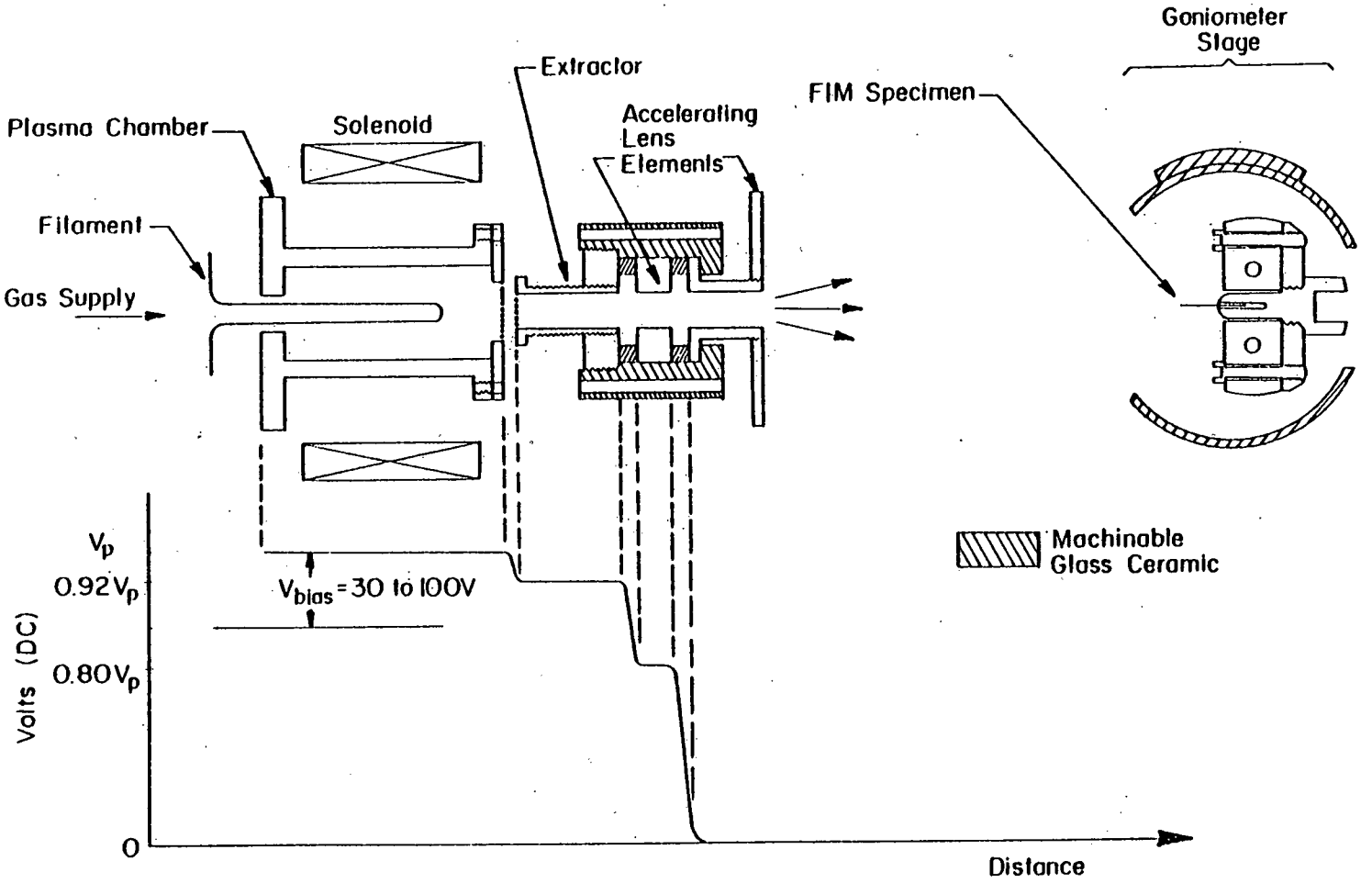

Figure 6. A schematic diagram of the low-energy ion gun.

chamber and the lens elements may be floated above ground potential which permited irradiations to be performed with the FIM specimen held at ground potential. This avoided the problem of field-emission induced melting and failure of the specimen which often occured when irradiations were performed with a negative potential applied to the specimen.

When operating the ion gun, a gas such as hydrogen, helium, neon or xenon was continously bled through a stainless steel cylindrical plasma chamber held at a positive potential. The plasma chamber was located in the center of a solenoid which produced a magnetic field of a few hundred gauss. The gas was ionized in the plasma chamber by a magnetically-confined 2 mA beam of 30 to 100 eV electrons emitted from a heated tungsten filament. The ions produced in the plasma chamber were extracted, accelerated and focused onto the FIM specimen. Since the FIM specimen was maintained at ground potential, the kinetic energy of the ions striking the specimen was equal to the product of the charge on the ion and the potential applied to the plasma chamber. Predominately singly-charged ions were produced by maintaining the energy of the ionizing electrons below the second ionization potential of the gas. The ion gun has produced a 4 cm diameter beam of 200 to 3000 eV gas ions at current densities of 0.01 to 10 $\mu A\ cm^{-2}$ with gas pressures of $3 \cdot 10^{-6}$ to $5 \cdot 10^{-4}$ torr respectively.

In order to preserve UHV conditions when the ion gun was operated, it was necessary to thoroughly outgas the ion source. This was accomplished by operating the ion gun during the UHV bakeout

cycle. The plasma chamber and all lens elements were placed at ground potential. The filament was then biased to -1000 Vdc and the filament current was increased until approximately 40 mA of emission current was obtained. The entire system was then baked for approximately 24 hours. The ion gun was then placed into the normal operating mode i.e., 10 mA emission current at -100 Vdc with respect to the plasma chamber, a plasma chamber potential (V_p) of 200 to 3000 Vdc, and the extraction and accelerating electrodes set at 0.92 and 0.80 of V_p respectively. After ~ 1 hr the bakeout ovens were turned off. This procedure was repeated each time a specimen was exchanged.

The low-energy ions can be employed to produce a sea of SIAs by the focused-replacement collision-sequence (RCS) mechanism.[45] As a result of the RCS mechanism, the immobile vacancies remain at the irradiated surface and the SIAs are injected into the bulk of the FIM specimen. The vacancies may then be completely removed by field evaporating several surface layers. This is the only presently known mechanism of producing a point defect state consisting solely of isolated SIAs. The ion gun can also be used to implant gas atoms such as helium in the tip of the FIM specimen (see section 7).

An experiment testing the performance of the low-energy gas ion gun was conducted in which a tungsten specimen maintained at 30 K was irradiated with 275 eV Ne^+ ions. After removing the damaged surface layer by field evaporation, an isochronal-annealing experiment was performed which revealed the presence of SIAs migrating to the surface of the FIM tip as expected.[10, 46-51]

2.4 Ultra-High Vacuum System

The use of an ultra-high vacuum system minimizes the interaction of residual gas atoms with the FIM specimen in two important ways; (1) it reduces the number of peaks observed in the (m/n) spectra by decreasing the absolute number of metal-atom gas-atom complexes which form, and (2) it reduces the concentration of artifact contrast effects which are produced as a result of impurity-gas-atom surface-atom interactions, for example artifact vacancies[8,9] and SIAs.[51] The minimization of artifact contrast effects was particularly important in the experiment described in section 7.

A schematic diagram of the vacuum system is shown in Fig. 7. The stainless steel main chamber was connected directly to a Varian 916-0014 titanium sublimation pump (TSP) and subsequently through a 4 inch diameter right-angle valve to a Varian 912-7000 140 liter sec^{-1} diode Vac-ion pump. The FIM was rough pumped by two Varian sorption pumps. The use of the TSP, ion pump and sorption pumps maintained ultra-clean conditions and avoided contamination with pump oils. The sorption pumps were connected through the specimen exchange port so that they could be used either for rough pumping the main chamber or for rough pumping the specimen-exchange air lock to be described in more detail in the following section. A small TSP and a Varian 20 liter sec^{-1} triode ion pump were also connected to the specimen-exchange air lock. In addition a 2 inch diameter Consolidated Vacuum Corporation diffusion pump, filled with DC 705 silicone-based oil, trapped with a Granville-Phillips liquid-nitrogen cold trap, and backed by an Alcatel Z2007 direct-drive mechanical

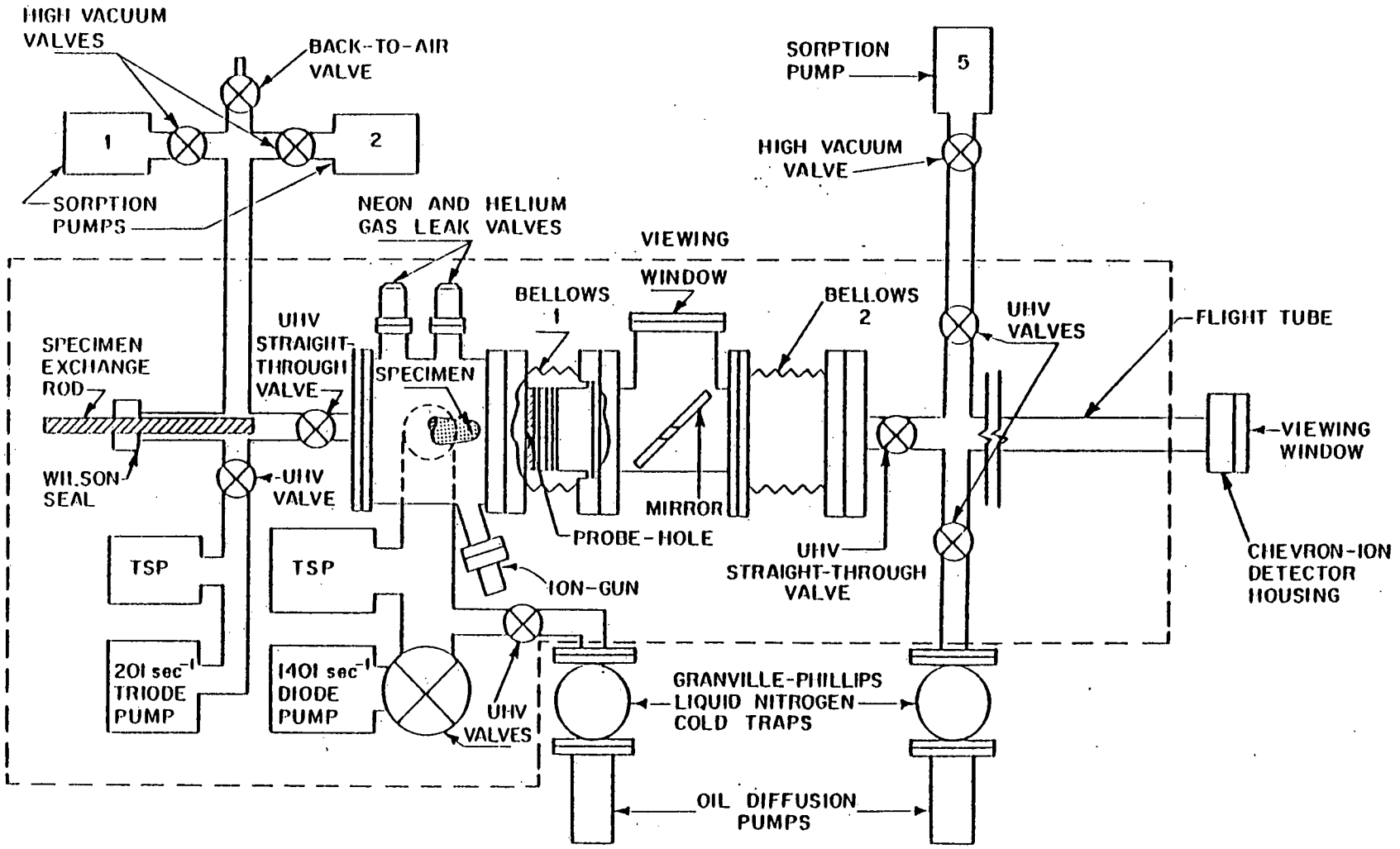

Figure 7. An overall view of the ultra-high vacuum system employed for the atom probe. Note that the flight tube has its own independent vacuum system. The dotted line indicates the extent of the bakeout ovens.

pump, was connected to the main chamber by a 1.5 inch diameter UHV valve. The diffusion pump was employed to pump the main chamber when the atom probe contained an imaging gas such as helium or neon, since the ion pumps and TSP cannot be used for this purpose. At all other times the diffusion pump was valved off to prevent possible back-streaming of oil into the vacuum system.

The internal image-intensification system containing the probe tube and the 45 degree viewing mirror was mounted on a double-sided 6 inch diameter flange which was connected to the fixed portions of the vacuum system by two 60190-5 bellows seals manufactured by the Metal Bellows Corporation.

The flight tube was isolated from the main chamber by a UHV straight-through valve and had a separate vacuum system consisting of a sorption pump and a liquid-nitrogen trapped oil-diffusion pump. This arrangement allowed a vacuum to be maintained in the ion-detector section even when the main chamber was not under vacuum and also provided the possibility of differentially pumping the flight tube to reduce the partial pressure of imaging gas in the flight tube.

As shown in Fig. 7 most of the vacuum equipment was located inside the electrically heated bake-out oven (indicated by the dotted line) so that adsorbed gases could be baked off the inner surfaces of the atom probe and thus lower the ultimate pressure which could be obtained. The sorption pumps, oil-diffusion pumps, and cold traps not inside the bake-out were all baked using separate heating mantles.

The entire vacuum system was carefully cleaned initially with tri-chlorethylene, acetone and ethanol using an ultrasonic cleaner

for the smaller pieces and mechanical scrubbing for the larger components. Ultimate pressures of $< 2 \cdot 10^{-10}$ torr were obtained after baking to ~ 160 C for several hours, while under typical operating conditions the pressure was $< 1 \cdot 10^{-9}$ torr. The pressure above the cold trap on the main-chamber diffusion pump was less than $3 \cdot 10^{-10}$ torr.

A Uthe Technology Inc. (UTI) Model 100C residual-gas analyser was installed on the atom probe which allowed the composition of residual gases in the vacuum system to be determined. This instrument proved to be particularly valuable for determining whether specific impurity atoms originated in the specimen or were artifacts of the vacuum conditions. For example, the instrument was used to determine the CO and CO_2 levels in the vacuum system thus aiding in the interpretation of the peaks observed at atomic mass 16 in the atom probe (m/n) spectra which could have been due to either titanium in the specimen or oxygen from the vacuum system. Oxygen can be produced as a result of the decomposition of CO or CO_2 on the surface of the FIM specimen.

In addition, the analyser was employed to determine the maximum partial pressure of residual helium which could be tolerated in measuring the range of low-energy helium ions in tungsten. The analyser was also employed to optimize the vacuum processing procedure in order to minimize the partial pressure of residual helium during the atom probe analysis (see sections 7.3 and 7.5).

The typical residual gas composition at an ultimate pressure of $\sim 2 \cdot 10^{-10}$ torr was: $H_2 = 1.88 \cdot 10^{-10}$ torr, $He = 1.8 \cdot 10^{-12}$ torr,

$CH_4 = 1.0 \cdot 10^{-12}$ torr, $CO = 9.0 \cdot 10^{-12}$ torr, $CO_2 = 4.0 \cdot 10^{-13}$ torr and other gases $< 1 \cdot 10^{-13}$ torr.

2.5 Specimen-Exchange Device

A novel specimen-exchange device was incorporated into the design of the goniometer stage which allowed the FIM specimen to be replaced without breaking vacuum in the main chamber. The essential features of this device are shown in Fig. 8. The copper specimen holder was attached to the end of a 1 m long, 9.5 mm diameter specimen-exchange rod with a bayonet-type clip. The copper specimen holder was surrounded by a retractable protection shield which served as an alignment guide when screwing the specimen holder into the goniometer stage. The specimen-exchange rod passed through a Vacuum Research Corporation S102 Wilson-type sliding-motion feedthrough that was sealed with two viton gaskets which were lubricated with Apeizon L vacuum grease. The specimen-exchange rod passed through a Varian UHV straight-through valve which sealed the main chamber until the air lock had been evacuated. The air lock was rough pumped using two Varian sorption pumps in sequence and was then further evacuated employing a small TSP and a 20 liter sec^{-1} Varian triode ion pump. The pressure in the air lock was reduced to $\sim 10^{-6}$ torr before the exchange took place. The pressure in the main chamber remained below 10^{-7} torr during the exchange and dropped to $\sim 3 \cdot 10^{-9}$ torr in less than 1 hr after the exchange. By eliminating the long pump-down period that was required if the main chamber was brought back to atmospheric pressure, the specimen exchange device reduced the time required for specimen replacement to $\sim$ 2 hours.

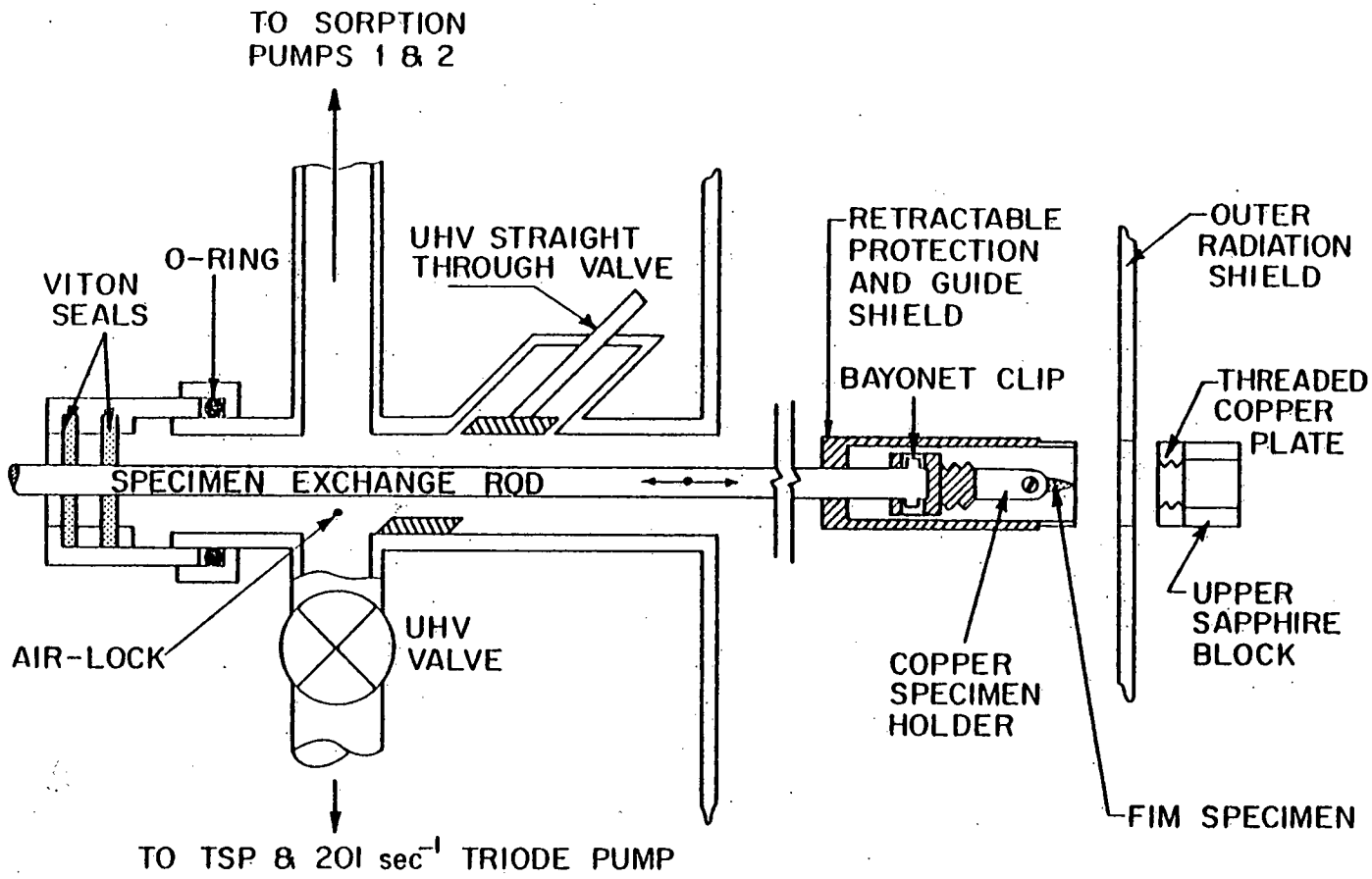

SPECIMEN EXCHANGE DEVICE

Figure 8. The high-vacuum specimen exchange device which allows a specimen to be changed without breaking the vacuum in the main chamber.

3. TIME-OF-FLIGHT MASS SPECTROMETER

This section contains a description of the components of the TOF atom probe FIM that were primarily employed to determine the (m/n) ratios of the pulsed field evaporated ions. The general features of the TOF mass spectrometer are described first and then some details of the most important subsystems namely, the specimen voltage system, the Chevron ion detector and the digital timer are described. The calibration procedure for the TOF atom probe FIM is also discussed. The computer system is described only to the extent necessary for understanding the operation of the mass spectrometer since a more detailed description is presented in section 4.

A block diagram of the TOF mass spectrometer is shown in Fig. 9. The FIM specimen was connected to a high-voltage dc power supply and was maintained at a positive potential sufficient to field ionize the imaging gas atoms but below the potential required to field evaporate the specimen atoms. A high-voltage pulse was capacitively coupled to the specimen which momentarily increased the potential on the specimen to a value which was sufficient to field evaporate a few atoms. This high-voltage pulse was triggered by the computer. The controls of the dc and pulse high-voltage power supplies as well as the power supply for the electrostatic lens were mechanically ganged together as shown in Fig. 10. By ganging the controls, the pulse and the lens voltages were maintained at a fixed fraction of the dc voltage. The advantages of having the pulse voltage track the dc voltage are discussed in sections 3.4 and 3.5 which deal with the calibration of

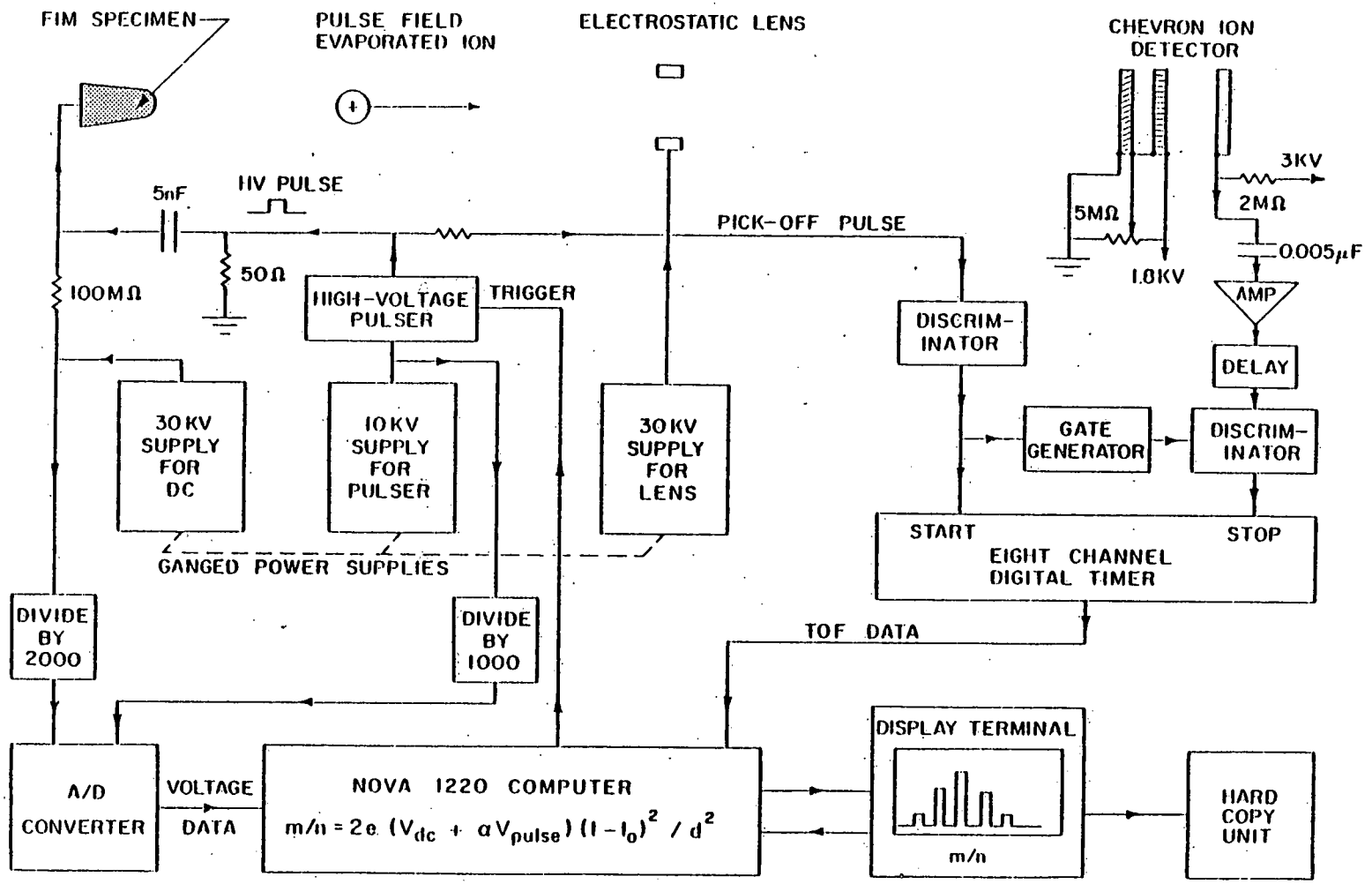

Figure 9. A block diagram of the TOF mass spectrometer illustrating the operation of the system. The digital timer and specimen voltage system shown in the lower part of the figure are operated automatically by a Nova 1220 minicomputer which is interfaced to a Tektronix 4010 graphics display terminal and a 4610 hardcopy unit so that data can be plotted on-line during the course of an experiment.

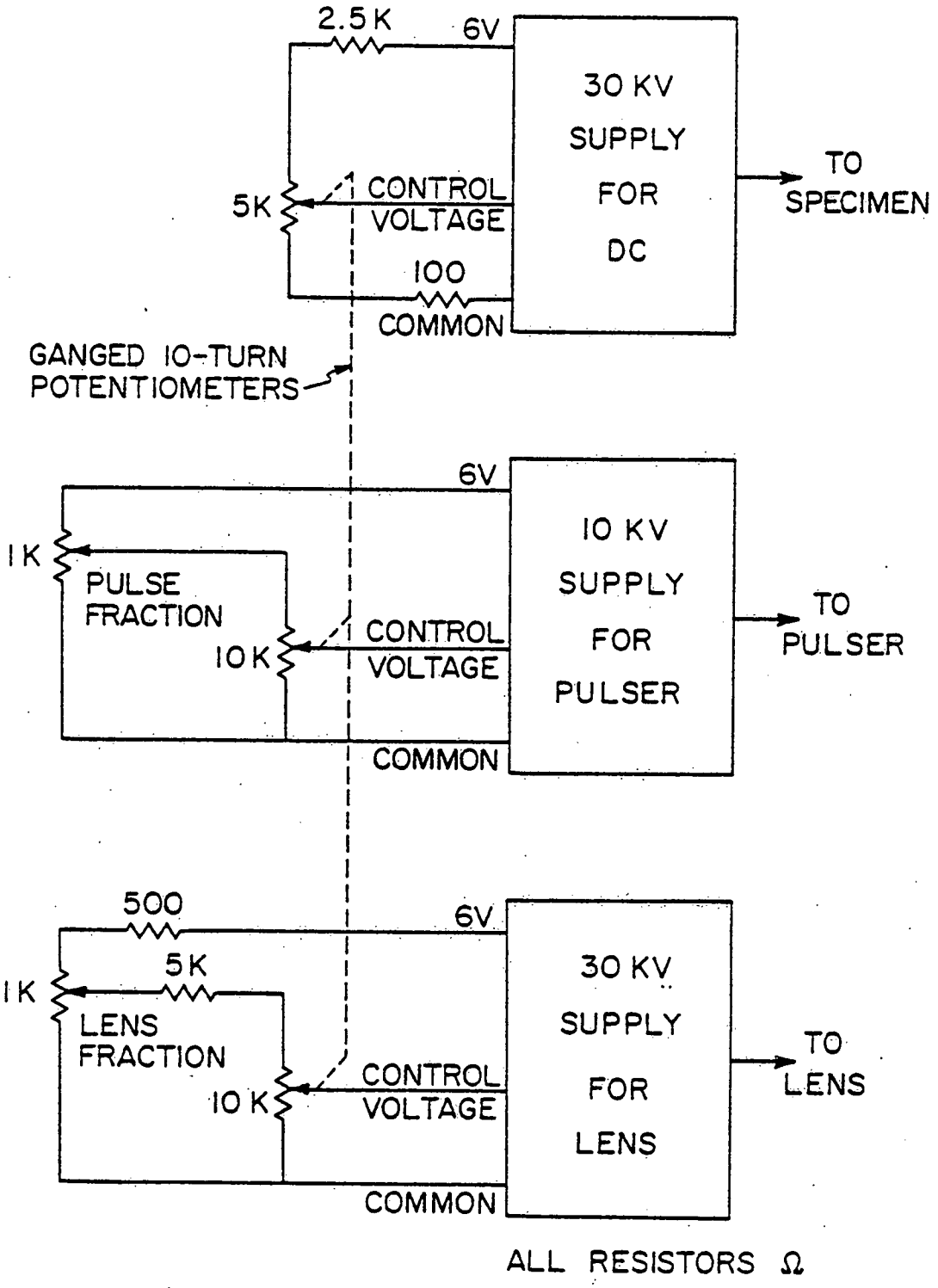

Figure 10. The voltage system for the atom probe indicating the method of coupling the controls for the power supplies so that the pulse and lens voltages are maintained at a constant fraction of the dc voltage.

the mass spectrometer and the mass resolution of the spectrometer respectively. The outputs of the high voltage power supplies were measured by the analog-to-digital (A/D) converter and input to the computer whenever a TOF measurement was made. A small fraction of the high-voltage pulse was picked off and fed to a discriminator which started the digital timer and also triggered a gate generator. The voltage pulse produced when an ion struck the Chevron ion detector was amplified, delayed ~ 500 nsec, and then fed to the stop discriminator. The stop discriminator was gated by the gate generator which was typically set to open ~ 600 nsec after the start pulse. Delaying the stop pulses and gating the stop discriminator ensured that any interference from the high-voltage pulse did not improperly trigger the stop discriminator and that only true events were detected*. A total of eight consecutive stop signals could be analyzed and thus eight ion species could be identified. The TOF data was stored in binary-coded-decimal (BCD) format within the timer until the computer was ready to read the TOF data. The computer calculated (m/n) using the TOF and voltage data employing a modified form of equation 2 as discussed in section 3.4.

After the (m/n) values were computed they were stored in the computer memory in the form of a histogram of the number of atoms

---

* Interference of the high-voltage pulse with the detector system was eliminated by thoroughly shielding the high-voltage pulse generator, the pulse termination resistor and the detector, and by employing only type 142 B/U coaxial cable for the high-voltage pulse cable and the detector cable. Type 142 B/U cable has a double braided shield with an inner Teflon dielectric. No pickup of the high-voltage pulse by the detector system occured for pulses which were less than 2 kV in amplitude.

detected versus (m/n). In addition the TOF and voltage data were stored on a magnetic cassette tape so that the results of the run could be re-analyzed in the future. The computer was interfaced to a Tektronix 4010 graphics display terminal and a Tektronix 4610 hard copy unit which enabled histograms of (m/n) to be displayed graphically and permanently recorded in less than 1 min. In the following subsections the specimen voltage system, the Chevron ion detector, and the digital timer are described in detail. Since the large number of interacting systems in this atom probe were principally under the control of the computer during operation, the performance of each system was thoroughly tested so that the data accumulated during an experiment could be treated with absolute confidence. Some of the results of these performance tests have been included in the following discussions.

3.1 Specimen Voltage System

This section contains a description of the dc and pulse high-voltage power supplies, the high-voltage pulser, and the high-voltage measuring system. Design of this system was found to be critical to the overall performance of the TOF mass spectrometer. As shown in Fig. 9 the FIM specimen was connected through a 100 MΩ pulse-blocking resistor to a Spellman RHR 30PN30* high-voltage power supply. A 20 nsec long high-voltage pulse with a rise time of < 1 nsec produced by a Cayuga Associates CA-101 mercury-relay charging-line

---

* Due to long term stability problems, this supply was replaced by a CPS 100R power supply.

pulser was coupled to the FIM specimen through a 4.7 nF, 30 kV capacitor. A Spellman RHR 10PN100 high-voltage power supply was used to provide the high-voltage to the pulser. The output of the charging-line pulser was approximately one-half of the supply voltage.

As shown in Fig. 10 the controls of the high-voltage dc, pulse and lens power supplies were coupled together so that the pulse and lens voltages were maintained at a constant fraction of the dc voltage. The 5 kΩ ten-turn potentiometer in the dc power-supply control circuit and the 10 kΩ ten-turn potentiometers in the pulse and the lens power-supply control circuits were mechanically ganged together so that they tracked one another to within 0.05 %. The two 1 kΩ potentiometers in the pulse and the lens supply circuits control the pulse and the lens fraction respectively. The 2.5 kΩ resistor in the dc supply circuit and the 500 Ω resistor in the lens supply circuit were included to limit the range of these two supplies to 20 kV maximum. The 100 Ω resistor in the common return line of the dc supply circuit was introduced to allow the zero points of the pulse and dc supplies to be adjusted for optimum linearity. The pulse voltage was typically maintained at 4 to 20 % of V_{dc} and the lens was maintained at 30 to 55 % of V_{dc}. Below approximately 4 % of V_{dc} the charging-line pulser behaved erratically and the continous dc field evaporation rate became comparable to the pulse field-evaporation rate. Above 20 % of V_{dc} the increased spread in the energy of the field evaporated ions degraded the mass resolution of spectrometer and breakdown within the mercury relay capsule in the

high-voltage pulser occured.

The values of V_{dc} and V_{pulse} were measured employing an Analogic 5800 series, 13 bit, 16 channel A/D converter which consisted of a multiplexer module with 16 differential inputs, a 50 nsec sample and hold module, and a 13 bit A/D converter module. The input channel was computer selected and analog inputs of 0 to $\pm$ 10 V were converted in $\sim$ 100 μsec to a 13 bit binary number. The first bit represented the sign and the remaining 12 bits represented the magnitude of the input voltage, hence the resolution of the A/D converter was 1 part in 4096.

The outputs of the high-voltage power supplies were reduced by precision voltage dividers so that these voltages were within the 10 V maximum range of the A/D converter. The dc voltage divider is shown in Fig. 11 and contained two voltage division stages. The first stage, which consisted of one-hundred-sixteen 0.825 MΩ half-watt metal-film resistors[52] in series with a single 0.825 MΩ resistor of the same type, was encapsulated in Dow Corning Sylgard 184 resin to prevent high-voltage breakdown. The second stage consisted of two 1.5 MΩ half-watt metal-film resistors in series with 0.233 MΩ. Since the first stage was constructed from 117 identical resistors, variations of resistance with either voltage or temperature did not affect the voltage division ratio of this stage. The use of identical resistors in the second stage was found to be unnecessary. The pulse voltage divider consisted of fifty 1.5 MΩ half-watt metal-film resistors in series with a 0.075 MΩ metal-film resistor. This simpler arrangement was found to be adequate for the pulse voltage

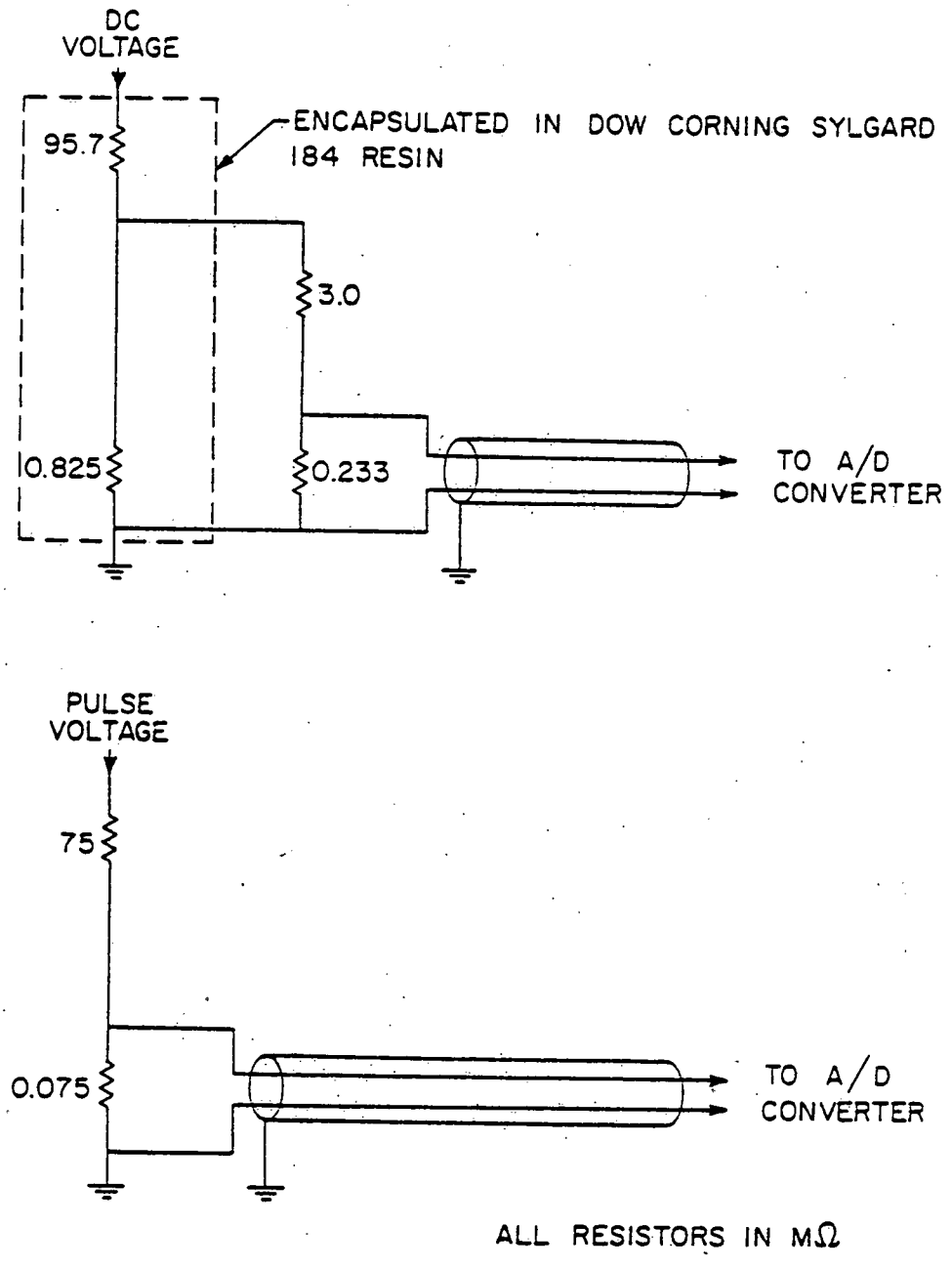

Figure 11. A schematic diagram of the voltage dividing networks for the dc and pulse voltages.

measurement because the pulse voltage was typically less than 2 kV. The high input impedances (> 75 MΩ) of the voltage dividers minimized heating and the use of metal film resistors contributed to the stability of the dividers. Electrical noise was reduced below the resolution of the A/D converter by connecting both the power supply chassis ground and the A/D converter analog ground to a grounded water pipe.

The high-voltage power supplies, the voltage dividers, and the A/D converter were tested by monitoring the measured voltage on the computer and comparing it with the known voltage obtained using a high-precision Hewlett Packard 3439A digital voltmeter. These tests indicated that the voltages were known to within 5 volts which corresponded to one bit in the A/D converter. In addition the stability of the power supplies was tested by programming the computer to detect any changes in the output voltage. These tests indicated that the voltages were stable to within 5 volts over periods of several hours.

The shape of the high-voltage pulse was measured employing a Tektronix 7904 oscilloscope with a 7S11 sampling plug-in unit and an S-2 sampling head. Both a P6056 10x passive probe with an input impedance of 500 Ω and a rise time of 0.10 nsec and a P6057 100x passive probe with an input impedance of 5 kΩ and a rise time of 0.25 nsec were connected to the point at which the specimen was normally attached.

Typical pulse shapes are shown in Fig. 12. Figure 12(a) is a sketch of the overall pulse shape showing the large initial peak

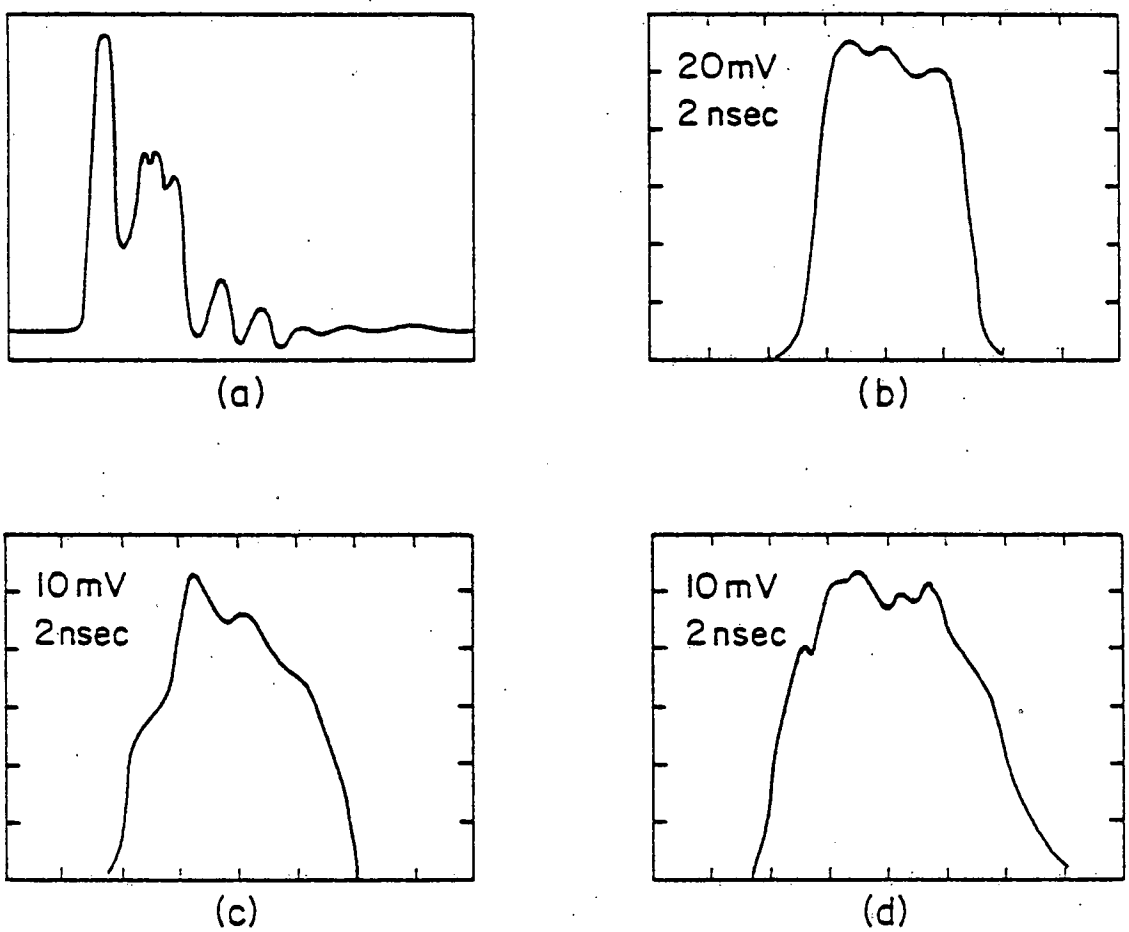

Figure 12. The shape of a 20 nsec high-voltage pulse at the specimen. Fig. 12(a) is a sketch of the overall pulse shape showing the large initial peak which is probably caused by reflections from the unterminated specimen. Figs. 12(b), (c), and (d) represent actual oscilloscope traces of the top of the initial peak which were measured with a Tektronix 7904 oscilliscope, 1S11 sampling plug-in, and S-2 sampling head. Fig. 12(b) was recorded with a P6056 10x probe connected to the specimen holder. Fig. 12(c) was recorded with a P6057 100x probe connected directly to the specimen holder while Fig 12(d) was recorded with the probe connected to the specimen holder by a wire 2 cm in length.

which was probably caused by reflections from the unterminated specimen. Figures 12(b), (c), and (d) represent actual oscilloscope traces of the top of the initial peak. Figure 12(b) was recorded with the 10x probe connected directly to the specimen holder. Figure 12(c) was recorded with the 100x probe connected directly to the specimen holder while Fig. 12(d) was recorded with the probe connected to the specimen holder by a 2 cm length of wire. The observed rise times were nearly equal to the inherent rise time of the probe and sampling head (0.35 nsec) which indicates that the pulse rise time was less than 0.2 nsec. Although the maximum height of the first peak was found to be sensitive to the position of the probe, the overall features of the pulse shape remained the same as can be seen from a comparison of Figs. 12(b), (c) and (d).

3.2 Chevron Ion Detector

In the TOF atom probe FIM the pulse field-evaporated ions are detected at the downstream end of the flight tube by a fast electron multiplier. A large number of electron multipliers such as the curved channel electron multiplier,[53] the Johnston detector,[54] the magnetic strip detector[55] and the channel electron multiplier array (CEMA)[15,38] have been used in atom probe FIMs. The Chevron CEMA was employed in this atom probe because it has particle detection characteristics which are comparable or superior to those of any other detector and because it also produces a visible image of the ion beam which was found to be extremely useful for the alignment and focusing of the TOF spectrometer.

Two 25 mm diameter CEMAs were used in the Chevron configuration as shown in Fig. 9. The 37.3 μm diameter channels in the first CEMA were oriented at an angle of 5 degrees with respect to the normal to the front surface of the CEMA. This prevented secondary ion feedback through both CEMAs. The magnitude of the voltage applied to each of the two CEMAs can be varied since the incidence of after-pulses due to ion feedback through the CEMAs was shown to be substantially reduced by applying 60 % of the total voltage across both CEMAs to the first CEMA.(53)

Behind the two CEMAs was a 25 mm diameter phosphor screen which was prepared in the same way as the viewing screen described in section 2.1. The screen at the detector was capacitively coupled to a LeCroy Research System (LRS) 133B dual amplifier which was operated at a gain of ~ 49. The output of the amplifier was delayed 500 nsec by ~ 150 m of RG 58 coaxial cable. This delayed output then triggered on channel of an LRS 161 dual discriminator which stopped the digital timer.

Two tests were performed on the Chevron ion detector to determine the frequency of spurious pulses. The first test was a measurement of the background count rate and the second test involved a measurement of the frequency of artifact pulses following the true pulse. The Chevron ion detector must be well characterized with respect to spurious pulses if small concentrations (e.g., in the 10^{-5} at. fraction or lower range) of impurities or alloying additions are to be reliably measured.

Background counts from the Chevron ion detector were produced

both by spontaneous emission within the CEMAs and by ionization of residual gases at the FIM tip. With the tip voltage off, a total voltage across both CEMAs of 1850 Vdc, and with 50 % of the total voltage applied to the first CEMA, the dark current due to spontaneous emission was found to be < 1 count sec^{-1}. With the specimen at the imaging voltage and with a background pressure of $\sim 4 \cdot 10^{-10}$ torr, the count rate rose to ~ 10 counts sec^{-1}. The increase in the count rate when a potential was applied to the specimen was attributed to field ionization of the residual gases in the FIM. For example, when the FIM was back-filled with helium gas to a pressure of $4 \cdot 10^{-6}$ torr the ion count rate was $\sim 10^5$ counts sec^{-1}. Thus with a pressure of $4 \cdot 10^{-10}$ torr a background count rate of ~ 10 counts sec^{-1} would be expected in agreement with the observation. Since the digital timer had a maximum range of 90 μsec the time window of the TOF mass spectrometer was open for $\sim 10^{-4}$ sec. Thus a background count rate of 10 sec^{-1} would lead to a background of $1:10^3$ over the whole spectrum of (m/n) from 0 to ~ 200 amu. This yields a background of $1:2 \cdot 10^{-5}$ per amu in the (m/n) spectra. Therefore impurities or alloying additions in the 10 appm range could be detected if more than 1 or 2 ions were detected.

Artifact pulses following the true pulse were caused by ringing in the detector circuit and by after-pulses produced when secondary ions feed back through the channels of the CEMAs. Ringing in the detector circuit was observed with a Tektronix 7904 oscilloscope with a 7A11 plug-in unit. Since the ringing decayed within ~ 50 nsec, it was possible to eliminate any effects of the ringing by increasing

the width of the discriminator output pulse to ~ 55 nsec. The addition of a small parallel inductance to the output screen of the detector employing a trial-and-error method resulted in a substantial decrease in the ringing. This allowed a decrease in the discriminator output pulse width to ~ 20 nsec without detecting any change in the incidence of after-pulsing. Thus the detector dead time was ~ 20 nsec.

The incidence of after-pulses was tested with the digital timer. The output of the discriminator which was connected to the Chevron ion detector was fed into both the start and the stop inputs of the digital timer. The digital timer was started by the first random pulse which occurred in the detector and was stopped when another random pulse or an after-pulse occurred. With a pressure of 10^{-7} torr of helium gas in the FIM, the count rate was 1400 counts sec^{-1} when a potential was applied to the FIM specimen. Since the timer was set to record all events occurring within 10 μsec after the first random pulse, a background of 0.014 counts following the first random pulse would be expected. The observed fraction was 0.018 ± 0.002 which indicated that the frequency of after-pulses was $\sim 0.004 \pm 0.002$.

The effect of gas pressure on the incidence of after-pulsing was determined by increasing the helium gas pressure to $2 \cdot 10^{-6}$ torr while maintaining the total count rate at 1400 counts sec^{-1} by deflecting the ion beam slightly. The observed fraction of random pulses was 0.016 ± 0.002 which indicated that the fraction of after-pulses was $\sim 0.002 \pm 0.002$. Thus the occurence of after-pulses under normal operating conditions was negligible.

3.3 Digital Timer

The digital timer which measured the TOF of the pulsed field evaporated ions was the key electronic instrument in the mass spectrometer. There are basically three types of timing instruments that could have been employed with the atom probe.

The most commonly used timer was either a fast oscilloscope[56] or a storage oscilloscope.[15] The oscilloscope has the advantage that it is simple and relatively inexpensive, and is capable of a high precision over a limited time range. For example, using the delayed sweep a short time interval can be expanded to obtain a time resolution of $\pm$ 1 nsec over a 100 nsec range which might correspond for typical conditions to $\pm$ 0.03 amu over a 3 amu range. The disadvantages of the oscilloscope are twofold. First, each event must be analyzed individually by examining photographs of the oscilloscope traces. Second, although the oscilloscope is very precise over short intervals the absolute accuracy over longer intervals is not good due to the nonlinearity of the sweep delaying circuit. Moreover only part of the (m/n) spectrum can be examined at one time and thus events occurring outside that region are not detected.

The second timing instrument that could be used is a time-to-amplitude converter (TAC).[57] In this instrument a constant current source begins charging a capacitor when a START pulse is received and stops charging it when a STOP pulse is received. Thus the voltage across the capacitor is proportional to the time interval between the start and stop signals. The TAC has the advantage that the measured times can be digitized and therefore automatically analyzed. In terms of time resolution it has the same advantages and disadvantages

as the oscilloscope. It can provide a high resolution over a limited time interval (± 50 psec over a 50 nsec range), but over longer time intervals the accuracy is limited by a non-linearity of ~ 0.1 %.

The third timing instrument, and the one which has been employed in this computer-operated atom probe, is the digital timer.[16,37,58] When operating the timer, a high precision oscillator produces clock pulses with a precisely known period. Digital circuits count the number of clock pulses which occurred between the start and stop signals of the time interval which is to be measured. The advantages of the digital timer are that the output is directly compatible with a computer and the accuracy over long time intervals is excellent. The principal disadvantage is that the resolution is limited to ± 1 clock period. Since digital counters with a bandwidth exceeding 100 MHz are difficult to construct, the time resolution is usually limited to ± 10 nsec.

The digital timer that has been constructed[37] was capable of measuring the TOF of up to eight consecutive ions for a TOF as large as 90.00 μsec with an accuracy of ± 0.01 μsec. A greatly simplified schematic diagram of this instrument is shown in Fig. 13. The START signal was derived from the high-voltage pulse applied to the specimen and was fed into the AND gate input of CLOCK-IN on the START SYNCHRONIZER FLIP-FLOP. The other input of this AND gate was supplied with CLOCK pulses from the 100 MHz oscillator. The TRUE OUTPUT opened the CLOCK AND GATE thus allowing CLOCK pulses to pass through to the eight counters. Using this arrangement, a START signal caused the OUTPUT of the START FLIP-FLOP to switch to the TRUE or + 1 state

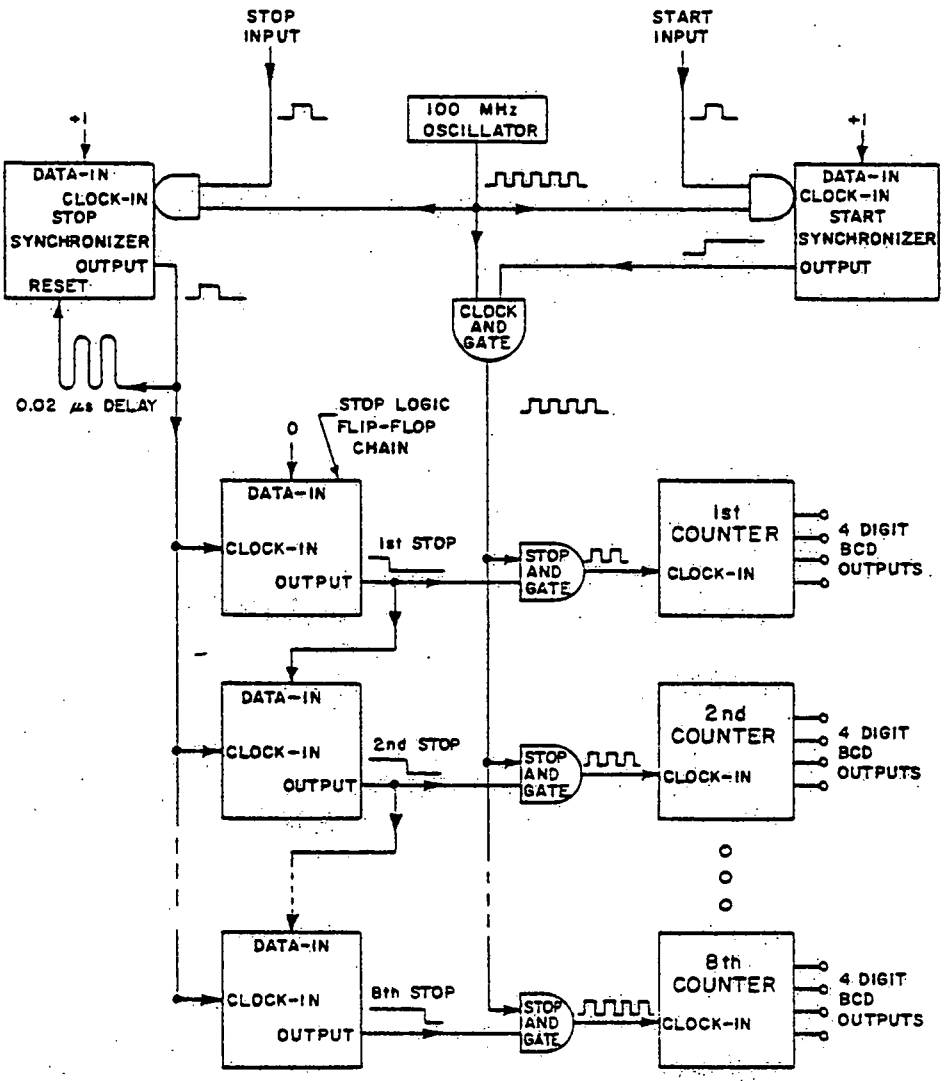

EIGHT-CHANNEL DIGITAL TIMER

Figure 13. A block diagram illustrating the principle of operation of the digital timer.

synchronously with the CLOCK thus ensuring that the amplitude and width of the first CLOCK pulse to the eight counters was identical to all subsequent pulses. This ensured that all eight counters were able to detect the first CLOCK pulse.

The STOP signal was synchronized in a similar way so that the OUTPUT of the STOP SYNCHRONIZER FLIP-FLOP switches to the TRUE state synchronously with the CLOCK. The OUTPUT signal was delayed by 0.02 0.02 μsec and fed into the RESET input of the STOP SYNCHRONIZER FLIP-FLOP which caused the OUTPUT to switch FALSE. Thus a STOP signal caused a pulse of approximately 0.02 μsec duration which was synchronous with the CLOCK to be produced at the OUTPUT of the STOP SYNCHRONIZER FLIP-FLOP. This STOP OUTPUT pulse was fed into the CLOCK-IN of the STOP-LOGIC FLIP-FLOP CHAIN.

The STOP-LOGIC FLIP-FLOPS, which have the property that the OUTPUT is switched to the value present at DATA-IN whenever a pulse is applied to CLOCK-IN, were interconnected so that each FLIP-FLOP was triggered in sequence when a STOP signal was received. This was accomplished by connecting DATA-IN of each FLIP-FLOP to the OUTPUT of the preceeding FLIP-FLOP. Thus when the first stop signal was received, only the first FLIP-FLOP changed state since its DATA-IN input was always equal to 0 or FALSE. None of the succeeding FLIP-FLOPS were triggered since their DATA-IN inputs were connected to the OUTPUTS, all of which were initially TRUE. When the second STOP signal was received the second FLIP-FLOP was triggered since the OUTPUT of the first FLIP-FLOP was now FALSE. Since the OUTPUTS of each of the STOP-LOGIC FLIP-FLOPS were connected to one of the inputs

of each of the eight STOP AND GATES of the corresponding COUNTER-CHAIN, the counters were stopped in sequence as the STOP signals were received. Since the STOP-LOGIC FLIP-FLOPS changed state synchronously with the CLOCK, the STOP AND GATES were closed in synchronization with the CLOCK. Thus the last CLOCK pulse to each of the COUNTER-CHAINS was identical to all preceeding CLOCK pulses. The TOFs were read into the computer and following this a RESET pulse was sent out from the computer to the digital timer which returned all of the FLIP-FLOPS to the untriggered state and also reset all of the COUNTERS to zero in preparation for the next measurement.

The digital timer was tested by injecting pulses with known relative delays into the start and stop inputs. The computer was programmed to read in the measured times and test them for any variations. The results of this test indicated that the timer performed greater than 10^6 simulated measurements without an error, which allowed the TOF measured during an experiment to be treated with confidence. The synchronization of the start and stop of the COUNTING CHAINS with the 100 MHz CLOCK was found to be essential in order to realize the theroetical time resolution of $\pm$ 10 nsec. Tests conducted with asynchronous START and STOP signals indicated errors in time measurement as large as $\pm$ 70 nsec in up to 5 % of the cases.

3.4 Calibration of the TOF Atom Probe FIM

The (m/n) values were computed from the measured TOF, V_{dc}, and V_{pulse} employing the equation[59]

$$\frac{m}{n} = 2e(V_{dc} + \alpha V_{pulse}) \frac{(t - t_o)^2}{d^2} , \qquad (3)$$

where (m/n) is in amu, V_{dc} and V_{pulse} are in volts, t and t_o are in μsec, d is in mm and α is the dimensionless pulse factor. For this choice of units the constant 2e is equal to 193.0. The value of V_{pulse} was taken to be one-half of the dc voltage applied to the charging-line pulser. The quantity α was required because the peak pulse voltage reaching the tip was not equal to V_{pulse}. This discrepancy was caused by deviations from the ideal operation of the charging-line pulser, impedance variations along the pulse line, and reflections at the unterminated specimen. The quantity t_o was required because of the 500 nsec delay time which was intentionally inserted between the amplifier and the stop discriminator and because of other smaller time shifts occurring in the electronics and the detector. The length d denotes the flight path length determined by calibrating the instrument from known (m/n) values. The flight length (d) was used rather than the physical length of the flight tube since they were not necessarily equivalent distances. For example, the actual trajectory of the ion was affected by the focusing lens, the earth's magnetic field, and stray electrical and magnetic fields. In general, the TOF atom probe FIM must be calibrated using ions with known values of (m/n) before unknown (m/n)s can be identified. Since there has been some uncertainty in the past concerning the best method of calibrating the instrument, the following two methods that have been employed will be described in detail.

The first method employed was similar to the first of two methods described by Panitz, McLane and Muller[59]. It involved a systematic determination of the calibration parameters α, t_o, and d using the

TOF of two species of ions with known (m/n) values. The value of t_o was determined first. If $(m/n)_1$ and $(m/n)_2$ were the known (m/n) values and t_1 and t_2 were the corresponding observed TOF of the two species, then the quantity t_o is given by

$$t_o = \left\{ t_2 \left[\frac{(m/n)_1}{(m/n)_2}\right]^{\frac{1}{2}} - t_1 \right\} \Bigg/ \left\{ \left[\frac{(m/n)_1}{(m/n)_2}\right]^{\frac{1}{2}} - 1 \right\} \quad . \qquad (4)$$

Thus, for example, for $(m/n)_1 = 62$ amu ($^{186}W^{+3}$) and $(m/n)_2 = 4$ amu ($^{4}He^{+}$) and values of t_1 and t_2 of 14.17 μsec and 4.02 μsec respectively, the value of t_o obtained from equation 4 would be $t_o = 0.56$ μsec. The determination of t_o is most sensitive to the measured TOF of the lighter ion since this TOF is weighted by the factor $[(m/n)_1/(m/n)_2]^{\frac{1}{2}}$ which was 3.9 for the above example. To obtain the pulse factor, TOF measurements are made with two different sets of pulse and dc voltages. If t_1 was the TOF for a given isotope when the pulse and dc voltages were $(V_{pulse})_1$ and $(V_{dc})_1$ respectively, while t_2 was the TOF for the same isotope when the voltages were $(V_{pulse})_2$ and $(V_{dc})_2$, then the pulse factor (α) is given by

$$\alpha = \frac{(V_{dc})_2 (t_2 - t_o)^2 - (V_{dc})_1 (t_1 - t_o)^2}{(V_{pulse})_1 (t_1 - t_o)^2 - (V_{pulse})_2 (t_2 - t_o)^2} \quad . \qquad (5)$$

For typical experimental conditions, the pulse factor was found to be approximately 1.5 ± 0.05. By determining α and t_o, d can be obtained by solving equation 3 for the flight path length. This yields the following expression for d

$$d = (t - t_o)\sqrt{193.0 \cdot (V_{dc} + \alpha V_{pulse}) \cdot (n/m)} \quad . \qquad (6)$$

Employing equation 6 with V_{dc} = 8000 V, V_{pulse} = 400 V, t = 14.18 μsec and m/n = 62 amu ($^{186}W^{+3}$) a value of d = 2228 mm was calculated. As mentioned this method was similar to the one described by Panitz, McLane and Muller[59]. The principal difference in the two methods was the order in which the calibration parameters were determined. Their method had the advantage that the pulse factor was obtained without varying the voltage. The method described here had the advantage that t_o was essentially determined by the position of the $^4He^+$ peak, and was therefore accurately known. Both methods suffer from the fact that in practice it was difficult to determine the pulse factor with sufficient precision to prevent broadening individual peaks in the (m/n) spectra. To eliminate the problem of determining the pulse factor, a new method of calibrating this atom probe was developed. The basis of this procedure was to make V_{pulse} a constant fraction of V_{dc}

$$V_{pulse} = f\, V_{dc} \quad , \qquad (7)$$

where f is a constant. This was accomplished by mechanically coupling the potentiometers controlling the dc and pulse power supplies. The equation for (m/n) can now be rewritten as

$$\frac{m}{n} = \frac{2e(1 + \alpha f) \cdot V_{dc} \cdot (t - t_o)^2}{d^2} \quad . \qquad (8)$$

The lumped parameter $(1 + \alpha f)/d^2$ can be considered to be simply one

adjustable parameter. This reduced the problem of calibrating the atom probe to finding only two parameters, t_o and the effective length (d_{eff}), where d_{eff} is given by

$$d_{eff} = d/(1 + \alpha f)^{\frac{1}{2}} \quad , \tag{9}$$

so that the equation for determining (m/n) reduces to

$$\frac{m}{n} = \frac{2e}{d_{eff}^2} \cdot V_{dc} \cdot (t - t_o)^2 \quad . \tag{10}$$

Employing the Spellman RHR 30PN30 power supply the linearity of V_{pulse} with V_{dc} was only $\pm$ 1 %, therefore $(V_{pulse}/V_{dc}) = f \pm 0.01f$. (The linearity of V_{pulse} with V_{dc} was improved by at least a factor of ten by replacing the Spellman power supply with the CPS 100R power supply). In view of this variation of f with voltage, both V_{dc} and V_{pulse} were measured independently and the data were analyzed employing equation 3. With the tracking power supplies for V_{dc} and V_{pulse}, the calibration procedure was quite straightforward. A histogram of the number of atoms detected versus (m/n) was constructed employing reasonable estimates of α, t_o, and d. In a typical case, the ions He^+ and W^{+3} were used to calibrate the (m/n) scale. The position of the He^+ peak was very sensitive to the value of t_o, hence t_o was varied until the He^+ peak occurred at exactly 4 amu. Similarly, d was varied until the observed isotope peaks of W^{+3} occurred at the correct (m/n) values. This process was iterated until a self consistent set of t_o and d values were obtained. The calibration

always converged rapidly and not more than two iterative approximations have been found necessary.

A computer simulation was performed to test the sensitivity of the spectrum to the choice of α in view of the measured variation of f with voltage. These calculations indicated that for f = 0.05 f = 0.05$\pm$0.0005, a 100 % error in α (e.g., α varying from 1.00 to 2.00) lead to a broadening in the (m/n) peaks of less than 0.03 amu at 60 amu with V_{dc} ranging from $4 \cdot 10^3$ to $16 \cdot 10^3$ V. This uncertainty in (m/n) is much smaller than the uncertainty introduced by the TOF measurement i.e., $2\Delta t/t$ where $\Delta t = \pm 10$ nsec for this atom probe. The principal advantages of keeping V_{pulse} a constant fraction of V_{dc} are: (1) the value of α employed in equation 3 has a negligible effect on the shape of the peaks in the observed (m/n) spectra; (2) the shapes of the observed peaks do not depend on an exact determination of the calibration parameters α, t_o, and d (although the absolute positions do depend on an exact determination); and (3) possible changes in α with the position of the goniometer or the specimen-to-image intensification system distance have a negligible effect on the observed spectra. In addition, the mass resolution of the atom probe is no longer dependent on an exact determination of the calibration parameters as discussed in the next section.

3.5 Resolution of the TOF Mass Spectrometer

The mass resolution of the TOF atom probe FIM has been discussed at length in the literature.[56,60,61] There are three major factors affecting the resolution: (1) inaccurate determination or variations of the calibration parameters α, t_o, and d; (2) uncertainty in the

measurement of the TOF and the voltage on the specimen; and (3) energy deficits.

By maintaining V_{pulse} at a constant fraction (f) of V_{dc} it was shown in section 3.4 that the number of calibration parameters was reduced to two, namely d_{eff} and t_o. This technique thus eliminated the need for an accurate, independent determination of α. Furthermore the calibration parameters α and d now only affected the absolute values of (m/n) so that inaccuracies in their determination did not affect the mass resolution (Δm/n) of the atom probe. The remaining calibration parameter t_o can be measured electronically to a high degree of accuracy and poses no additional problems. In all of the results presented in this work the basic shape of the (m/n) spectrum has never been found to depend on an exact determination of the calibration parameters. Both α and t_o were maintained at constant values by employing high-quality, low-drift electronics. Thus the only remaining factors which affected the resolution were the uncertainties in the TOF and voltage measurement, variations in d and energy deficits.

For this mass spectrometer with a time uncertainty of $\pm$ 10 nsec, a voltage uncertainty of $\pm$ 3 V and a flight path length variation of $< \pm$ 0.05 mm, a standard calculation of the (m/n) uncertainty for $^{186}W^{+3}$ (m/n = 62 amu) with a total voltage ($V_{dc} + \alpha V_{pulse}$) of 15 kV and d = 1600.3 mm predicted a full width at half maximum (FWHM) of $\sim$ 0.20 amu and a full width at 0.1 maximum of $\sim$ 0.34 amu. The measured FWHM for $^{186}W^{+3}$ was $\sim$ 0.2 amu while the full width at 0.1 maximum was $\sim$ 0.7 amu; the first criterion yields a (Δm/m) $\approx$ 1/300 while the

latter criterion yields a $(\Delta m/m) \approx 1/90$.

The observed FWHM value was in good agreement with the predicted value while the observed full width at 0.1 maximum was considerably greater than the predicted value. All of the (m/n) peaks observed to date were sharp on the leading edge with a tail extending to the high-mass side of each peak (e.g., see section 5). This large tail contributes strongly to the observed full width at 0.1 maximum value and only weakly to the FWHM value. The observation of this high-mass tail appears to be quite general for all straight flight path TOF atom probes and has been attributed to energy deficits associated with the field evaporation process.[56,62] In addition, Regan et. al.[61] have also analyzed the energy deficit problem in terms of pulse shape and the decay behavior of the evaporation pulse.

Figures 14(a) and (b) show semilogarithmic plots of the number of $^{92}Mo^{+2}$ ions detected versus the mass-to-charge ratio for field evaporated molybdenum employing an evaporation pulse of 7.4 % and 3.7 % of the dc voltage respectively (i.e., αf was 0.074 and 0.037 respectively). Note that the tails in each peak decayed approximately exponentially. This indicates that the number of events in the tail decreased as $\exp\left[-\frac{\Delta m}{n}\left(\frac{1}{\beta}\right)\right]$ where $(\Delta m/n)$ is the deviation in amu from the maximum in the (m/n) peak and β is the characteristic decay constant. The results presented in Figs. 14(a) and (b) show that the energy deficits decreased as the ratio of the pulse voltage to the dc voltage decreased. For $\alpha f = 0.074$ the observed decay constant (β) was 0.22 amu while for $\alpha f = 0.037$ the value of β was 0.11 amu. Thus the maximum mass resolution is achieved by employing the smallest

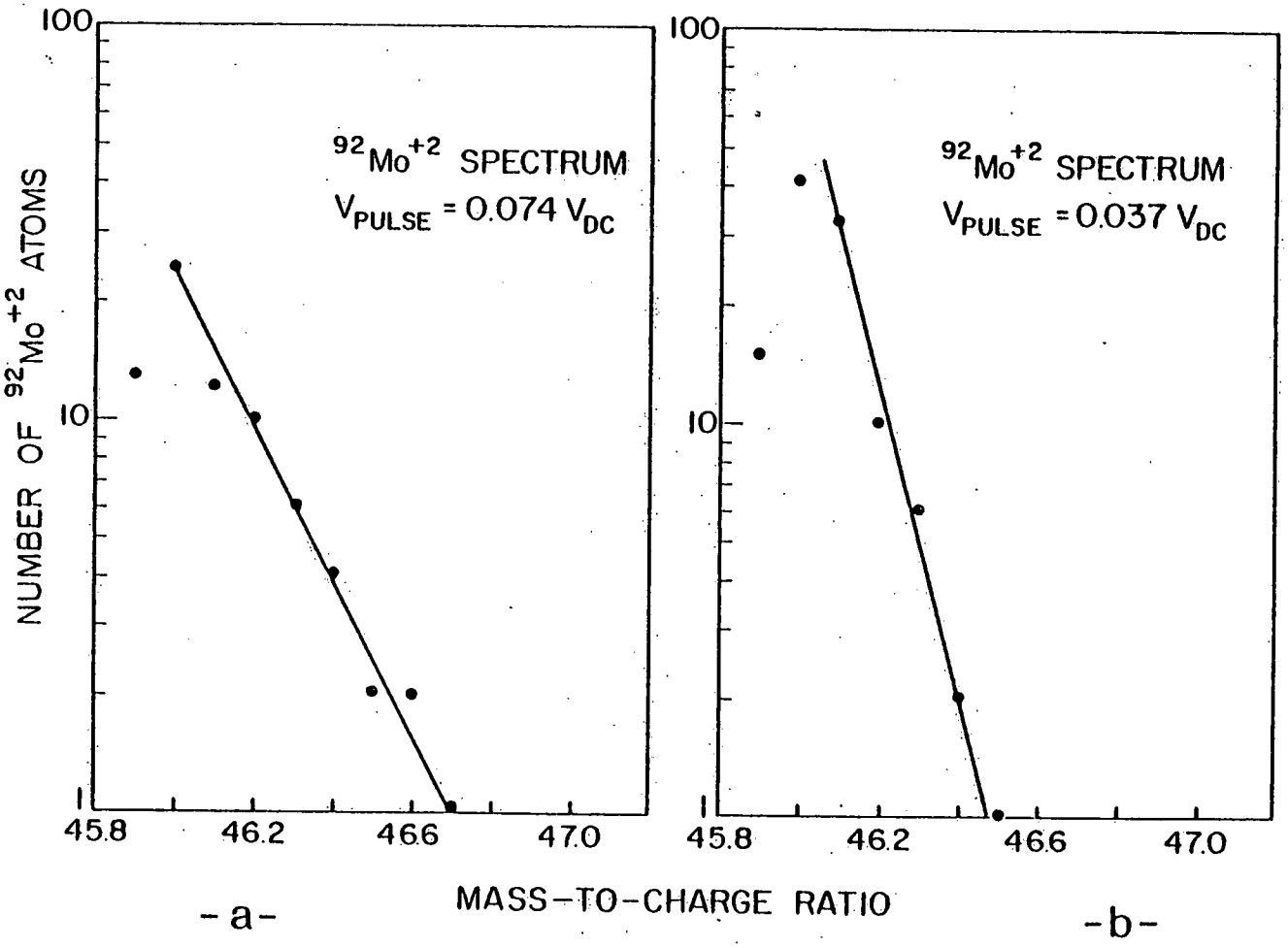

Figure 14. Semilogarithmic plot of the number of $^{92}Mo^{+2}$ ions detected versus the mass-to-charge ratio. The ratio (αf) of the pulse voltage to the dc voltage was 0.074 and 0.037 for for the plots shown in Figs. 14(a) and (b) respectively. Note that as (αf) decreased, the mass resolution increased.

possible value of αf. The lower limit on αf was found to be approximately 0.02; below this value the dc field evaporation rate became comparable to the pulsed field evaporation rate.

At present the best approach to eliminate energy deficits, and thereby increase the $(\Delta m/n)$ value to approximately 1/1000, appears to be through the use of the isochronous focusing lens designed by Poschenrieder[63] and adapted by Muller and Krishnaswamy[56] to the atom probe. However the conventional atom probe has a resolution which is sufficient for the study of a wide range of materials. For example, the practical resolution of the Cornell atom probe is clearly approximately 1/200 since the five stable isotopes of tungsten (^{180}W, ^{182}W, ^{183}W, ^{184}W, and ^{186}W) and the two stable isotopes of rhenium (^{185}Re and ^{187}Re) in a W-25 at. % Re alloy have been resolved (see Figs. 21 and 28). Furthermore the results presented in section 5 amply demonstrate the adequacy of the mass resolution of the Cornell atom probe.

4. COMPUTER SYSTEM

This section describes the computer system which has been interfaced to the TOF atom probe FIM. The system was under complete software control and, in the course of an experiment, it rapidly collected, stored and analyzed the mass spectrometer data and also presented results in both graphical and numerical form.

The system hardware consisted of: (1) a Nova 1220 minicomputer; (2) three cassette tape transports; (3) a teletype; (4) a graphics display terminal; (5) an A/D converter for measuring the dc and pulse voltage applied to the specimen; and (6) the atom probe interface which connected the digital timer and the high-voltage pulser to the computer. The vast majority of the software material consisted of the programs which controlled the operation of the atom probe. The four primary functions of these programs during an experiment were as follows:

(1) Take data - Pulse the tip, read the TOFS from the digital timer, and read V_{dc} and V_{pulse} from the A/D converter;

(2) Store data on cassette - The TOFs V_{dc} and V_{pulse}, and the number of pulses necessary to field evaporate the atoms that were detected was stored on cassette tapes;

(3) Analyze data - Calculate the (m/n) values and store the histogram in core memory;

(4) Present results - Plot the histograms in the form of the number of atoms detected versus (m/n), tabulate the histogram in numerical form and plot a composition profile.

Section 4.1 contains a description of all hardware except the atom probe interface which is described in section 4.2. Section 4.3 contains a discussion of the programming languages used and a description of the program employed to operate the atom probe. Several auxiliary programs that have been developed for use in conjunction with the atom probe are described in section 4.4.

4.1 The Nova 1220 Computer and Peripherals

In its most elementary form the typical computer consists of: (1) a central processor which is the computational and control element of the computer; (2) an information storage device, (e.g., core memory); (3) a front panel which contains a series of switches and lights through which an individual can exchange information with the central processor and core memory; (4) a power supply; and (5) a chassis housing all of the above components. The combination of a chassis, power supply and front panel constitutes the computer main frame. The central processor and memory are contained on circuit boards inserted into this main frame. The typical computer system also contains several peripheral components; notably an auxiliary storage medium which supplements core memory, such as a disk memory or a magnetic tape, and standard input-output (I/O) devices which supplement the front panel such as a teletype, a line printer, and a graphics display terminal. In addition, computer systems linked to experiments contain non-standard I/O devices. For example, from the point-of-view of the computer, the digital timer and the high-voltage pulser used with the atom probe appear as non-standard I/O devices.

Each auxiliary storage device and each I/O device requires an interface. The interface is contained on a circuit board housed in the computer main frame and serves as the electronic link through which the device may communicate with the computer.

The central element in this computer system was the Nova 1220 computer. This computer consisted of a four-accumulator central processor, 32 K (i.e., 32,768), sixteen bit words of core memory, and the computer main frame. The accumulators were static 16 bit storage devices in the central processor through which all data that entered or left the computer passed. The central processor and memory occupied four of the ten circuit board slots in the Nova 1220 main frame. The memory capacity of the computer was sufficient to store the BASIC language interpreter occupying approximately 12 K of core memory and a BASIC program of roughly 2000 statements and 1000 variables as well as all of the assembly language programs required for the atom probe and A/D converter to communicate with the computer.

Three cassette tape transports served as high speed auxiliary storage devices. The three transports were housed in one chassis and shared a common interface which required one circuit board slot in the computer main frame. The cassette tapes served as a high density medium for the storage of programs and data which greatly reduced the use of paper tape. Each cassette tape was capable of storing approximately 50,000 sixteen bit words. With the present software, this corresponded to the storage of the TOF, V_{dc} and V_{pulse}, and number of evaporation pulses applied to the specimen for approximately 10^4 atoms. An entire tape could be read and analyzed in

approximately 15 minutes.

The standard I/O devices were: (1) an ASR 33 teletype; (2) a Tektronix 4010 graphics display terminal and 4610 hard-copy unit; and (3) an Analogic 5800 series analog-to-digital (A/D) converter. The teletype, terminal and hard-copy unit shared a common interface which occupied one circuit board slot in the computer main frame. The teletype was generally used only for reading and punching paper tapes. All alphanumeric and graphics I/O was handled by the 4010 terminal. Permanent copies of the information displayed on the terminal were made by the 4610 hard-copy unit.

The Analogic 5800 series A/D converter was used to measure the dc and pulse voltages applied to the specimen. The interface for the A/D converter occupied one circuit board slot in the computer main frame. Further details concerning the A/D converter voltage measurement system can be found in section 3.1. With the exception of the 4010 terminal and 4610 hard-copy unit, all equipment was supplied as a functioning system by the Data General Corporation. The terminal and hard-copy unit, purchased directly from Tektronix, were found to be both hardware and software compatible with the Data General Corporation system.

4.2 The TOF Atom Probe FIM Interface

Since the computer system hardware described in section 4.1 could not communicate with either the digital timer or the high-voltage pulser, additional hardware was required to make communication possible. This section contains a description of the atom probe

interface which provided the link through which information passed between the computer and the atom probe.

The interface allowed the computer to perform the following four functions: (1) trigger the high voltage pulser; (2) select any one of the eight timing chains in the digital timer; (3) read in the TOF stored in the previously selected timing chain; and (4) reset the digital timer in preparation for another TOF measurement. In addition, the interface signaled the computer when the pulser was ready to produce another high-voltage pulse. The interface was constructed on a Data General Corp. model 4040 general purpose interface board and occupied one circuit board slot in the main frame. Approximately one-half of the interface board contained the manufacturer's circuits while the other half of the board was reserved for user electronics. This board was constructed to allow the parallel input of a 16 bit number, the parallel output of a 3 bit number and the output of two independent control pulses. A block diagram of the interface is shown in Fig. 15. The interface functions, and the corresponding assembly language program instructions are shown on the left hand side and the instrument functions are shown on the right hand side of the figure. The tip was pulsed once whenever a DOCS 0, 44 instruction was encountered in the program. Here the key identifiers were the S, which stands for output a start pulse and the device code 44, which directed the start pulse to the atom probe interface. This pulse then triggered the high-voltage pulser, set the BUSY-DONE flip-flop on the interface into the BUSY state, and triggered a monostable multivibrator. After a delay equal to the cycle time of the high-

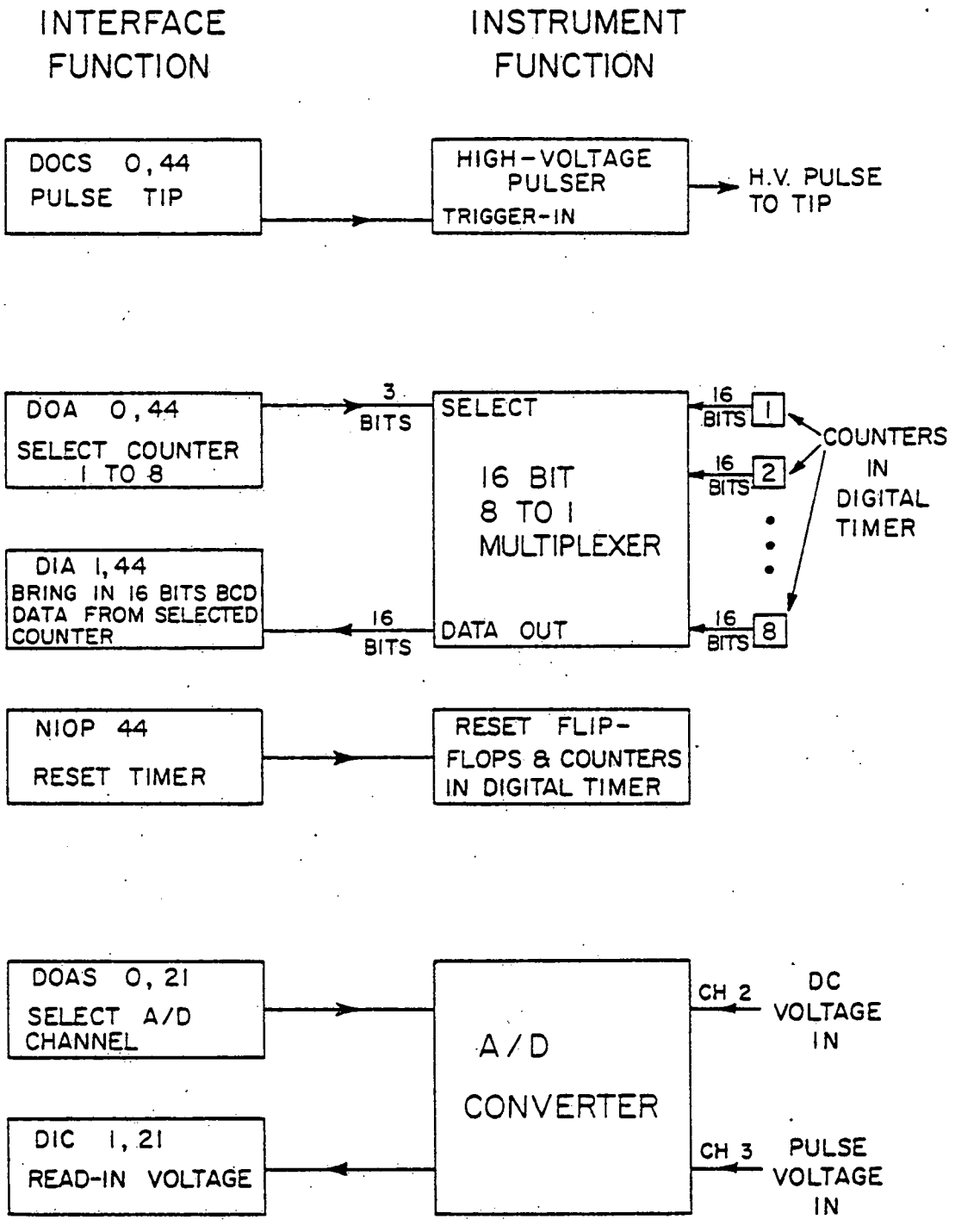

COMPUTER – INSTRUMENT INTERFACE

Figure 15. A block diagram illustrating the function of the interface circuit.

voltage pulser (~ 10 msec) the monostable multivibrator reset the BUSY-DONE flip-flop into the DONE state. By monitoring the state of this flip-flop, the computer was able to determine if the high-voltage pulser was ready to produce another pulse (i.e., done) or if it was in the process of producing a pulse (i.e., busy).

Since there were only 16 binary inputs to the computer and since there were eight separate TOF counters each of which contained 16 bits of data, a multiplexer was needed to read one counter at a time into the computer. The counters were selected by first loading the number of the desired counter into accumulator 0 and then issuing a DOA 0, 44 command (Data Out A, from accumulator 0, to device 44). This caused the three bit number (0 to 7) in accumulator 0 to be output from the interface board to the multiplexer in the digital timer which caused the appropiate counter to be connected to the 16 data input lines into the atom probe interface. After a specific counter had been selected, a DIA 1, 44 command (Data In A, into accumulator 1, from device 44) was issued which loaded the 16 bit BCD TOF data into accumulator 1.

After all of the TOFS had been read into the computer, the command NIOP 0, 44 (No Input Output Pulse) was issued which caused a pulse to be sent to the digital timer which reset all of the flip-flops and counters in preparation for the next TOF measurement.

If any ions were detected the dc and pulse voltages were read in from the A/D converter in essentially the same manner in which the TOF were read in from the digital timer. First the channel was selected by loading the number 2 or 3 into accumulator 0 and executing

the command DOAS 0, 21. This selected either the dc or the pulse voltage channel and initiated an A/D conversion. A DIC 1, 21 command was then executed which loaded the 13 bit voltage data into accumulator 1.

4.3 Computer Programs which Operate the Atom Probe

The software that has been developed consisted of four programs written in BASIC and ASSEMBLY programming languages which: (1) operate the atom probe; (2) prepare a dictionary of (m/n) values; (3) generate simulated mass spectrometer data; and (4) diagnose hardware malfunctions. This section begins with a description of the programming languages employed and the reasons for their selection, followed by a description of the program used to operate the atom probe. The three remaining programs are described in section 4.4.

A combination of BASIC and ASSEMBLY languages was found to provide the most flexible and efficient system for operating the atom probe, since BASIC language programs can be easily modified during an experiment and ASSEMBLY language subroutines execute fast. ASSEMBLY language is the least abstract of all programming languages since each statement can be directly translated into a single hardware function. Thus, ASSEMBLY language provides the most direct control of the computer functions on the finest possible scale. For example, the instruction LDA 0, 100 would cause the contents of core memory location 100 to be loaded into accumulator 0. In contrast, the BASIC instruction X = Y expresses a much more abstract idea and would require translation by a computer into many

ASSEMBLY language statements. Since ASSEMBLY language programming is extremely tedious, it has been employed only when absolutely necessary. The majority of the ASSEMBLY language subroutines were developed only to implement functions not provided by BASIC. For example, since there were no BASIC statement which allowed communication of the atom probe with the computer, it was necessary to develop ASSEMBLY language subroutines which would pulse the tip, read in the four digit BCD TOF, etc. In addition, four ASSEMBLY language subroutines which create, read and clear the histogram and find the peak containing the maximum number of (m/n) values in the histogram were written to replace equivalent but much slower BASIC program sections. All of these subroutines were able to be called by BASIC statements. The general form of a BASIC call was: (statement number) CALL (subroutine number), (up to 8 arguments). For example, the statement 100 CALL 6, T(1), T(2), T(3), T(4), T(5), T(6), T(7), T(8) caused the eight TOFS stored in the digital timer to be transmitted to the computer, translated from BCD to floating point notation and passed to variables T(1) through T(8).

Most BASIC statements have FORTRAN analogs and in general the languages are similar in most respects. The major difference between the languages is that an entire FORTRAN program must first be compiled and then executed, thus involving a two step process, while BASIC programs are interpreted and executed simultaneously in one step, one statement at a time. Thus BASIC allowed on-line development and modification of programs without requiring time consuming recompilation of the entire program. For example, modification of even a

single statement in a FORTRAN program always required recompliation of the entire program which, for this computer system, would have required over 1 hr. The same modification to a BASIC program required only the time which was necessary to retype the statement. Thus program developement and, in particular, program modification during an experiment was found to be much easier in BASIC than in FORTRAN. The major drawback of BASIC was that BASIC programs run slower than equivalent FORTRAN or ASSEMBLY language programs since each BASIC statement must be re-interpreted each time it is executed. However, the execution time was substantially reduced by suitable replacement of particularly time consuming sections of BASIC programs with functionally equivalent but faster executing ASSEMBLY language subroutines.

An extensive computer program which operated the atom probe called the Atom-Probe-Operating-System (APOS) was written and tested. The program was arranged in a three-level heirarchy as shown in Fig. 16. At the top was the controlling EXECUTIVE program which initialized variables and selected the appropriate function of APOS. Under the EXECUTIVE program were the five main BASIC language subroutines: PULSE, GRAPH, READ, CALIBRATION, and DICTIONARY SCANNING. At the lowest level in the heirarchy was the ASSEMBLY language subroutines. A sample computer-operator dialogue which demonstrates the various capabilities of APOS is presented in APPENDIX A.

4.4 Auxiliary Programs

This section describes three programs which: (1) created an

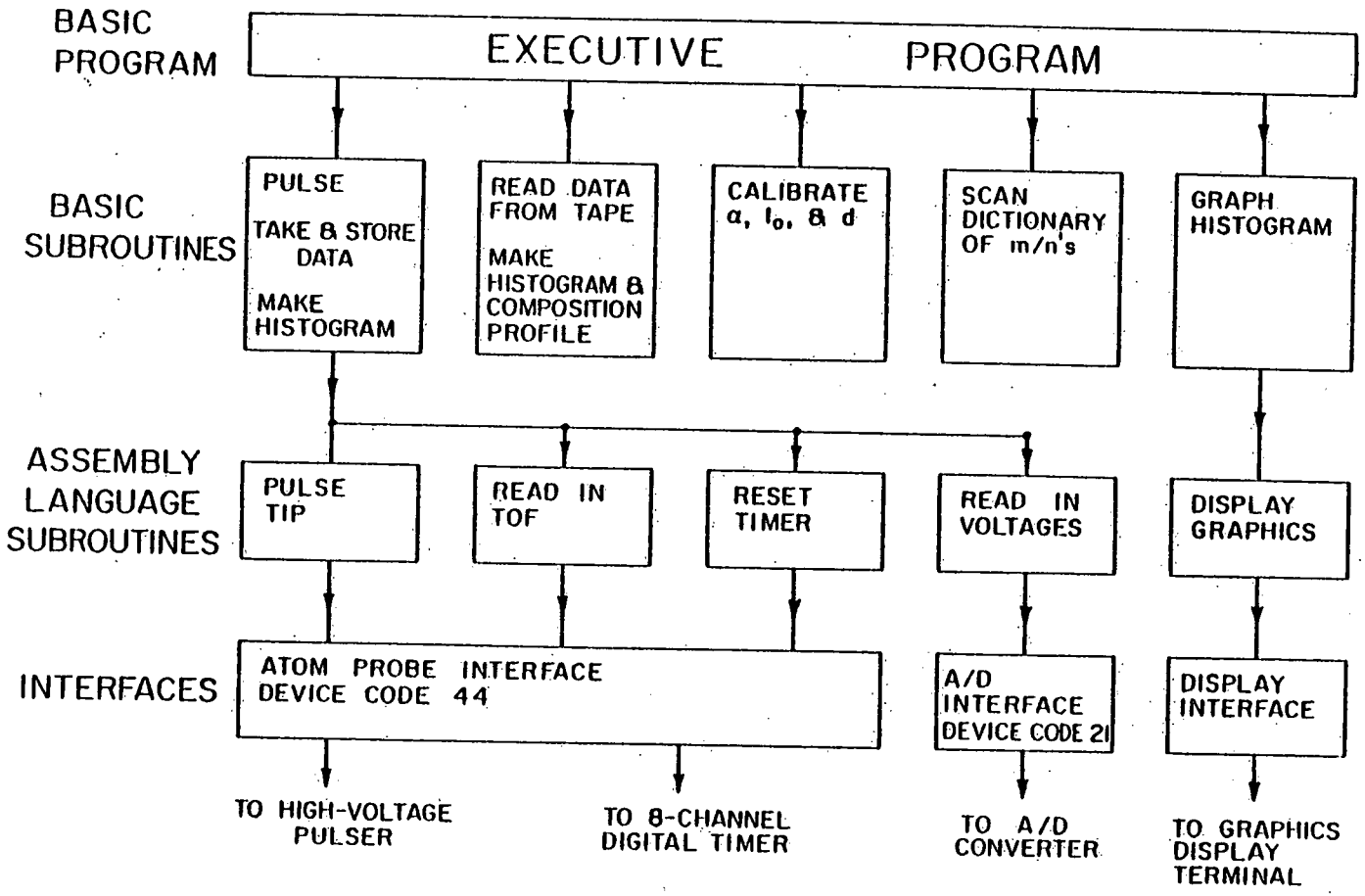

COMPUTER PROGRAM HIERARCHY

Figure 16. Computer program hierarchy showing the EXECUTIVE program, the BASIC language subroutines and the ASSEMBLY language subroutines employed to operate the atom probe.

ordered table of (m/n) values of selected elements; (2) generated simulated mass spectrometer data; and (3) diagnosed hardware malfunctions. Although these programs have contributed to the maintenance of the atom probe and the interpretation of experimental results, they have been classified as auxiliary since they were not essential to the operation of the atom probe. The DICTIONARY GENERATING program prepared an ordered table of (m/n) values for selected combinations of elements. An example of the information provided in the dictionary is given in Appendix A on the dictionary scanning subroutine of APOS. The dictionary contained the (m/n) value and the percent natural abundance of selected combinations of elements in various charge states. The dictionary of (m/n) values has proven to be useful for indicating potential difficulties in unambiguously identifying the peaks observed in the experimental spectra. When preparing the dictionary, the isotopic masses and percent natural abundance of the elements[64] of interest were first stored in the computer. The range of charge states desired for each element and the names of the elements which were to be paired with all other elements, (e.g., the gases hydrogen and helium) were obtained and stored. Special cases, such as combinations of three atoms, were typed in individually. The dictionary generating program then calculated the (m/n) values of all of the desired combinations of elements and charge states. The (m/n) value, the atomic numbers of the elements, the charge state, and the percent natural abundance of each combination was then written onto a cassette tape. This tape was then reread and the entries were arranged in order of increasing

(m/n) values on a second cassette tape. Since the computer storage was far too small to accomodate all of the data at once, a multiple-pass process was required. The first tape was scanned and the range of (m/n) values which could be stored and hence ordered on each pass of the tape was determined. The tape was then re-read and the first group of (m/n) values were arranged in increasing order of the (m/n) value and written to a second cassette tape. This process of reading the first tape, selecting successively increasing ranges of (m/n) values and ordering them according to their (m/n) value, and then writting the (m/n) value, the atomic number of the elements, the charge state, etc. to a second tape was repeated until all of the entries on the first tape were ordered. For a dictionary containing 50 elements there were approximately 5000 entries and the ordering process consisted of 5 passes requiring a total time of approximately 0.5 hr.

An empirical data simulation program was written which tested the effect of voltage and TOF uncertainty on the mass resolution of the spectrometer. The total number of atoms to be simulated (N), the voltage range, the length of the flight path, the resolution of the dc and pulse voltage measurements, the pulse fraction, and the resolution of the digital timer were first input into the computer. In addition an exponential tail of the form $\exp\left[-\frac{m}{n}\left(\frac{1}{\beta}\right)\right]$, where β is a constant, was added to each of the (m/n) peaks. The physical origin of this exponential tail was discussed in section 3.5. The program began by breaking the voltage range into N equal segments. For each atom, the actual voltage (V_a) was picked at random from within

the corresponding segment. This randomizing feature was incorporated to prevent any systematic errors from being introduced due to the voltages being equally spaced for each atom. The measured voltage (V_m) was computed from the true voltage by first calculating the dc and pulse voltage employing the pulse fraction, and then rounding these voltages off so that they corresponded with the resolution of the dc and pulse voltage measurements. The sum was taken as V_m. The (m/n) value (M_i) of an isotope of the element to be simulated was selected at random and weighted by the known isotopic concentration. An energy deficit of exponential form was added using the relationship

$$M_o = M_i - \beta \cdot \ln(r) \tag{11}$$

where M_o was the observed (m/n) values including energy deficits, and r was a random number in the range $0 < r < 1$. The actual TOF (t_a) was calculated employing the expression

$$t_a = \sqrt{\frac{M_o d^2}{2eV_a}} \tag{12}$$

and the measured time (t_m) was determined by rounding off t_a to within the resolution of the digital timer. The measured (m/n) value was then calculated from the values of t_m and V_m given above employing equation

$$M_m = 2eV_m t_m^2/d^2 \quad , \tag{13}$$

and the calculated (m/n) value, M_m, was stored as a histogram. Since β was the only unknown parameter when modelling experimental results,

the value of β provided a measure of the relative importance of energy deficits on the mass resolution. In addition, the program has proven useful as a guide for predicting the minimum detectable concentration of solute in an alloy.

A synthetic histogram generated by this program for a tungsten-25 at. % rhenium alloy is shown in Fig. 17. The voltage range was 3600 to 4400 V, the flight distance was 2222 mm, the dc and pulse voltage resolution was ± 2 and ± 0.5 V respectively, the time resolution was ± 10 nsec, the total number of W and Re atoms was 2000, and the energy deficit parameter (β) was 0.25 amu. This figure may be compared with Fig. 26 for an actual W-25 at. % Re spectrum taken under equivalent conditions. The good agreement between the two histograms indicates that this rather simple model was adequate for reproducing the shape of the observed spectrum and that, except for the energy deficit tails, the actual mass resolution of the TOF atom probe FIM approached the theoretical limits of resolution imposed by the measurement of the voltages and the TOF.

A program which simulated composition profiles was also developed. The program was employed as a guide for determining whether the local fluctuations in the concentration indicated in an experimental composition profile were within the range expected for a random solid solution. The input variables were: (1) the total number of atoms detected (N); (2) the total number of atoms of a particular species detected (P); (3) the concentration of a specific fluctuation; and (4) the size of the fluctuation i.e., the total number of atoms involved in the fluctuation (F). The program then randomly

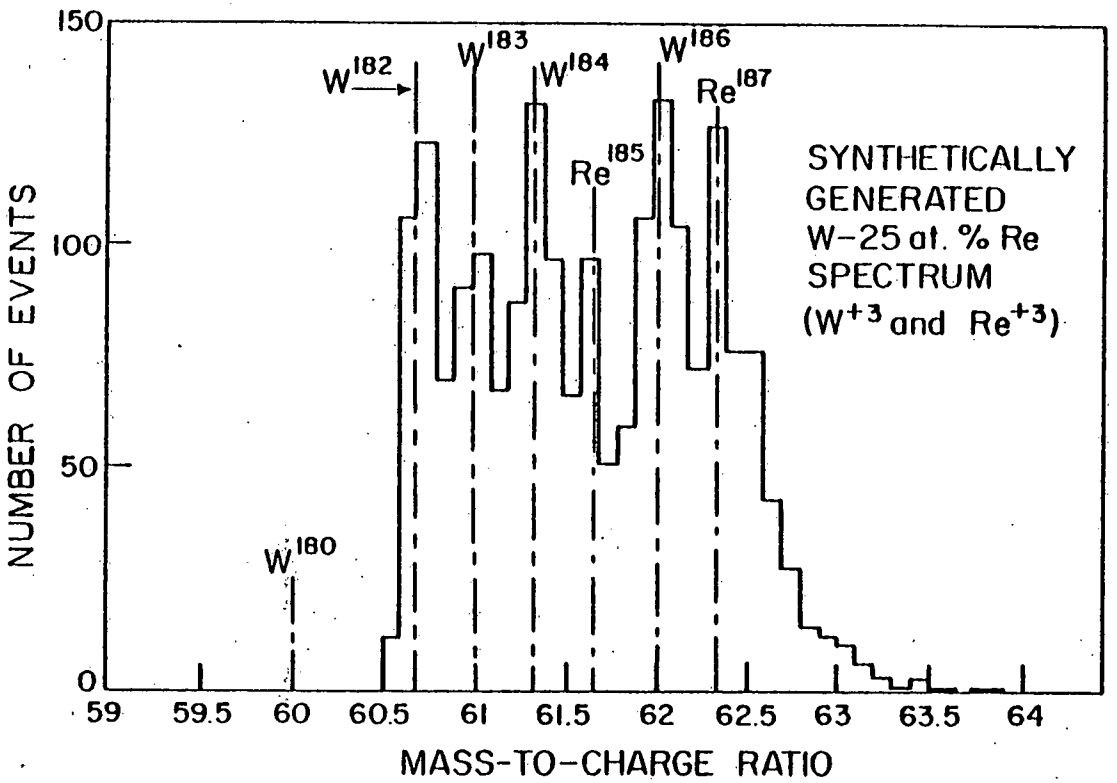

Figure 17. A simulated (m/n) spectrum for a tungsten-25 at. % rhenium alloy.

selected P numbers in the range of 1 to N, thus simulating a composition profile. This composition profile was then tested for any fluctuations of size F which had a concentration equal to or greater than the observed experimental fluctuation. This process was repeated until an ensemble of simulated profiles was generated. The probability, or rate of occurrence, of the simulated fluctuation in a random solid solution was thereby determined and compared with the experimentally measured probability. In addition, a representative sample of the simulated profiles were plotted which allowed a visual comparison with the entire experimental profile. This technique was applied to the composition fluctuations observed in the tungsten-rhenium, molybdenum-titanium-zirconium, stainless steel and metallic glass alloys presented in section 5.

The program was also employed to estimate the statistical fluctuations expected in the experimental range profiles of helium in tungsten which are presented in section 7. In this case the input variables were: (1) the theoretical range profile; (2) the total number of helium atoms detected experimentally (H); and (3) the fraction (K) of random helium atoms expected based on the experimentally observed concentration of helium in control experiments. Note that H(1 - K) is the number of detected helium atoms which were injected into the specimen during the implantation while HK is the number of background helium atoms observed in the control runs. The theoretical range profile was integrated and normilized to yield an integral probability versus depth profile. A composition profile for the H(1 - K) helium atoms was then generated by selecting H(1 - K)

random numbers between 0 and 1 and then picking off the expected range from the theoretical probability profile. This composition profile was then plotted and the mean range and standard deviation were recorded. A random distribution in depth (range) of HK helium atoms was then superimposed on the composition profile to simulate the measured concentration of helium in the control runs. The composition profile, mean range and standard deviation were again recorded. An ensemble was generated which yielded the expected statistical fluctuations in the experimental range profile, mean range and standard deviation in the presence and absence of random background helium. A representative sample of simulated profiles were also plotted for comparison with the shape of the experimental profiles. The effect of background helium and random statistical fluctuations on the experimental profiles was therefore estimated and detailed comparison with the theory were possible (see section 7.5).

In order to insure the reliable operation of the computer system, an extensive diagnostic program which tested all hardware functions was run periodically. The computer system was supplied with a diagnostic program capable of testing the central processor, core memory, the cassette transports and the three standard I/O devices. The scope of this program was extended to allow testing of the atom probe interface, the digital timer, the voltage measurement system and the high-voltage pulser.

The description of the testing procedure for the voltage measurement system was presented in section 3.1. The high-voltage pulser

and associated interface circuits were tested by comparing the total number of high-voltage pulses produced with the number of pulse commands issued by the computer. Since only high-voltage pulses which were able to trigger a discriminator set approximately 5 % below the peak pulse voltage were counted, the incidence of substandard pulses was determined. The test was usually run for 1 hr, in which time approximately 10^5 pulses were produced. Thus far no substandard pulses have been detected in over $3 \cdot 10^5$ pulses. There were two tests performed on the digital timer and associated interface circuits. In the first test, four digit numbers were manually entered into each of the eight counting chains in the digital timer such that none of the counting chains contained the same number. The computer then repeatedly read the digital timer and compared the number read with the number which was entered. Any error in the selection of the counting chain or in the transmission of the contents of the counting chain to the computer was detected. In the second test, pulses with known relative delays were sent to the start and stop inputs of the digital timer. The measured times were read by the computer and tested for any variations. In over 10^6 operations, no errors were detected by either of these two tests.

5. PERFORMANCE OF THE ATOM PROBE

In this section, analyses of a number of pure metals and alloys by the atom probe technique are presented. The materials which were examined included tungsten, molybdenum, tungsten-25 at. % rhenium, molybdenum-1.0 at. % titanium, molybdenum-1.0 at. % titanium-0.08 at. % zirconium (TZM), a type 316 stainless steel (LS1A) and a metallic glass (Metglas 2826). The results clearly demonstrate that these materials can be chemically analyzed quantitatively with the atom probe.

Before presenting the experimental results, the sequence of events that took place in a typical experiment and the forms in which the data were presented are described. After certain variables such as the calibration parameters had been initialized, high-voltage field evaporation pulses were repeatedly applied to the FIM specimen under the control of the computer. As the specimen was pulse field-evaporated, the voltage was slowly increased by the operator to maintain a steady evaporation rate as monitored by an audio ratemeter. After each pulse the computer read in the TOF and voltage data, computed the (m/n) values of the evaporated ions, incremented the appropiate bins of a histogram of (m/n) values versus number of atoms, and stored the TOF and voltage data on magnetic cassette tape. When sufficient data was accumulated, the histogram was displayed on the graphics display terminal. The information stored on the cassette tape was read back to reproduce the histogram, to determine the effect of evaporation rate on the quantitative aspects of the chemical analysis as discussed in section 6, or to determine the spatial

distribution of the elements in the specimen which were detected during the atom probe analysis. The results presented in the following sections make extensive use of the composition profile to indicate the spatial distribution of the elements in an alloy.

The physical principle behind the composition profile is illustrated in Fig 18. Figure 18(a) shows a FIM specimen formed from a solid solution alloy consisting of solvent A and solute B. A precipitate rich in B (the B atoms are denoted by the full circles) is also indicated in the figure. The tip-to-image intensification system was adjusted so that during the course of the pulsed field evaporation of the specimen, all of the atoms (A and B) contained within the indicated cylindrical volume element were chemically analyzed by the atom probe. Figure 18(b) shows the corresponding composition profile in which the cumulative number of B atoms is plotted versus the cumulative number of A and B atoms. The cumulative number of A and B atoms is proportional to depth (z) since the specimen was chemically analyzed by dissecting atomic planes sequentially. In a typical experiment the specimen was analyzed to a depth of ~ 250 A. If the B atoms were distributed uniformly*, the average slope of the plot determines the average composition of the alloy. In the region of the precipitate, the average slope of the plot yields the precipitate's average composition. Thus there are three types of information which can be obtained from the composition profile: (1) average composition; (2) local composition changes or fluctuations;

---

* The word uniform is used to indicate the absence of any gross clustering effects within the analyzed volume.

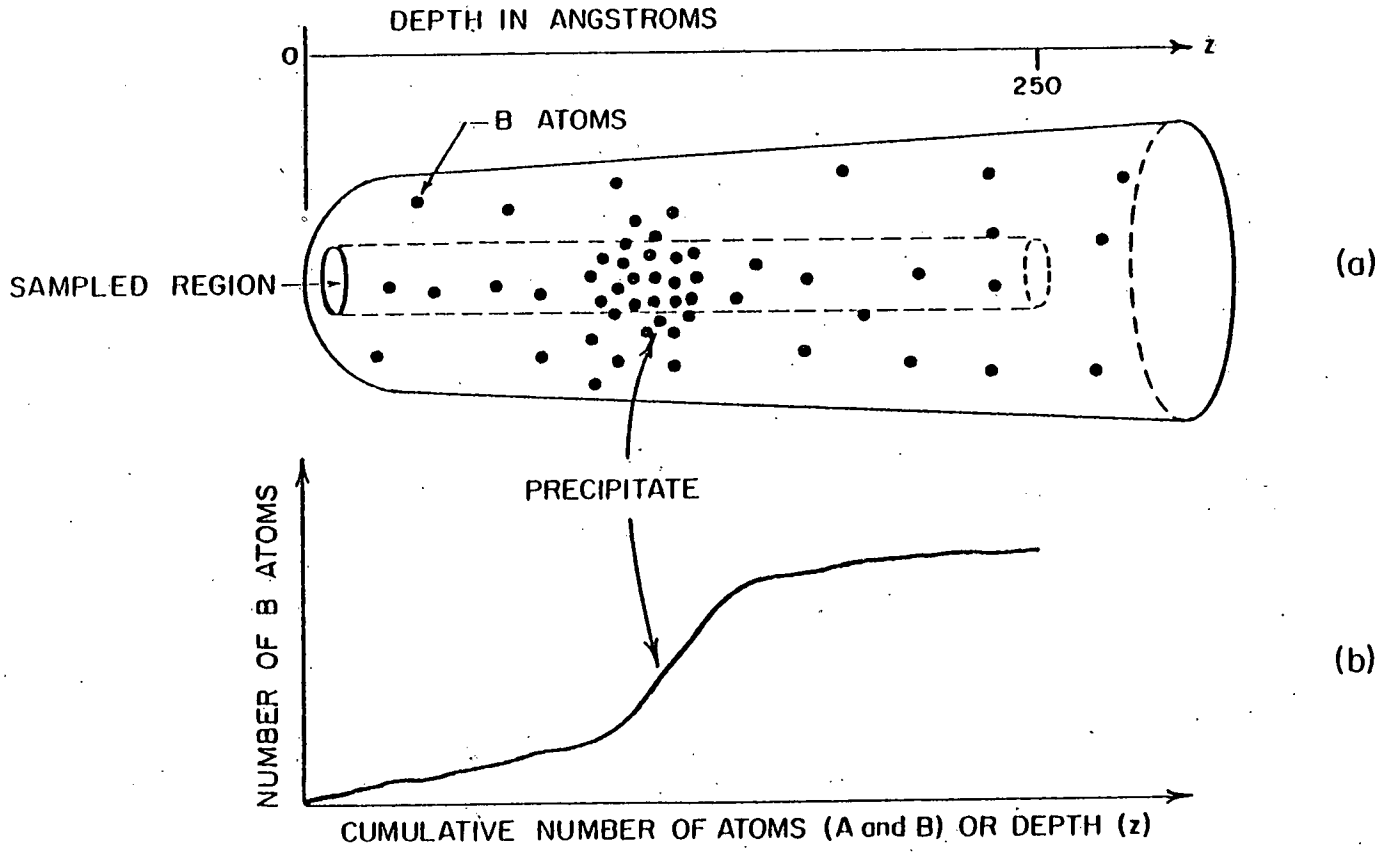

Figure 18. During the course of an atom-by-atom disection of a FIM specimen by the pulsed-field evaporation technique, the atom probe determines the distribution of chemical species in an approximately cylindrical volume element as shown in Fig. 18 (a). A plot of the number of B atoms (we consider the case of a binary alloy consisting of A and B atoms) as a function of the total number of atoms (A plus B) detected yields a composition profile. The presence of a local composition variation produced by a precipitate results in a change of slope of the composition profile as indicated in Fig. 18(b).

and (3) the depth distribution of the local composition fluctuations. The FIM image can be used in conjunction with the composition profile to determine the nature of a local change in composition. For example, it is possible to distinguish amoung clustering, precipitation, and random solid solution composition fluctuations. The term cluster is used to indicate any local composition change which is obviously greater than the fluctuations expected in a random solid solution.

5.1 Pure Metals (Tungsten and Molybdenum)

This section contains a description of typical spectra obtained for pure tungsten and molybdenum specimens. These sample spectra clearly show the mass resolution capability of this atom probe.

FIM specimens were prepared from MRC VP grade polycrystalline tungsten wire by electropolishing the wire in a 1 Normal NaOH solution at 4.3 Vac. Histograms of the (m/n) data obtained for tungsten are shown in Figs. 19 to 22. Figure 19 shows the entire mass range from 0 to 100 amu. The W^{+3} and W^{+4} peaks located near 60 and 45 amu respectively are clearly visible. A small peak due to residual helium gas at 4 amu can also be seen. Histograms of the W^{+3}, W^{+4} and He^{+} peaks are shown on expanded scales in Figs. 20, 21 and 22 respectively. Peaks associated with the five naturally occurring isotopes of W (^{180}W, ^{182}W, ^{183}W, ^{184}W, and ^{186}W) can be readily distinguished from one another in the W^{+3} spectrum shown in Fig. 20 which contained 6009 W atoms. The W^{+4} spectrum (Fig. 21) shows only three clearly distinguishable peaks because the mass resolution in the W^{+4} range was less than in the W^{+3} range. This

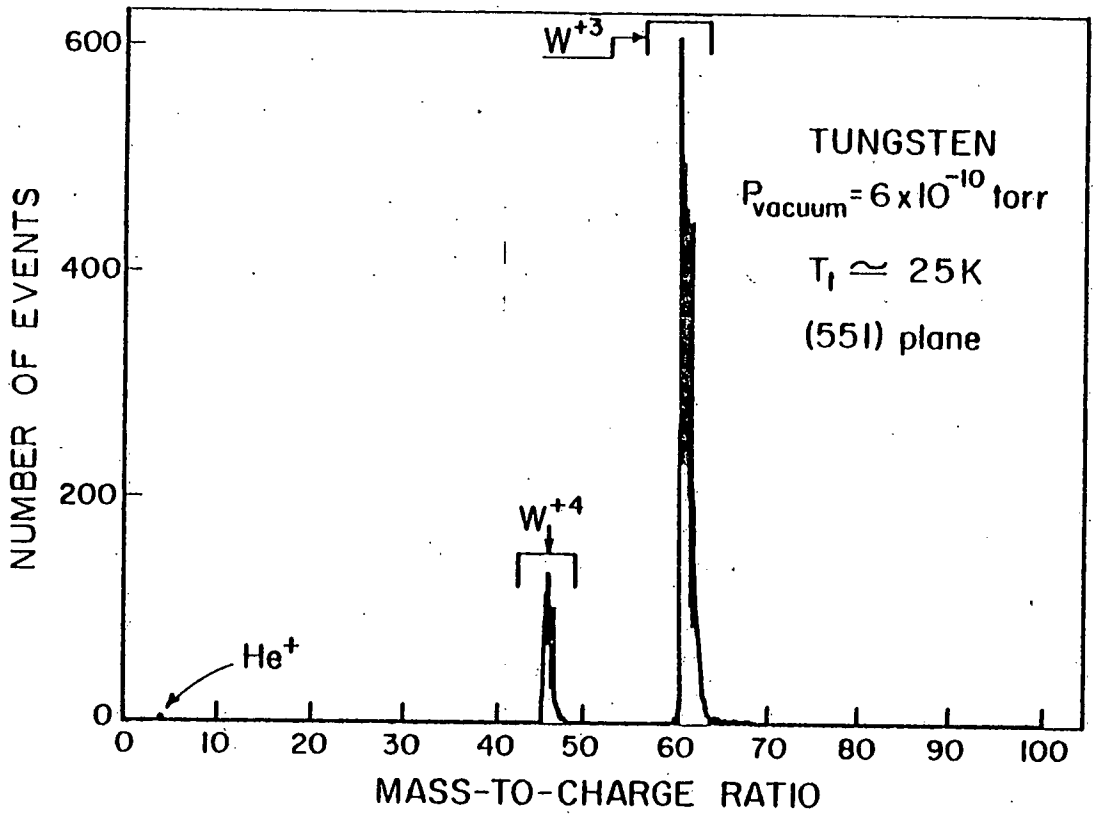

Figure 19. A spectrum for tungsten covering the (m/n) range of 0 to 100 amu. Note that the spectrum consists solely of W^{+3}, W^{+4}, and a small He^{+} peak.

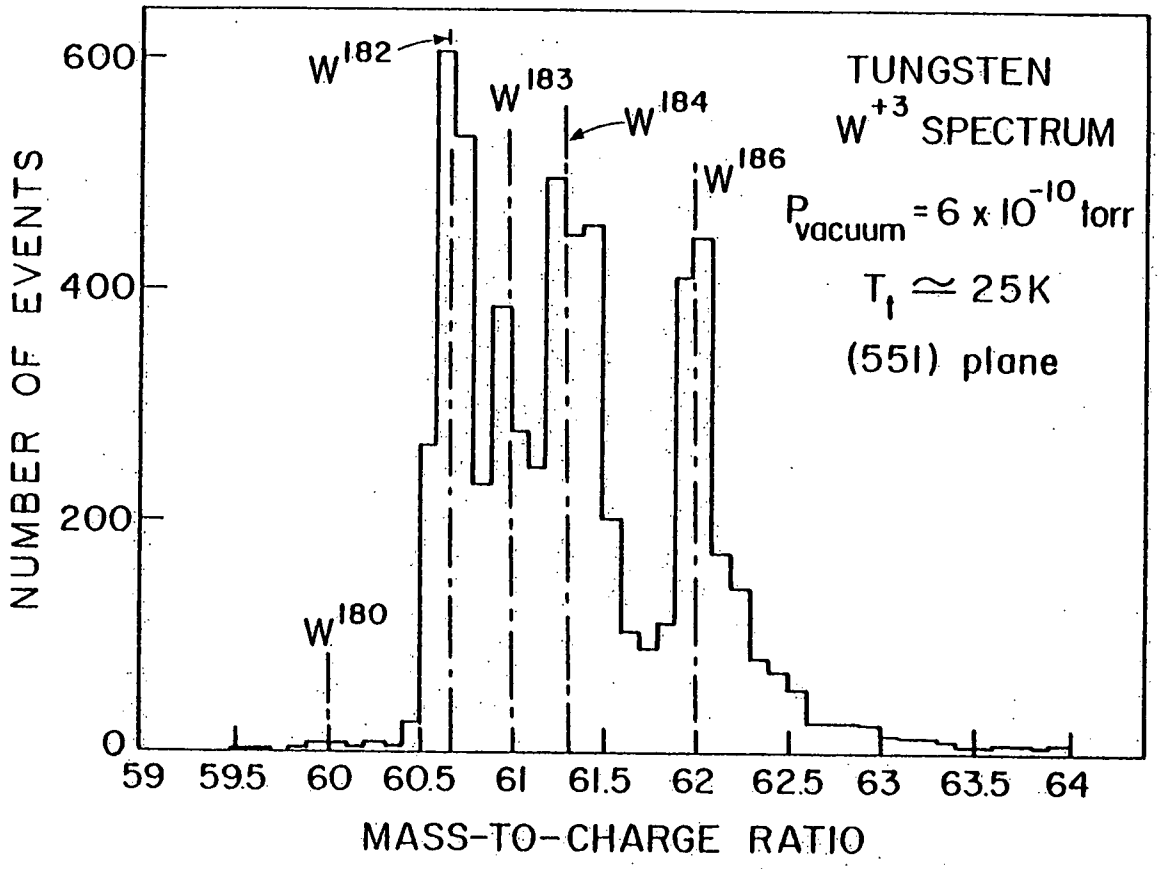

Figure 20. A blow-up of the W^{+3} portion of the spectrum shown in Fig. 19. Note the clear separation of the five naturally occurring isotopes of tungsten.

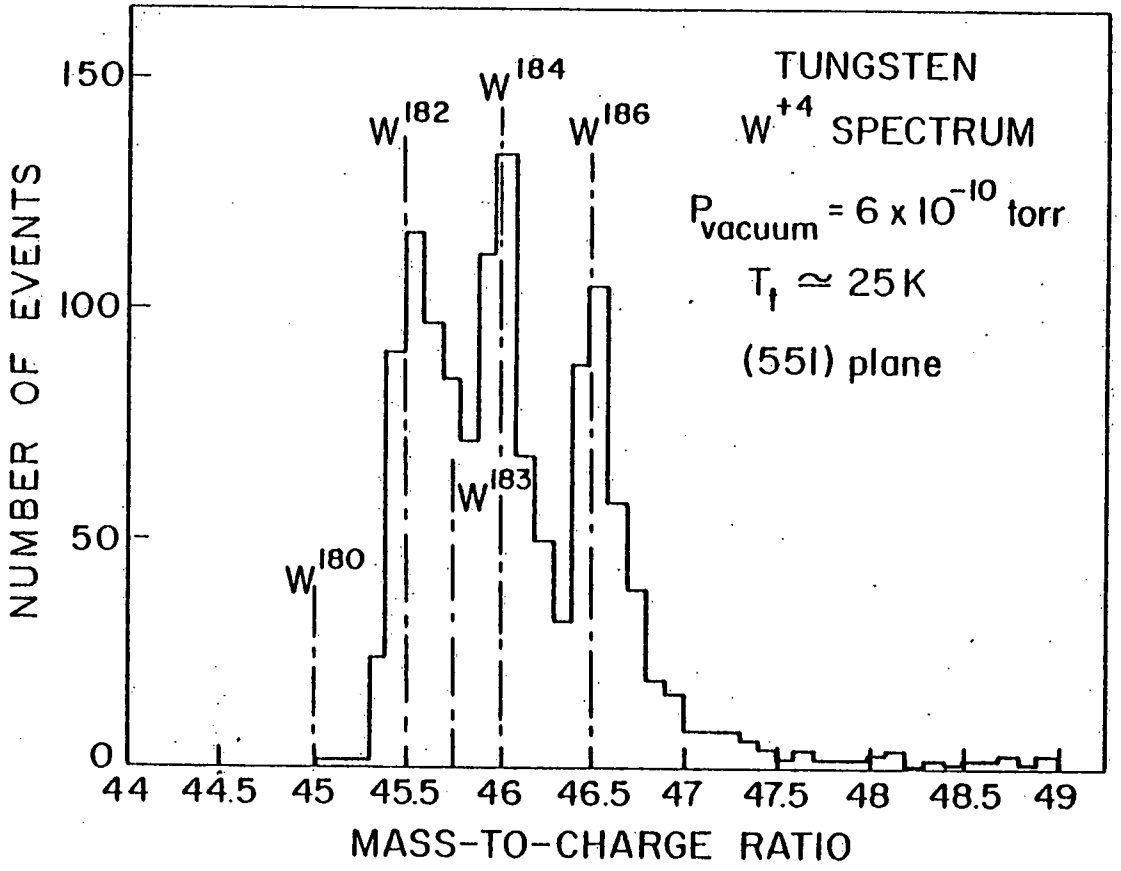

Figure 21. A blow-up of the W^{+4} portion of the spectrum shown in Fig. 19.

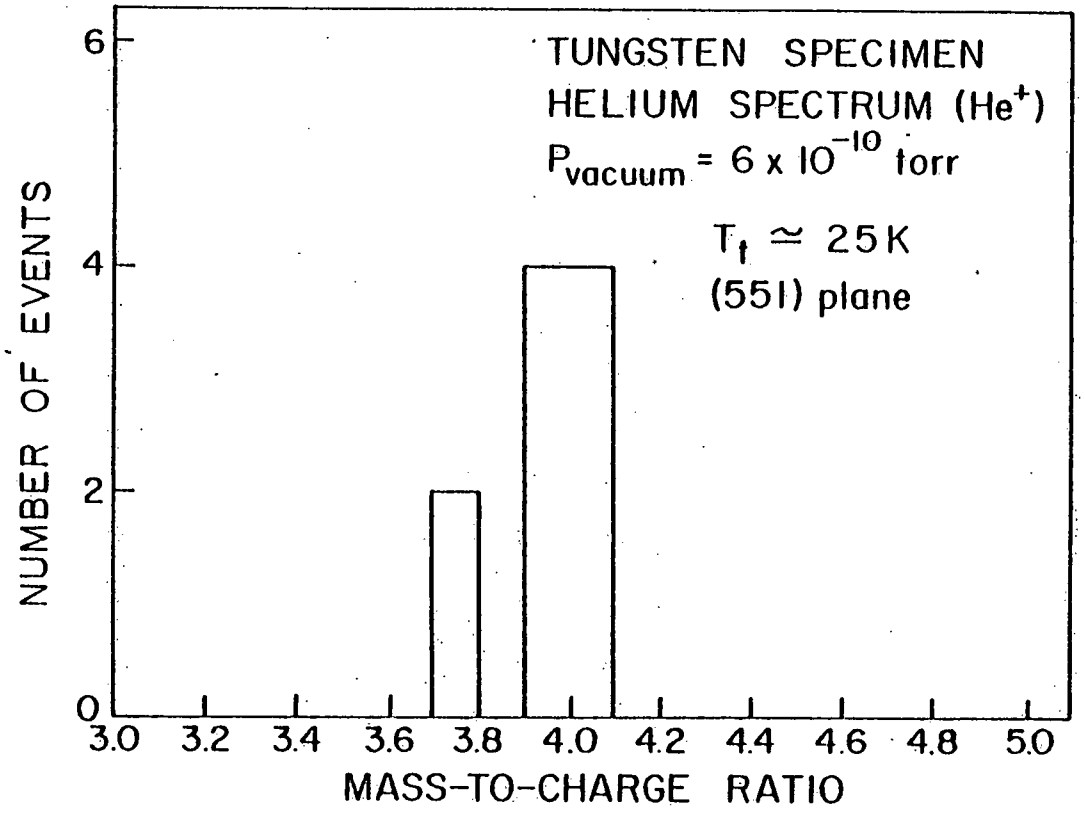

Figure 22. A blow-up of the He^+ portion of the spectrum shown in Fig. 19.

decrease in resolution was principally attributed to the ± 10 nsec time resolution of the digital timer used to measure the TOFS. The 1240 W^{+4} atoms detected represented 17 % of the total number of W atoms recorded. A comparison of the experimental W^{+3} isotopic abundances with handbook values[64] of these quantities is shown in Table 1. Note that the agreement is good. The fact that the W^{+4} peaks fell where expected indicated that the mass scale calibrated from the He^{+} and W^{+3} peaks was linear.

The tungsten spectrum was recorded with the atom probe at a background pressure of $\sim 6 \cdot 10^{-10}$ torr, at a tip temperature of ~ 25 K, and with the probe hole in the internal image intensification system over the (551) plane. The value of f was set at ~ 0.05 and the calibration parameters employed were $\alpha = 2.0$, $t_o = 0.56$ μsec, and d = 1600.3 mm.

The molybdenum FIM specimens were prepared from 0.005 inch diameter polycrystalline wire by electropolishing in 25 % H_2SO_4 in CH_3OH at 4 Vac. The histograms of the data obtained for molybdenum are shown in Figs. 23 to 25. Figure 23 shows the entire mass range from 0 to 100 amu. The Mo^{+2}, Mo^{+3}, and Mo^{+4} peaks at approximately 50, 33, and 25 amu respectively can be clearly seen. In addition, there are peaks at 1 and 4 amu which were associated with residual hydrogen and helium in the atom probe. Histograms with expanded scales of the Mo^{+2} and Mo^{+3} spectra are shown in Figs. 24 and 25 respectively. Peaks associated with the seven naturally occurring isotopes of Mo (^{92}Mo, ^{94}Mo, ^{95}Mo, ^{96}Mo, ^{97}Mo, ^{98}Mo, and ^{100}Mo) can be readily distinguished from one another. A comparison of the experimental

Table 1

Comparison of the experimental W^{+3} isotopic abundances calculated from Fig. 20 with the actual[64] isotopic abundances.

Isotope	AMU Range	Number of Atoms	Experimental* %	Actual %
^{180}W	59.8 to 60.2	20±4	0.33±0.07	0.14
^{182}W	60.5 to 60.85	1520.5±39	25.3±0.6	26.41
^{183}W	60.85 to 61.2	1026.5±32	17.1±0.5	14.4
^{184}W	61.2 to 61.8	1789±42	29.9±0.7	30.64
^{186}W	61.8 to 64.0	1644±41	27.4±0.7	28.41
Totals		6009	100	100

* The ± values were calculated from the $\sqrt{N}/\Sigma N$ where N is the number of atoms detected.

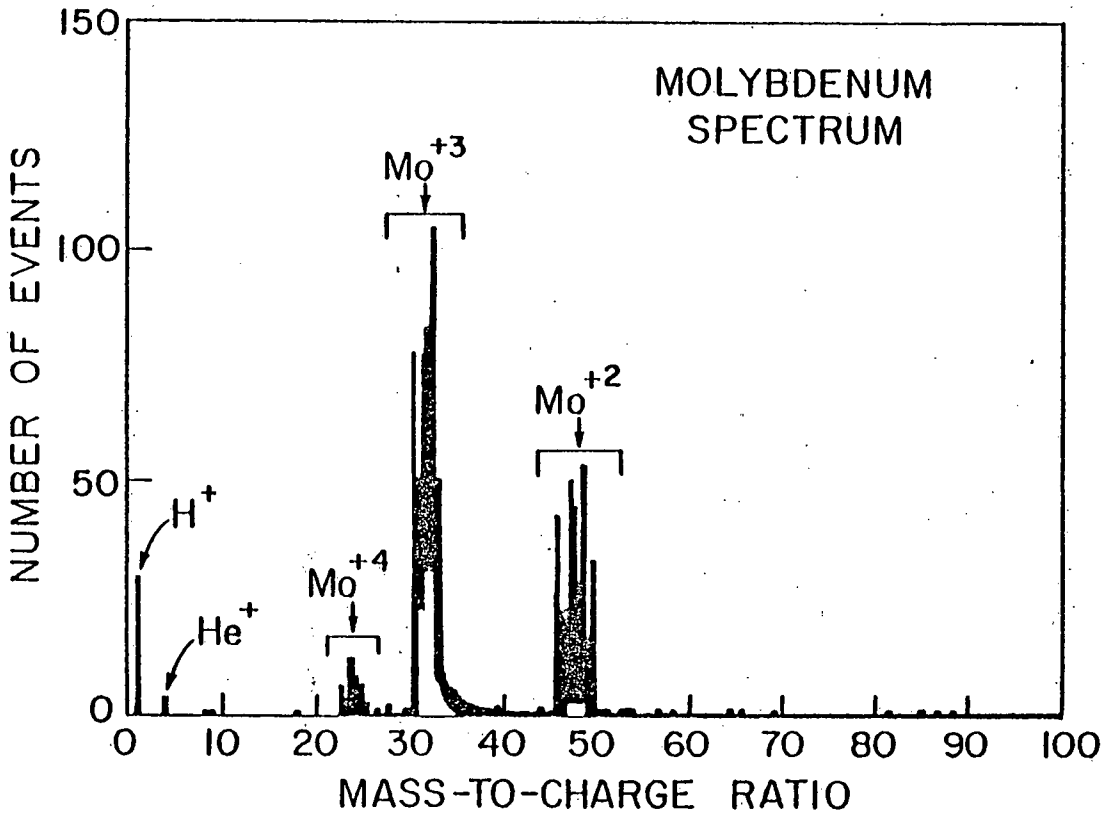

Figure 23. A spectrum for molybdenum, between 0 and 100 amu, recorded at a specimen temperature of 60K in a background vacuum of $5 \cdot 10^{-9}$ torr from a region near the (110) plane. Note that the spectrum consists of Mo^{+2}, Mo^{+3}, Mo^{+4}, He^{+}, and H^{+}.

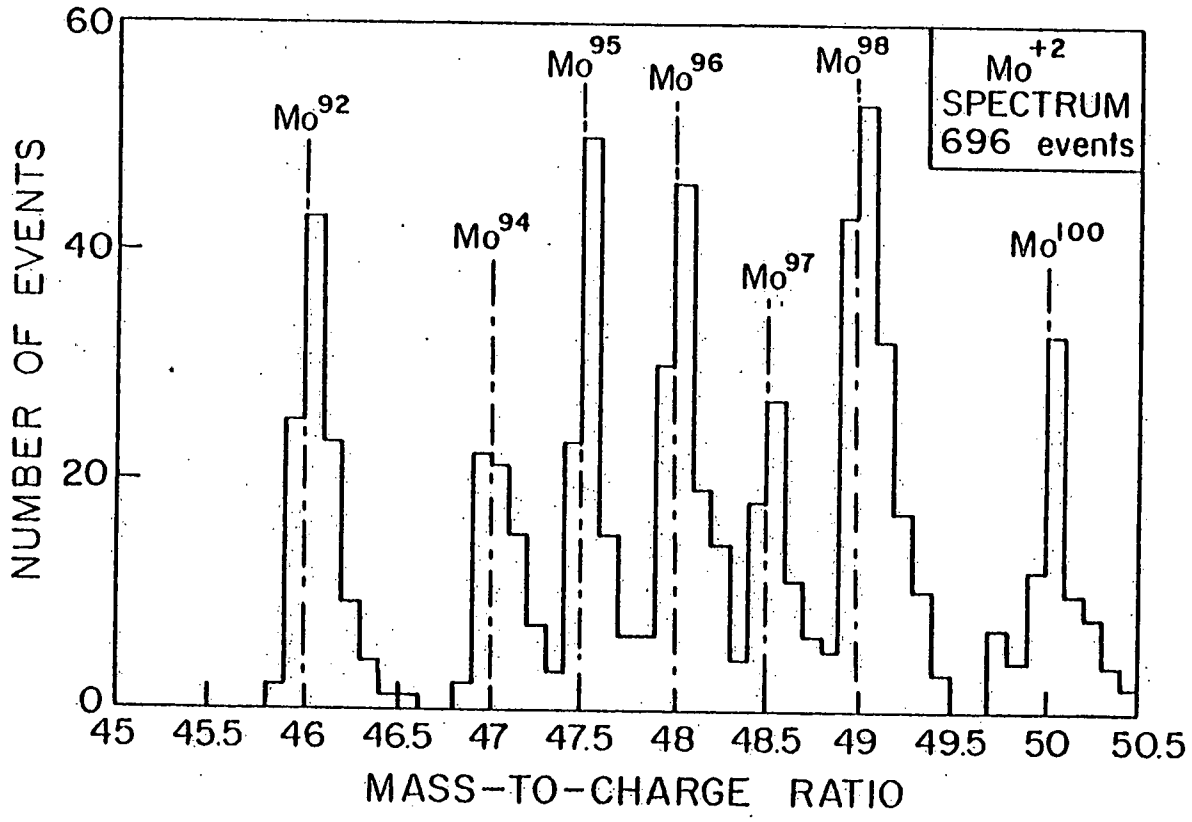

Figure 24. A blow-up of the Mo^{+2} portion of the spectrum shown in Fig. 23. Note the clear separation of the seven naturally occurring isotopes of molybdenum.

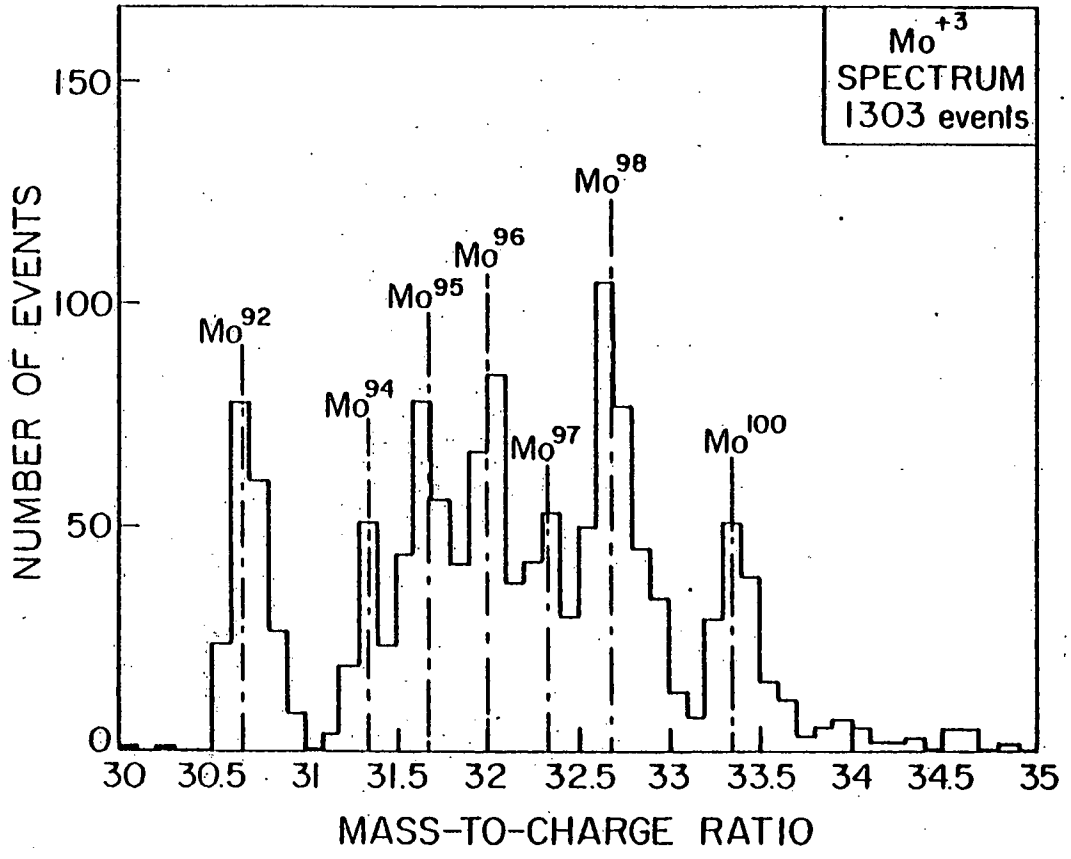

Figure 25. A blow-up of the Mo^{+3} portion of the spectrum shown in Fig. 23.

isotopic abundances for Mo^{+2} and Mo^{+3} with the handbook values is shown in Tables 2 and 3 respectively. There was good agreement between the experimental and handbook abundances for both the Mo^{+2} and Mo^{+3} data. The number of Mo^{+4}, Mo^{+3}, and Mo^{+2} atoms detected were 158, 1303, and 696 respectively for a total of 2157 molybdenum atoms. This yields relative abundances for the Mo^{+4}, Mo^{+3}, and Mo^{+2} of 0.073, 0.604, and 0.323 respectively.

The molybdenum data were recorded with a specimen temperature of 57 to 69 K and with V_{dc} varied continuously from 11.6 to 15.5 kV. The ions were collected from a region near the (110) pole and the background vacuum in the atom probe was $\sim 5 \cdot 10^{-9}$ torr (the FIM was not baked after the specimen was exchanged). The pulse fraction f was set at 0.025 and the calibration parameters were $\alpha = 1.482$, $t_o = 0.56$ μsec, and $d = 2213$ mm.

5.2 Tungsten- 25 atomic % Rhenium Alloy

While pure tungsten exhibits considerable swelling (void formation) as a result of fast neutron irradiation at about 0.3 to 0.6 of the absolute melting point, the addition of rhenium to tungsten strongly suppresses this swelling.[65,66] Instead of voids forming in irradiated tungsten-rhenium, precipitation occurs.[67] The results on tungsten described in the previous section and on tungsten-25 at. % rhenium described in this section will serve as controls for future experiments on fast neutron irradiated samples of these materials. The objective of these experiments is to measure the composition of the precipitates and to determine the rhenium distribution in regions leading away from the precipitates. The ultimate

Table 2

Comparison of the experimental Mo^{+2} isotopic abundances calculated from Fig. 24 with the actual[64] isotopic abundances.

Isotope	AMU Range	Number of Atoms	Experimental % *	Actual %
^{92}Mo	45.8 to 46.6	108±10	15.5±1.5	15.84
^{94}Mo	46.8 to 47.4	70±8	10.1±1.2	9.04
^{95}Mo	47.4 to 47.9	100±10	14.4±1.4	15.72
^{96}Mo	47.9 to 48.4	113±11	16.2±1.5	16.53
^{97}Mo	48.4 to 48.9	67±8	9.6±1.2	9.46
^{98}Mo	48.9 to 49.5	158±13	22.6±1.8	23.78
^{100}Mo	49.7 to 50.5	80±9	11.5±1.3	9.63
Totals		696	100	100

* The ± values were calculated from the $\sqrt{N}/\Sigma N$ values where N is the number of atoms detected

Table 3

Comparison of the experimental Mo^{+3} isotopic abundances calculated from Fig. 25 with the actual[64] isotopic abundances.

Isotope	AMU Range	Number of Atoms	Experimental* %	Actual %
^{92}Mo	30.5 to 31.0	197±14	15.1±1.1	15.84
^{94}Mo	31.1 to 31.5	97±10	7.5±0.8	9.04
^{95}Mo	31.5 to 31.9	219±15	16.8±1.1	15.72
^{96}Mo	31.9 to 32.2	188±14	14.4±1.1	16.53
^{97}Mo	32.2 to 32.5	125±11	9.6±0.9	9.46
^{98}Mo	32.5 to 33.1	324±18	24.9±1.4	23.78
^{100}Mo	33.1 to 33.7	153±12	11.7±0.9	9.63
	Totals	1303	100	100

* The ± values were calculated from the $\sqrt{N}/\Sigma N$ values where N is the number of atoms detected.

goal is to elucidate the mechanism responsible for the suppression of void formation in the W-25 at. % Re alloy.

The FIM specimens were prepared from tungsten-25 at. % rhenium thermocouple wire supplied by Englehard Industries. The wire was electropolished in 1 Normal NaOH at 4.3 Vac. Superior specimens were obtained if, prior to electropolishing the specimen, approximately 1 cm of the W-25 at. % Re wire was electrolytically dissolved into 20 to 30 ml of the 1 Normal NaOH solution.

Histograms showing the entire mass range of 0 to 100 amu and the triply charged tungsten and rhenium mass range are presented in Figs. 26 and 27 respectively. The $^{185}Re^{+3}$ peak at 61.67 amu and the $^{187}Re^{+3}$ peak at 62.33 amu are readily seen. The total number of atoms detected was 1834 of which approximately 95 % had a charge state of +3 while only 5 % had a charge state of +4; this result is in strong contrast to the previous observation on pure tungsten in which 17 % of the W atoms field evaporated in the +4 charge state.

A comparison of the experimental isotopic abundances with handbook values for a W-25 at. % Re alloy is presented in Table 4. The indicated total Re concentration of 28.5 at. % was obtained by counting only those atoms in the ranges shown in the table. In contrast, concentrations of 10.7 at. % $^{185}Re^{+3}$ and 14.7 at. % $^{187}Re^{+3}$ for a total concentration of 25.4 at. % Re are indicated in the rhenium composition profiles shown in Figs. 28 and 29 respectively. This result was obtained by counting the atoms in the ranges 61.6 to 62.0 and 62.3 to 62.6 amu as $^{185}Re^{+3}$ and $^{187}Re^{+3}$ respectively, and then dividing by the total number of atoms in the entire W-Re $^{+3}$ peak,

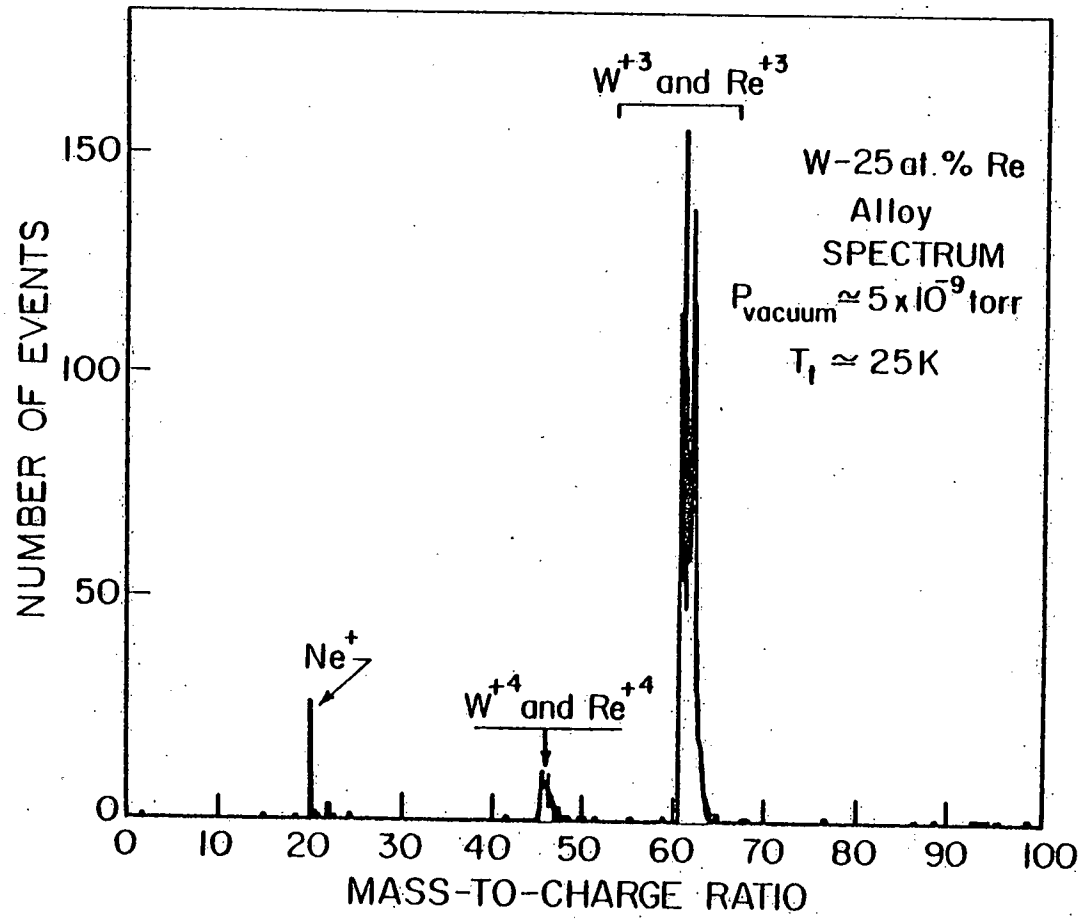

Figure 26. A spectrum for a tungsten-25 at. % rhenium alloy, between 0 and 100 amu, recorded at a specimen temperature of 25K in a background vacuum of $5 \cdot 10^{-9}$ torr. Note that the spectrum consists of W^{+3}, Re^{+3}, W^{+4}, Re^{+4}, and Ne^{+}.

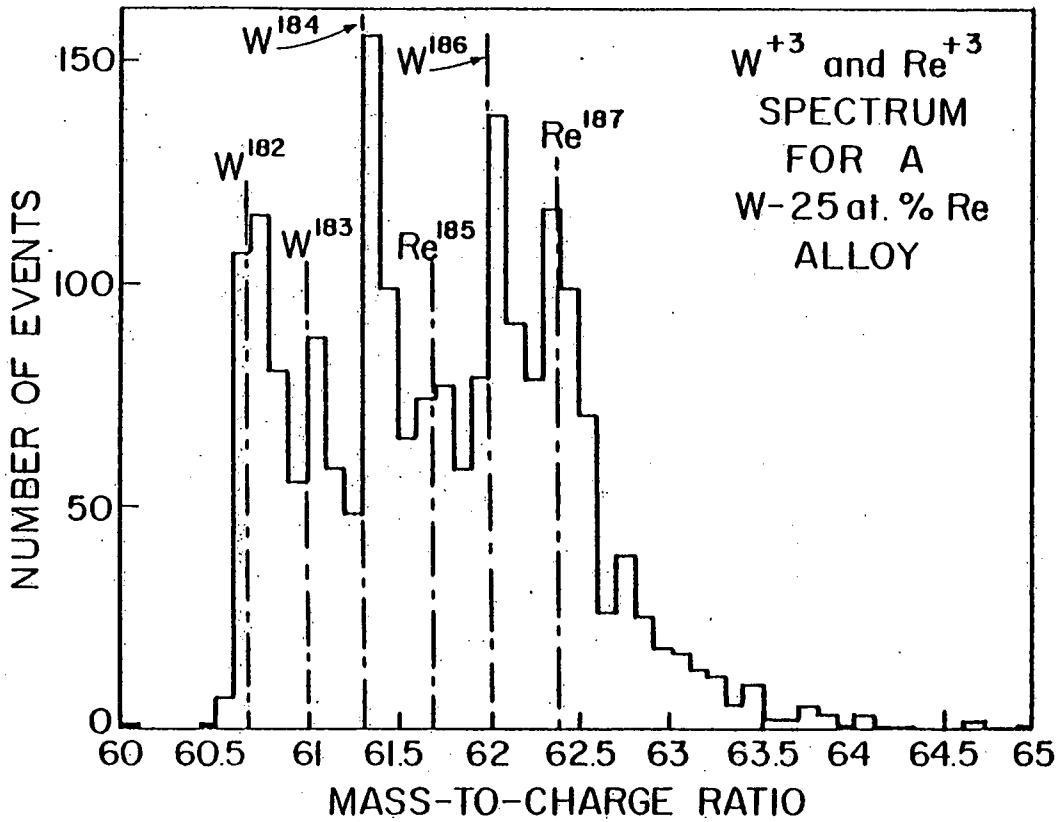

Figure 27. A blow-up of the W^{+3} and Re^{+3} portion of the spectrum shown in Fig. 26. Note the clear separation of the two rhenium isotopes from the five tungsten isotopes.

Table 4

Comparison of the experimental W-25 at. % Re $^{+3}$ isotopic abundances with the actual[64] isotopic abundances.

(a) Tungsten Isotopes

Isotope	AMU Range	Number of Atoms	Experimental* %	Actual %
^{180}W	59.9 to 60.4	1±1	0.1±0.1	0.1
^{182}W	60.4 to 60.9	310±18	24.7±1.4	26.4
^{183}W	60.9 to 61.3	243±16	19.3±1.2	14.4
^{184}W	61.3 to 61.6	394±20	31.4±1.6	30.7
^{186}W	62.0 to 62.3	307±18	24.5±1.4	28.4
	Totals	1255	100.0	100.0

(b) Rhenium Isotopes

Isotope	AMU Range	Number of Atoms	Experimental %	Actual %
^{185}Re	61.6 to 62.0	214±15	42.8±3.1	37.1
^{187}Re	62.3 to 62.6	286±17	57.2±3.1	62.9
	Totals	500	100.0	100.0

* The ± values were calculated from the $\sqrt{N}/\Sigma N$ values where N is the number of atoms detected.

Table 4 (continued)

(c) Relative Concentrations

Element	Number of Atoms	Experimental %	Nominal %
W	1255±35	71.5±1.6	75.0
Re	500±22	28.5±1.6	25.0
Totals	1755	100.0	100.0

including the tail from 62.6 to 65 amu.

Clearly there was a problem accounting for the atoms in the tail in a simple way because each peak had its own tail which interfered with the peaks at higher (m/n) values. To resolve this, a third method was employed to obtain the rhenium concentration. A relatively simple least-squares procedure was used to fit all seven peaks in the W-Re $^{+3}$ spectrum assuming that the peaks decayed exponentially. The adjustable parameters were the concentration of rhenium and the decay constant of the exponential tail. In addition, a third parameter which compensated for any error in the absolute position of the (m/n) spectrum was least-squares adjusted. The results of the fitting procedure were a rhenium concentration of 22±2 at. %, a decay constant (β) of 0.31 amu, and 0.065 amu for the required shift in the (m/n) scale to obtain the best fit.

A simulated triply charged W-25 at. % Re histogram employing a decay constant of 0.25 amu was shown in Fig. 16 and discussed in section 4.4. There was good agreement between the simulated histogram and the experimental data.

The composition profiles for the Re in the W-25 at. % Re alloy are shown in Figs. 28 and 29. The profiles clearly demonstrate that there was no evidence for clustering of rhenium. The absence of clustering was confirmed by testing the Re distribution in a manor analogous to a pair distribution function. For a random solid solution of Re in W:

(1) the probability of detecting a Re atom = C;

(2) the probability of detecting x W atoms = $(1 - C)^x$; and

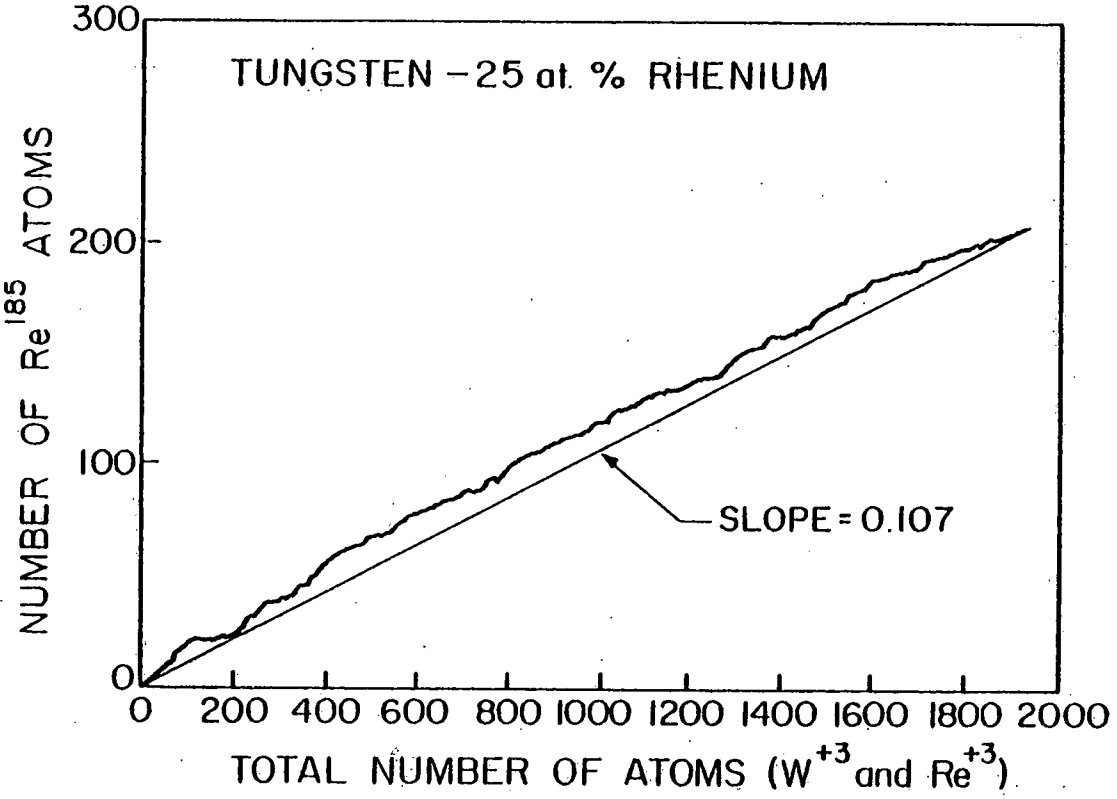

Figure 28. A composition profile for the $^{185}Re^{+3}$ isotope in the W-25 at. % Re alloy. The cumulative number of atoms in the range 61.6 to 62.0 amu is plotted as a function of the cumulative number of atoms in the entire W-Re^{+3} peak from 59.9 to 65 amu.

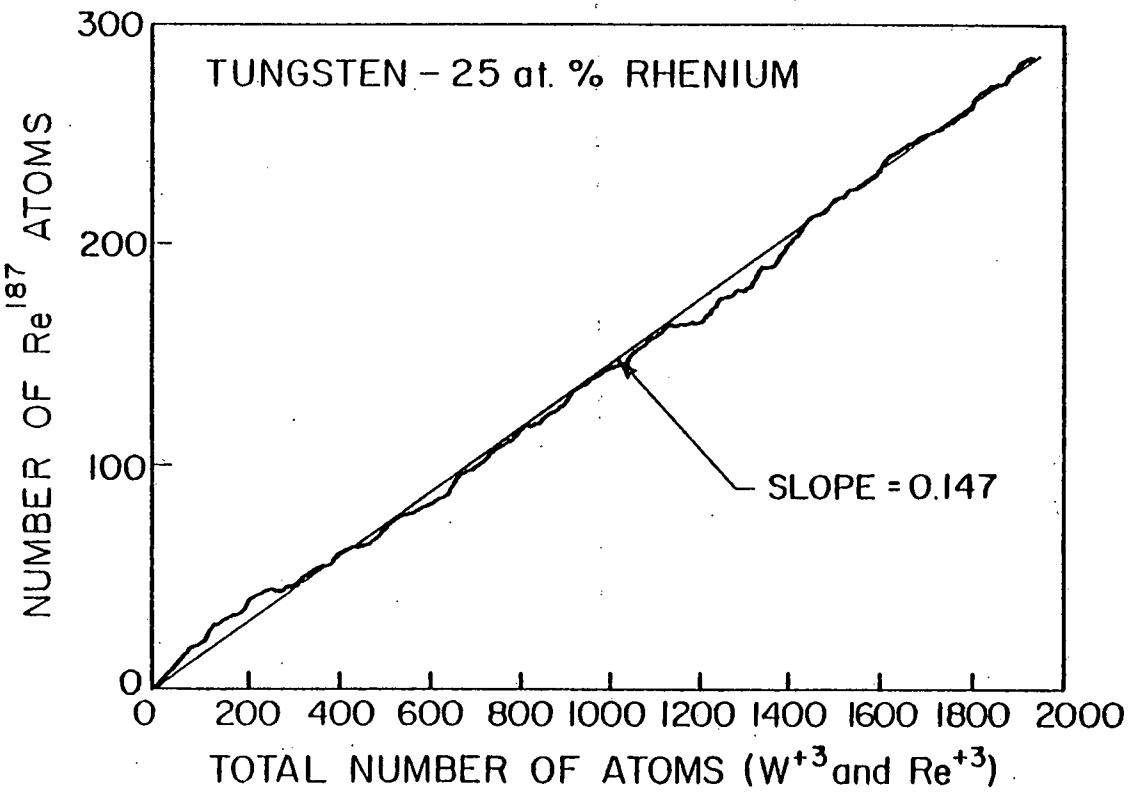

Figure 29. A composition profile for the $^{187}Re^{+3}$ isotope in the W-25 at. % Re alloy. The cumulative number of atoms in the range 62.3 to 62.6 amu is plotted as a function of the cumulative number of atoms in the entire W-Re^{+3} peak from 59.9 to 65 amu. The average composition of ^{185}Re and ^{187}Re obtained from Figs. 28 and 29 were 10.7 and 14.7 at. % respectively. This yields a total concentration of 25.4 at. % rhenium which agrees with the nominal rhenium concentration of 25 at. %.

(3) the probability of detecting a second Re atom = C,

where C is the concentration of rhenium. Therefore the probability of detecting a rhenium atom followed by exactly x tungsten atoms before the next rhenium atom is detected is equal to $C^2(1 - C)^x$. If N is the total number of atoms (W+Re) detected then $NC^2(1 - C)^x$ for x = 0,1,2,3... is simply equal to the absolute number of times a specified sequence should occur in a random solid solution of rhenium in tungsten. For example the first few sequences are, Re-Re, Re-W-Re, Re-W-W-Re, etc. If significant fine scale clustering of rhenium had taken place in the alloy then the experimentally measured incidence of Re-Re pairs would have been significantly greater than the expected incidence for a random solid solution. In Fig. 30 a comparison is presented between the experimental results and the random solid solution prediction for the W-25 at. % Re alloy. The close correspondence between the experimental results and the random solution results clearly indicate and absence of a strong tendency toward the clustering of Re atoms. The small differences between the experimental results and the random solution model were within the expected statistical variations.

The W-Re spectrum was recorded at a specimen temperature of 25 K, with f = 0.10 and with V_{dc} ranging over 3600 to 4400 V. The calibration parameters were $\alpha = 1.5$, $t_o = 0.56$ μsec, and d = 2232 mm.

The first conclusion drawn from this experiment was that a Re concentration of 25 at. % or higher could be easily detected in W. A second conclusion was that the vast majority of the Re atoms were in solid solution in this specimen; this conclusion was based on the fact

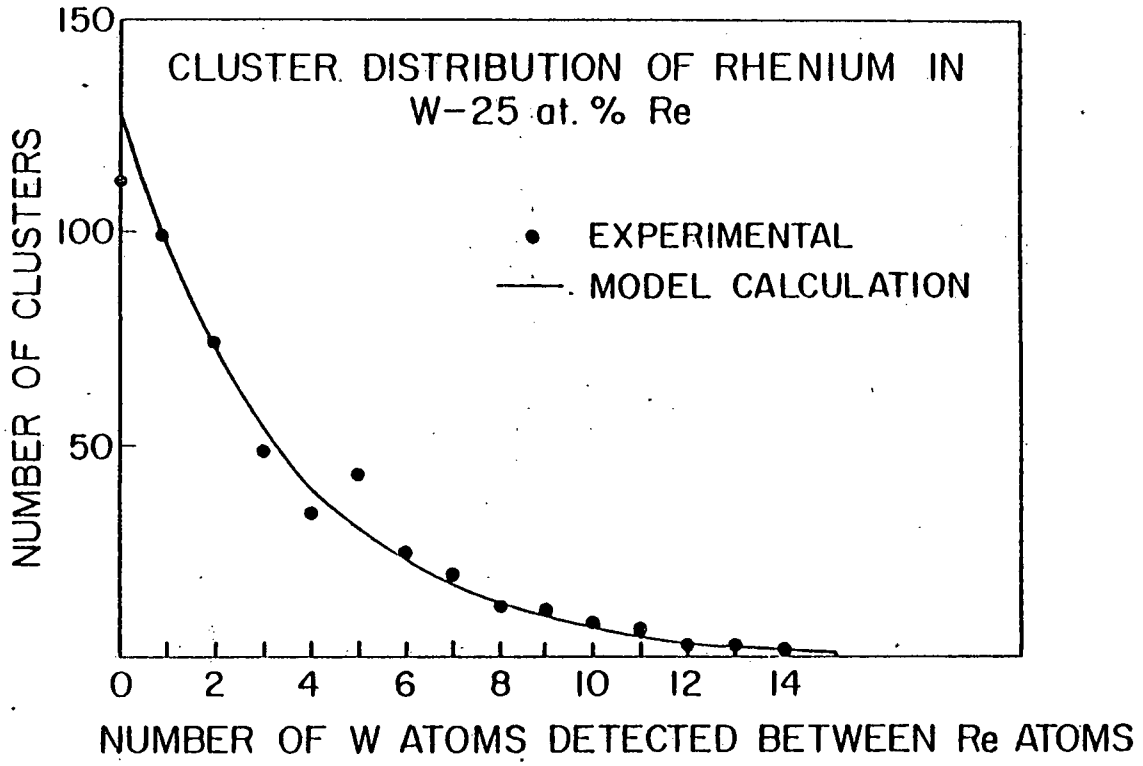

Figure 30. The cluster size distribution for the W-25 at. % Re alloy which shows that there was no strong tendency for the rhenium atoms to cluster in this alloy.

that the measured Re concentration was approximately equal to the nominal concentration in the alloy and also that the FIM image showed no evidence for precipitation. The third conclusion was that the observed fluctuations in the Re concentration were within the range expected for a random solid solution i.e., no evidence of clustering was found. Based on the present results, no conclusions could be drawn on the extent of any short range order (anti-clustering) which may have been present.

5.3 Molybdenum-Titanium Alloy

The Mo-1.0 at. % Ti alloy exhibits an enhanced swelling behavior compared to pure molybdenum specimens irradiated under identical conditions to the same fast neutron fluence.[65,68] The purpose of the present experiment was to determine the role played by the titanium in the swelling enhancement behavior of the neutron Mo-Ti alloy. It is interesting to note by contrast that Ti is an effective swelling inhibitor in model Fe-Cr-Ni alloys i.e., stainless steels (see section 5.5).

Atom probe analyses were performed on unirradiated specimens of a Mo-1.0 at. % Ti alloy. The results served as controls for a series of experiments on neutron irradiated Mo-1.0 at. % Ti presented in section 8.

The alloy was originally swaged from re-roll stock which had been recrystallized at 1090 C and then hot drawn to 1.5 mm diameter between 815 and 980 C. A wire specimen was prepared from the 1.5 mm diameter rod by thinning it electrolytically to 0.2 mm in diameter

using a solution which consisted of 25 parts H_2SO_4 to 175 parts CH_3OH (by volume). The FIM specimens were prepared by electropolishing at 5 Vac in a solution of 1 part H_2SO_4: 4 parts HCl: 8 parts CH_3OH (by volume).

The Ti^{+3} spectrum for the as-received Mo-1.0 at. % Ti alloy is shown in Fig. 31. The five isotopes of titanium (^{46}Ti, ^{47}Ti, ^{48}Ti, ^{49}Ti, and ^{50}Ti) can be clearly seen. Table 5 shows a comparison of the experimental Ti^{+3} isotopic abundance with the actual isotopic abundance. The agreement is reasonable considering that the sample size involved only 30 Ti^{+3} ions for all five isotopes. The agreement between the experimental and handbook values of the isotopic abundances of titanium presents a decisive indicator that Ti^{+3} was actually detected and not, for example, singly charged oxygen atoms; oxygen has only three isotopes with ^{16}O having a natural abundance of 99.8 at. %. This is an important point since CO and/or CO_2 which adsorbed on the surface of the FIM specimen was found, during the course of this work, to field evaporate as $^{12}C^{+1}$, $^{12}C^{+2}$, $\underline{^{16}O^{+1}}$, and $^{28}CO^{+1}$. The $^{16}O^{+1}$ is indistinguishable from $^{48}Ti^{+3}$.

The experimentally measured composition for three runs is compared with the nominal composition supplied by the manufacturer[69] in Table 6. There are three observations worthy of note: (1) the measured Ti concentration was consistently less than the nominal concentration supplied by the manufacturer; (2) the measured carbon concentration was much smaller than the nominal concentration; and (3) the variation in the experimentally measured Ti concentration was greater than the expected statistical uncertainty. There are

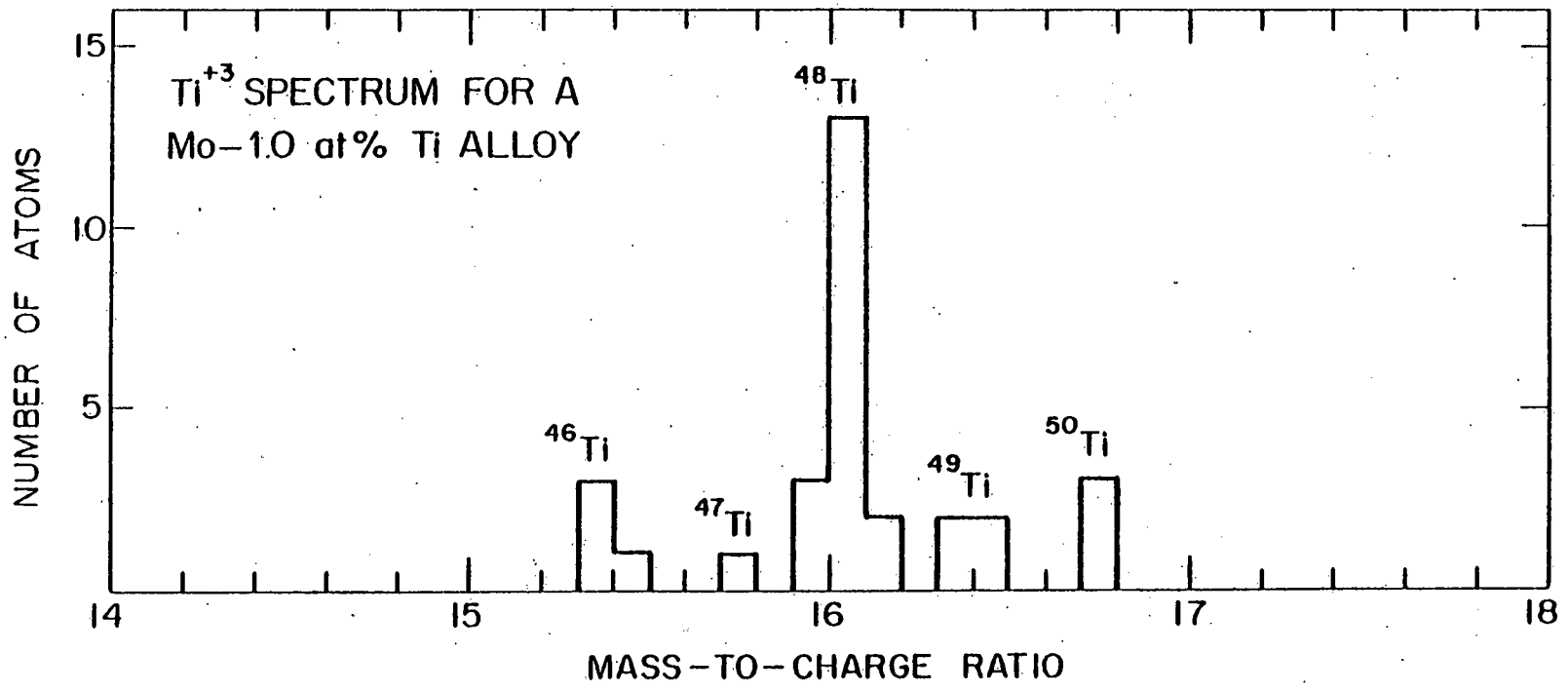

Figure 31. The Ti^{+3} spectrum for an unirradiated Mo-1.0 at. % Ti alloy showing the five stable isotopes of Ti.

Table 5

Comparison of the experimental Ti^{+3} isotopic abundances in an as-received Mo-1.0 at. % Ti alloy with the actual isotopic abundances.

Isotope	Number of Atoms (N)	Experimental* %	Actual %
^{46}Ti	4	13±7	7.9
^{47}Ti	1	3±3	7.3
^{48}Ti	18	60±14	73.9
^{49}Ti	4	13±7	5.5
^{50}Ti	3	10±6	5.4
Totals	30	99	100

* The ± values were calculated from the $\sqrt{N}/\Sigma N$ values where N is the number of atoms detected.

Table 6

Comparison of the composition of a Mo-1.0 at. % Ti alloy determined with the atom probe versus the manufacturer's composition.

Run Number	NUMBER OF ATOMS			CONCENTRATION (atomic %)*	
	Mo	Ti	C	Ti	C
1	10680	40	0	0.37±0.06	< 0.01
2	5408	28	0	0.52±0.10	< 0.02
3	10884	30	0	0.27±0.05	< 0.01
Manufacturer				0.90	0.24

* The ± values were calculated from the $\sqrt{N}/\Sigma N$ values where N is the number of atoms detected.

two possible explanations for the low measured Ti concentration. Titanium may have also field evaporated in the +2 charge state and would therefore have been superimposed directly on the Mo^{+4} portion of the (m/n) spectrum. Thus all of the doubly charged titanium would be indistinguishable from the much more abundant Mo^{+4}. An alternate explanation is that the remaining titanium was not in solid solution. Considerable evidence exists which shows that TiC precipitates can form in both Mo-1.0 at. % Ti and TZM.[70] These precipitates are large and at a low number density on the scale of an FIM observation and hence the probability of detecting any Ti contained within a TiC precipitate is extremely small. In the course of developing a sucessful specimen preparation technique for the Mo-1.0 at. % Ti alloy, extensive transmission electron microscope examination of the electropolished specimen tips were made. Occasionally large precipitates (> 1000 A in diameter) were observed; presumably they were TiC precipitates. This clearly indicated that precipitates were present in the material used in this experiment. Since the manufacturer's Ti concentration included the Ti contained in the TiC precipitates, there must have been less than 0.9 at. % Ti in solid solution. Obviously the Ti concentration measured with the atom probe represents a lower limit on the amount of Ti in solid solution. This argument is also consistent with the experimental observation that no carbon was detected; this shows that the vast majority of the carbon was not in solid solution and that it may reside completely in the TiC precipitates.

However both the low value and the variations in the measured

Ti concentration can also be explained if a significant fraction of the Ti field evaporates as Ti^{+2} and if the ratio of Ti^{+2} to Ti^{+3} was changing from runs 1 to 3. Unfortunately the ratio of Ti^{+2} to Ti^{+3} cannot be measured directly since Ti^{+2} is indistinguishable from Mo^{+4}. However the average charge state of the field evaporating Mo would be expected to be related to the average charge state of the Ti. Thus a significant increase in the ratio of Ti^{+3} to Ti^{+2} should be reflected by a significant increase in the average Mo charge state. Fig. 32 shows a plot of the measured Ti concentration versus average Mo charge state for the three runs on unirradiated Mo-1.0 at. % Ti. Also included are two runs on unirradiated TZM which had the same nominal Ti concentration as the Mo-1.0 at. % Ti alloy and a run on fast neutron irradiated Mo-1.0 at. % Ti. There are two points to be noted: (1) the change in the average Mo charge state was small relative to the change in the measured Ti concentration; and (2) there was no obvious correlation between Ti concentration and Mo charge state i.e., there was no evidence that as the measured Ti concentration increased that the average Mo charge state and hence the ratio of Ti^{+3} to Ti^{+2} increased. These results suggest that it is unlikely that the observed variations in the Ti concentration were due to variations in the Ti^{+3} to Ti^{+2} ratio and that it is unlikely that a significant fraction of the Ti field evaporated as Ti^{+2}.

The final observation that the variation in the measured Ti concentration was somewhat greater that the expected statistical variation indicates that the titanium may not be homogenously

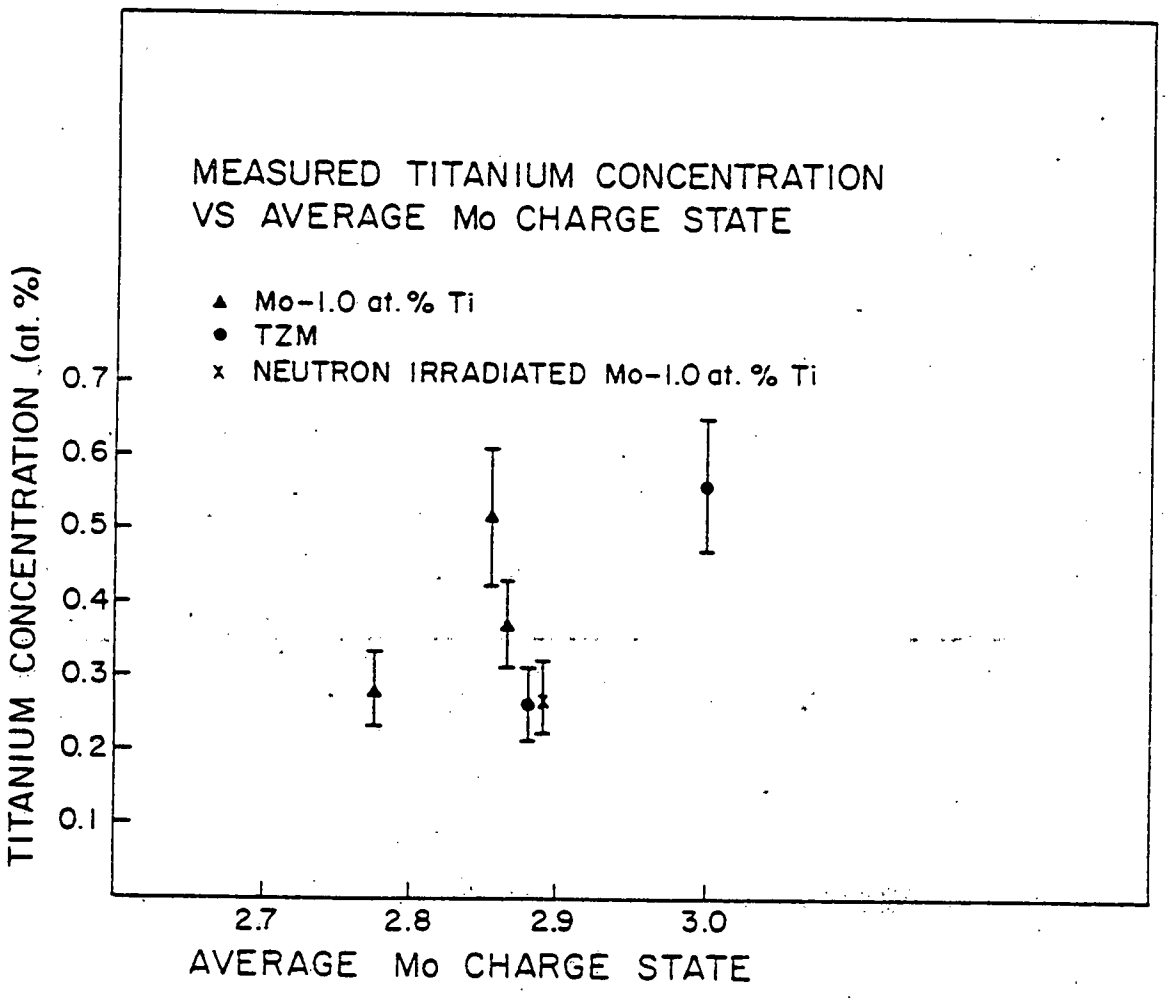

Figure 32. The average measured titanium concentration versus the average molybdenum charge state for several Mo-Ti alloys.

distributed in the alloy. The spatial distribution of the titanium in the alloy is displayed in the composition profiles shown in Figs. 33 to 35. The Ti appears to be uniformly distributed within the entire volume analyzed during run number 1 as shown in Fig. 33. Since the total depth of analysis in this run (and runs number 2 and 3) was approximately 100 to 300 A, the results presented in Fig. 33 indicate that clustering of Ti atoms on a scale less than approximately 100 A did not occur. However the profiles shown in Figs. 34 and 35 may indicate some evidence of a non-uniform titanium distribution. The probability of the indicated steep increases in the Ti concentration shown in Figs. 34 and 35 occurring as a result of a fluctuation in a random solid solution were estimated to be less than 0.1 for each fluctuation based on the computer simulation technique described in section 4.4. In order to rule out the possibility that these fluctuations were an artifact induced by an increased rate of field evaporation (see section 6) an evaporation rate profile for run number 3 was generated. Figure 36 shows the evaporation rate versus cumulative number of Mo+Ti atoms. Note that the evaporation rate was approximately constant throughout the entire run with no evidence of an increased rate in the region of the observed fluctuation in the titanium concentration. The average charge state of the Mo was also approximately constant throughout the entire run. This suggests that the average charge state of the titanium was also a constant throughout the run since the same physical process (field evaporation) which affects the molybdenum charge state also operated on the titanium. Thus it is highly unlikely that the observed fluctuation in the

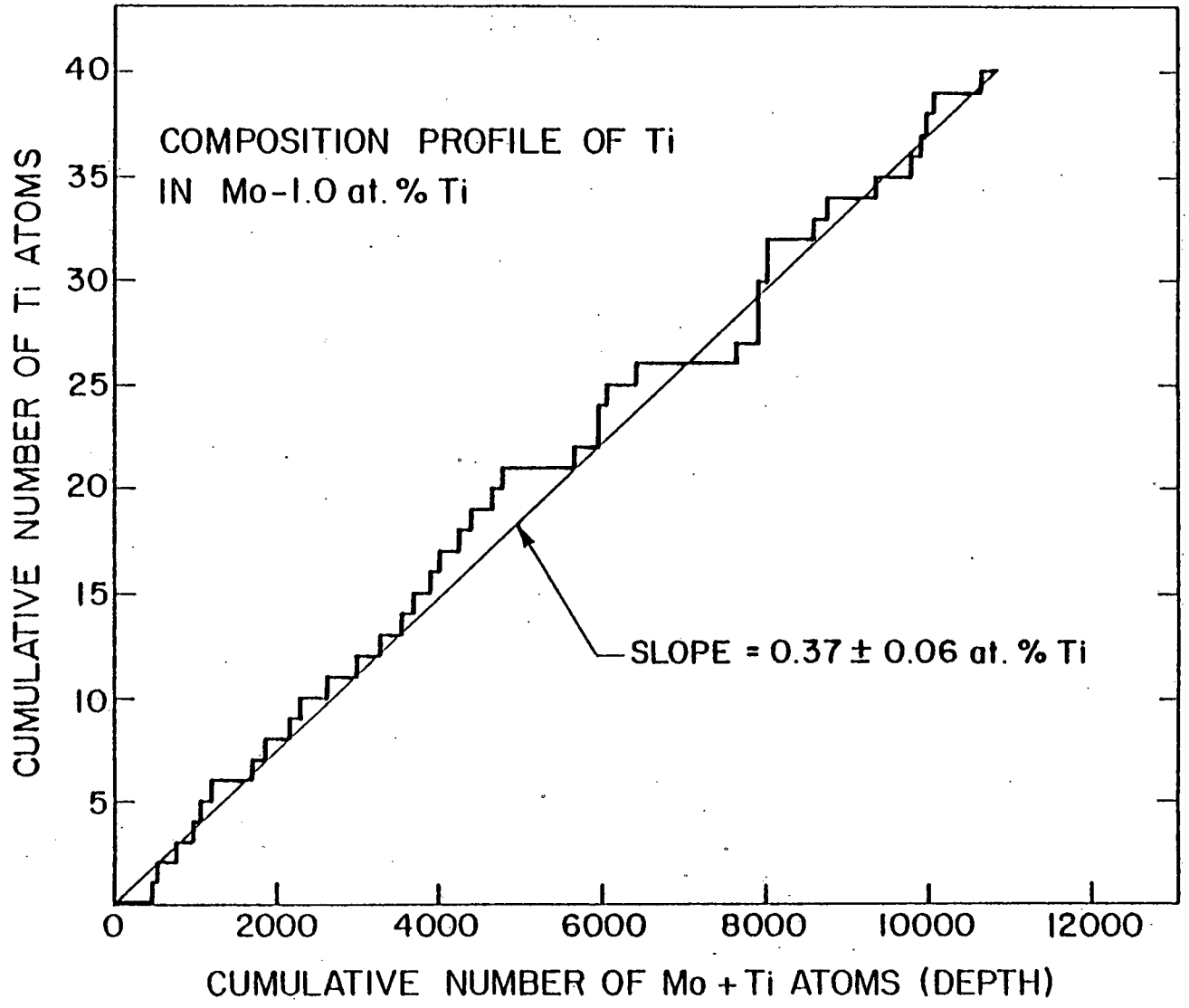

Figure 33. The composition profile for titanium in an unirradiated Mo-1.0 at. % Ti alloy.

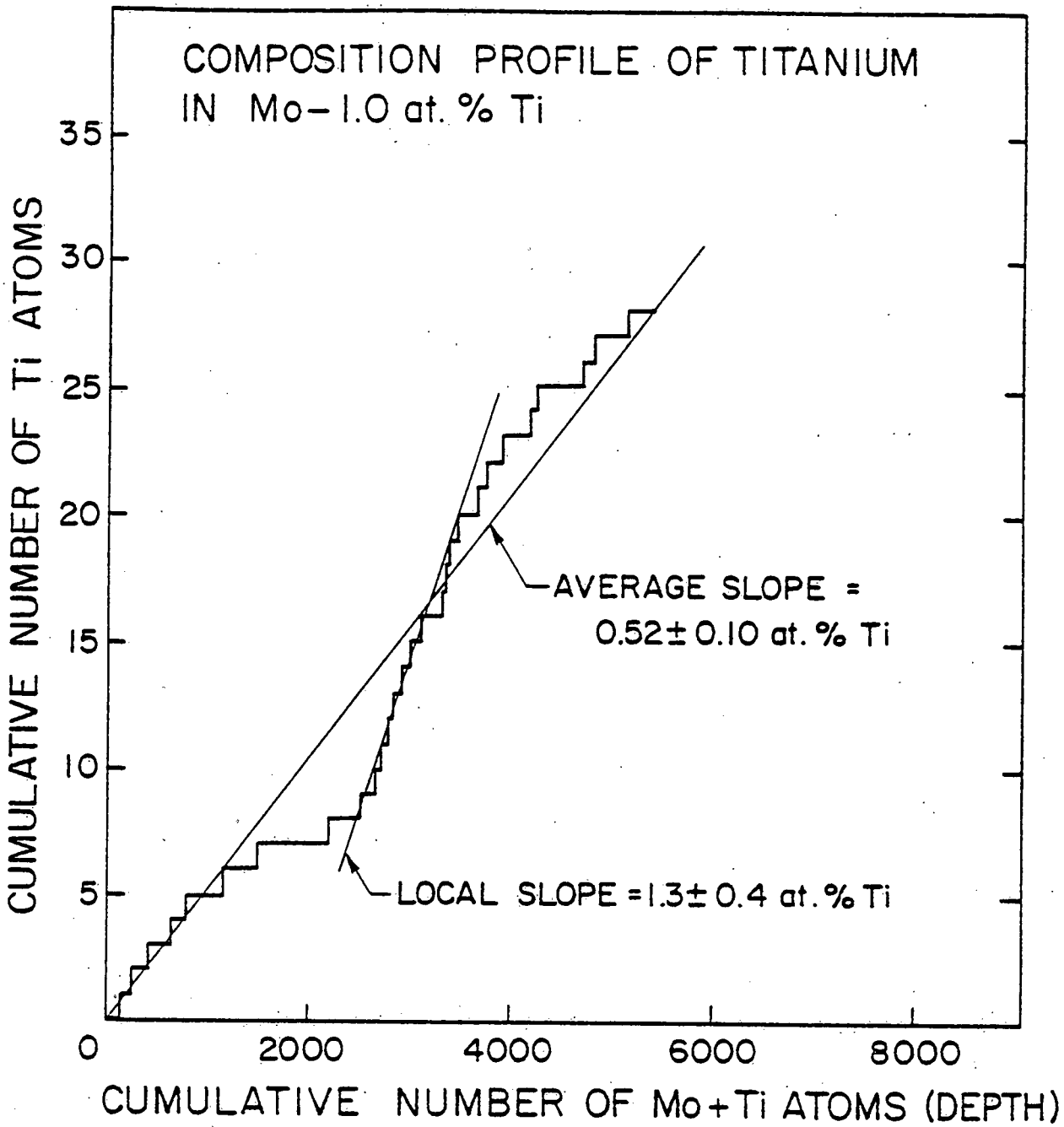

Figure 34. The composition profile for titanium in an unirradiated Mo-1.0 at. % Ti alloy. A large local fluctuation in the Ti concentration is indicated.

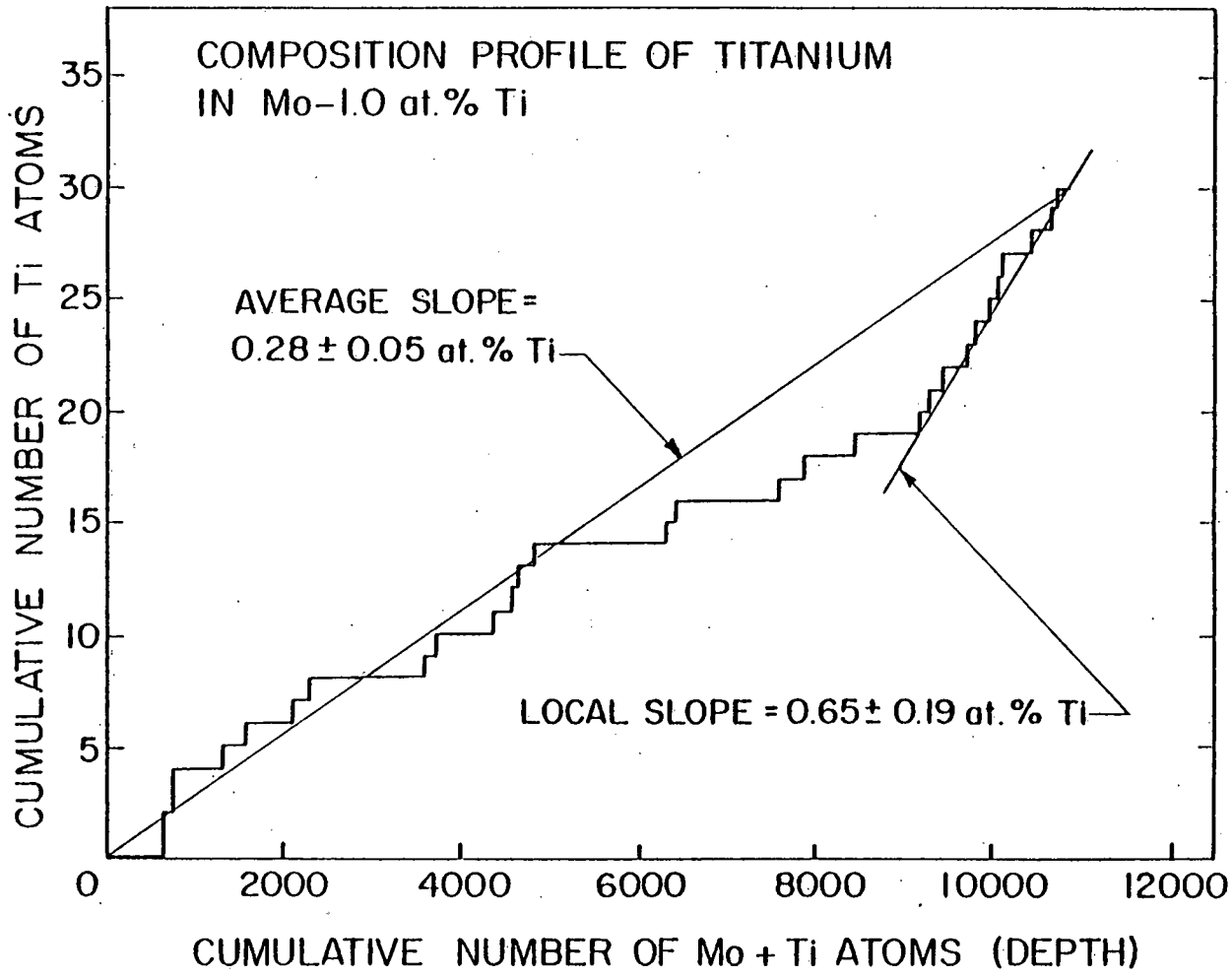

Figure 35. The composition profile for titanium in an unirradiated Mo-1.0 at. % Ti alloy. A large local fluctuation in the Ti concentration is indicated.

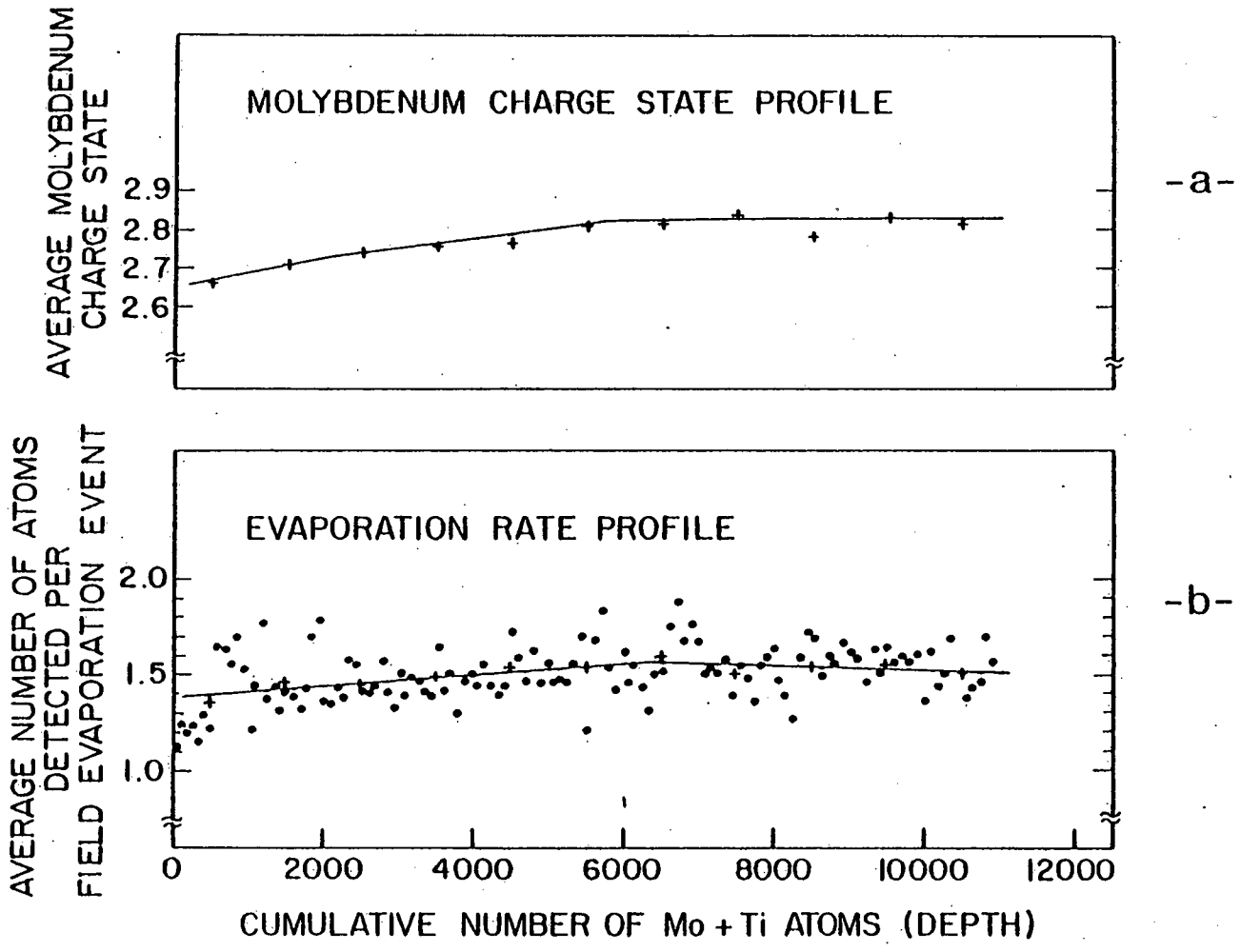

Figure 36. (a) The average molybdenum charge state versus the cumulative number of Mo plus Ti atoms (depth) corresponding to the composition profile shown in Fig. 35.

(b) The average number of atoms detected per field evaporation event versus the cumulative number of Mo plus Ti atoms (depth) corresponding to the composition profile shown in Fig. 35.

titanium concentration was caused by a sudden increase in the ratio of Ti^{+3} to Ti^{+2}.

The most reasonable interpretation of the experimental results is as follows. There was at least 0.25 at. % Ti in solid solution and it was not associated with and other element. The titanium in solid solution was uniformly distributed on a fine scale (< 100 A) but may have been non-uniformly distributed on a scale > 100 A i.e., the alloy was not homogenous on a coarse scale. There was less than 0.004 at. % carbon in solid solution and a significant fraction of the titanium was not in solid solution. These results are compared in section 8 with the results on the spatial distribution of the elements in neutron irradiated Mo-1.0 at. % Ti.

The data for a typical run of the Mo-1.0 at. % Ti were recorded with the atom probe at a background pressure of $5.2 \cdot 10^{-10}$ torr and at a specimen temperature of 42 K. The partial pressures of the major residual gas components were: $H_2 = 4.73 \cdot 10^{-10}$ torr, He = $2.0 \cdot 10^{-12}$ torr, $CH_4 = 1.7 \cdot 10^{-11}$ torr, $CO = 2.4 \cdot 10^{-11}$ torr, and $CO_2 = 4.0 \cdot 10^{-12}$ torr. The calibration parameters were $\alpha = 1.2$, $t_o = 0.56$ μsec, and d = 2218 mm while the voltage range was $V_{dc} = 5600$ to 9400 V with a value of f = 0.05.

5.4 Molybdenum-Titanium-Zirconium Alloy (TZM)

The alloy Mo-1.0 at. % Ti-0.08 at. % Zr (TZM) has been found to exhibit an enhanced swelling behavior and a very fine dislocation substructure when compared to pure molybdenum for fast neutron irradiation at temperatures less than 650 C[71]. The atom probe data on

TZM presented in this section will serve as a control for future experiments on fast neutron irradiated TZM specimens. The objective is to determine the mechanism responsible for the enhancement in swelling when Ti and Zr are added to molybdenum.

The 0.2 mm diameter wire was cold drawn from a 1 mm diameter rod of TZM which had been stress relieved between 870 and 980 C. After the cold drawing operation, the wire was brittle and somewhat fibrous. The FIM specimens were prepared by the dipping technique in the electropolishing solution developed for the Mo-1.0 at. % Ti alloy.

Figure 37 shows a semilogarithmic plot of the (m/n) histogram of TZM between 0 and 55 amu. The peaks near 24, 32, and 48 amu are associated with Mo^{+4}, Mo^{+3}, and Mo^{+2} respectively. The cluster of peaks near 16 amu is associated with Ti^{+3} while the peaks at 30 and 45 amu are associated with $^{90}Zr^{+3}$ and $^{90}Zr^{+2}$ respectively.

The experimentally measured concentration of Ti, Zr, and C for this histogram and for one additional run are compared with the manufacturer's composition[72] in Table 7. The comments made in section 5.3 on the difference between the measured and the nominal Ti concentration and the carbon concentration in the Mo-1.0 at. % Ti alloy also apply to the TZM. The large variation in the experimentally measured Zr concentration suggesta that the Zr was non-uniformly distributed in the TZM specimens employed in these experiments.

The composition profiles of Ti and Zr in TZM for run numbers 1 and 2 are shown in Figs. 38 and 39 respectively. Note that the Ti appears to be uniformly distributed in both runs while the Zr profile

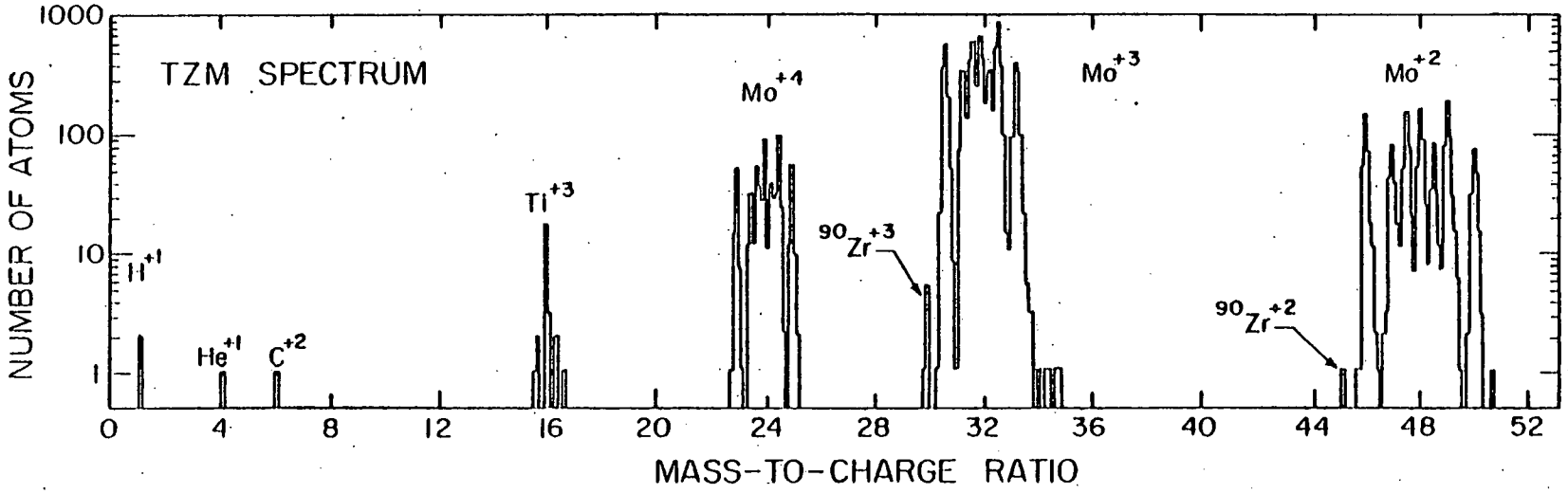

Figure 37. Semilogarithmic plot of the (m/n) spectrum for TZM. Note that the seven isotopes of molybdenum, the ^{90}Zr isotope, and four of the five isotopes of titanium are clearly visible. The absence of ^{46}Ti and ^{91}Zr peaks is not surprising since these isotopes would be expected to produce only 1 ± 1 event on a statistical basis. The measured Ti and Zr concentrations were 0.26 and 0.13 at. % respectively.

Table 7

Comparison of the composition of TZM determined with the atom probe versus the manufacturer's composition.

	NUMBER OF ATOMS				CONCENTRATION (atomic %)*		
Run Number	Mo	Ti	Zr	C	Ti	Zr	C
1	10818	28	7	2	0.26±0.05	0.13±0.03	0.02±0.01
2	6422	36	0	2	0.56±0.09	0.02	0.03±0.02
Manufacturer					0.90	0.09	0.13

* The ± values were calculated from the $\sqrt{N}/\Sigma N$ values where N is the number of atoms detected.

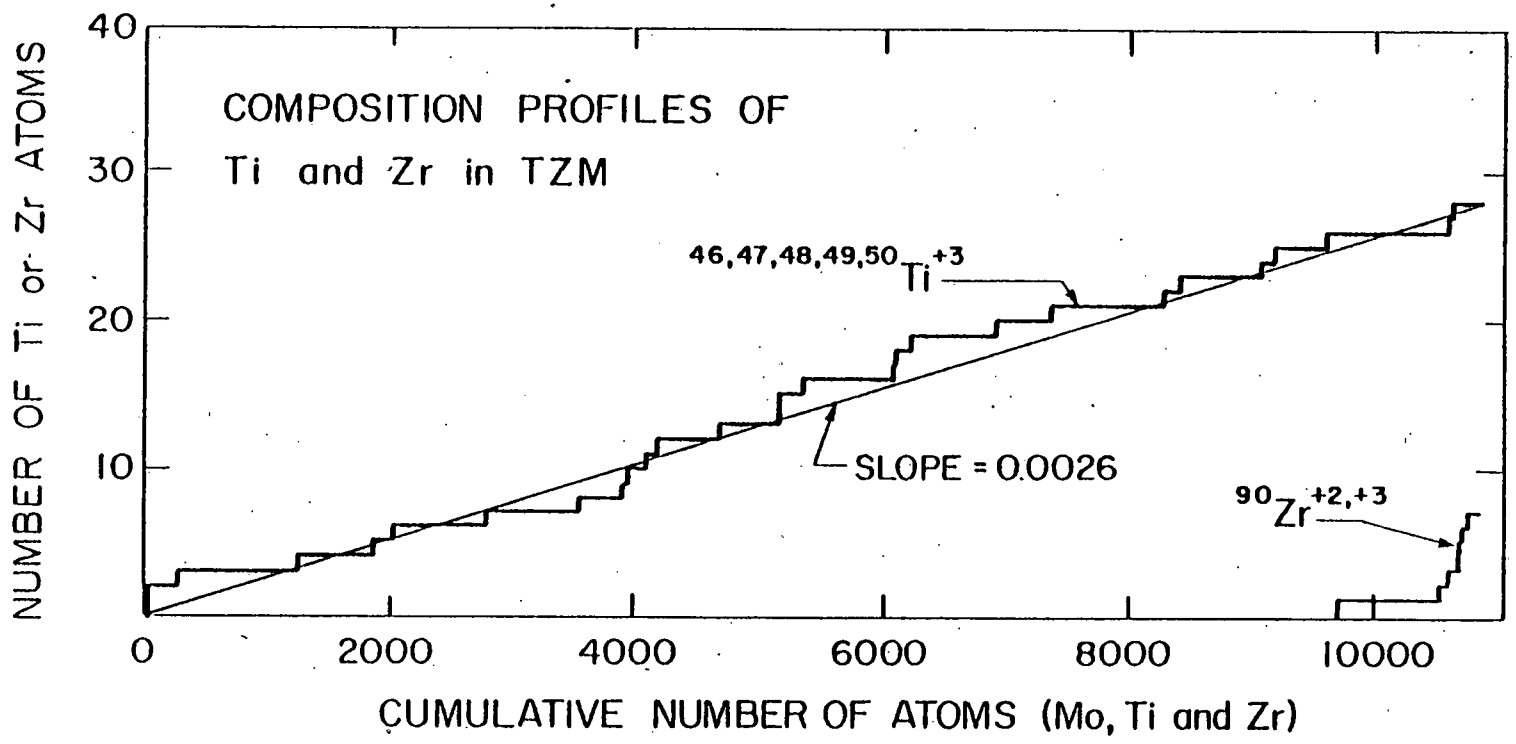

Figure 38. The composition profile for Ti and Zr corresponding to the TZM spectrum shown in Fig. 37. The Ti appears to have been uniformly distributed within the volume analyzed in this specimen while the Zr was non-uniformly distributed.

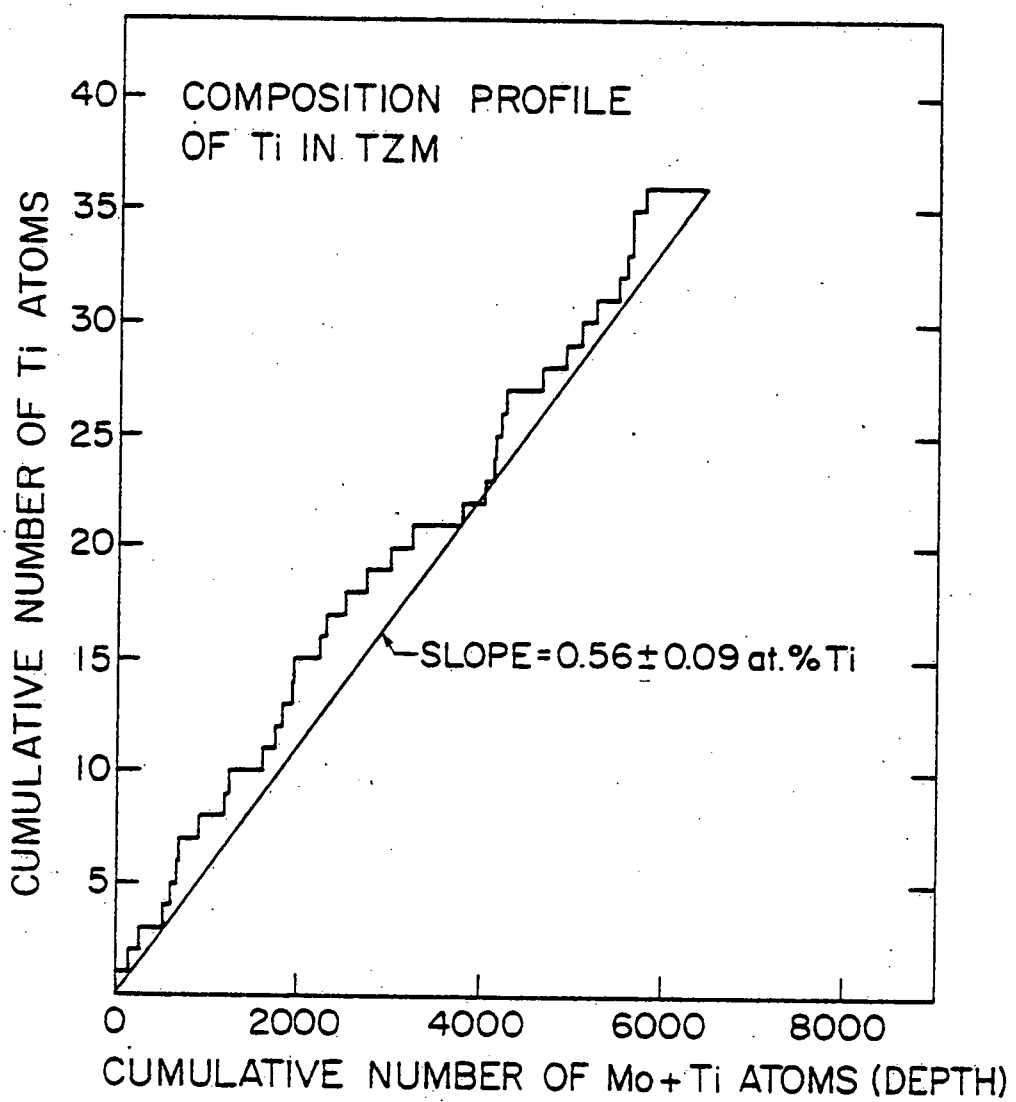

Figure 39. The composition profile for Ti in a second sample of TZM. The Ti appears to have been uniformly distributed. No Zr was detected in this experiment indicating that the Zr was non-uniformly distributed.

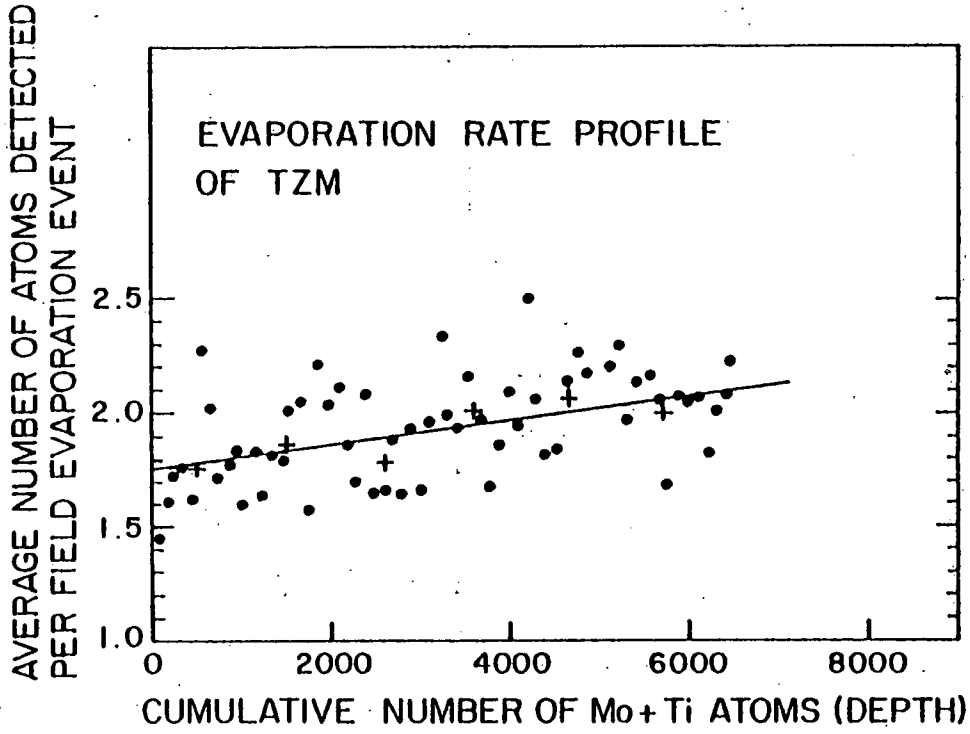

Figure 40. The evaporation rate profile corresponding to the composition profile shown in Fig. 39. The slowly increasing evaporation rate indicated in this figure had no demonstrable effect on the Ti composition profile shown in Fig. 39.

in Fig. 38 shows that all of the Zr was contained in a single cluster. The probability of this cluster resulting from a statistical fluctuation in a random solid solution was calculated to be approximately 10^{-6} (see Appendix C). An evaporation rate analysis revealed that each Zr atom was detected individually with an evaporation rate of 1 atom detected per evaporation event. Therefore the Zr cluster was not an artifact induced by a high local evaporation rate. This is conclusive evidence that the fluctuation in the Zr concentration was non-random which indicates a positive binding enthalpy between Zr atoms in TZM. Carbon was not associated with either the Ti or the Zr and therefore the observed Zr cluster was not due to a small carbide precipitate. The Zr cluster was detected just before the FIM tip failed and may have contributed to the failure. These experiments will serve as controls for future experiments on neutron irradiated TZM.

The data for a typical run on TZM were recorded with the atom probe at a background pressure of $4.5 \cdot 10^{-10}$ torr and a specimen temperature of 35 K. The major residual gas components during the analysis were: $H_2 = 4.22 \cdot 10^{-10}$ torr, $CH_4 = 8.0 \cdot 10^{-12}$ torr, CO = $1.8 \cdot 10^{-11}$ torr, and $CO_2 = 3.0 \cdot 10^{-12}$ torr. The voltage range was V_{dc} = 12,200 to 13,300 V, the value of f was 0.05, and the calibration parameters were $\alpha = 1.2$, $t_o = 0.56$ μsec, and d = 2218 mm.

5.5 Low Swelling Stainless Steel (LS1A)

Results on an unirradiated low swelling stainless steel alloy (LS1A) developed at Oak Ridge National Laboratory by Bloom et. al.[73]

are presented in this section. This alloy is a type 316 stainless steel which has been modified by additions of Si and Ti. The addition of Si and Ti to stainless steel results in a large decrease in swelling due to fast neutron irradiation. Furthermore the addition of both Si and Ti results in a larger reduction in swelling than expected from swelling data when only one element was added i.e., there appears to be a synergistic effect when both Si and Ti are present.[74] The ultimate objective of this work is to determine the mechanism by which the Si and Ti additions suppress swelling.

The material was examined in the cold worked state after having been drawn from a 0.24 mm to a 0.20 diameter wire. After each drawing pass except the last one, the material was annealed at 1050 C for approximately 15 min in an argon atmosphere. The FIM specimens were prepared by dipping 4 mm of the wire into a solution of 33 % H_3PO_4 in H_2O (by volume) and then electropolishing at 10 Vdc until 2 mm of the wire end was removed. If more than 2 mm of the wire was removed or if a more dilute solution of H_3PO_4 were employed, the specimen always failed prematurely in the FIM often before any image was produced. Electron microscope examination of the electropolished specimens revealed that as the length of material electrolytically removed increased, or as the concentration of the H_3PO_4 solution decreased, the shank angle on the specimen would decrease. This indicates that as the shank angle decreased, the failure rate increased probably due to an increased probability of a flaw residing in the stressed region of the specimen shank. A minimum shank angle of ~ 15 degrees was estimated.

Figure 41 shows the FIM image of LS1A taken at 60 K employing neon as the imaging gas. The non-crystalline appearance of the image is characteristic of disordered concentrated alloys.[75,76]

All of the alloying elements (Fe, Cr, Ni, Mn, Mo, C, Si, and Ti) in LS1A were readily identified by the atom-probe FIM technique as shown in Figs. 42 and 43. In particular the isotopes $^{52}Cr^{+4}$, $^{28}Si^{+2}$, $^{29}Si^{+2}$, $^{30}Si^{+2}$, and $^{48}Ti^{+3}$ can be easily seen in the 12 to 17 amu portion of the spectrum. The $^{48}Ti^{+3}$ peak at 16 amu may contain an undetermined amount of oxygen. The most probable source of the oxygen is residual CO and CO_2 in the FIM which can decompose on the surface of the FIM tip. The isotopes $^{50}Cr^{+2}$, $^{52}Cr^{+2}$, $^{54}Fe^{+2}$, $^{55}Mn^{+2}$, $^{56}Fe^{+2}$, $^{58}Ni^{+2}$, and $^{60}Ni^{+2}$ can be clearly identified in the 24 to 34 amu portion of the spectrum.

Table 8 shows the composition of each element in this alloy as determined by the atom-probe technique. The first column in the table gives the chemical composition as supplied by ORNL wile the second column gives the average composition as determined by the atom probe. The number of atoms of atoms of a particular species was determined by counting all of the atoms contained between the leading edge of the (m/n) peak of the species and the leading edge of the next higher (m/n) peak. For example, all of the Cr atoms counted were contained between the leading edge of the $^{50}Cr^{+2}$ peak and the $^{54}Fe^{+2}$ peak. Thus no attempt was made to fit an exponential energy deficit tail to the (m/n) peaks. This would cause the reported concentrations of Ni, Mn, and Mo to be somewhat higher than the actual measurement and Cr to be somewhat lower. In spite of this the agreement between conventional

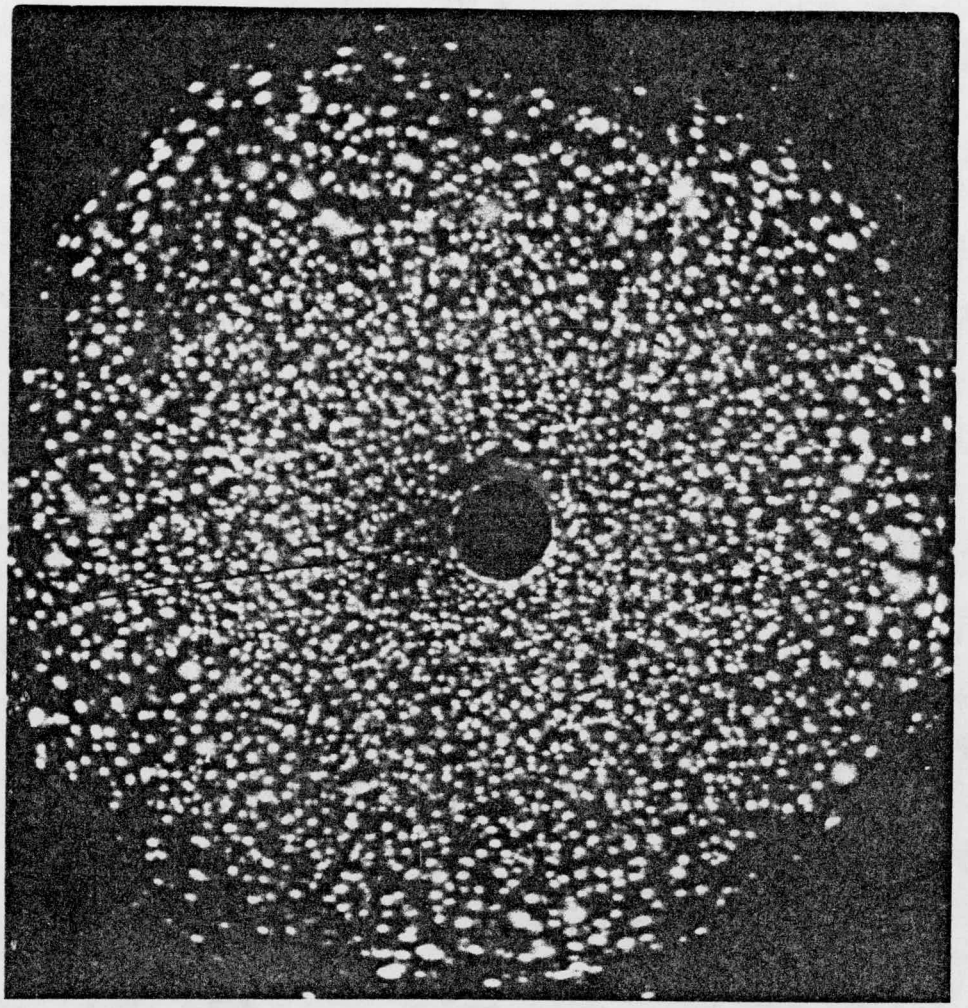

Figure 41. A FIM micrograph of a low swelling stainless steel (LS1A).

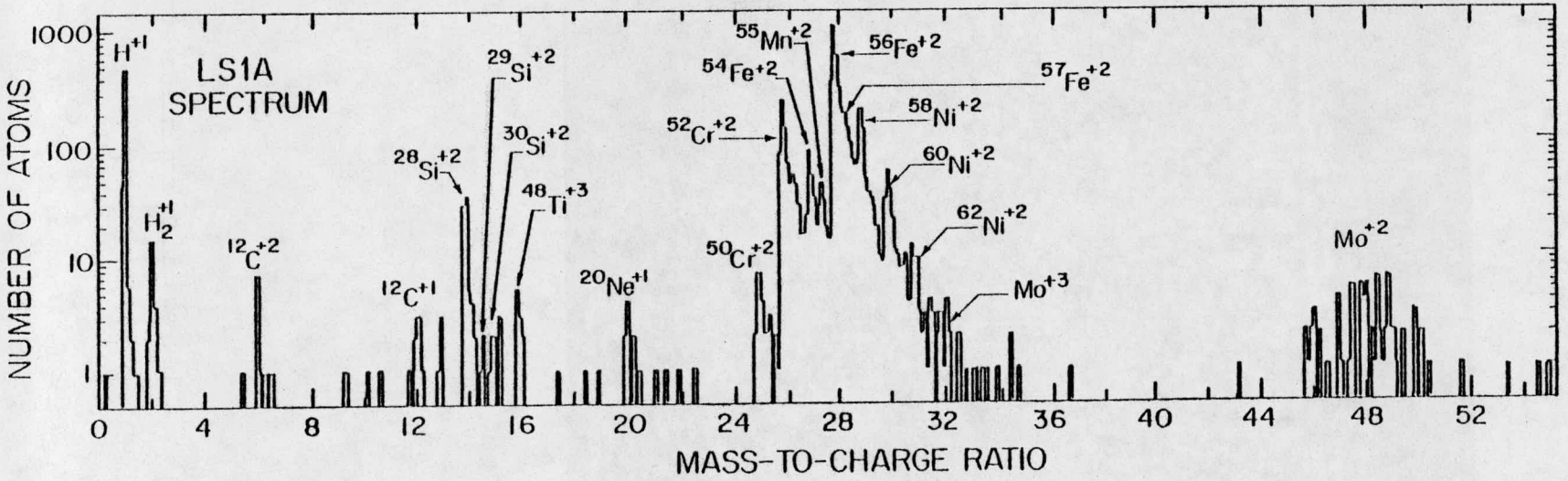

Figure 42. Semilogarithmic plot of the (m/n) spectrum for LS1A. The main constituents (Fe, Ni, Cr) as well as the minor alloying additions with concentrations of fractions of an atomic percent (Mn, Mo, Si, Ti) were easily detected by the atom probe technique.

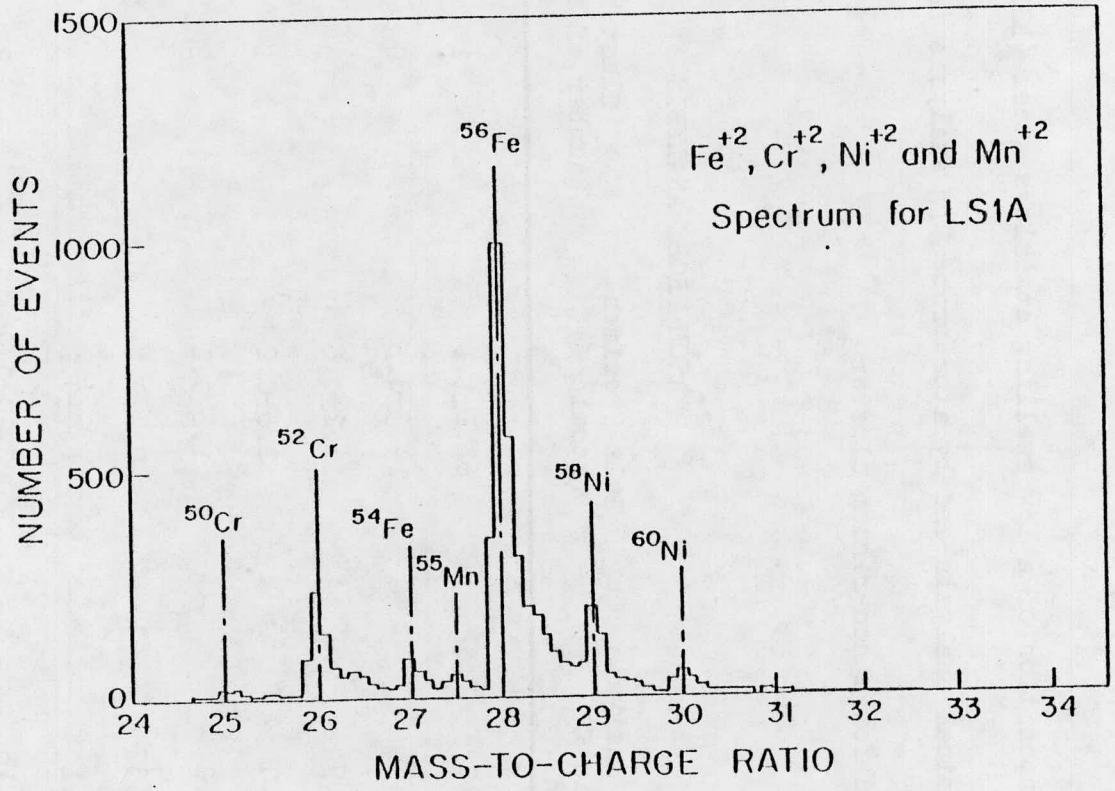

Figure 43. The 24 to 34 amu portion of the LS1A spectrum shown in Fig. 42. The major alloying elements (Fe, Cr, Ni) and one minor alloying element (Mn) are clearly visible.

Table 8

Comparison of the composition of a low swelling stainless steel (LS1A) as determined by chemical analysis and by atom probe FIM analysis for the bulk specimen and for a non-random cluster

Element	Chemical Analysis (atomic %)	ATOM PROBE ANALYSIS Bulk Specimen (atomic %)*	Cluster (number of atoms)
Fe	64.0	62.2±1.1	1
Cr	17.4	14.5±0.5	0
Ni	12.9	16.2±0.6	3
Mn	2.0	2.6±0.2	1
Mo	1.0	1.8±0.2	2
C	0.37	0.4±0.1	2
Si	2.1	1.7±0.2	3
Ti	0.16	0.20±0.06	2
Other	0.15	0.5±0.1	0
Totals	100.1	100.1	14

* The uncertainties were calculated from the $\sqrt{N}/\Sigma N$ values where N is the number of atoms detected.

chemical analysis and the atom probe analysis is good. The differences which do exist were all in the expected direction so that the agreement is probably better than is indicated in Table 8. Note that hydrogen detected in the atom probe analysis has not been included in the table. The measured H atom concentration of ~ 10 at. % is much greater than the known bulk concentration. This discrepancy was due either to electrolytic charging of the specimen with hydrogen during electropolishing or was the result of adsorbtion on the surface of the FIM specimen of residual hydrogen in the vacuum system which subsequently was field evaporated.

An analysis of the spatial distribution of each alloying element revealed the existence of a cluster of 14 atoms which was rich in all of the minor alloying elements (Si, Ti, C, Mo, and Mn) and poor in two of the major components (Fe and Cr) as shown in the last column of Table 8. The probability of this cluster forming as the result of a statistical fluctuation in a random alloy was calculated to be less than 10^{-11} (see appendix C), hence this was clearly a non-random fluctuation in composition. This indicated that a positive binding enthalpy exists between all of the minor alloying additions. It is possible that clusters such as the one described are responsible for the observed enhanced reduction in swelling when both Si and Ti are added to stainless steel. A possible mechanism would involve the trapping of SIAs and/or vacancies at these clusters. This would increase defect recombination and thereby decrease the number of defects which could contribute to void growth i.e., swelling. Although only one cluster was detected, the fact that the total volume

of material analyzed was less than $5 \cdot 10^{-19}$ cm^3 suggests that these clusters are present at a very high number density.

The spectrum for the LS1A was recorded with the atom probe at a background pressure of $1 \cdot 10^{-9}$ torr and at a specimen temperature of 50 K. The voltage range was 16,600 to 19,900 Vdc, the value of f was 0.075 and the calibration parameters were $\alpha = 1.482$, $t_o = 0.56$ μsec, and d = 2227 mm.

5.6 Metallic Glass (Metglas 2826)

A metallic glass* (Metglas 2826) with a nominal composition of 40 at. % Fe, 40 at. % Ni, 14 at. % P, and 6 at. % B was examined with the atom probe. The experiment was performed to establish the feasibility of studying the clustering behavior of the phosphorus and boron in this alloy. The clustering of phosphorus had been suggested as a possible mechanism for the embrittlement of this alloy following heat treatment below its crystallization temperature(78).

The FIM specimen was prepared employing an electropolishing solution which consisted of 4 parts ethanol: 1 part perchloric acid (by volume). Prior to the atom probe analysis, the specimen was annealed at 150 to 170 C for about 6 hours during the routine UHV bakeout procedure for the atom probe.

The (m/n) histogram for Metglas 2826 in Fig. 44 shows that the various constituents can be easily identified. The composition as determined by the atom probe was 35.8±1.3 at. % Fe, 37.1±1.3 at. % Ni,

---

* See reference 77 for a review on metallic glasses.

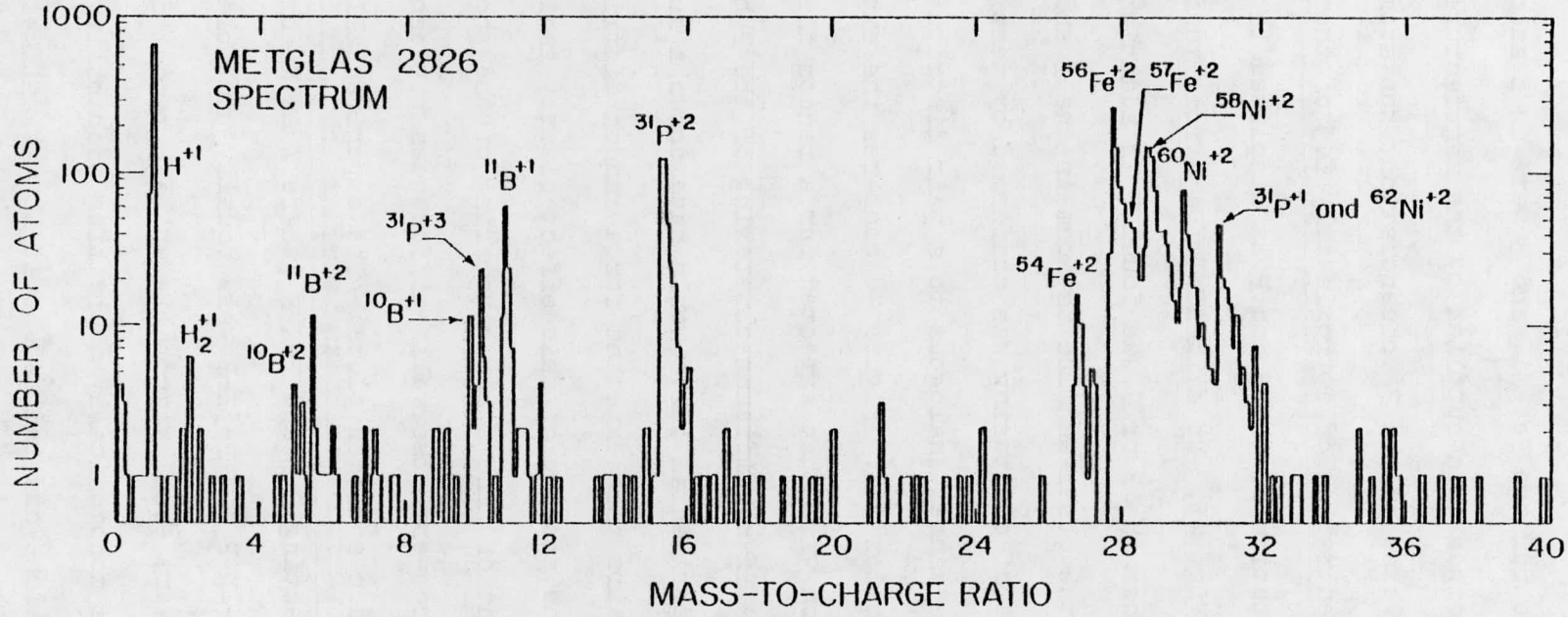

Figure 44. Semilogarithmic plot of the (m/n) spectrum for Metglas 2826. The constituents of this metallic glass (Fe, Ni, P, B) were easily identified. Note the random background counts which are clearly visible in this semilogarithmic plot caused by the $1 \cdot 10^{-7}$ torr Ne imaging gas which was present during the atom probe analysis.

20.9±1.0 at. % P, and 6.2±0.5 at. % B. The composition determined with the atom probe for the Fe, Ni, and B were in reasonable agreement with the nominal composition supplied by the manufacturer (Allied Chemical). In the case of the P concentration, the atom probe analysis indicated a P concentration of approximately 1.5 of the nominal value. The spatial distribution of the B and P is displayed in the composition profiles shown in Fig. 45. No evidence of a strong tendency for clustering for either the B or P was found. In addition no correlation was found between the observed fluctuations in the B and P concentrations. The absence of clustering was confirmed by testing the P distribution in the manner analogous to a pair distribution function as discussed in section 5.2. Figure 46 compares the experimental cluster distribution with that expected for a random distribution of P in the alloy. If significant clustering of the P had taken place, then the experimental curve would have shown a much higher incidence of P-P pairs than expected for a random distribution of P in the alloy. The absence of this effect clearly indicates that a significant amount of fine scale clustering of the phosphorus had not occurred. There were observable differences between the experimental and the random solution plots. The experimentally measured probability of detecting P-P and P-X-P (where X is Ni or Fe) were equal, similarly P-2X-P and P-3X-P were equally probable, also P-4X-P, P-5X-P and P-6X-P were equally probable while a random distribution should have shown a monotonically decreasing probability. An ensemble of computer simulations did indicate that it was unlikely that this pattern was the result of simple statistical fluctuations in a random

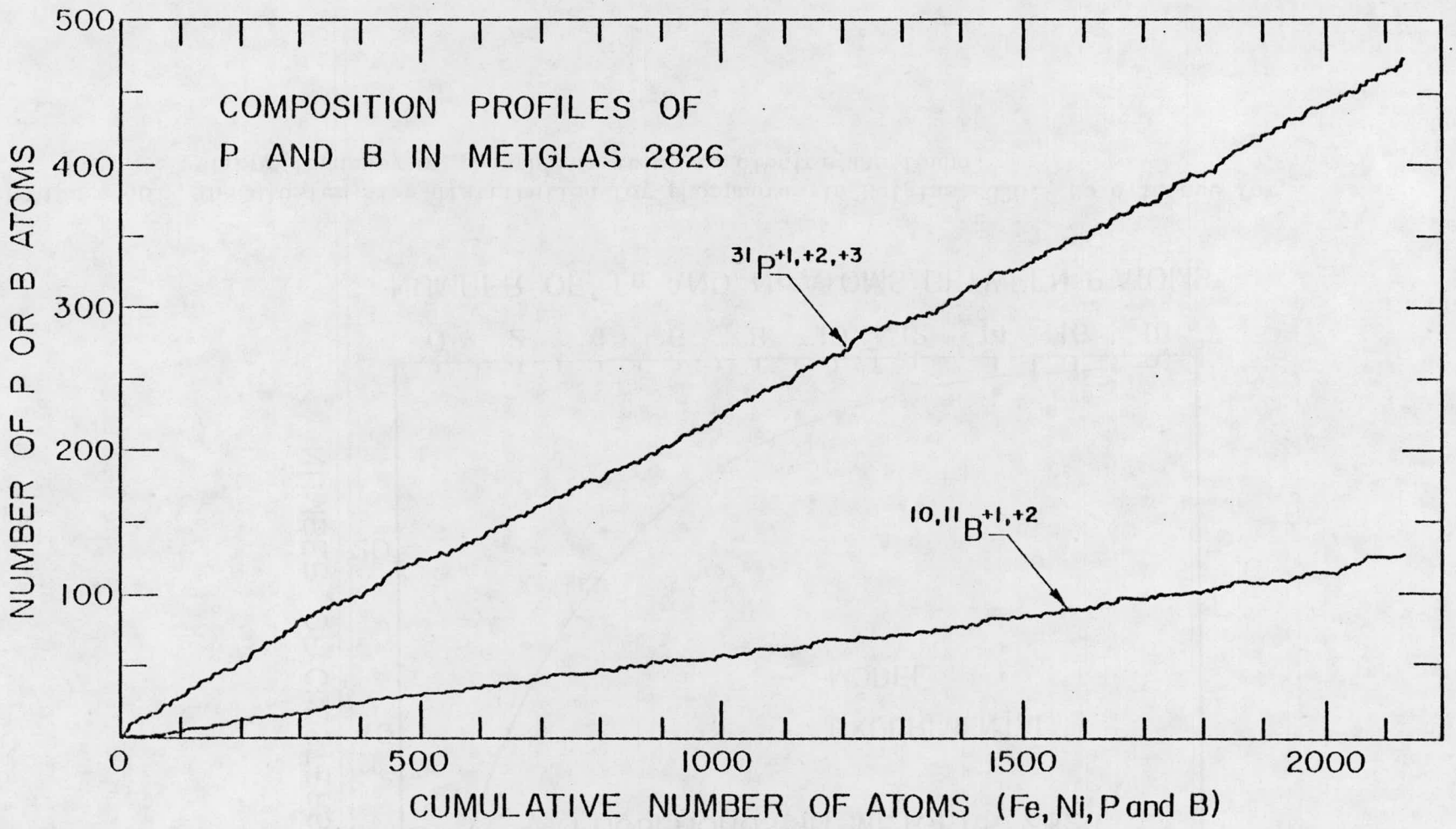

Figure 45. The composition profiles for boron and phosphorus in Metglas 2826. This specimen was heated to approximately 430 K for less than 6 hours. The B and P appear to be uniformly distributed.

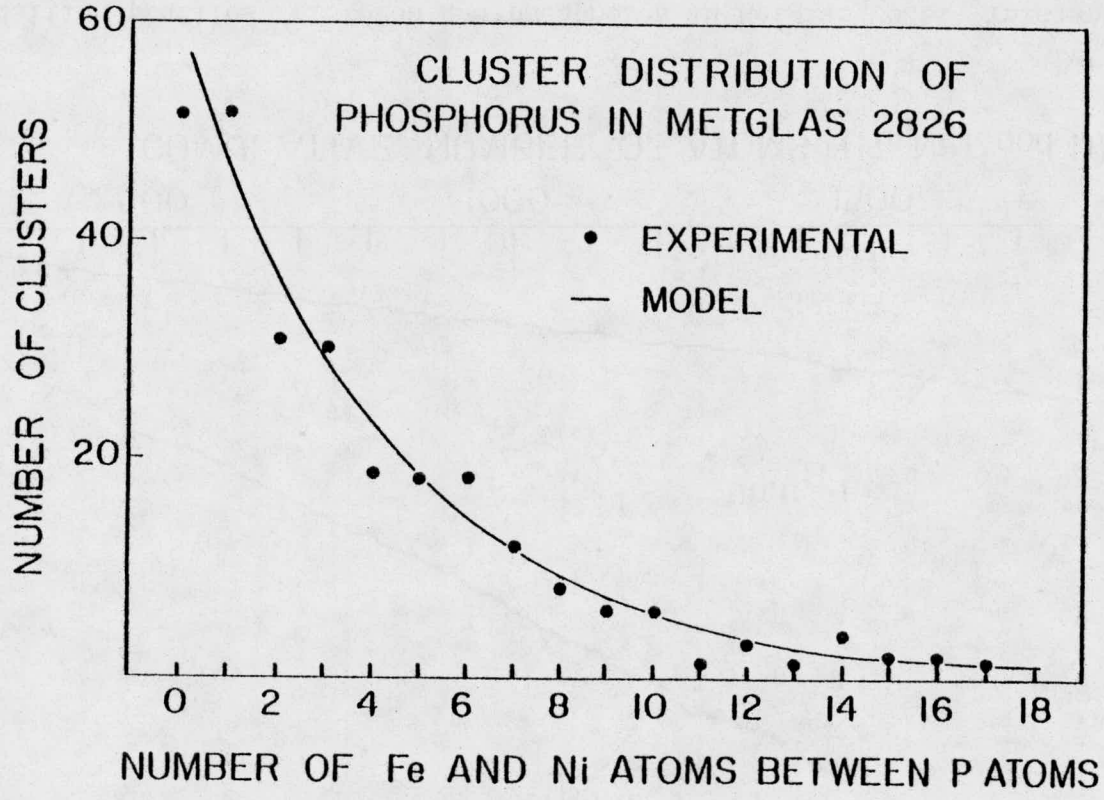

Figure 46. The cluster size distribution for phosphorus in Metglas 2826. No evidence for a strong tendency of phosphorus atoms to cluster was found.

distribution of P in the alloy. However it is not clear what the physical significance of this pattern is in terms of the P distribution. For example, this pattern may reflect the field evaporation characteristics of the P in the alloy and not the actual spatial distribution of the phosphorus.

There are two possible explanations consistent with the large experimentally measured P concentration and absence of fine scale clustering: (1) the nominal composition determined by the manufacturer was incorrect for the material used in this experiment; or (2) the entire volume of the specimen which was analyzed contained a cluster rich in phosphorus.

The FIM image of the Metglas 2826 is shown in Fig 47. Although the image generally appeared amorphous, evidence of a ring structure which is characteristic of crystallinity was present. This apparent crystallization occurred at a temperature (150 to 170 C) which is well below the crystallization temperature as determined by electron microscopy (~ 320 C) and may be related to the embrittlement which occurs in this material when it is heated to temperature > 100 C for several hours. Unfortunately the specimen failed before an atom probe analysis of the region in question could be obtained.

The Metglas 2826 data were recorded in the presence of $\sim 1 \cdot 10^{-7}$ torr neon at a background pressure of $\sim 2 \cdot 10^{-9}$ torr and a specimen temperature of 63 K. The voltage range was varied from 18,500 to 19,400 V_{dc}, the value of f was 0.10 and the calibration parameters were $\alpha = 1.482$, $t_o = 0.56$ μsec, and d = 2231 mm.

Figure 47. A FIM micrograph of a metallic glass (Metglas 2826).

6. THE EFFECT OF FIELD-EVAPORATION RATE ON QUANTITATIVE ATOM PROBE ANALYSIS

In this section the effect of a high rate of field evaporation on the quantitative chemical analysis of materials by atom probe field ion microscopy is discussed. Several examples of erroneously high measured values of the titanium concentration in a Mo-1.0 at. % Ti alloy are presented and the cause is shown to have been due to a high field-evaporation rate. Although only examples from the Mo-Ti system are presented, the basic arguments are applicable to the quantitative analysis of all alloy systems examined with the atom probe.

During a typical atom probe analysis, high-voltage pulses were repeatedly applied to the specimen until one or more atoms were field evaporated in the form of positively charged ions. The ions were then rapidly accelerated to their terminal velocities with the smaller (m/n) ions achieving the higher terminal velocities (see section 1.1). The ions then traveled down a flight tube approximately 2.2 meters in length to a Chevron CEMA detector which sensed the arrival of each ion at the detector. If several ions were field evaporated by the application of a single field-evaporation pulse and if each of the ions had different (m/n) values, then each ion would be detected and an exact quantitative chemical analysis would be obtained. However if several ions with the same (m/n) value field evaporated simultaneously, they would all arrive at the detector at the same instant in time and hence only one signal from the Chevron CEMA would be produced. This

signal* would then be interpreted erroneously as the arrival of a single ion and would result in an error in the determination of the chemical composition (or isotopic distribution in the case of a pure material). In general the evaporation of more than one atom always results in the measured composition indicating a higher concentration than was actually present in the material of the least abundant species (and correspondingly a lower measured concentration of the most abundant species).

A specific example is presented to illustrate this point. Consider a material which contains two species**, A and B. Let C_a and C_b equal the concentrations of species A and B respectively. In the case of different charge states or isotopes, the concentration of each species is simply determined by the relative population of each species after field evaporation. Assume that exactly two atoms field evaporate for each evaporation event. Then there are three possible

---

* The assumption has been made that a detector pulse-height analysis was not performed. If the output pulse height was proportional to the number of ions striking the detector simultaneously, an exact quantitative analysis could have been obtained even if several ions had field evaporated simultaneously. No evidence presently exists demonstrating a proportionality between pulse height and number of incident ions. In fact considerable evidence does exist (15, 80) which indicates a very broad pulse-height distribution resulting from a single incident ion. This strongly suggests that establishing an accurate and useful proportionality between number of incident ions and detector pulse height would be extremely difficult.

** The term species was used here in a general sense to indicate any atom which field evaporated with a unique (m/n) value. This could include chemically different atoms which have different (m/n) values or chemically identical atoms which have different (m/n) values; e.g., different isotopes of the same element or a single isotope which field evaporated in several charge states or both.

field evaporation products, two A atoms, two B atoms, or one A atom and one B atom. If one A and one B atom evaporate, they are both detected. However if two A or two B atoms evaporate, they are detected as one A or one B atom respectively. The probability of formation for each evaporation product is:

Evaporation Product	Probability	Number of Atoms Detected
2A	C_a^2	1A
2B	C_b^2	1B
1A + 1B	$2C_aC_b$	1A + 1B

Note that the sum of the individual probabilities is $(C_a + C_b)^2 = 1$ as it must be. After N evaporation events (2N total atoms evaporated),

the number of A atoms detected = $N(C_a^2 + 2C_aC_b)$,

the number of B atoms detected = $N(C_b^2 + 2C_aC_b)$, and

the total number of atoms detected = $N(1 + 2C_aC_b)$.

Note that the total number of atoms detected is less than the number field evaporated (2N). The measured concentrations of A and B, C_a' and C_b' respectively are:

$$C_a' = \frac{C_a^2 + 2C_aC_b}{(1 + 2C_aC_b)} \quad \text{and} \quad C_b' = \frac{C_b^2 + 2C_aC_b}{(1 + 2C_aC_b)} \quad . \tag{14}$$

$$\text{Therefore,} \quad \frac{C_b'}{C_a'} = \frac{C_b^2 + 2C_aC_b}{C_a^2 + 2C_aC_b} \quad . \tag{15}$$

Employing equation 14, if $C_b < C_a$ then

$$\frac{C_b'}{C_a'} > \frac{C_b}{C_a} \quad . \tag{16}$$

Thus the measured concentration of solute (C_b') is higher than the actual concentration (C_b). For an infinitely dilute alloy of B in A (i.e., $C_b \ll C_a$), the measured concentration of B approaches twice the actual concentration i.e., C_b' approaches $2C_b$ and a 100 % error results. Note also that the number of atoms detected is significantly less than the number field evaporated. The ratio (γ) of atoms detected to atoms evaporated equals ($\frac{1}{2} + C_a C_b$) so that $1/2 < \gamma < 3/4$. For a multi-species system in which two atoms field evaporate, the measured concentration of component i (C_i') is given by

$$C_i' = \frac{C_i^2 + 2C_i(1 - C_i)}{1 + \Sigma\, C_i(1 - C_i)} \qquad \text{and} \qquad \gamma = 0.5[1 + \Sigma\, C_i(1 - C_i)] \,. \quad (17)$$

Note that $0.5 < \delta < 0.5 + (S - 1)/(2S)$ where S is the number of species.

The previous discussion assumed that the number of species field evaporating during any one evaporation event was less than the maximum number of TOFs which could be measured with the digital timer (eight in this case, see section 3.3). If more than eight species were field evaporated, only the first eight species which struck the detector would be analyzed. This would bias the chemical analysis toward smaller (m/n) values and thus the measured concentration of small (m/n) value species would be greater than the actual concentration. This is an instrumentation problem and is not a fundamental limitation of the technique since it can be avoided completely by constructing a digital timer with a sufficient number of timing chains. Thus there are two distinctly different mechanisms which can result in

an inaccurate quantitative chemical analysis. The common feature of both is that the errors in the chemical analysis increase as the rate of field evaporation increases.

A composition profile showing the spatial distribution of Ti in a Mo-1.0 at. % Ti alloy is presented in Fig. 48. The analysis was performed with the specimen at 35 K, with a pulse fraction (f) of 0.10 from a region near the (110) pole. Two local fluctuations in the Ti concentration showing very large local concentrations of Ti are indicated. Fig. 49 shows the corresponding rate of field evaporation during the atom-probe analysis in the form of a graph of the number of molybdenum atoms detected per evaporation event, averaged over approximately 100 Mo atoms, versus the cumulative number of molybdenum atoms or depth. Note that both fluctuations in the Ti concentration were directly correlated with high local evaporation-rates. However, Fig. 50 shows that fluctuation A in the Ti concentration shown in Fig. 49 was also associated with a large increase in the carbon concentration. Since no carbon was detected in the three runs on Mo-1.0 at. % Ti presented in section 5.3 and since the decomposition of CO on the surface of the specimen would result in a carbon and an oxygen profile, with O appearing at the same (m/n) value as the major Ti isotope, it is possible that fluctuation A in the Ti profile was actually due to oxygen and was not associated with the high evaporation rate. In the case of fluctuation B, no carbon fluctuation was present and hence the large Ti concentration can only be attributed to the high local evaporation rate. A more detailed analysis of the evaporation rate revealed that seven of the nine Ti atoms contained in

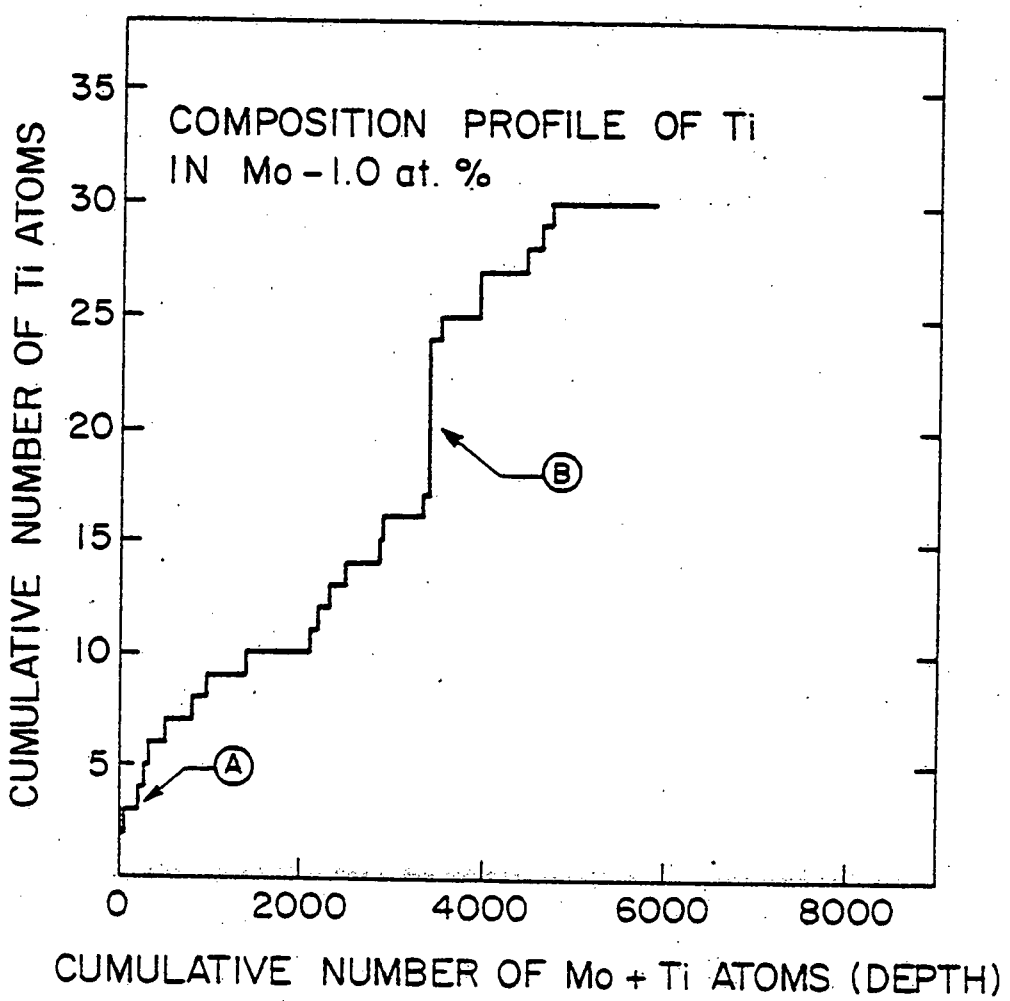

Figure 48. The composition profile for titanium in an unirradiated Mo-1.0 at. % Ti alloy. Two large fluctuations in the Ti concentration labelled A and B are indicated.

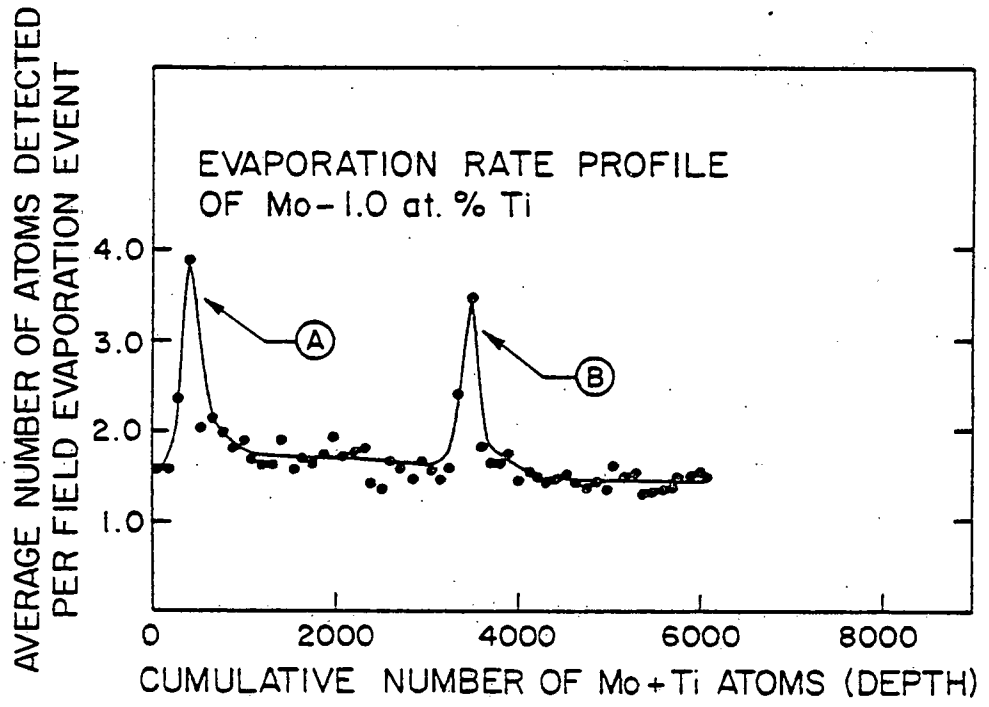

Figure 49. The evaporation rate profile corresponding to the composition profile shown in Fig. 48. The two large increases in the field evaporation rate shown in this figure correlate directly with the fluctuations in the Ti concentration indicated in Fig. 48.

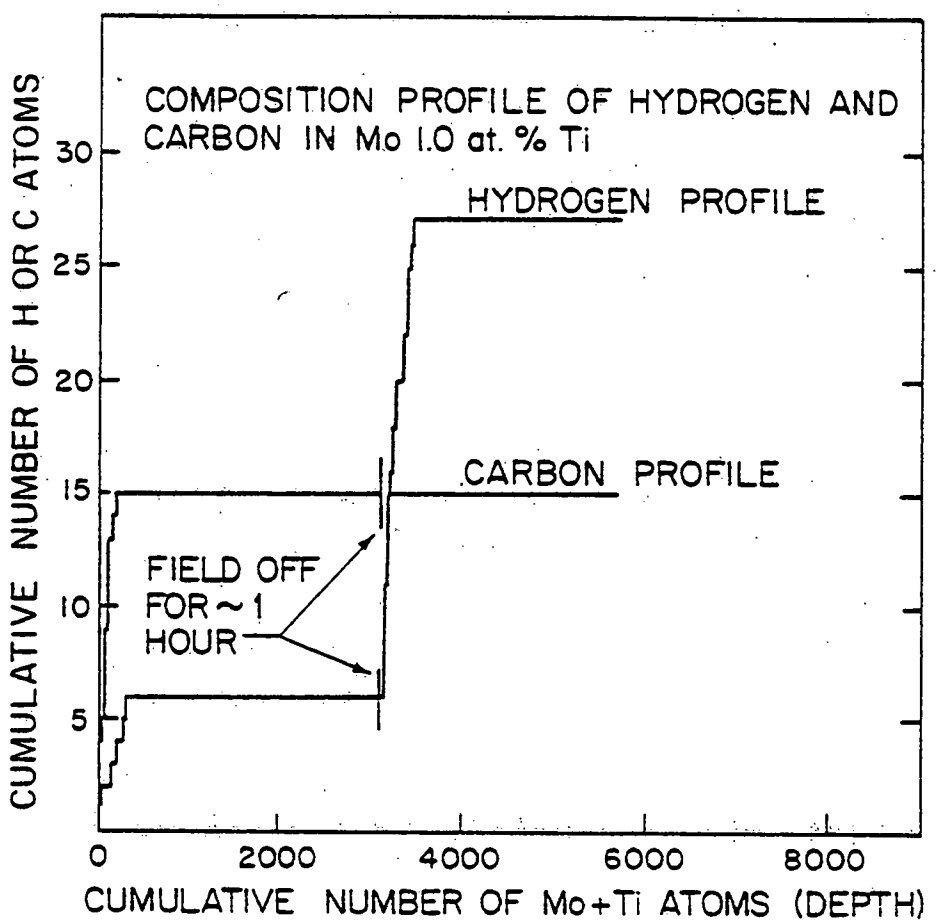

Figure 50. The carbon and hydrogen composition profiles which correspond to the Ti composition profile shown in Fig. 48.

fluctuation B were detected in three consecutive evaporation events in which a total of eight atoms per evaporation event were detected. Since a maximum of eight species per evaporation event can be detected employing the digital timer described in section 3.3, considerable more than eight atoms probably field evaporated per evaporation event. This high evaporation rate caused the erroneously large measured Ti concentration via the two mechanisms previously described. For both fluctuations the high local evaporation-rates were caused by the application of excessively high voltages to the specimen. This was determined by monitoring both the rate of increase of the specimen voltage and the evaporation efficiency (defined as the number of atoms detected per field evaporation pulse). In the vicinity of fluctuations A and B in the Ti profile, the voltage on the specimen was increased rapidly with a resultant increase in the evaporation efficiency and thus the evaporation rate. The overall average evaporation efficiency was ~ 0.05 atoms per pulse versus an average evaporation efficiency of greater than 1 atom per pulse near fluctuations A and B. In the region away from these local fluctuations, the average Ti concentration was 0.35 ± 0.08 at. % Ti which is in good agreement with the analyses presented in section 5.3.

Another example of a high evaporation rate causing an erroneously high measured Ti concentration occurred in examining the (111) plane of the same Mo-1.0 at. % Ti alloy specimen previously described. In this case the average measured Ti concentration was 2.1 at. % Ti. The measured Ti concentration versus evaporation rate is shown in Fig. 51 and tabulated in Table 9. Note that as the evaporation rate

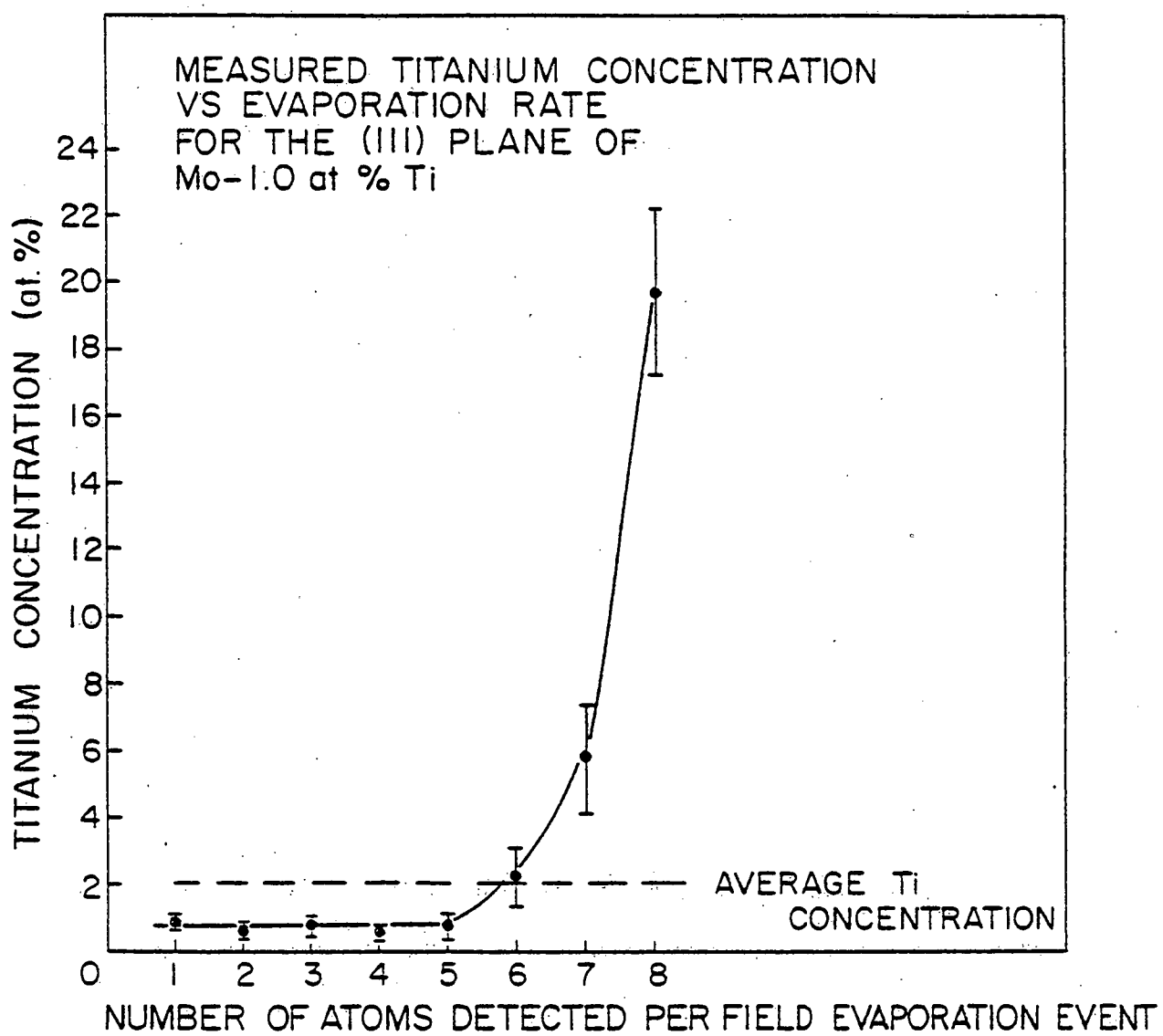

Figure 51. The measured titanium concentration versus the evaporation rate for the (111) plane of an unirradiated Mo-1.0 at. % Ti alloy.

Table 9

The measured titanium concentration as a function of evaporation rate for a Mo-1.0 at. % Ti alloy.

EVAPORATION RATE (number of atoms detected per evaporation event)	NUMBER OF ATOMS				TITANIUM CONCENTRATION* (atomic %)
	Mo^{+2}	Mo^{+3}	Mo^{+4}	Ti^{+3}	
1	21	1220	125	12	0.87±0.25
2	15	969	128	7	0.63±0.24
3	7	667	121	6	0.75±0.31
4	7	607	137	4	0.53±0.26
5	2	353	75	3	0.69±0.40
6	4	208	58	6	2.2±0.9
7	9	140	47	12	5.8±1.7
8	18	119	115	62	19.7±2.5

* The ± values were calculated from the $\sqrt{N}/\Sigma N$ values where N is the number of atoms detected.

increased, the measured Ti concentration increased rapidly. For example, when eight atoms were detected per evaporation event the average measured Ti concentration was approximately 19.7 at. % Ti. In this case several hundred Mo+Ti atoms must have been field evaporated in order to yield a measured Ti concentration of 19.7 at. % Ti versus the nominal 1.0 at. % Ti. This erroneously large measured Ti concentration was attributed to both of the previously described mechanisms. Since over one-half of the total Ti atoms detected from the (111) plane were associated with an evaporation rate corresponding to eight atoms detected per evaporation event (see Table 9), the overall measured Ti concentration was erroneously high. By way of comparison, Fig. 52 shows the measured Ti concentration versus evaporation rate for TZM (see Fig. 38 for the corresponding composition profile). Note that the same general tendency for the measured Ti concentration to increase with evaporation rate was observed. However the overall measured Ti concentration was not significantly influenced by high evaporation rates (i.e., 6, 7, or 8 atoms detected per evaporation event), since only a small fraction of the total number of Ti atoms detected were associated with high evaporation rates (see Table 10).

An important observation during the analysis of the (111) plane of the Mo-1.0 at. % Ti alloy was that the average evaporation efficiency was less than 0.1 atom per pulse. This was comparable to the evaporation efficiency employed in all of the other atom probe analyses of this material from the vicinity of the (110) plane which yielded quite satisfactory evaporation rates and hence reasonable accurate quantitative measurements of the Ti concentration. Thus the

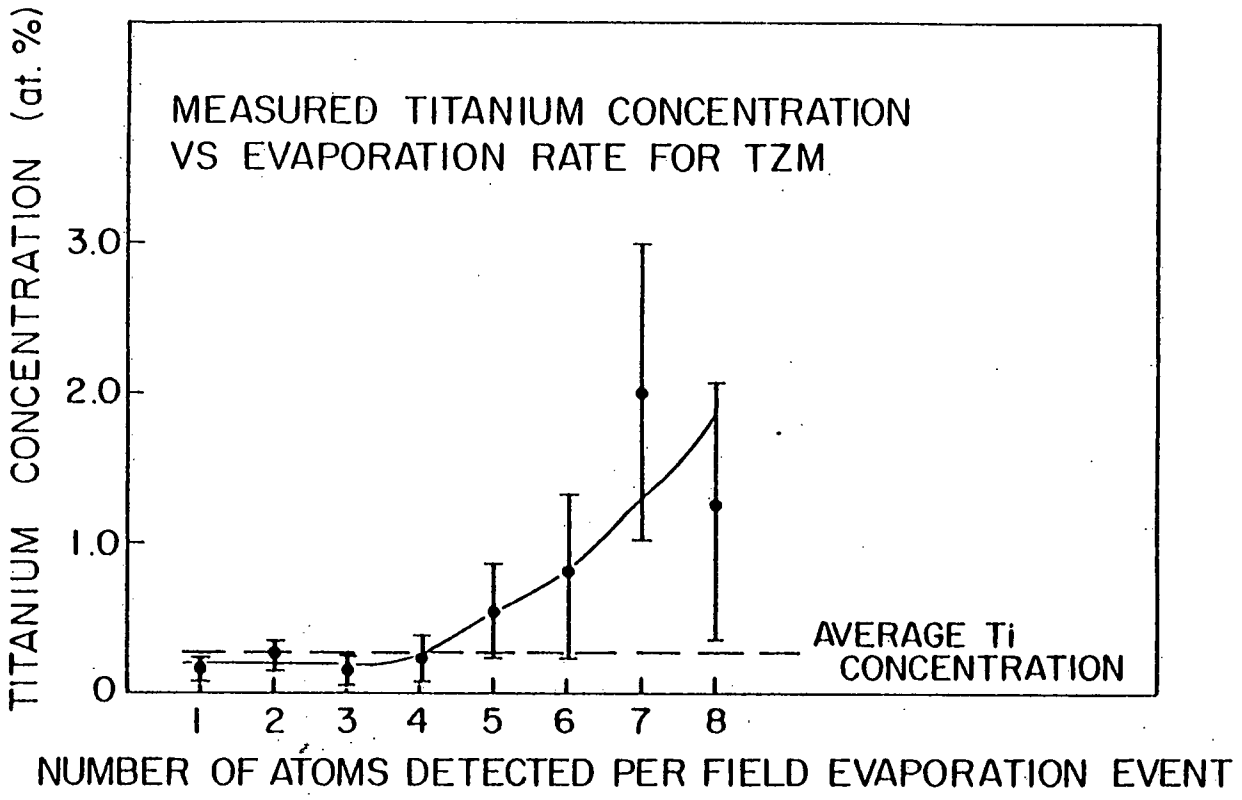

Figure 52. The measured titanium concentration versus the evaporation rate for an unirradiated alloy of Mo-Ti-Zr (TZM).

Table 10

The measured titanium concentration as a function of evaporation rate for Mo-1.0 at. % Ti-0.08 at. % Zr (TZM).

EVAPORATION RATE (number of atoms detected per evaporation event)	NUMBER OF ATOMS					TITANIUM CONCENTRATION* (atomic %)
	Mo^{+2}	Mo^{+3}	Mo^{+4}	Ti^{+3}	(Zr)	
1	858	3422	131	6	(7)	0.14±0.06
2	464	2193	153	7		0.25±0.09
3	219	1162	126	2		0.13±0.09
4	151	688	74	2		0.22±0.15
5	92	387	53	3		0.56±0.32
6	40	187	29	2		0.78±0.55
7	45	125	29	4		1.97±0.99
8	23	108	27	2		1.25±0.88

* The ± values were calculated from the $\sqrt{N}/\Sigma N$ values where N is the number of atoms detected.

large evaporation rate was the result of the intrinsic mode of field evaporation of the molybdenum (111) plane and was not due to the application of an excessively high voltage to the specimen. A visual observation of the evaporation of the (111) plane confirmed this conclusion. It was observed that the evaporation from the (111) plane in molybdenum was highly non-uniform; repeated application of evaporation pulses resulted in little or no field evaporation until suddenly, with the application of only a few additional pulses, an entire plane was removed. It was the intrinsic mode of field evaporation of the (111) plane of molybdenum which caused the high evaporation rate in spite of the low evaporation efficiency employed. Thus the (111) plane and in general any non-uniformly field evaporating region in any material, may not be suitable for quantitative atom probe analysis.

Detailed evaporation rate analyses were performed in order to insure that gross errors in the measured compositions have not occurred in any of the other analyses presented in this work.

Although only experimental results from the Mo-Ti system were presented, the following conclusions which are applicable in general to all alloy systems were reached.

(1) The field evaporation rate, defined as the number of atoms detected per evaporation event, has a strong influence on the accuracy of an atom probe analysis. As the evaporation rate increases, the measured concentration of the less abundant species increases and in general, when more than one atom field evaporates the measured concentration of the less abundant species is greater than the actual concentration.

(2) For very high field evaporation rates in which the number of species field evaporating exceeds the number of TOFs which can be measured, the measured concentration of the lowest (m/n) value species is greater than the actual concentration; i.e., the analysis is biased toward lower (m/n) values.

(3) The evaporation rate was not always related to evaporation efficiency. In the case of a non-uniformly field evaporating plane (e.g., the (111) plane of molybdenum), a very high field evaporation rate was observed although small evaporation efficiencies were maintained. Thus non-uniformly field evaporating regions of a specimen may be intrinsically unsuited for quantitative atom probe analysis.

(4) Local fluctuations in the composition indicated in a composition profile may be artifacts induced by a high local evaporation rate.

(5) The ability to measure a large number of TOFs is a distinct advantage in atom probe field ion microscopy since

   (a) the field evaporation rate and its effect on quantitative atom probe analysis can be estimated, and

   (b) a significant fraction of all atoms detected have field evaporated as two or more atoms per evaporation event. Thus the ability to measure a large number of TOFs is essential in order to insure a high detection efficiency.

7. THE RANGE AND DIFFUSIVITY OF HELIUM IN TUNGSTEN

The behavior of helium in metals is currently an active area of scientific investigation. This interest has been generated primarily by materials problems in two technologically important areas of energy research, namely the controlled thermonuclear reactor (CTR) and the liquid metal cooled fast breeder reactor (LMFBR).

The major materials problems associated with the successful developement of the CTR[81-84] are: (1) the blistering of metals exposed to low energy (< 100 KeV) helium ions; and (2) the sputtering of first wall material and the reflection of low energy helium from the first wall which can quench the thermonuclear reaction by cooling the plasma. The problem of void formation and the swelling of the fuel cladding material in the LMFBR[85-90] is believed to be strongly affected by the helium produced as a result of (n,α) reactions. The helium is believed to play an integral role in the nucleation and stabilization of the voids.[91-94]

The purpose of the present work was to provide fundamental information on the properties of helium in a prototype bcc metal, namely tungsten. As an introduction to the present state of knowledge on the behavior of helium in tungsten (see reference 95 for a recent review on the fundamental properties of helium in metals), the sequence of events which take place as an incident helium ion enters a metal and eventually comes to rest is described.

A high energy (>> 100 KeV) incident helium ion loses energy primarily through electronic excitation of the target. The scattering

of the ion is well understood and is accurately described by low angle Rutherford type collisions with the target atoms. As the energy of the ion approaches approximately 1 KeV electronic losses become less important and hard-sphere nuclear scattering becomes the dominant factor determining the range profile*. The maximum energy transferred to a target atom (E_t) in a hard-sphere two-body collision between an incident ion of mass m_i and energy E_i and a target atom of mass m_t is

$$E_t = \frac{4m_i m_t}{(m_i + m_t)^2} E_i \qquad (18)$$

Because of the large mass difference between helium and tungsten, E_t is only a small fraction of E_i ($E_t = 0.083E_i$ for He on W) and thus small energy transfers and large angle scattering events occur. Therefore the trajectory of a low energy helium ion within the tungsten lattice can be visualized as an almost diffusive like motion of the helium[97], so that strong forward scattering does not occur. The

---

* Note that electronic losses may still dominate the total energy loss. The ratio of nuclear stopping (S_n) to the total stopping power, nuclear plus electronic (S_n+S_e), was approximately constant at a value of 0.3 to 0.4 for helium ions incident on tungsten with $E_i < 1$ KeV. This was determined by employing the S_n given in ref. 99 and the value of S_e calculated from the Lindhard expression for electronic stopping. Although the Lindhard value for S_e has been reported to have been experimentally verified for helium ions incident on Cu, Ag, and Au with E_i in the range of 4 to 10 KeV (96), the present theoretical and experimental evaluation of low energy nuclear and electronic stopping is an area of considerable controversy. Because of the large angle scattering which occurs for low energy helium on tungsten, the range profile is only weakly dependent on the total path length of the helium ion and thus, since S_e affects the path length and not the scattering angle, large changes in the electronic stopping have only a minor effect on the range profile.(97,98)

diffusive like motion of the incident helium ion is indicated by the fact that the mean penetration depth of the ion from the initial irradiated surface (i.e., the mean range) is small compared to the total path length travelled by the ion. Since the collisions between the helium and tungsten atoms involve large angle scattering of the helium, a large fraction of the incident helium ions are reflected from the tungsten target. No measurements of this reflection coefficient for helium on tungsten presently exist. At low energies (< 1 KeV) the range profile of helium is dominated by nuclear collisions with the target atoms.[97,98] Since the nuclear scattering is determined by the repulsive part of the helium-metal interatomic potential, measurements of the range of low-energy ions yield information on the strength of the potential at large distances (i.e., low energies). In the low energy region the potential is dominated by electron screening effects which represent a particularly difficult theoretical problem. Recent theoretical[99] and experimental[100-102] work indicates that the convential interatomic potentials overestimate the strength of the interaction between atoms at large separations (low energies) and hence the theories predict much shorter ranges than experimentally observed at low energy. The lowest energy for which range data for helium on any metal has been obtained is for 1.6 KeV helium on niobium.[103] In addition the helium range data which does exist relied on the trapping of helium at vacancies created during the irradiation or the clustering of helium atoms to immobilize the helium. Thus these measurements were not true range profile measurements but must have represented some combination of a range and a damage profile. In the present work, true range measurements

for low energy helium ions (300 and 475 eV) on tungsten have been performed.

As the helium atom continues to lose energy, eventually the energy of the helium atom approaches kT. The theoretical calculations of Rimmer and Cottrell[104] and Wilson et. al. [105-107] indicated that in all of the fcc and bcc metals investigated (including W), the helium atom comes to rest in an interstitial position and that it is energetically unfavorable for a Frenkel pair to be created with the helium atom residing in the resultant vacancy.[108] In addition the calculations of Wilson et. al.[105-107] indicate that an interstitial helium atom undergoes rapid migration at room temperature in the bcc metals investigated, for example Nb, Ta, and W. This rapidly migrating helium atom is immobilized either through self-clustering or trapping at lattice defects, for example vacancies, dislocations and grain boundaries. The experimental work of Kornelsen[109] on He in W, which predates Wilson's theoretical work, showed that helium is highly mobile in tungsten above ~ 100 K if no vacancies and SIAs are present. He also demonstrated that vacancies act as strong traps for helium atoms in tungsten and measured binding energies which were in good agreement with the subsequent predictions of Wilson et. al.[110,111] However no experimental evidence exists which demonstrates the existence of an isolated, immobile, interstitial helium atom in any metal. Furthermore no unambiguous measurements of the migration energy of an isolated interstitial helium atom exist. Clearly an experimental value of the migration energy of helium in tungsten, in addition to supplying fundamental diffusion data, would provide a check of the

predictive capability of Wilson's calculations.

The objectives of the present work were:

(1) to evaluate the applicability of the atom probe to the study of gases in metals and more specifically, to establish the ability of the atom probe to detect helium atoms retained in a tungsten lattice;

(2) to establish the existence of an isolated, immobile, interstitial helium atom in tungsten;

(3) to measure the range profile and the reflection coefficient of low-energy helium ions in tungsten; and

(4) to determine the temperature at which interstitial helium atoms become mobile in tungsten. This temperature yields an approximate migration energy for interstitial helium atoms in tungsten.

7.1 Description of the Experiment

A tungsten FIM specimen at a temperature T_i was irradiated in-situ with 300 eV $^4He^+$ ions parallel to the wire axis as shown in Fig. 53(a). A 300 eV helium atom can transfer a maximum energy of ~ 25 eV to a W atom in a two-body collision (see equation 18). Since the displacement energy of W is ~ 44 eV,[112] no SIAs or vacancies can be created within the specimen. With no vacancies or SIAs present to act as traps, the injected helium remained in the specimen only if the helium was immobile at the irradiation temperature T_i. Thus the state of the specimen after irradiation consisted of immobile, interstitial helium atoms deposited in a perfect tungsten lattice with a depth distribution determined solely by the range profile of the 300 eV helium ions.

The specimen was then chemically analyzed at a temperature T_a ($\leq T_i$)

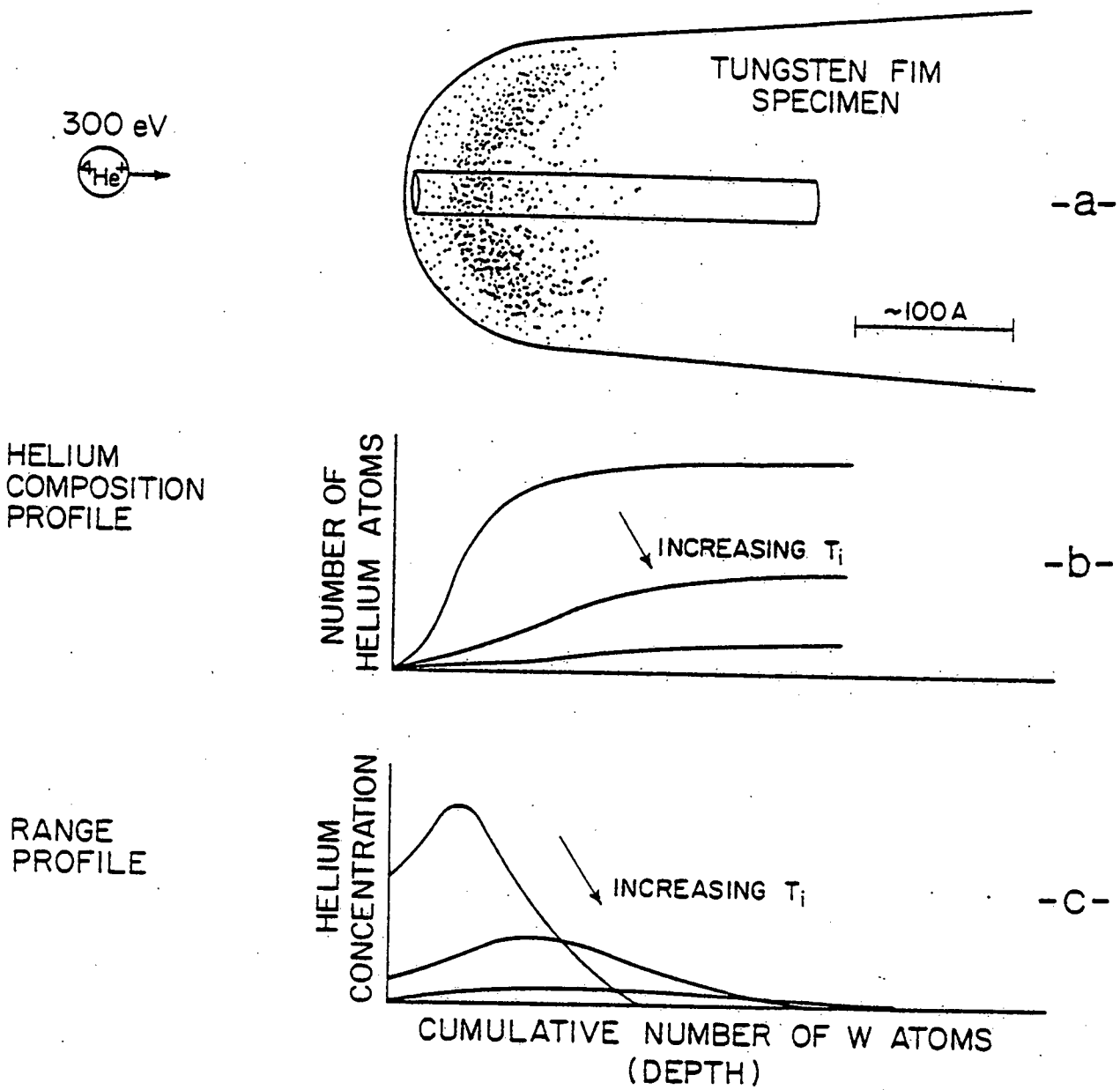

Figure 53. (a) The in-situ irradiation of a tungsten FIM specimen with 300 eV He^+ ions at a temperature (T_i) where the injected helium atoms are immobile. The density of spots corresponds to the approximate range profile of helium in tungsten.

(b) The number of helium atoms versus depth as a function of T_i. Note that the helium composition profiles tend to flatten out as T_i is increased.

(c) The range profiles of helium in tungsten as a function of T_i. The range profiles are obtained by taking the first derivative of the composition profiles shown in Fig. 53(b).

with the atom probe and a helium composition profile was plotted as shown in Fig. 53(b). The first derivative of this profile yields the desired range profile as shown in Fig. 53(c). Note that the depth scale in Fig. 53 is in cumulative number of atoms which is proportional to depth. Section 7.2 describes the technique which was developed to generate an accurate, absolute depth scale.

The temperature at which the interstitial helium atoms become mobile in tungsten was determined by irradiating an FIM specimen at a series of temperatures (T_i) and then performing the atom-probe analysis at a common low temperature (T_a). The helium composition profile determined at T_a was independent of the irradiation temperature only if the helium was immobile at all T_i. However when T_i was above the temperature at which the helium interstitials became mobile, the helium injected during the irradiation diffused to the surface of the FIM specimen and entered the gas phase. Therefore a sharp decrease in the measured helium concentration was expected as the irradiation temperature was increased. This assumes that no surface barrier existed which prevented the helium from entering the gas phase and that immobile clusters of helium did not form. Even if a surface barrier existed or if clustering took place, a dramatic change in the shape of the helium profile should occur as T_i was increased above the helium migration temperature. Since only T_i was varied, significant changes in the shape of the helium profile could only be attributed to a sharp increase in the mobility of the interstitial helium atoms at the irradiation temperature. By determining the temperature at which the helium atoms became mobile, an approximate migration energy for

interstitial helium diffusion was obtained employing the isothermal diffusion model described in section 7.5.

The fraction of the incident helium ions reflected from the W surface was obtained by comparing the absolute number of helium atoms detected within the specimen to the number of helium ions incident on the specimen. The number of incident helium ions is equal to the product of the helium fluence and the area under analysis. The fluence (ions cm^{-2}) was determined by measuring the total charge collected on a known area surrounding the specimen during the irradiation, while the area analyzed was determined employing the technique described in section 7.2.

7.2 The Determination of an Absolute Depth Scale

An important aspect of the present experiment was the developement of a technique for producing an accurate, absolute depth scale for the helium composition profile indicated schematically in Fig. 53. Employing the technique described in this section, the depth of each deposited helium atom from the initial irradiated surface has been measured with an accuracy of 2.2 A [the interplanar spacing for the W (110) planes], independent of the absolute depth of analysis.

During the atom probe analysis the specimen was oriented and the magnification adjusted so that only the central portion of the tungsten (110) plane was chemically analyzed; i.e., the probe hole was placed in the center of the image of the (110) plane. The specimen was then field evaporated through the repeated application of high-voltage pulses. Three successive stages in the field evaporation of one (110) plane are indicated in Fig. 54(a). When the (110) plane was near the

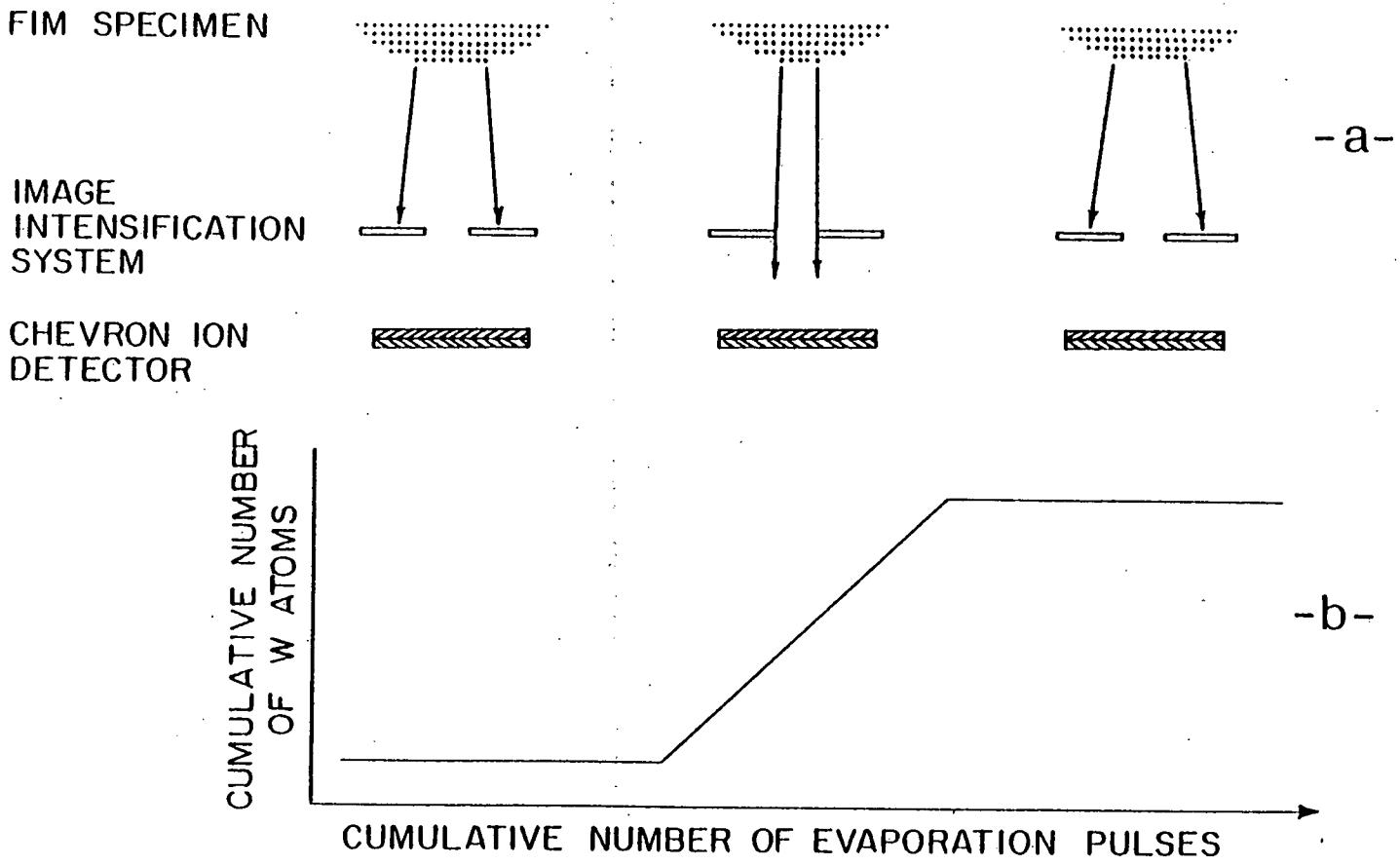

Figure 54. A schematic diagram illustrating the method employed to determine an absolute depth scale. Three stages in the field evaporation of one (110) plane of W are shown in Fig. 54(a). The field evaporation of this plane is indicated in Fig. 54(b) by the steplike increase in the rate at which tungsten atoms are detected.

maximum size, no W atoms were detected as the plane field evaporated since the trajectory of the field evaporated atoms did not pass through the probe hole as shown in the left hand illustration of Fig. 54(a). As the field evaporating plane decreased in size, atoms began travelling through the probe hole and were chemically analyzed [center illustration of Fig. 54(a)] until the entire (110) plane was removed [right hand illustration of Fig. 54(a)]. When this (110) plane had been entirely field evaporated, atoms again were no longer detected until the next (110) plane was field evaporated to the size indicated in the center illustration of Fig. 54(a). A plot of the cumulative number of W atoms detected versus the cumulative number of evaporation pulses applied to the specimen allowed the detection of the successive stages in the field evaporation of one (110) plane as illustrated in Fig 54(b). Initially the slope was zero since no W atoms were detected when the plane was near the maximum size. As the plane field evaporated, atoms began to be detected as indicated by the positive slope in the plot until the plane was completely evaporated at which point the slope returned to zero. Therefore the removal of one (110) plane resulted in a single step increase in the plot of the number of W atoms detected versus the number of evaporation pulses applied to the specimen. This step-like increase in the evaporation rate also caused a step-like increase in the output of the audio ratemeter; therefore the removal of each plane was monitored in real time during the atom probe analysis. A sample of experimental data illustrating the removal of five sucessive (110) planes and the detection of two helium atoms is shown in Fig. 55. Each step corresponded to the removal of one (110)

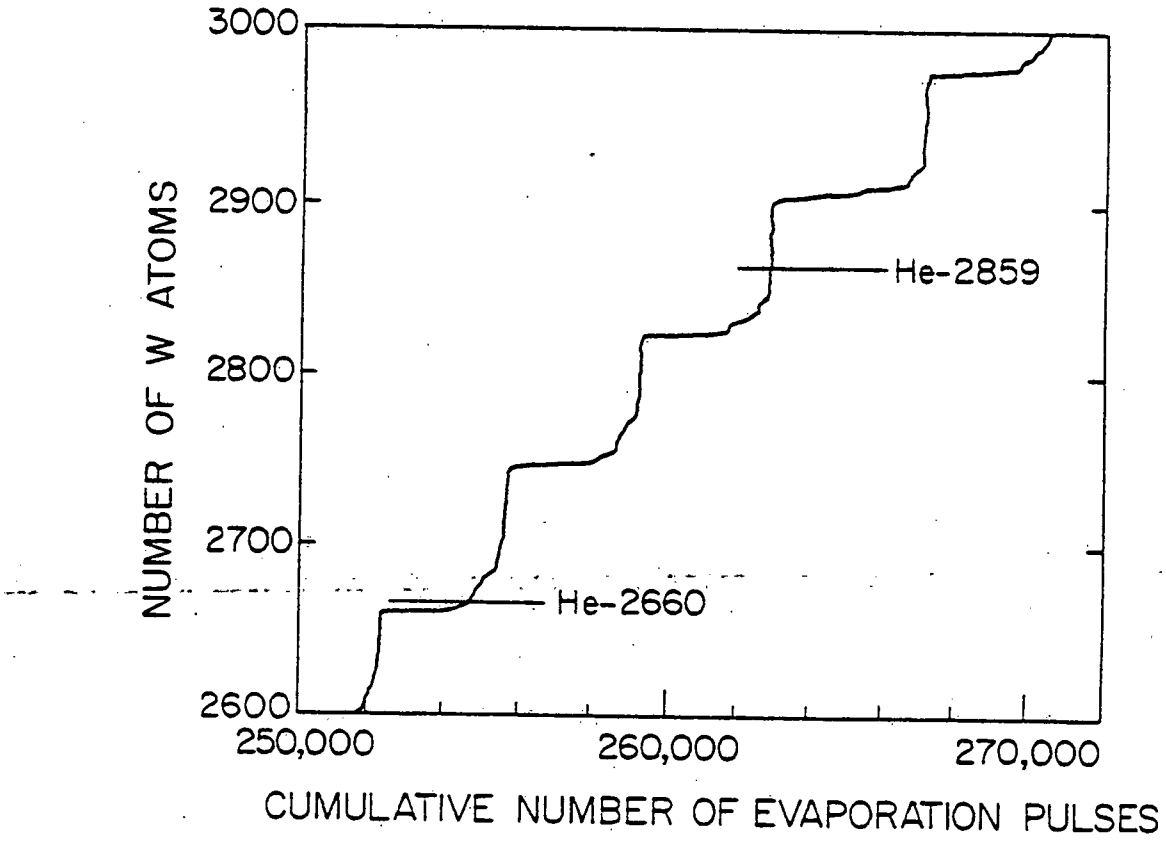

Figure 55. A sample of experimental data showing the successive removal of five (110) planes from a tungsten FIM specimen employing the method illustrated in Fig. 54. The detection of two helium atoms separated by a depth of two (110) interplanar spacings (4.43 A) is indicated by He-2660 and He-2859.

plane from the surface of the specimen. Since the tungsten lattice was employed as a depth marker, the absolute depth of each deposited helium atom from the initial irradiated surface was measured to within one (110) interplanar spacing (i.e., 2.2 A) independent of the total depth of analysis. The mean range ($\bar{x}$) and standard deviation (Δx) were calculated employing the standard expressions[113,114]

$$\bar{x} = \Sigma\, x_i \qquad \text{and} \qquad \Delta x = [\Sigma(x_i - \bar{x})^2/(N - 1)]^{0.5} \tag{19}$$

where N is the total number of helium atoms detected and x_i is the measured depth of the i^{th} detected helium atom from the initial irradiated surface. Helium atoms detected during the removal of the first (110) plane were assigned a depth $x_i = 0$. At the present time, potential information regarding the location of the helium atoms within the plane has not been utilized.

The number of tungsten atoms detected in each step has been used to calculate the magnitude of the irradiated area analyzed by the atom probe. Figure 56 shows the number of W atoms detected per (110) plane as a function of depth from the initial irradiated surface. The number of atoms detected from the initial surface layer was taken to be equal to the number of atoms per plane averaged over approximately the first 35 planes. Using the known crystallography of the tungsten (110) plane, the area was determined. The product of the helium ion fluence and the magnitude of the area analyzed yields the absolute number of helium ions (H_i) which entered the specimen through this area. By comparing the number of helium atoms detected (H_d) to the

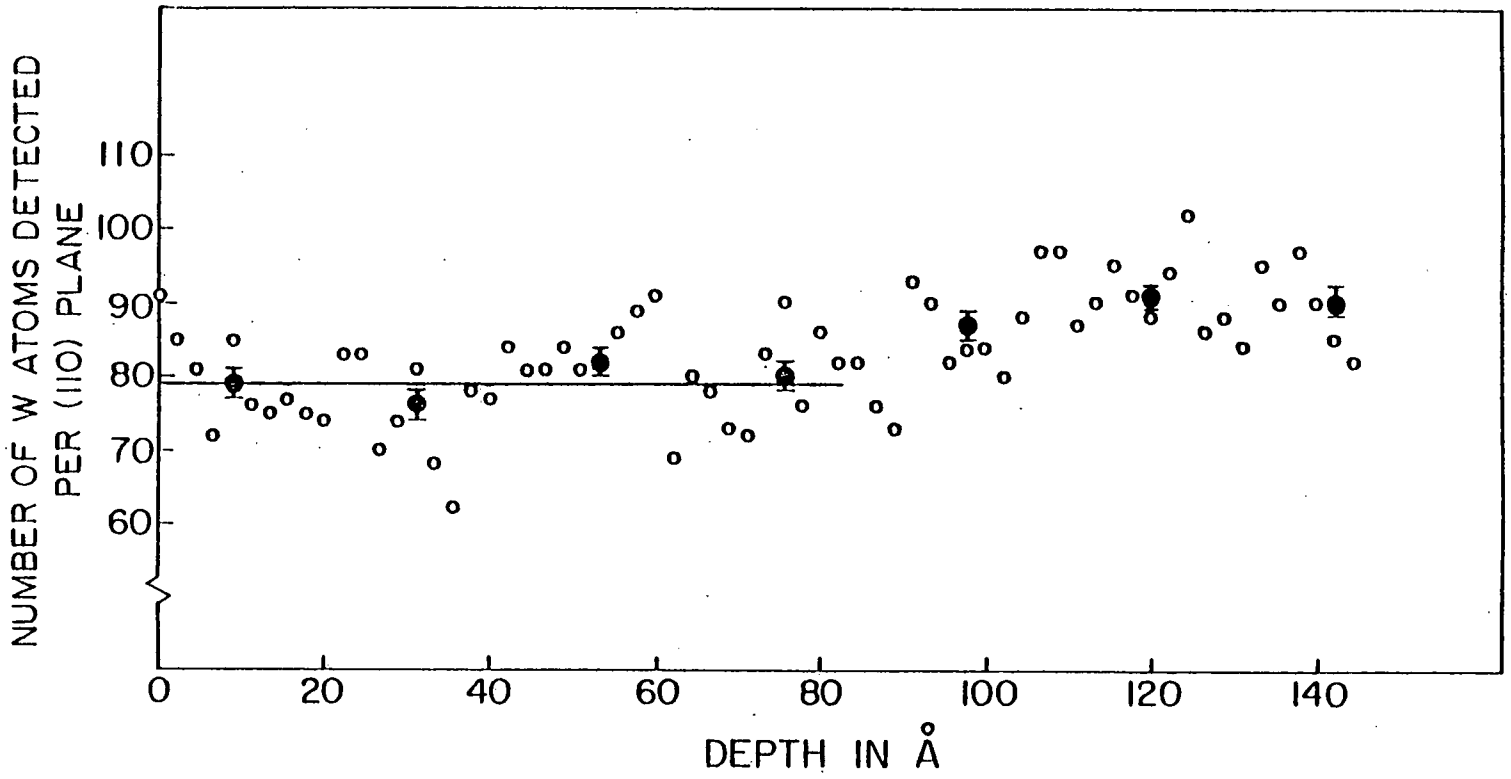

Figure 56. The number of tungsten atoms detected from each {110} plane versus depth. The open circles indicate the number of W atoms for each {110} plane field evaporated while the solid circles represent averages over ten (110) planes.

incident number, the fraction of the helium ions reflected from the tungsten surface (i.e., the reflection coefficient (R) for helium on tungsten) was determined employing the expression

$$R = (H_i - H_d)/H_i \ . \qquad (20)$$

The assumption has been made that the detection efficiencies for helium and tungsten were identical. Note that they need not be equal to unity. The results presented in section 7.5 suggest that this assumption was not valid since a significant fraction of the helium may have field evaporated as WHe^{+3} which was not resolved by the mass spectrometer.

The technique described in this section should be applicable to all uniformly field evaporating planes in any metal. In addition to allowing accurate depth measurements for range profiles, the technique may also allow accurate, absolute depth scales to be obtained for routinely generated composition profiles such as the ones shown in section 5. This would be particularly useful for concentrated alloys where depth information is difficult to obtain from the FIM image due to the absence of prominent crystallographic features (see Fig. 41).

7.3 Experimental Procedure

The following is a detailed description, from specimen preparation to final data analysis, of the procedure employed in measuring the range and diffusivity of helium in tungsten.

Tungsten FIM specimens were prepared from MRC VP grade polycrystalline wire, 0.13 mm in diameter with the wire axis parallel to

the [110] direction. The wire was recrystallized at 2000 C for approximately one hour in a background pressure of $2 \cdot 10^{-9}$ torr. The wire was mounted in the specimen holder and electropolished to a sharp point in a 1 Normal solution of NaOH in H_2O at 4.3 Vac employing a stainless steel counter-electrode. Approximately 5 of the 6 mm of wire protruding from the specimen holder was dipped into the solution and 2.5 mm was electrolytically removed. The specimen was then inserted into the FIM employing the specimen exchange device and when the system pressure fell below $1 \cdot 10^{-8}$ torr, the specimen was imaged at room temperature in $5 \cdot 10^{-5}$ torr helium. Good specimens typically yielded fully symmetrical images at 2 to 3 kV and were then field evaporated to approximately 6 kV. The FIM was then baked for at least 24 hours at 160 to 180 C with the ion gun degassing as described in section 2.3.

The specimen was then cooled to the atom probe analysis temperature (T_a) of 60 K and field evaporated in the presence of $1 \cdot 10^{-5}$ torr helium gas to a total voltage of approximately 10 kV. This yielded a specimen radius on the order of 300 A which was large enough to allow the hemispherical shape of the FIM specimen to adequately approximate a flat surface for the range profile measurements (see appendix D). The cold finger was then warmed to approximately 160 C for several hours and the system was allowed to return to the base pressure for 12 hours. Whenever the helium gas was present in the FIM, the RGA, ion gauges, and emission current from the ion gun were turned off.

The previous procedure constituted the preliminary preparation for a new specimen while the following is the procedure employed during an experiment. The specimen was cooled from room temperature to $\sim$ 20 K

in ~ 1.0 hr, held at ~ 10 K for ~ 0.5 hr and then warmed up to and stabilized at T_i. Approximately 50 to 100 A of tungsten was field evaporated, leaving the (110) plane at the maximum size. The specimen was then aligned with the detector and positioned with respect to the image intensification system so that the center of the (110) plane would be chemically analyzed. The goniometer and image intensification system carriage positions were recorded. With the dc potential still applied, the specimen was rotated 60 degrees toward the ion gun for an irradiation parallel to the [110] direction (± 5 degrees) or 45 degrees away from the ion gun for a control. The magnitude of the rotation was measured with the rotation scale attached to the goniometer stage within the vacuum system. Each division on the scale corresponded to a rotation of 5 degrees. The image intensification system was then withdrawn and turned off, the ion gun emission current was increased to 10 ma and the helium pressure increased to $1 \cdot 10^{-4}$ torr. The RGA was not operated at any time while the helium gas was present and the ion gauge was used only momentarily to adjust the helium pressure. The dc potential was then removed from the specimen and the irradiation initiated by applying the solenoidal magnetic field to the ion gun. The specimen was irradiated at a flux of ~ $3 \cdot 10^{12}$ ions cm^{-2} sec^{-1} for ~ 25 min to a fluence of ~ $4.7 \cdot 10^{15}$ ions cm^{-2}. The actual fluence may have been ~ 25 % less than the reported value due to a contribution of secondary electrons in the flux measurements. Thus the reported fluence was an upper limit. At the end of the irradiation the magnetic field was removed, the emission current was turned off and the helium gas was pumped from the FIM

employing the diffusion pump for two hours. The specimen and image intensification system were returned to their previous positions and the ion pump was then opened to the FIM. The specimen was cooled to T_a and the temperature was allowed to stabilize for one hour. RGA and total pressure measurements were then taken which typically indicated a total pressure less than $2.6 \cdot 10^{-10}$ torr and a residual gas background of $H_2 = 2.3 \cdot 10^{-10}$ torr; $He = 5.0 \cdot 10^{-12}$ torr; $CH_4 = 1.6 \cdot 10^{-12}$ torr; and $CO = 2.2 \cdot 10^{-11}$ torr.

The atom probe analysis was then performed starting at a dc voltage of ~ 1 kV with a pulse fraction (f) equal to 0.10. The voltage was slowly increased over a period of ~ 30 min until the tungsten substrate atoms began to field evaporate. The specimen was then field evaporated at the rate of one (110) plane in 1 to 2 min using the audio ratemeter to monitor the removal of each plane. The analysis was continued until either the specimen failed or the concentration of helium detected was at or below the level present in the controls. The instaneous local helium concentration was obtained through on-line data analysis. During the irradiation and the atom probe analysis the temperature was maintained to within ±1 % of the desired value unless otherwise indicated in the results. At the end of the atom probe analysis the ion gun was returned to the normal operating conditions, the cold finger was baked to 160 C for several hours and the system was allowed to return to the base pressure for ~ 36 hours before the next run.

7.4 Experimental Results

In this section range profiles and upper estimates of the reflection coefficient of 300 and 475 eV helium ions on tungsten are presented. In addition, range profiles of 300 eV He^+ ions incident on a W specimen at 60, 80, 90, and 110 K are presented which demonstrate that interstitial helium atoms become mobile in tungsten between 90 and 110 K. The damage state of the specimen after irradiation with 300 eV He^+ ions has been investigated. The results showed that the injected helium atoms were located interstitially in the tungsten lattice. The spatial distribution of impurities (H, C, O) detected during the atom-probe analysis for irradiated and unirradiated tungsten specimens is also presented. The results showed that the range and diffusivity measurements were not affected by trapping of the helium at these impurities.

Four helium composition profiles are shown in Fig. 57. Profiles 1 and 3 were obtained for a tungsten specimen irradiated at 80±5 K with 300 eV He^+ ions* to a fluence of $4.7 \cdot 10^{15}$ ions cm^{-2} along the [110] direction (±5 degrees) with the atom probe analysis performed at 60±2 K. Profiles 2 and 4 were obtained for unirradiated specimens and served as controls. All four runs were performed on the same specimen in the sequence indicated by the numbering of the profiles (i.e., 1 was first, 2 second etc.). Between each run the specimen was annealed to 160 C for several hours. Controls 2 and 4 were performed under identical conditions as irradiations 1 and 3 except

---

* The fraction of He^{+2} in the ion beam was estimated to be less than 0.001 (see reference 115).

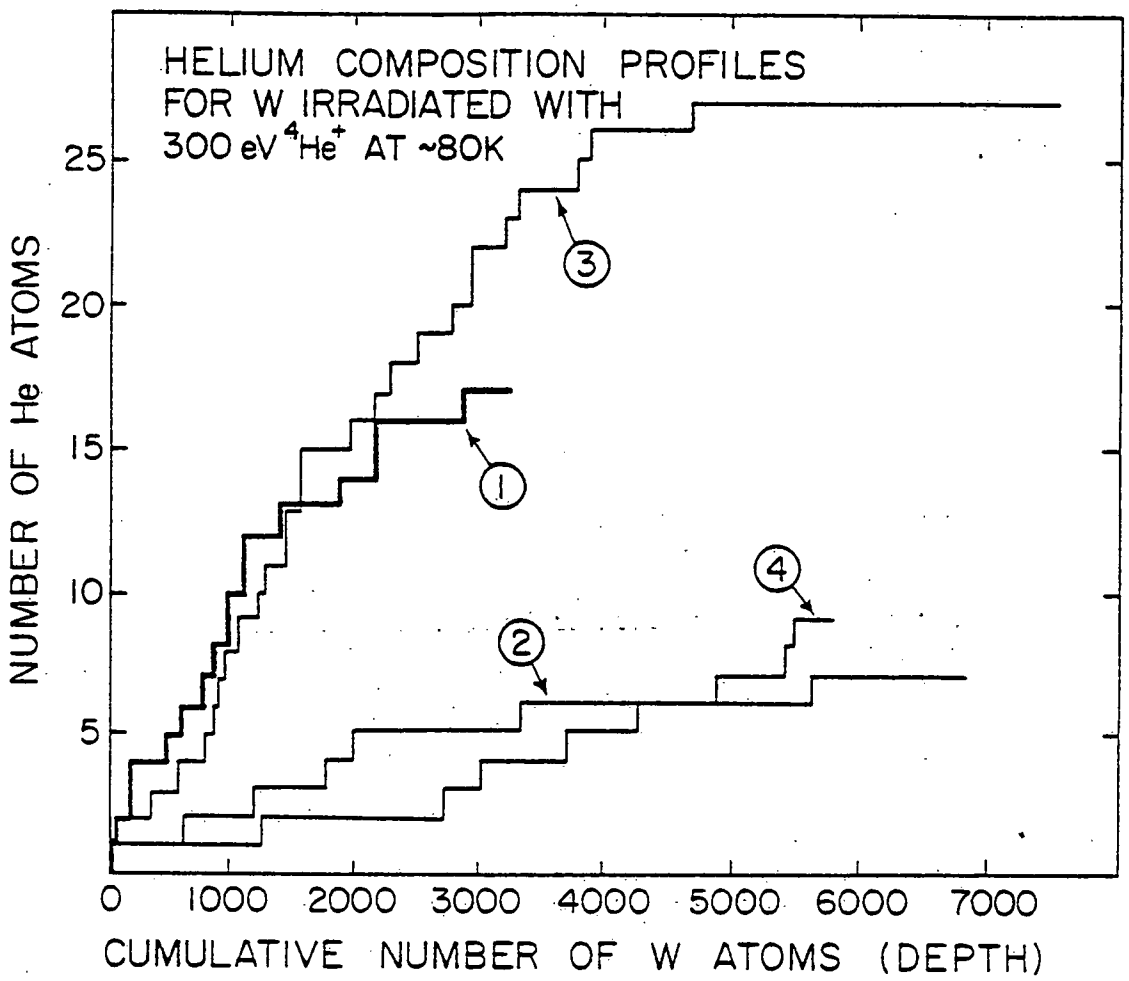

Figure 57. Composition profiles showing the spatial distribution of helium in tungsten. Profiles 1 and 3 are for W irradiated with 300 eV He^+ ions along the [110] direction at ~ 80 K. Profiles 2 and 4 are for unirradiated samples and constitute control experiments.

that the specimen was shielded from the ion beam in control 2 while in control 4 the specimen was held at a positive potential of 450 Vdc and thus only neutral helium atoms from the ion gun could reach the specimen.

The presence of helium in the controls was due to the random arrival at the surface of the specimen of helium atoms from the gas phase. These helium atoms field adsorbed[116,117] on the surface of the specimen and subsequently were field evaporated when the underlying W atoms were field evaporated. The small difference in the total number of helium atoms detected between controls 2 and 4 indicated that the measurements were not significantly affected by a low-energy neutral component of helium in the ion beam. This result was consistent with a calculation based on data reported in reference 118 which showed that the neutral fraction of the 300 ev He^+ ion beam was less than 10 % under the present experimental conditions.

The difference in the slopes of the helium profiles for the irradiated versus the unirradiated tungsten shows that the helium was retained in the W lattice after irradiation at 80 K. Results presented later in this section showed that trapping of the helium at defects did not take place and that homogenous nucleation of immobile helium clusters did not occur; in fact, clustering can probably be ruled out based solely on the observed sigmoidal shape of the profile. Therefore the results presented in Fig. 57 indicate that intersittial helium atoms are immobile in tungsten at 80 K.

Employing the technique described in section 7.3, an absolute depth scale has been assigned to profile 3 as shown in Fig. 58(a).

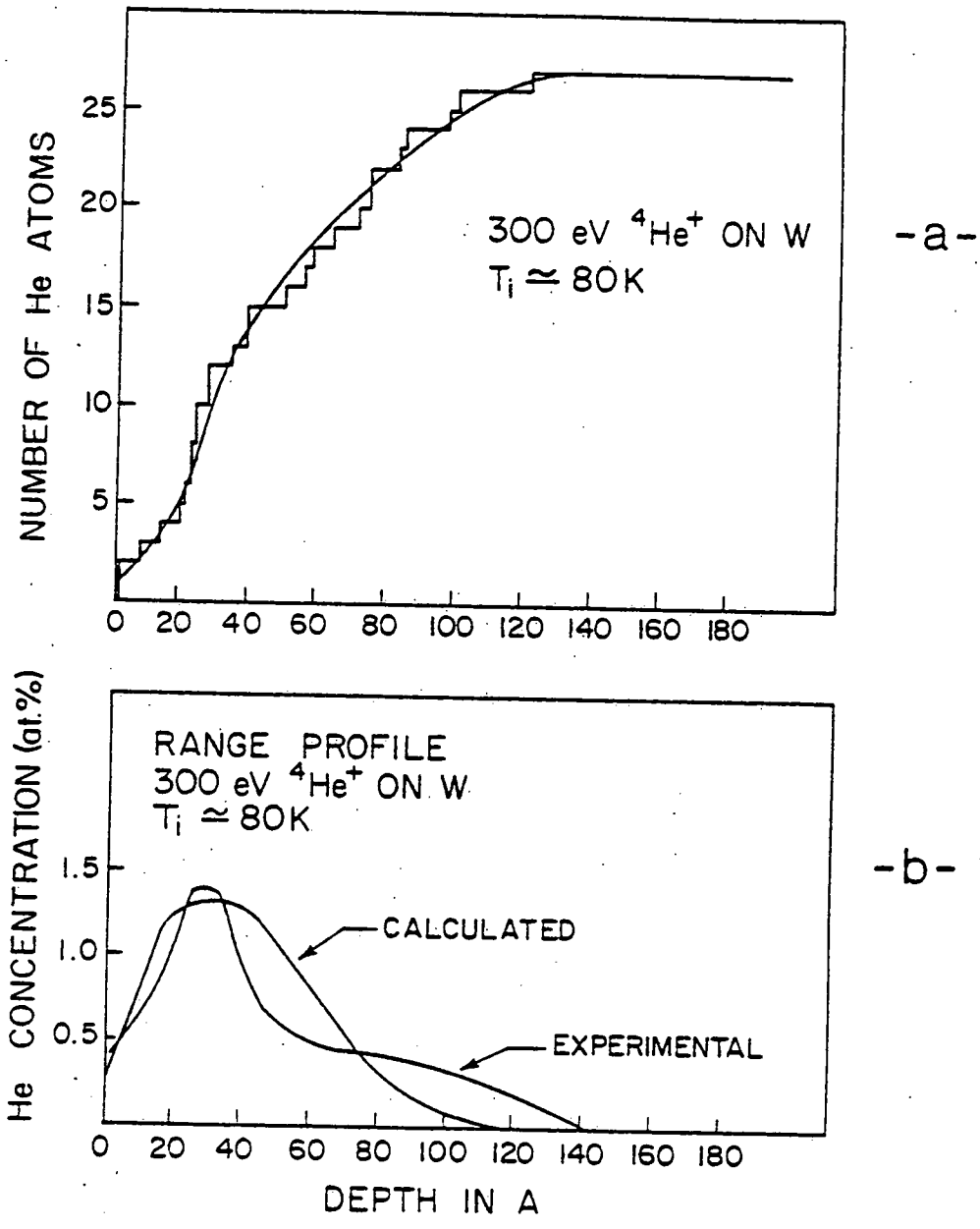

Figure 58. (a) A smooth curve drawn through helium composition profile number 3 shown in Fig. 57.

(b) A comparison of the experimental range profile [the first derivative of Fig. 58(a)] with the theoretical range profile of Haggmark et. al.

A smooth curve has been drawn through the profile and differentiated graphically to obtain the range profile shown in Fig. 58(b). Also shown in Fig 58(b) is a theoretical calculation of the range of 300 eV helium ions on tungsten performed by Haggmark et. al.[119]. Although the statistical validity of the detailed shape of the range profile is questionable due to the small number of helium atoms detected, the overall skewness of the profile is significant. The skewness is clearly indicated by the fact that the mean range was greater than the most probable range and by the long tail extending to a depth greater than 100 A. The measured mean range ($\bar{x}$), standard deviation (Δx), and reflection coefficient (R) were 47.1 A, 35.0 A, and 0.90 respectively.

In order to definitively establish that the helium detected in the previous experiment was not trapped at structural defects in the tungsten lattice, the following isochronal recovery experiment was performed. A tungsten specimen was irradiated along the [110] direction with 300 eV He^+ ions at ~ 30 K. After the irradiation approximately two (110) planes corresponding to ~ 4 A of material were field evaporated from the specimen. This procedure removed the sputtered surface* and restored the surface to a nearly perfect condition. The specimen was then warmed from approximately 30 to 90 K at a rate of ~ 1.5 K min^{-1} while the FIM image was continously

* Sputtering of the surface occurred since the energy required to produce a surface vacancy is lower than the displacement energy in the bulk. Low-energy sputtering has been studied employing the FIM by Walls et. al. (see references 120 to 122).

photographed. No SIA contrast effects were observed during this experiment indicating that no SIAs crossed the surface of the FIM specimen. Previous work[46-50] indicated that if SIAs were present in the specimen, they would have appeared throughout the entire temperature range of ~ 38 to 90 K. Unfortunately no contrast effects which could be associated with the arrival of interstitial helium atoms at the surface were observed. This is not surprising in view of the contrast mechanism for SIAs[123]. The specimen was then disected by pulsed field evaporation and was examined for structural defects. If immobile complexes of structural defects and helium atoms had formed, then a very high density (greater than $1 \cdot 10^{21}$ cm^{-3} in the region of the peak helium concentration) of defects would have been observed. The observed density of contrast effects which could not be associated with the perfect tungsten lattice was much lower than the measured helium concentration (i.e., the density of defects was less than $5 \cdot 10^{19}$ cm^{-3}). In addition the depth distribution of the contrast effects was not strongly related to the helium distribution observed in the composition profiles. For example, the maximum depth at which these contrast effects were observed was typically less than one-half of the maximum range of the 300 eV He^+ ions as measured with the atom probe. These results, coupled with the range profile measurements, constitute conclusive evidence that the helium was not trapped at structural defects.

The exact nature and source of the observed contrast effects was not determined although a possible source was a small heavy mass component in the helium ion beam. This supposition was based on the

observation of extensive damage in specimens irradiated with 300 eV helium ions at 60 K if the ion source was not thoroughly outgassed. Residual gases, e.g. CO, adsorbed within the ion gun are decomposed and ionized by electron impact when the ion source is operated. Since the ion beam was not mass analyzed, heavy mass (relative to helium) residual gas fragments were able to strike the specimen during the irradiation. A 300 eV C^+ or O^+ ion can transfer up to 69 or 88 eV respectively to a W atom. This is greater than the displacement energy in W and thus these species will create defects in the W specimen. The majority of the damage was easily identified in this case as dislocation loops which must be interstitial in nature since vacancies are immobile at 60 K.

In addition to the helium and tungsten atoms indicated in the four composition profiles shown in Fig. 57, hydrogen, carbon, and oxygen atoms were also detected. Figures 59 and 60 show the composition profiles for the hydrogen, carbon, and oxygen corresponding to these four helium profiles. The results presented in Fig. 60 show that C and O were only present on the surface of the specimen while H^* was detected to a depth of less than $\sim$ 30 A as indicated in Fig. 59. This result shows that the helium atoms retained in the tungsten

---

* Note that hydrogen was detected in both the irradiations and the control runs. This indicates that the H was not injected into the specimen as a result of the irradiation. The fact that a profile of H into the specimen was observed may indicate that H which adsorbed on the surface of the specimen diffused into the specimen at 60 K. This result does not agree with an extrapolation of high temperature permeability measurements of H through W (see references 124-129).

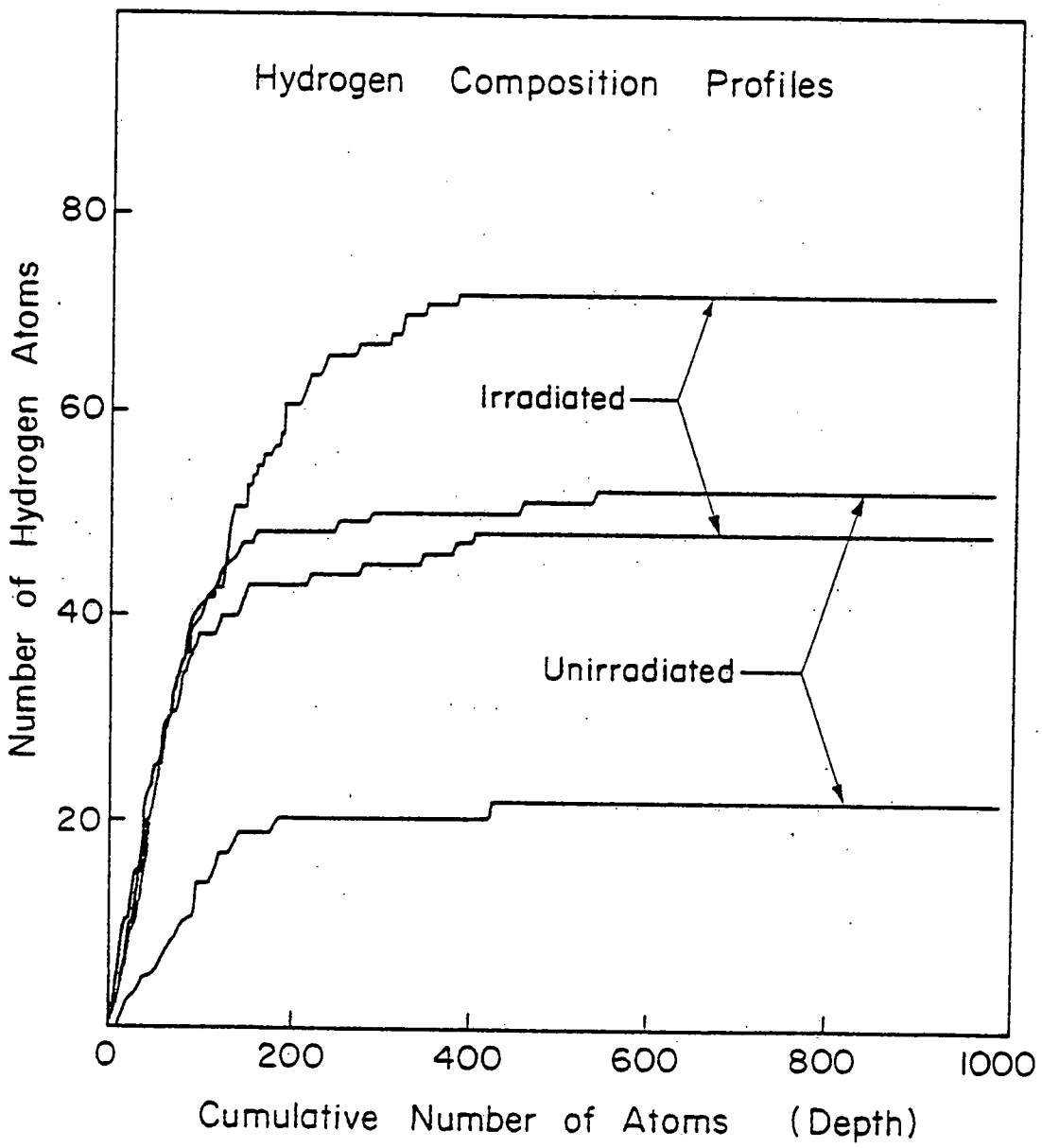

Figure 59. The hydrogen composition profiles which correspond to the four helium composition profiles shown in Fig. 57.

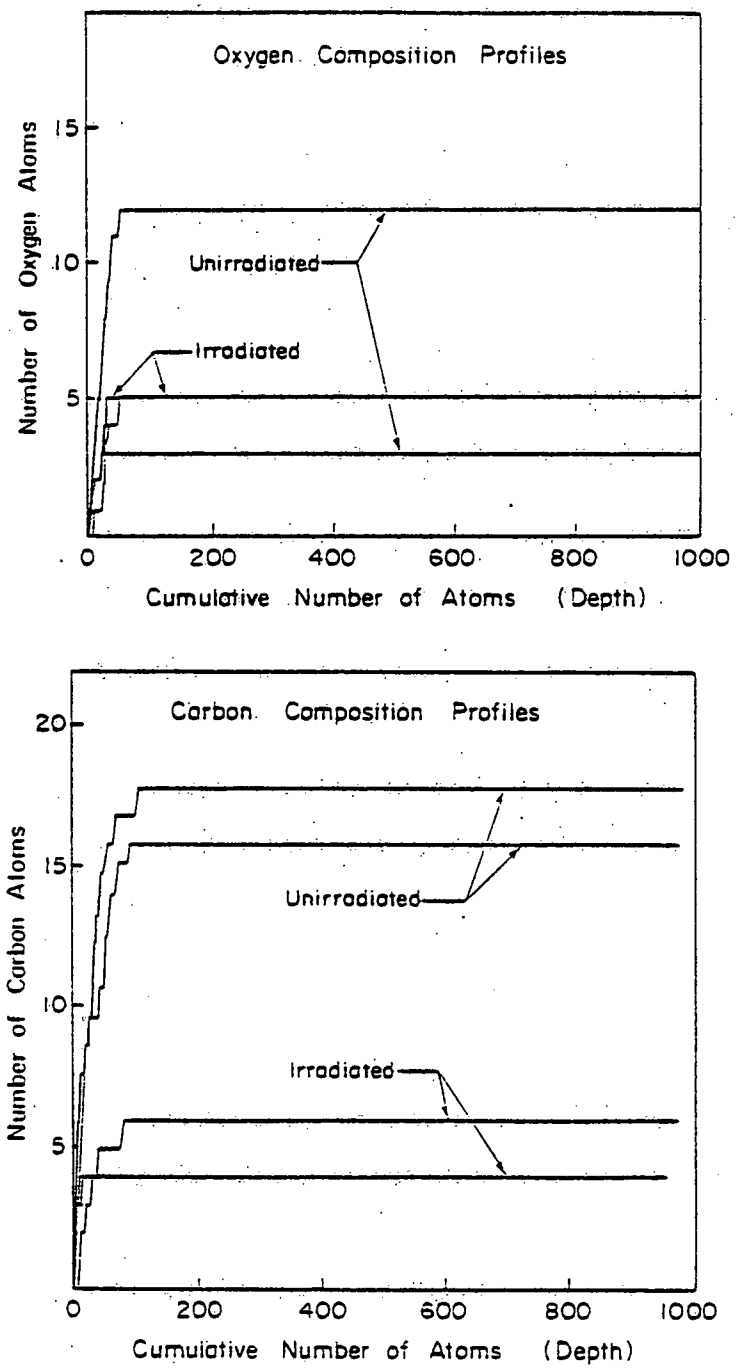

Figure 60. The carbon and oxygen composition profiles which correspond to the four helium composition profiles shown in Fig. 57.

specimen after irradiation with 300 eV helium ions at 80 K were not trapped at impurities since the majority of the helium was detected at a depth greater than 30 A. The most probable source of the H, C, and O was residual gases in the FIM which adsorbed on the surface of the specimen during the approximately 3.5 hours from the initial field evaporation of the specimen until the atom probe analysis. During the atom probe analysis the electric field prevented the adsorbtion of most of the residual gases.

A composition profile for a W specimen irradiated and analyzed at 60±1 K and a control are shown in Fig. 61. The measured $\bar{x}$, Δx, and R were 43.9 A, 36.4 A, and 0.89 respectively which agree, within the experimental uncertainty, with the measured values for the 80 K irradiation. Based on the previously described experimental results, trapping of helium at structural defects or impurities in the T_i = 60 K run can be ruled out. Since trapping did not occur and since the flux and fluence of helium was a constant at both T_i, the temperature independence of the range profile and the reflection coefficient shows that homogenous nucleation of immobile helium clusters did not occur. Therefore the helium detected in the T_i = 60 and 80 K runs must have been isolated, immobile interstitial helium atoms. The hydrogen composition profiles corresponding to the helium profiles shown in Fig. 61 are presented in Fig. 62.

A composite of two profiles for 300 eV helium ion irradiations performed at 60 K is shown in Fig. 63. Also indicated in the figure is a composition profile generated from the theoretical range profile shown in Fig. 58(b). The theoretical profile was scaled to the number

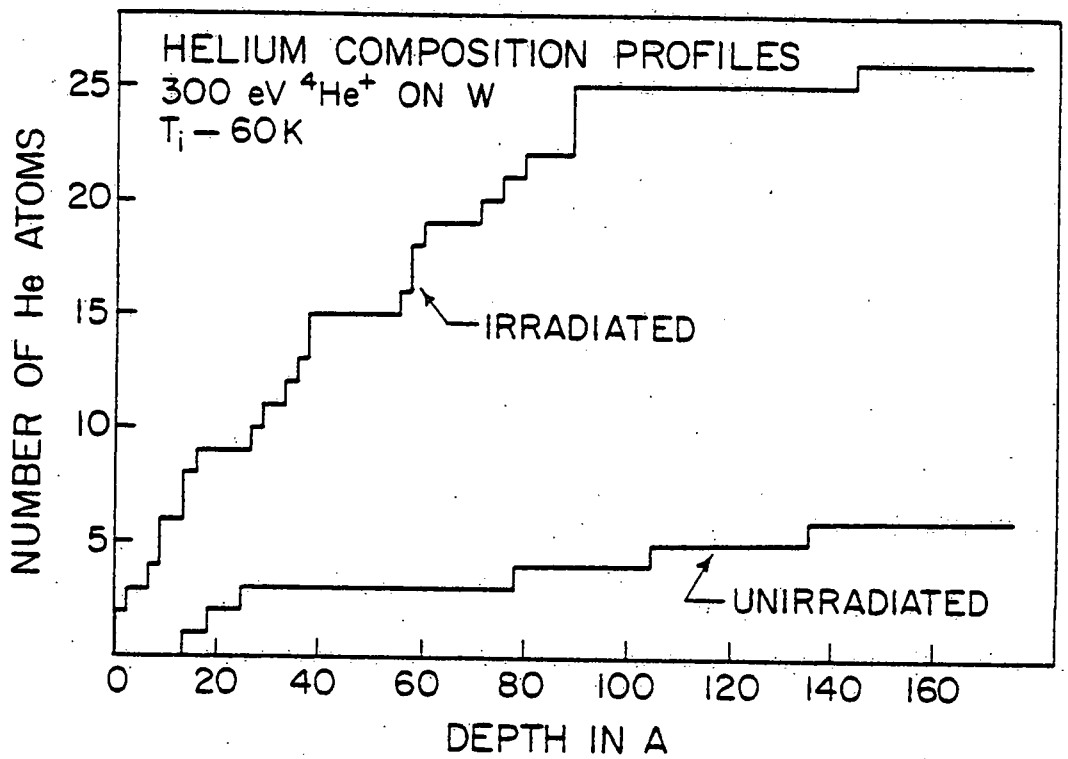

Figure 61. Helium composition profiles for a tungsten specimen irradiated at 60 K with 300 eV He^+ ions along the [110] direction and an unirradiated specimen.

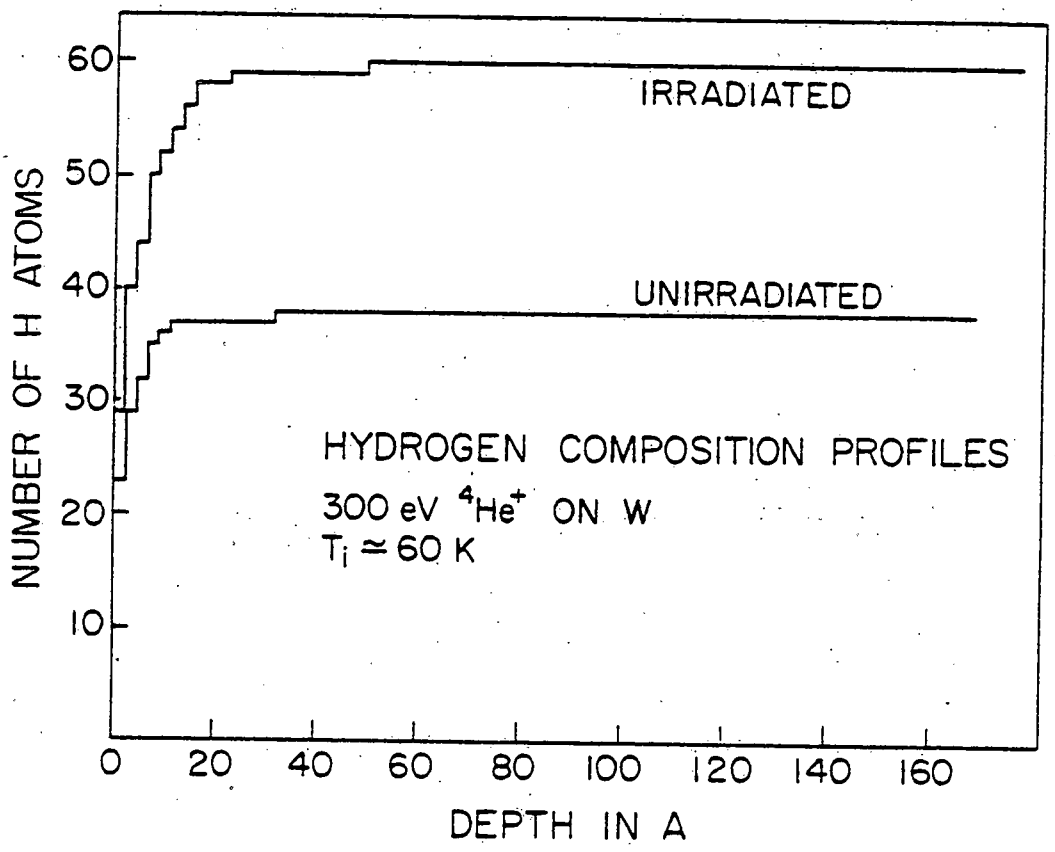

Figure 62. The hydrogen composition profiles which correspond to the helium profiles shown in Fig. 61.

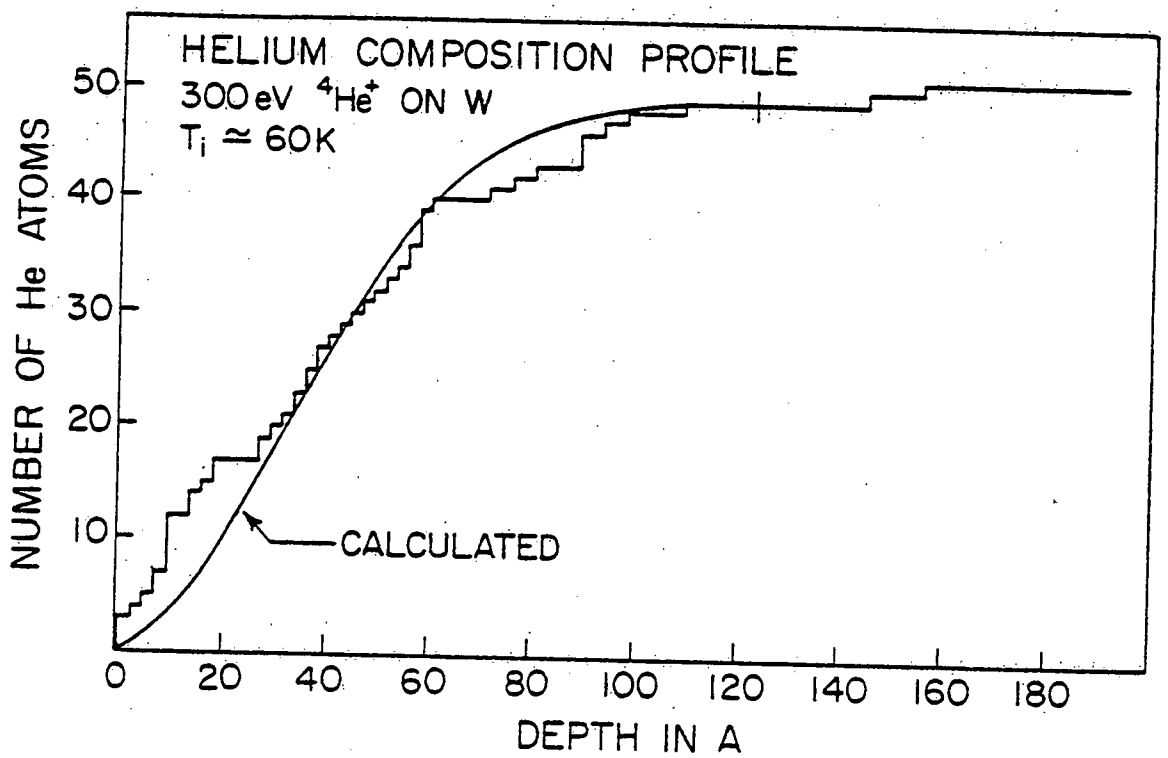

Figure 63. A composite of two helium composition profiles for a tungsten specimen irradiated with 300 eV He^+ ions at 60 K. The calculated profile of Haggmark et. al. is superimposed on the experimental profile.

of helium atoms detected at the maximum range predicted by the calculation. The shape of the experimental profile is consistent with the calculated profile. This result again indicates that the helium atoms were immobile in tungsten at 60 and 80 K, and that true range profiles of 300 eV He^+ ions in W were measured. The measured $\bar{x}$, Δx, and R for this composite profile were 44.0 A, 36.8 A, and 0.90 respectively.

A profile for an irradiation performed at 90 K and analyzed at the common temperature of 60 K is shown in Fig. 64. This run was terminated before the detected concentration of helium decreased to the level present in the controls due to specimen failure. In spite of this, the measured $\bar{x}$, Δx, and R of 40.7 A, 34.7 A, and 0.89 respectively, and the general shape of the profile, are in reasonable agreement with the previous measurements. A surface peak of helium which is much more pronounced in this profile than in the 60 or 80 K irradiations has appeared. This surface peak may be due to surface trapping of diffusing helium which would indicate a small amount of diffusion (< 10 A) at 90 K. However the results clearly indicate that interstitial helium atoms must be essentially immobile at a temperature of 90 K.

Figure 65 shows a helium profile for an irradiation performed at 110 K with the atom probe analysis performed at 60 K. The basic shape of this profile is dramatically different than the previous experimental profiles or the theoretical profile. The absence of helium at a depth greater than approximately 30 A indicates that a significant amount of diffusion (> 100 A) must have taken place.

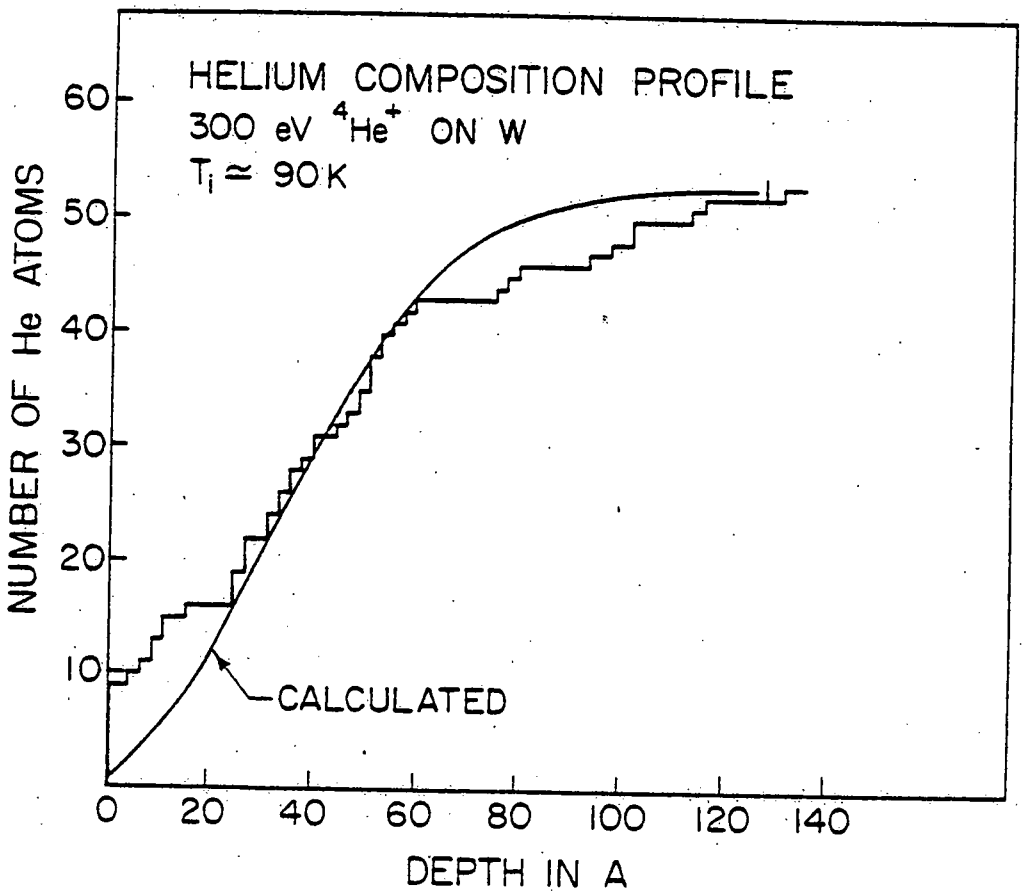

Figure 64. The helium composition profile for a tungsten specimen irradiated with 300 eV He^+ ions at 90 K. The calculated profile of Haggmark et. al. is superimposed on the experimental profile.

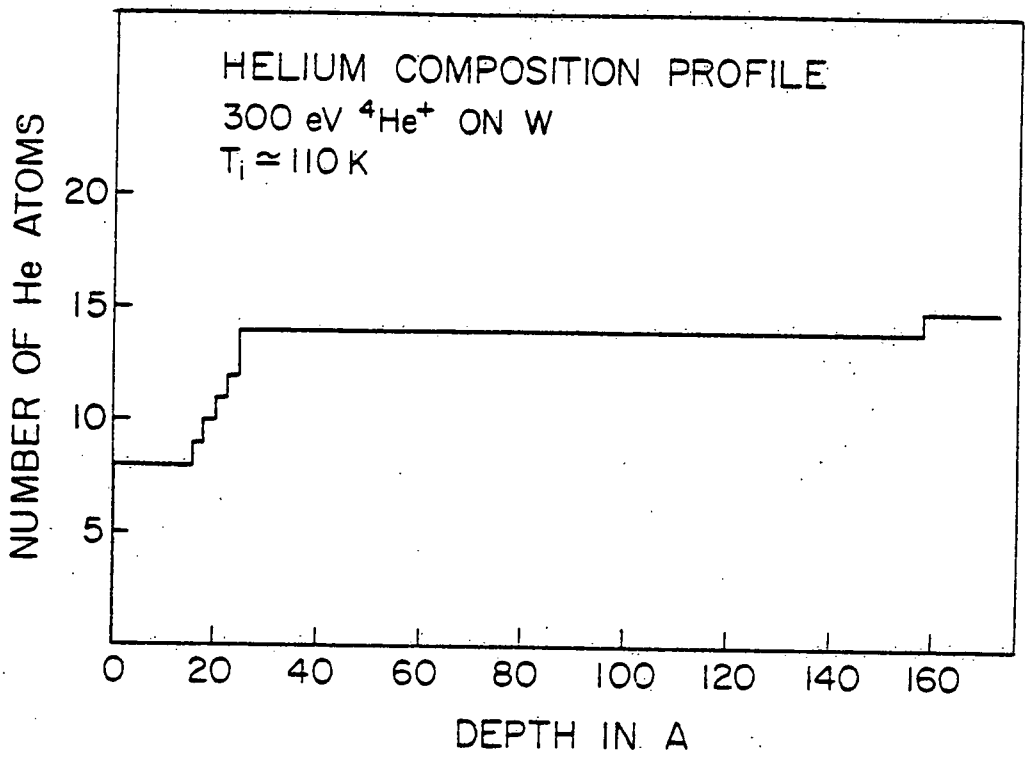

Figure 65. The helium composition profile for a tungsten specimen irradiated with 300 eV He^+ ions at 110 K.

This result shows that interstitial helium atoms became mobile in tungsten in the temperature range of 90 to 110 K. This implies an activation energy for interstitial helium diffusion in W of 0.24 to 0.32 eV as discussed in section 7.5. This result is in good agreement with the theoretical value[110] of 0.24±0.1 eV. The large surface peak of helium shown in this run indicates that trapping of the diffu diffusing helium atoms has occurred at the surface. It is not clear whether this trapping was an intrinsic property of the W (110) plane or was occurring at defects in the surface which were created through sputtering by the 300 eV He^+ ion beam. An immobile cluster of helium was detected at a depth corresponding to the peak concentration in the range profile. This cluster may have been homogenously nucleated, or heterogenously nucleated on a hydrogen atom (see Fig. 66) or a lattice defect (see page 177).

Two helium composition profiles for irradiations performed at 80±5 K and 110 to 120 K with the atom probe analyses performed at 60±2 and 85±5 K respectively are shown in Fig. 67. These profiles are consistent with the observation that helium becomes mobile in tungsten between 90 and 110 K. In this case it is possible that some of the observed changes in the profile can be attributed to the fact that the atom probe analyses were performed at different temperatures (60 and 85 K). However helium from the gas phase does field adsorb on the (110) plane of W for temperature below ~ 140 K[116,117], so that the atom probe analysis performed at 85 K should have been able to indicate the presence of helium had it been retained in the specimen after irradiation at 110 to 120 K. Note that some helium, approximately

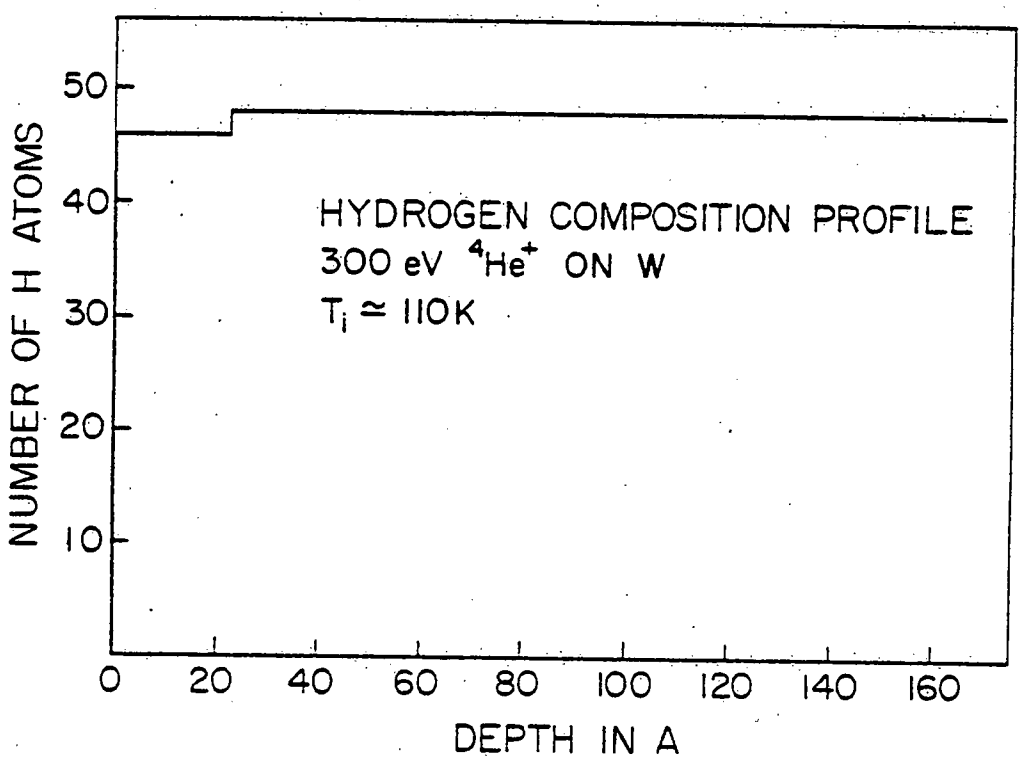

Figure 66. The hydrogen composition profile corresponding to the helium profile shown in Fig. 65.

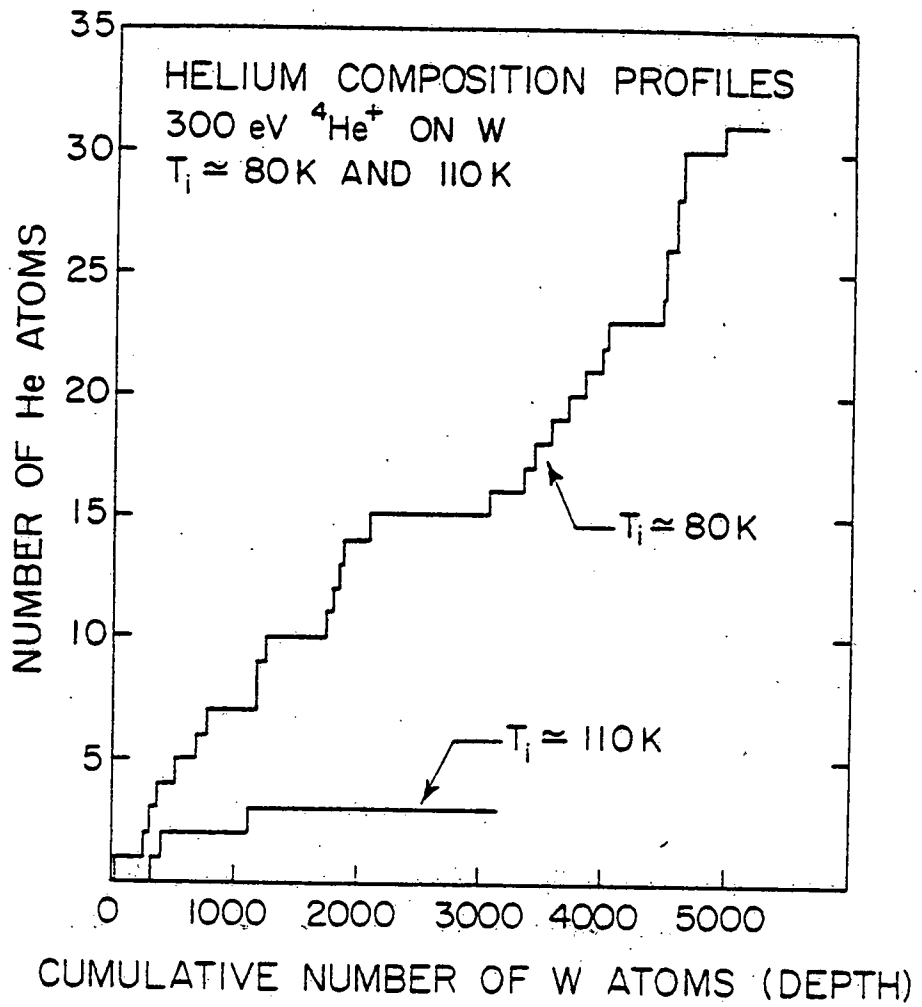

Figure 67. A comparison of the helium composition profiles for a tungsten specimen irradiated at ~ 80 and ~ 110 K.

at the level of the control runs, was detected for the T_a = 85 K run which clearly indicates that helium could be detected at 85 K. Unfortunately the center of the (110) plane was not well aligned with the probe hole so that an accurate, absolute depth scale could not be assigned to either of the last two runs. However an upper estimate of the total depth of analysis for the T_i = 80 K run was ~ 70 A.

An additional test of the fundamental validity of the helium range measurements presented previously was performed by determining the range profile of 475 eV He^+ ions on W. If the range measurements of 300 eV He^+ ions were valid, then by increasing the incident ion energy from 300 to 475 eV an increase in the measured mean range and standard deviation and a decrease in the reflection coefficient should occur. A helium composition profile for 475 eV He^+ ions incident on a W specimen with T_i = 60 K and T_a = 60 K and a control profile are shown in Fig. 68. The measured $\bar{x}$, Δx, and R were 55.8 A, 40.3 A and 0.85 respectively. A comparison with the results at 300 eV shows that $\bar{x}$ and Δx increased and that R decreased as expected. Note that the ratio of the number of helium atoms detected in the control to the number detected in the irradiation was ~ 0.25 for the 300 eV irradiations while it was less than 0.1 for the 475 eV run. This substantial reduction in the background helium level was the result of an improvement in the vacuum processing procedure which resulted in a decrease in the partial pressure of helium in the FIM during the atom probe analysis. Only the improved procedure is described in section 7.3.

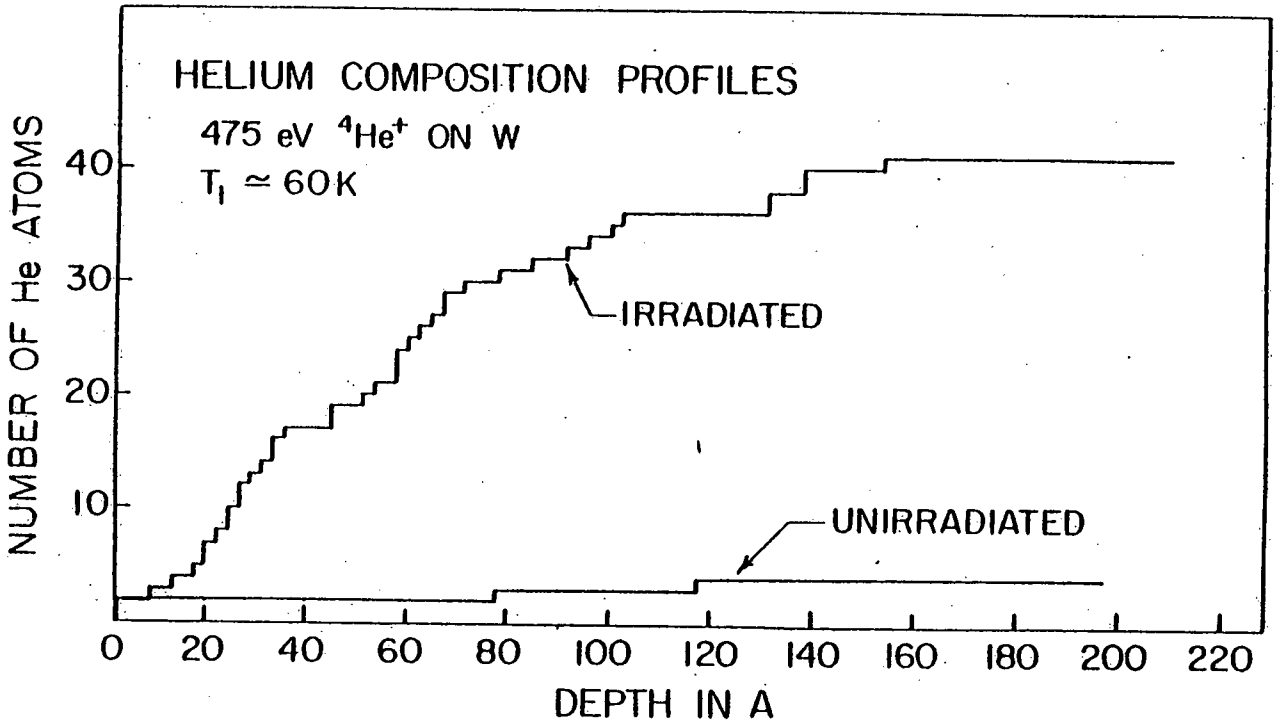

Figure 68. The helium composition profiles for a tungsten specimen irradiated at 60 K with 475 eV He^+ ions and an unirradiated specimen.

A helium profile for 500 eV He^+ ions on W with T_i = 60 K and T_a = 60 K is shown in Fig. 69. The measured $\bar{x}$, Δx, and R were 51 A, 42 A, and 0.89 respectively. This run was terminated prematurely due to specimen failure and thus the actual $\bar{x}$ was greater than 51 A and the actual R was less than 0.89. This result is consistent with the expected increase in $\bar{x}$ and Δx and the expected decrease in R as E_i was increased. The results of the range measurements are summarized in Table 11. The calculated range parameters of Haggmark et. al.[119] are also shown for comparison with the experimental values. The experimental $\bar{x}$, Δx, and R include a contribution due to the random arrival of helium from the gas phase onto the specimen; i.e., no correction has been made for the observed level of helium detected in the controls. The sources and magnitude of the uncertainty in the experimental values are discussed in section 7.5.

7.5 Discussion

This section begins with a discussion of the major sources of error in the measurement of $\bar{x}$, Δx, and R. The expected variations in the shape of the range profile due to statistical fluctuations is also described. The experimental results are compared with the calculations of Haggmark et. al. and the origin of the differences are discussed. The model employed to calculate the migration energy of the interstitial helium atoms is also presented.

There were two sources of systematic error in the measurement of $\bar{x}$ and Δx reported in section 7.4. The first source of systematic error was due to the hemispherical geometry of the FIM specimen which caused the measured values of $\bar{x}$ and Δx to be greater than the

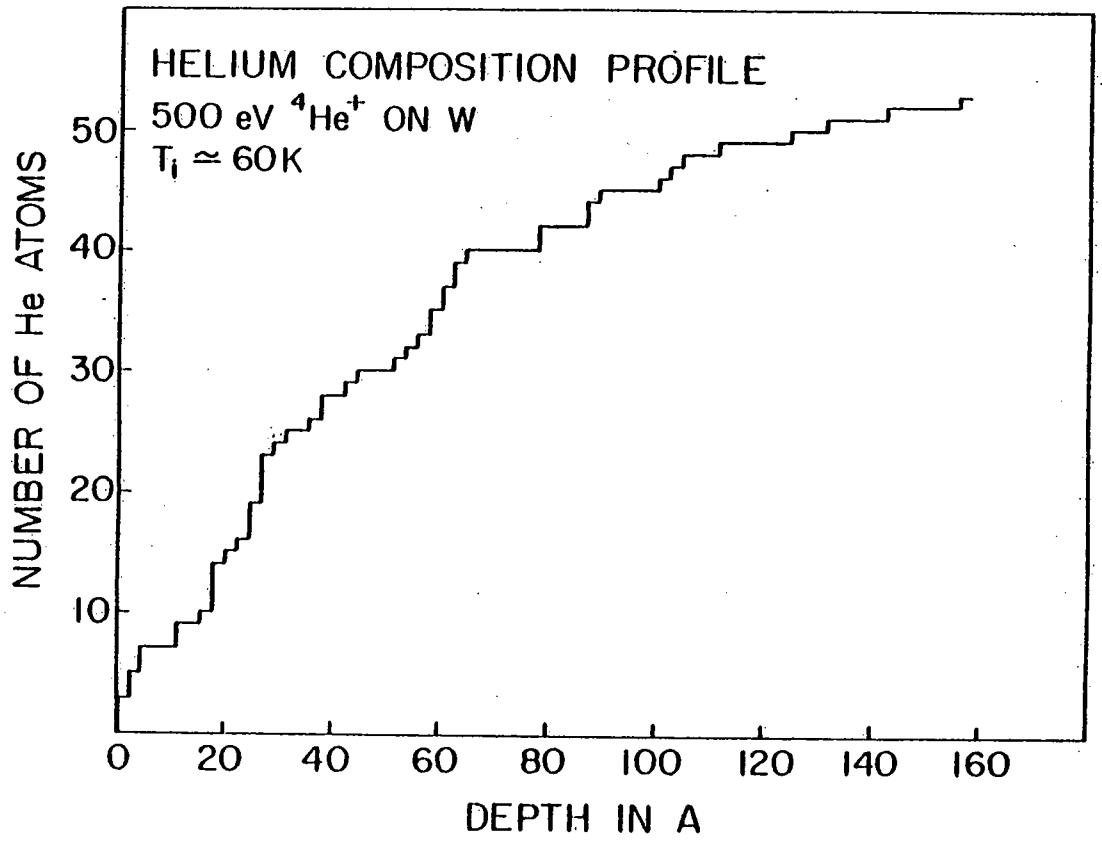

Figure 69. The helium composition profile for a tungsten specimen irradiated at 60 K with 500 eV He^+ ions.

Table 11

A summary of the range measurements for 300 and 475 eV $^4He^+$ ions on W.

Energy (eV)	Irradiation Temperature (K)	Total Number of Helium Atoms (H_d)	Number of W Atoms per (110) Plane (W_d)	$\frac{H_d}{W_d}$	Mean Range ($\bar{x}$) (A)	Standard Deviation (Δx) (A)	Reflection Coefficient (R)
300	60	26	68.3	0.38	43.9	36.4	0.89
300	61	25	70.4	0.36	44.0	37.3	0.90
300	80	27	79	0.34	47.1	35.0	0.90
300	90	53	140	0.38	40.7	34.7	0.89
300	110	15	58	0.26			
475	60	41	85	0.48	55.8	40.3	0.85
300		Theory			42.0	23.1	0.55
475		Theory			53.6	29.7	0.53

values expected for measurements on a planar surface. The magnitude of the error in $\bar{x}$ and Δx was estimated employing the model described in appendix D. This model indicated that the measured mean range of the 300 and 475 eV helium ions exceeded the actual mean range by a maximum of 2.2 A due to the non-planar geometry of the FIM specimen. In addition the model demonstrated that the actual standard deviations of the range profiles were unaffected by the curvature of the FIM specimen; i.e., the measured Δx was essentially unchanged by the correction indicated in the model.

The second source of systematic error in the measurement of $\bar{x}$ and Δx was due to the background contribution of helium indicated in the control runs. This source of error usually resulted in the measured values of $\bar{x}$ and Δx exceeding the actual values. An analysis of the magnitude of the contribution to $\bar{x}$ and Δx due to the background helium is presented in appendix D.

The analysis showed that the error in the measured mean range depended on two factors: (1) the ratio (ϵ) of the number of helium atoms detected in a control run (C) to the number of helium atoms detected in an irradiated specimen (N); and (2) the mean depth ($\bar{x}_c$) of the helium atoms detected in the control runs. Typical values of ϵ and $\bar{x}_c$ for the 300 eV He^+ irradiations were 0.2 and 65 A respectively. The average value of $\bar{x}$ for the 300 eV irradiations* indicated in

---

* The data for the 300 eV irradiation at 90 K were excluded from the analysis due to the premature termination of this run caused by specimen failure and due to the possibility of a small amount of helium diffusion. The 300 eV irradiation at 110 K was excluded due to the extensive diffusion which occurred in this run.

Table 11 was 45.0 A. Employing the values of $\bar{x}$, $\bar{x}_c$ and ϵ given above, equation D11 in appendix D indicated that the measured mean range exceeded the actual mean range by < 5 A due to the background helium. As discussed in appendix D, the correction to the standard deviation (Δx) requires an accurate determination of the spatial distribution of the background helium in addition to requiring the values of $\bar{x}$, $\bar{x}_c$ and ϵ given above. Due to the finite number of control runs, an accurate distribution was not obtained. In order to allow an approximate evaluation of the error in Δx, a random distribution in depth of the background helium was assumed. For a random distribution, $\bar{x}_c$ equals one-half of the maximum depth (D) analyzed in the run. Generally the measured $\bar{x}_c$ was less than D/2. This can probably be attributed to the fact that the arrival of helium atoms at the specimen from the gas phase was not random in depth of analysis but was governed by the product of the helium partial pressure and the time of analysis. Since the helium partial pressure decreased during the atom probe analysis and since the field evaporation rate for the first few (110) planes was less than the rate during the remainder of the analysis, the probability of detecting background helium atoms decreased as the analysis proceeded. Therefore the appropiate choice of $\bar{x}_c$ for the correction to Δx was somewhat uncertain. An upper limit on $\bar{x}_c$ was D/2 which yielded an $\bar{x}_c$ of ~ 90 A. This upper limit on $\bar{x}_c$ also yielded an approximate upper limit to the error in Δx. Employing equation D18, the error in Δx was estimated for $\bar{x}_c$ equal to 90 to 65 A which yielded an approximate upper and lower bound on the actual value of Δx. The average measured value of Δx for the 300 eV

irradiations was 36.6 A. Employing a value of ϵ of 0.2 and a corrected mean range of 40.0 A, the standard deviation (Δx) calculated with the aid of equation D17 yielded upper and lower limits on Δx of 34.5 A and 21.3 A as $\bar{x}_c$ was varied from 65 A to 90 A.

The expected statistical fluctuation in the mean range was estimated from the standard deviation of the mean (σ_m) which is given by the expression

$$\sigma_m = \frac{\Delta x}{\sqrt{N}} \quad . \tag{21}$$

The value of σ_m for the average of the 300 eV irradiations was < 4 A. The expected fluctuation (σ_s) in the standard deviation was obtained by approximating the actual range profile with a normal distribution. For a normal distribution

$$\sigma_s = \frac{\Delta x}{\sqrt{2N}} \tag{22}$$

which yielded a σ_s of ~ 3 A for the 300 eV irradiations. This value was consistent (within 1 A) with the σ_s determined in the simulations of the theoretical range profile for N = 50.

A reasonable estimate of $\bar{x}$ and Δx for the 300 eV He^+ irradiations on W, including the effects of background helium, curvature of the FIM specimen and random statistical fluctuations was $\bar{x}$ = 40±4 A and Δx = 20 to 36 A. The uncorrected values were $\bar{x}$ = 45.0 A and Δx = 36.3 A.

For the 475 eV irradiation, $\bar{x}_c$ was ~ 46 A and ϵ was ~ 0.1. Applying the same error analysis to the 475 eV range data yielded a corrected value for $\bar{x}$ of 56±6 A versus the measured $\bar{x}$ of 55.8 A. The upper and lower bounds on Δx were 41.4 and 36.9 A for $\bar{x}_c$ = 46 and 90 A

respectively, while σ_s was ~ 4 A. Thus the most reasonable estimate for the values of $\bar{x}$ and Δx for the 475 eV helium irradiation were $\bar{x} = 56 \pm 6$ A and $\Delta x \approx 35$ to 43 A. Note that the systematic errors were comparable to the statistical uncertainties for both the 300 eV and the 475 eV irradiations. Thus a significant improvement in the measured values of $\bar{x}$ and Δx would require an increase in the total number of helium atoms detected (i.e., N must be increased) and a decrease in the magnitude of the systematic errors (notably by a decrease in ϵ).

Due to the finite number of helium atoms detected in each run, significant variations in the shape of the range profiles were expected due to random statistical fluctuations. Simulated profiles of 300 eV He^+ ions on W for 25, 50, and 100 helium atoms are shown in Fig. 70(a), (b), and (c) respectively. The differences in the simulated profiles were due to random statistical fluctuations only; background helium was not included in the simulations. Approximately 500 helium atoms were required before the detailed shape of the simulated profile accurately reflected the generating profile. Therefore a comparison of the detailed shape of the experimental profiles shown in section 7.4 with the theoretical profile of Haggmark et. al. has no statistical validity although detailed comparisons of average range parameters such as $\bar{x}$ and Δx are certainly justified.

The range calculations of Haggmark et. al. were based on an improved He-W interatomic potential[106] and employed an amorphous solid, Monte Carlo simulation of the scattering of He on W. Although the calculated $\bar{x}$ and Δx for 300 eV He on W of 42.0 and 23.1 A

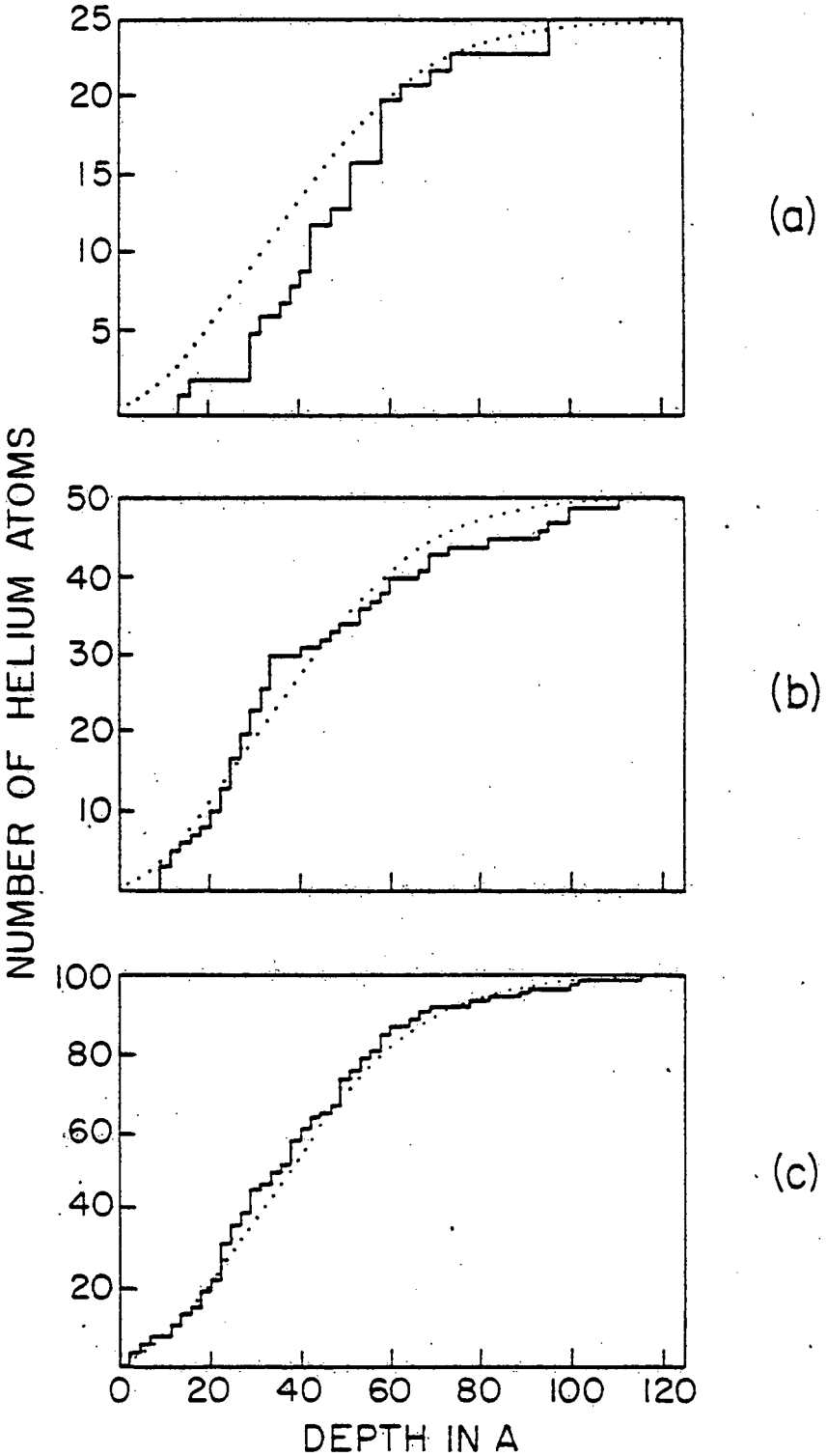

Figure 70. Computer simulated helium composition profiles. The dotted curve is the theoretical proflie of Haggmark et. al. which has been simulated by the stepped curve.

respectively were in approximate agreement with the experimental measurements, the present experimental uncertainties and the finite amount of data did not allow a critical evaluation of the calculation to be made. For example, although the experimental results did show that a major fraction of the helium had not been channeled in the [110] direction, the general validity of an amorphous solid model was not demonstrated. However these calculations were in much better agreement with the experimental results than the analytical model of Schiott.[130] The analytical model predicted a mean range of less than 14 A for 300 eV helium on tungsten which is not in agreement with the experimental results.

While the experimental range measurements were in reasonable agreement with the calculations, the measured reflection coefficient of 0.89 was considerably larger than the value of 0.55 predicted by Haggmark for 300 eV helium on tungsten. If the calculated value was correct then approximately 75 % of the helium retained in the specimen was not detected. A plausible quantitative explanation involves the forms in which helium field evaporates from the (110) plane of W. Considerable evidence exists[131] which has demonstrated that helium which has been field adsorbed from the gas phase on the surface of the FIM specimen field evaporates in two forms: (1) He^{+} accompanied by a W^{+3} ion; and (2) a WHe^{+3} molecular ion. The mass resolution of the present instrument did not permit a small number of WHe^{+3} ions to be distinguished from a large number of W^{+3} ions due to the energy deficit tails in the W^{+3} peaks (see Fig. 20). Therefore only helium which field evaporated as He^{+} was identified and included in the measurements

reported in section 7.4. The relative abundance of WHe^{+3} relative to He^{+} was estimated by performing an atom probe analysis of the (110) plane of unirradiated W in the presence of $2 \cdot 10^{-6}$ torr helium with $T_a \approx 60$ K; 80 He^{+}, 84 W^{+3}, and 224 WHe^{+3} ions were detected. This yielded a ratio of WHe^{+3} to He^{+} of 2.8 ± 0.2 which was in approximate agreement with the value reported in reference 131. If the helium retained in the W lattice also field evaporated with a ratio of WHe^{+3} to He^{+} of 2.8 ± 0.2, then the measured reflection coefficient of 0.89 corresponded to an actual R of 0.5 to 0.6 which agrees with the calculated value of 0.55.

The migration energy for diffusion of interstitial helium atoms in tungsten (ΔE^{m}_{He}) was estimated by employing the following model for the diffusion process.

The irradiated FIM specimen was approximated by a sphere of radius (r_t) which contained an initially uniform concentration of helium. The surface concentration of helium was held fixed at a value of zero. The solution to this time dependent diffusion model is given in reference 132 which shows that the radial concentration profile through the sphere is a function of a dimensionless parameter (δ) given by the expression

$$\delta = \frac{Dt}{r_t^2} \tag{23}$$

where D is the helium diffusivity and t is the diffusion time at T_i. Since

$$D = D_o \exp\left(\frac{-\Delta H^{m}_{He}}{kT_i}\right) , \tag{24}$$

the migration enthalpy (ΔH^m_{He}) is given by

$$\Delta H^m_{He} = kT_i \log_e \left(\frac{D_o t}{\delta r_t^2} \right) \qquad (25)$$

where k is Boltzmann's constant and D_o is the pre-exponential factor for helium diffusion in tungsten. The results of the 110 K He^+ irradiation allowed an upper limit on ΔH^m_{He} to be determined by employing the maximum possible value of D_o and t and the minimum values of δ and r_t. The extensive diffusion which occurred in the 110 K irradiation indicates that most of the helium would have diffused from the model sphere under the conditions present during this irradiation. The average concentration of helium decreased to approximately 0.1 of the initial concentration for $\delta \approx 0.3$. This represents an approximate lower limit on δ. The diffusion time (t) was less than 3 hr. Although the specimen radius was greater than 300 A, the effective r_t was somewhat smaller than this value since the helium injected during the irradiation was not uniformly distributed throughout the entire volume of the specimen tip. The minimum effective r_t was approximately 100 A since the injected helium was deposited within a spherical shell with a thickness greater than 100 A. An approximate value of D_o was calculated employing the Zener model for the diffusion process[133]. For interstitial diffusion in the bcc lattice between octahedral sites (the calculations of Wilson et. al.[105-107] indicated that interstitial helium atoms reside in the octahedral sites in tungsten), the pre-exponential factor (D_o) is given by the expression

$$D_o = \frac{1}{6} a_o^2 \nu \exp\left(\frac{\Delta S^m_{He}}{k}\right) \tag{26}$$

where ΔS^m_{He} is the migration entropy, ν is the attempt frequency, and a_o is the lattice parameter of tungsten (3.16 A). In the Zener theory, the major contribution to the free energy of migration was assumed to be the energy expended in straining the lattice during the elementary diffusion step. This assumption yielded the following estimate for the migration entropy,

$$\Delta S^m_{He} = \beta \frac{\Delta H^m_{He}}{T_m} \tag{27}$$

where T_m is the absolute melting point of the metal,

$$\beta = \frac{-\partial(\mu/\mu_o)}{\partial(T/T_m)} \quad , \tag{28}$$

μ is the elastic modulus of the metal at the temperature T_i and μ_o is the modulus at 0 K. For tungsten, β is equal to 0.38.[134] The value of ΔH^m_{He} is approximately 0.3 eV hence the calculated value of ΔS^m_{He} is approximately equal to 0.4k for tungsten. The attempt frequency (ν) was estimated employing the expression

$$\nu = \left[\frac{2\Delta H^m_{He}}{m a_o^2}\right]^{0.5} \tag{29}$$

where m is the mass of the helium atom. This expression yielded a value of $\nu = 1.2 \cdot 10^{13}$ sec^{-1}. Employing equation 26, D_o was calculated to be $\sim 3 \cdot 10^{-3}$ cm^2 sec^{-1}. In view of the approximations involved in the model, the actual value of D_o probably lies within the range of values from approximately $1 \cdot 10^{-3}$ to $1 \cdot 10^{-2}$ cm^2 sec^{-1}.

Employing equation 25 with r_t = 100 A, δ = 0.3, t = 3 hr and

$D_o = 1 \cdot 10^{-2}$, an upper limit on ΔH^m_{He} was calculated to be 0.32 eV. A lower limit on ΔH^m_{He} was obtained employing equation 25 by taking the maximum values of δ and r_t and the minimum values of D_o and t for the 90 K irradiation. Since the range profile at 90 K indicated that essentially no diffusion had taken place, the maximum value of δ in the model was taken to be the value at which a very noticeable change in the range profile would have occurred. This yielded a maximum value for δ of ~ 0.02. Since the specimen was maintained at $T_i = 90$ K for more than 1 hr after the irradiation, the minimum value of t was 1 hr. Employing equation 25, with $r_t = 300$ A, $\delta = 0.02$, t = 1 hr and $D_o = 1 \cdot 10^{-3}$ cm^2 sec^{-1}, a lower limit on ΔH^m_{He} was calculated to be 0.24 eV.

Therefore the migration enthalpy of interstitial helium atoms in tungsten must be within the range of 0.24 to 0.32 eV. Employing equation 25 and constant values of r_t and D_o of 300 A and $3 \cdot 10^{-3}$ cm^2 sec^{-1} respectively yielded a ΔH^m_{He} in the range of 0.25 to 0.29 eV. Thus the present uncertainty in ΔH^m_{He} of 0.08 eV was divided equally between the uncertainties in the choice of the diffusion parameters D_o and r_t, and the experimental range in the diffusion temperature (i.e., 90 to 110 K).

The migration energy (ΔE^m_{He}) is defined by the expression

$$\Delta H^m_{He} = \Delta E^m_{He} + p\Delta V^m_{He} \qquad (30)$$

where p is the pressure and ΔV^m_{He} is the volume change of migration. Since essentially no external pressure was applied to the specimen during the diffusion interval at T_i then $\Delta E^m_{He} \approx \Delta H^m_{He}$.

8. SOLUTE SEGREGATION TO VOIDS IN FAST NEUTRON IRRADIATED Mo-1.0 at.% Ti

The alloy Mo-1.0 at.% Ti exhibits an enhanced swelling compared to pure Mo when both materials are irradiated with fast neutrons at the same flux, fluence and temperature.[65,68] Although the composition of the alloy is related to the enhanced swelling, the mechanism by which the solute additions cause the enhanced swelling is unknown. In the present work the nature and extent of the solute redistribution in a fast-neutron irradiated Mo-1.0 at.% Ti alloy was investigated. The objective was to elucidate the mechanism which was responsible for the enhanced swelling of the alloy compared to pure Mo. Before presenting the experimental results, several aspects of the swelling phenomena which are particularly relevant to the present experiment are discussed.

Most pure metals and alloys exhibit a volume increase when irradiated in a fast-breeder reactor at approximately 0.3 to 0.6 of the absolute melting point of the metal. This volume increase or swelling is typically in the range of 0.1 to 10 % of the initial volume after approximately two years of irradiation to a fluence of $\sim 10^{22}$ neutrons cm^{-2}. A large number of defects are produced during the irradiation; on the average every atom in the metal is displaced from a normal lattice site approximately 10 to 100 times. The microstructure after irradiation is dominated by empty cavities (voids) and interstitial dislocation loops (or a dislocation network at large fluences). Since the voids do not appreciably relax there is a resultant increase in the volume of the material.

A number of mechanisms for the nucleation and growth of the voids and the interstitial dislocation loops have been proposed. Void nucleation mechanisms have received the most theoretical[91-94] and experimental[88,135] attention. It has been suggested that void nucleation may occur homogenously or heterogenously at defects such as impurity atoms (particulary interstitial impurities C, N, and O), depleted zones, precipitates and gas bubbles. Although no single mechanism is able to explain all of the experimental observations, impurities or alloying additions are believed to be a major factor controlling the nucleation rate.[135]

The growth of the voids and interstitial dislocation loops is a result of the preferential bias of the edge dislocation for SIAs. The larger relaxation volume of the SIA when compared to the vacancy induces a preferential drift of SIAs to the dislocation. This causes the interstitial loops to grow and therefore leaves a net surplus of vacancies in the material. As a result, the flux of vacancies into a neutral sink, for example a void, is greater than the flux of SIAs into this sink and thus the voids also grow. Since the dislocation bias is small, the total mass transport into a sink due to the SIAs and away from a sink due to the vacancies is much greater than the net mass transport.

Models of void growth have usually employed either diffusion limited kinetics[90] in which the rate of growth of the voids is determined by the vacancy diffusivity or surface reaction limited kinetics[136,137] in which the void growth rate is determined by the ability of the sink-lattice interface to absorb point defects. In

both models impurity atoms or alloying additions are expected to have a strong effect on the growth rate. For example trapping of point defects at foreign atoms in solid solution would enhance the recombination rate and hence reduce both the nucleation and the growth rate of voids and dislocations. In addition segregation of foreign atoms to the dislocation or the voids may have a profound influence on their sink properties by, for example: (1) changing the elastic strain field around a sink and hence changing the bias of the sink to vacancies and SIAs; (2) pinning of the dislocations; and (3) modifying the surface reaction kinetics. While equilibrium segregation of foreign elements to the voids and dislocations may occur* an even greater degree of nonequilibrium segregation is possible due to the large flux of defects into these sinks. If mobile SIA-solute atom or vacancy-solute atom complexes have a high probability of forming, then a substantial amount of nonequilibrium segregation of the solute to sinks for point defects must occur.

The nonequilibrium segregation of impurity atoms or alloying elements to voids was first suggested by Anthony.[138] Okamoto and Wiedersich then formulated a kinetic model for the irradiation induced segregation of solute to voids which described the steady state solute concentration profile around a void.[139] Employing this model the strain field which they observed around voids in an electron irradiated stainless steel was attributed to the segregation of undersized solute

---

* The driving force in this case is a lowering of the surface energy of the void or the line energy of the dislocation.

atoms (possibly Si and Ni) to the voids. A more sophisticated model based on the numerical solution of a series of simultaneous rate equations was subsequently developed by Lam and Johnson.[140] Several additional observations of massive nonequilibrium solute segregation have been made which were based either on the segregation induced strain field around the void or on the irradiation induced precipitation of second phase particles.[141-144] Direct chemical identification of Si segregation to voids in neutron irradiated aluminum[145] and Si segregation to dislocation loops in ion irradiated stainless steel[146] has been obtained employing a scanning transmission electron microscope equipped with an energy dispersive x-ray analyser. Although this technique is clearly superior to the more indirect methods previously described, it is presently of limited usefulness in the study of segregation effects in the bcc metals for the following reasons: (1) the distance between voids in the bcc metals (~200 A) is much less than the minimum diameter which can be chemically analyzed (~1000 A); and (2) the technique cannot detect low atomic number elements such as helium, carbon, oxygen, and nitrogen which are believed to be particularly important impurities in the bcc metals. Because of the unique capability of the atom probe to chemically identify all of the elements in addition to providing chemical analysis on the atomic scale, the atom-probe FIM is ideally suited to segregation studies in the bcc metals.

8.1 Material Preparation

The starting material consisted of a rod 3 cm in length and 0.1 cm in diameter of a Mo-1.0 at.% Ti alloy. This rod was irradiated

along with several other pure Mo and Mo-1.0 at.% Ti rods with fast neutrons at ~700 C to a fluence of ~1x10^{22} n cm^{-2} (E > 1MeV) in row 7 midplane position of EBR II. This rod was thinned to approximately 0.015 cm in diameter by electropolishing in a solution of 1 part H_2SO_4 to 7 parts CH_3OH by volume at ~10 Vdc. The FIM specimen was prepared by the drop off technique employing a 1 normal solution of NaOH in H_2O at ~2 Vac.

This specimen was known to contain voids based on extensive electron microscope examination of the other irradiated rods. In addition the electron microscopy revealed that the Mo-1.0 at.% Ti alloy had a slightly higher density of voids with a somewhat larger average diameter than the irradiated pure Mo rods.[65,147] Thus the alloy exhibited an enhanced swelling relative to the pure Mo. The observation of a higher void density and a larger average void diameter in the alloy agrees with the earlier observations of Wiffen.[68]

8.2 Experimental Results

Atom probe analyses of the region surrounding two voids in the Mo-1.0 at.% Ti alloy have been performed. In addition an analysis of a region in which no voids were present was also performed.

An FIM image showing the first void before and after the atom probe analysis is presented in figure 71 (a) and (b) respectively. The area enclosed by the white circle represents the region which was chemically analysed. Note that the void was still present after the atom-probe analysis and thus the entire analysis was performed on material which was contained within a thin shell surrounding the void.

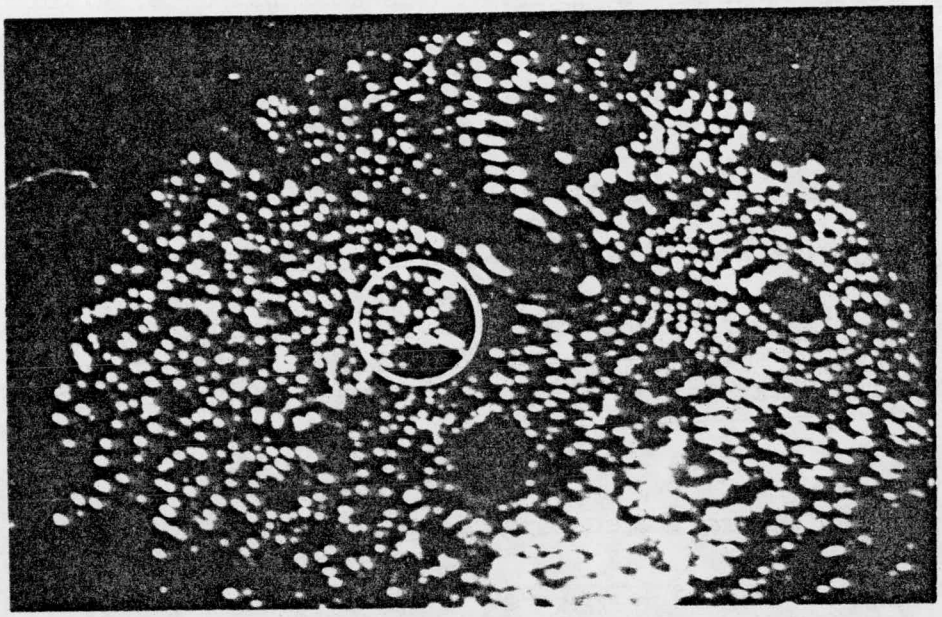

a

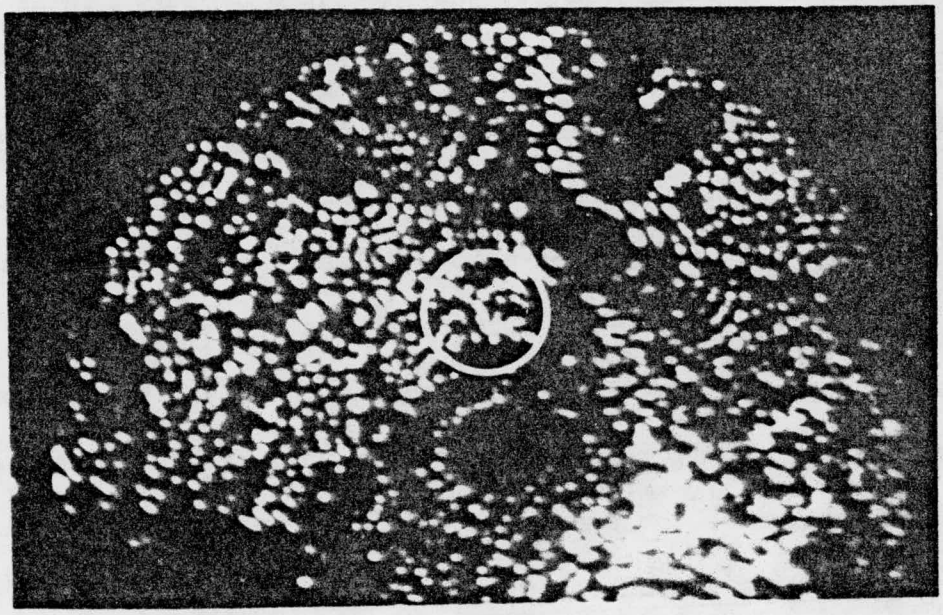

b

Figure 71. Two FIM micrographs showing a void in a neutron irradiated Mo-1.0 at. % Ti specimen (a) before and (b) after an atom probe analysis.

The image contrast shown in figure 71 was attributed to a void for the following reasons: (1) the specimen was known to contain voids; (2) the observed contrast was different than the contrast due to defects other than voids e.g. vacancies, SIAs, depleted zones, dislocations and grain boundaries; (3) the observed contrast was similar to the predicted FIM image contrast from a cavity[148]; and (4) the observed contrast was similar to the FIM image contrast reported by Brenner and Seidman[13] for voids in neutron irradiated molybdenum.

A composition profile showing the spatial distribution of titanium in the region surrounding this void is presented in figure 72. The measured Ti concentration was 0.4 ± 0.2 at.% Ti which is within the range of the measured Ti concentration for the unirradiated alloy. The absence of a statistically significant difference in the Ti concentration or in the spatial distribution of the Ti in the region around the void versus the unirradiated alloy indicated that a significant amount of Ti segregation to the void had not occurred.

Three successive stages in the examination of the second void are shown in figure 73. Figure 73(a) shows the void prior to the atom-probe analysis and indicates the chemically analyzed region. The analysis was interupted and a second observation of the void was made as shown in figure 73(b). Note that the void was still present in the specimen which indicated that the material adjacent to this void was still in the process of being chemically analyzed. The atom-probe analysis was then continued until the entire region surrounding the void had been field evaporated and hence chemically analyzed. The FIM image of the specimen taken after the atom probe analysis clearly indicated that

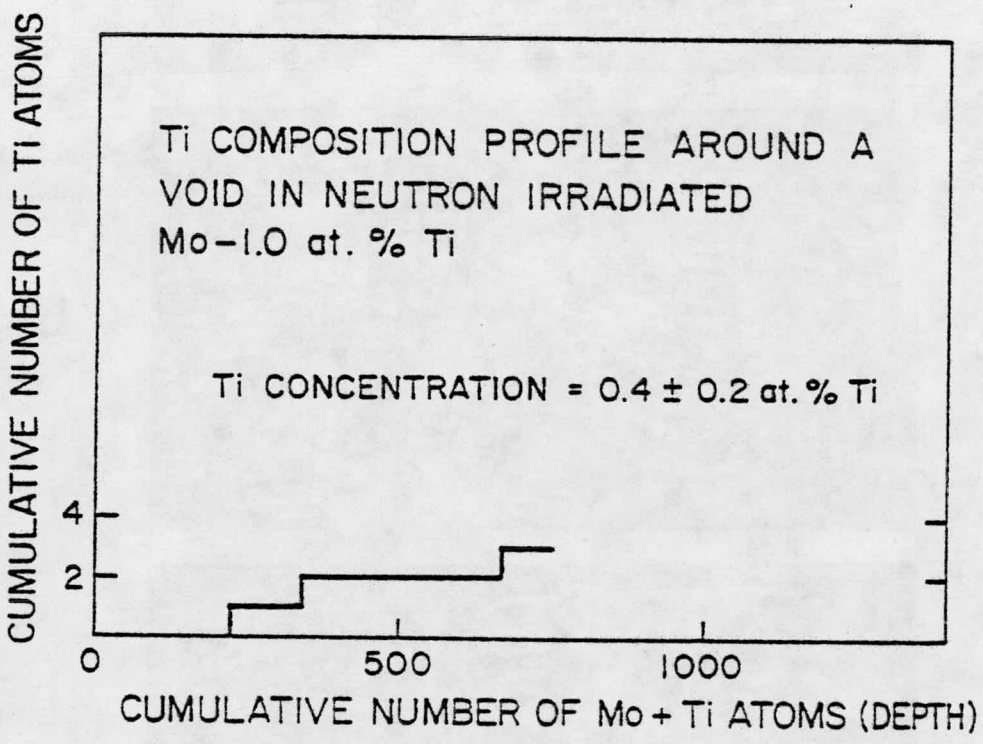

Figure 72. The titanium composition profile for the region surrounding the void shown in Fig. 71 for a neutron irradiated Mo-1.0 at. % Ti alloy.

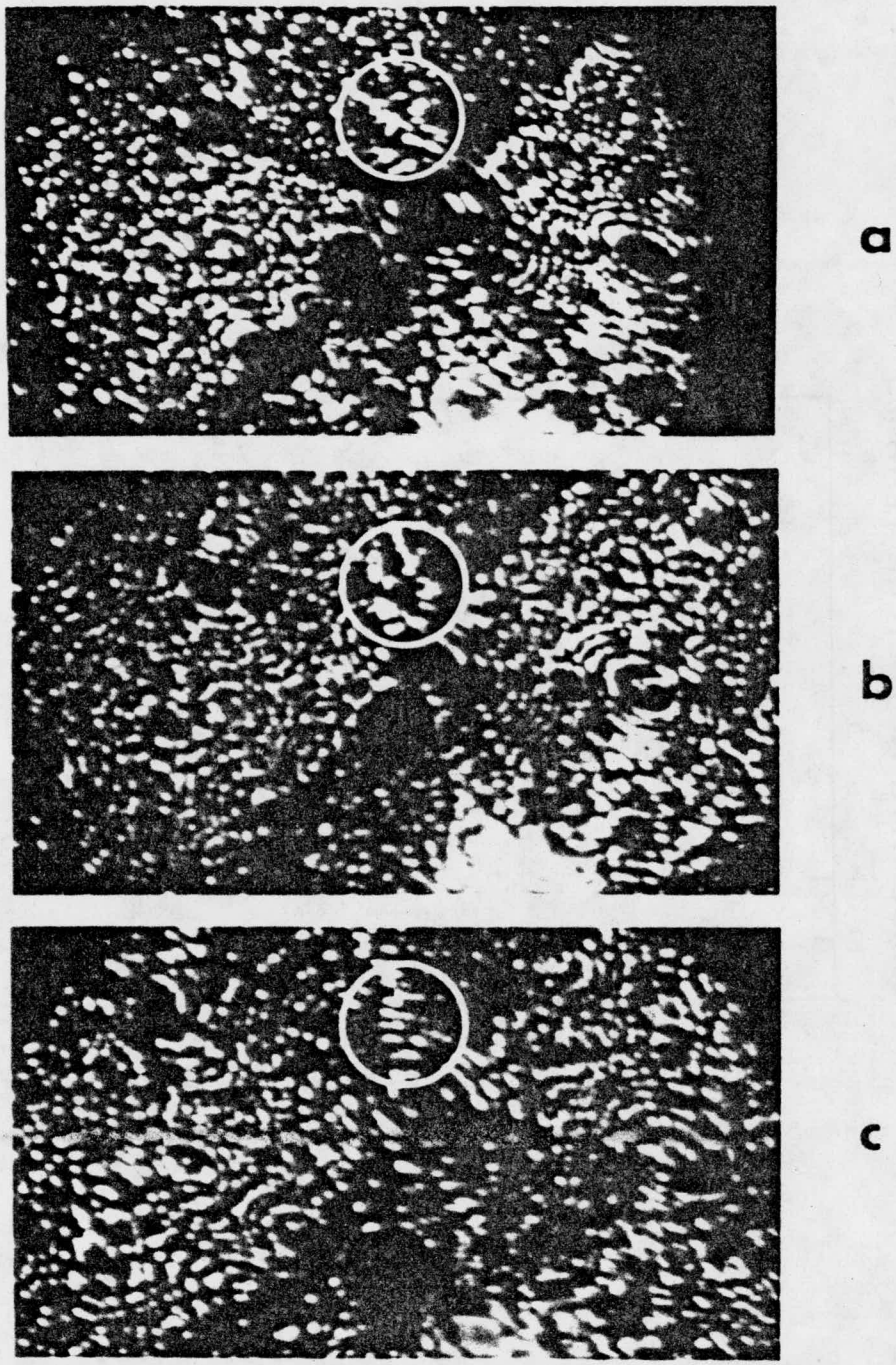

Figure 73. A series of FIM micrographs showing a void in a neutron irradiated Mo-1.0 at. % Ti specimen (a) before, (b) during, and (c) after an atom probe analysis.

the void was no longer present in the specimen as shown in figure 73(c).

The titanium composition profile showing the spatial distribution of Ti in the region surrounding the void and for the region leading away from the void is presented in figure 74. The point at which the atom-probe analysis was interrupted and a visual observation of the void was made is also indicated in the figure. Within the expected statistical fluctuations, the slope of the profile in the region of the void was essentially the same as the slope in the region leading away from the void. Thus the Ti was approximately uniformly distributed within the analyzed region. Furthermore the measured Ti concentration was 0.20 ± 0.05 at.% Ti which is in approximate agreement with the measured range of Ti concentration for the unirradiated alloy (see table 6). Therefore no evidence of the anticipated massive segregation of Ti to the voids was found. In addition to titanium, carbon was also detected at a concentration of $\sim 0.08 \pm 0.03$ at.% C.* The spatial distribution of the carbon is presented in figure 75 which shows an approximately uniform distribution of carbon throughout the analyzed region. This indicates that the carbon was probably not contained in a TiC precipitate associated with the void. No evidence of a precipitate was found in the FIM image. The presence of carbon around this void is in sharp contrast with the failure to detect any carbon in solid solution in the unirradiated alloy. This result indicates that

---

* The failure to detect carbon during the analysis of the first void is not surprising in view of the small total number of atoms detected. Based on a carbon concentration of 0.08 at.%, the calculated probability of detecting no carbon atoms during the analysis of the first void was greater than 0.5.

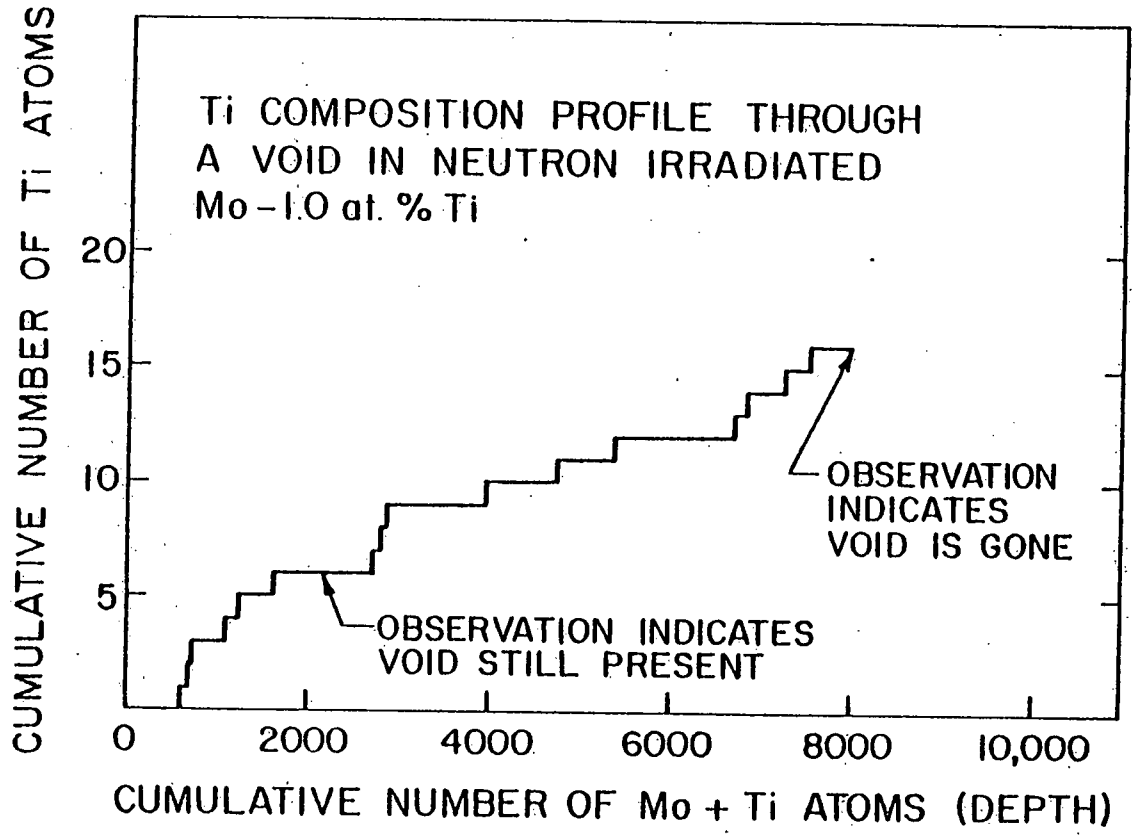

Figure 74. The titanium composition profile for the region surrounding and leading away from the void shown in Fig. 73 for a neutron irradiated Mo-1.0 at. % Ti alloy.

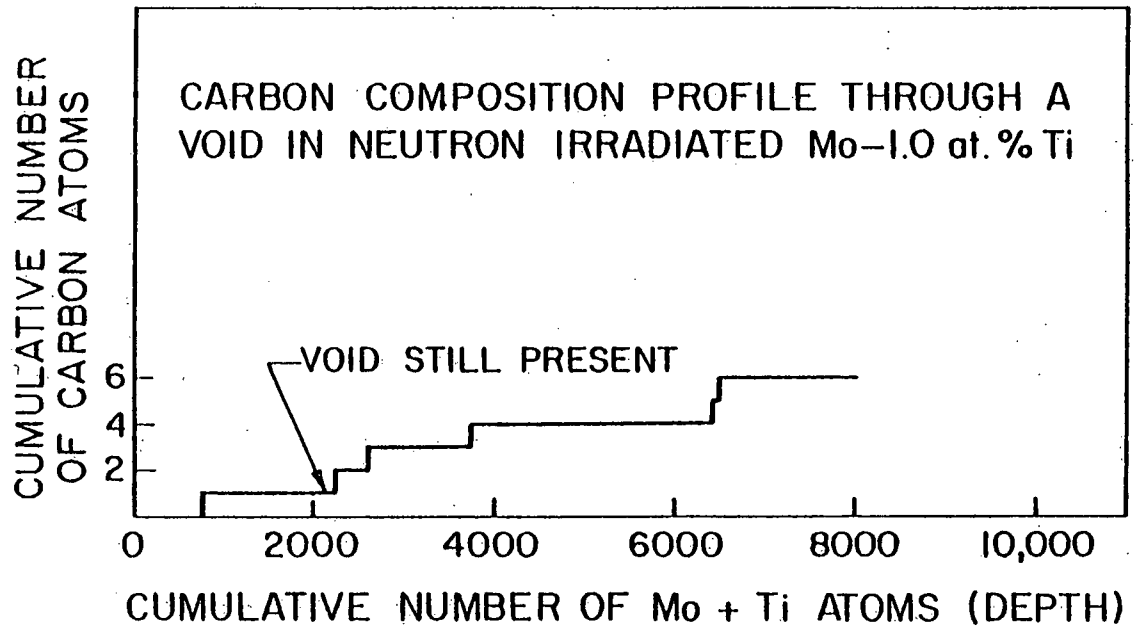

Figure 75. The carbon composition profile for the region surrounding and leading away from the void shown in Fig. 73 for a neutron irradiated Mo-1.0 at. % Ti alloy.

either: (1) the carbon segregated to a pre-existing void during the irradiation; or (2) the carbon was incorporated into a void embryo which subsequently grew into a void. In order to eliminate the possibility that the carbon detected in this run was due to the decomposition of CO, CO_2 or CH_4 on the surface of the specimen, the following control experiment was performed. An unirradiated Mo-1.0 at.% Ti specimen was exposed for periods in excess of 1 hour (which exceeded the time required to chemically analyze the voids) to the typical residual gases in the FIM in the presence and the absence of the helium imaging gas. The exposures were made with the electric field applied to the specimen and with no electric field applied to the specimen. Carbon was not detected in any of these control runs. Thus the carbon detected during the analysis of the void must have been present within the specimen and was not an artifact of the vacuum conditions.

An atom-probe analysis of a region which did not contain any voids was also performed. The composition profile indicating the spatial distribution of the titanium remaining in solid solution in the irradiated alloy is shown in figure 76. The titanium appears to be uniformly distributed with no evidence that clustering of Ti atoms had occurred. A concentration of 0.27 ± 0.05 at.% Ti was measured which is within the range of the measured Ti concentration for the unirradiated alloy. This result shows that both the concentration of the Ti remaining in solid solution and the spatial distribution of the Ti was not affected by the irradiation. Thus a substantial irradiation induced

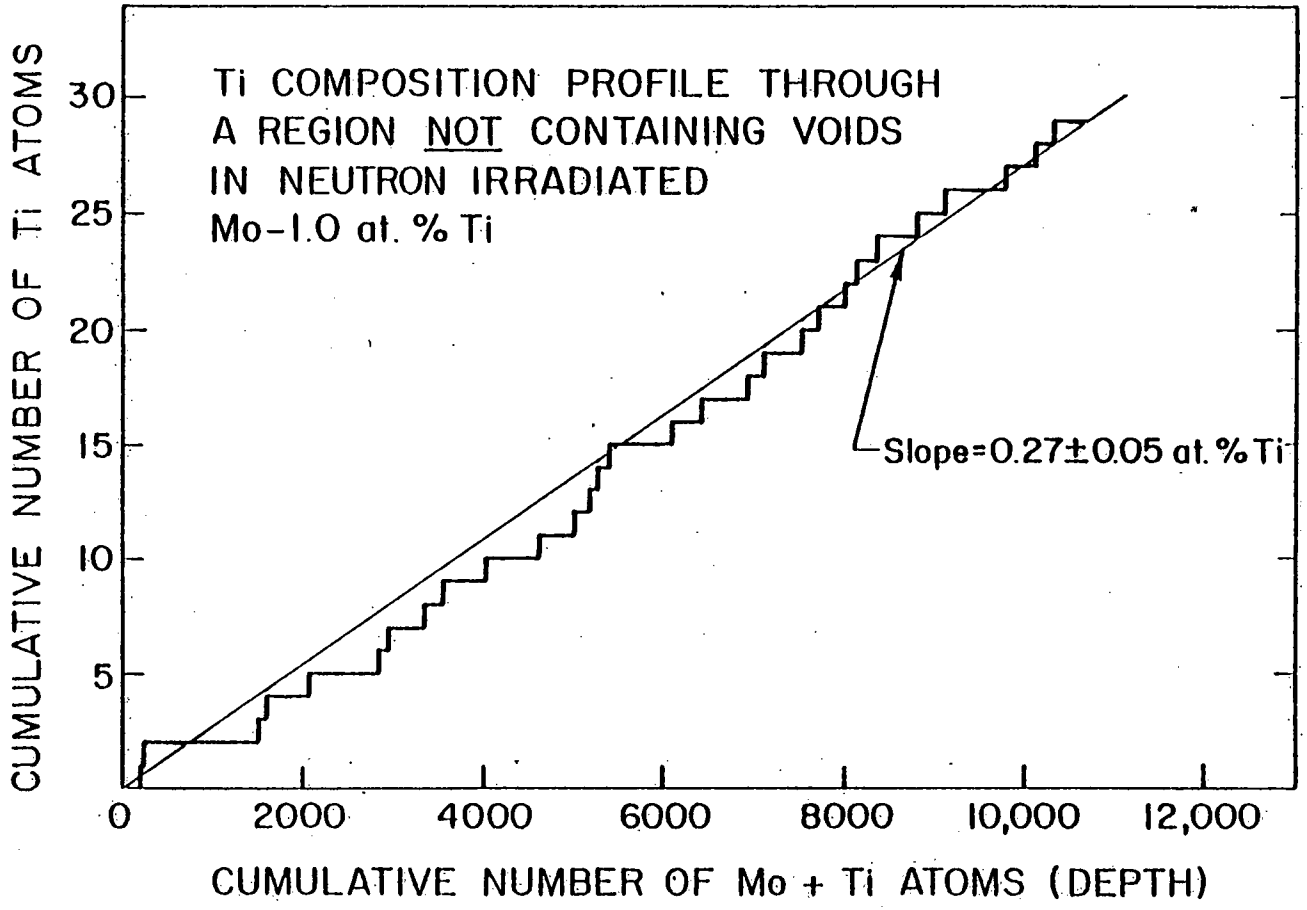

Figure 76. A titanium composition profile through a region not containing any voids in a neutron irradiated Mo-1.0 at. % Ti alloy.

re-solution of Ti from the TiC precipitates did not occur*. Furthermore no carbon was detected in this run which indicates that carbon was not left in solid solution in the irradiated material. This result confirms the observation that the carbon detected during the analysis of the void must have been associated with the void. The measured composition for the irradiated alloy is summarized in table 12 while the chemical analysis of the unirradiated alloy is presented in table 6.

The results on the irradiated and the unirradiated Mo-1.0 at.% Ti are summarized below:

(1) no evidence of significant segregation of titanium to voids in the neutron irradiated alloy has been found;

(2) the concentration of Ti remaining in solid solution and the spatial distribution of the titanium was not significantly affected by fast neutron irradiation at 700 C;

(3) carbon was not detected in solid solution in either the irradiated or the unirradiated alloy;

(4) results 2 and 3 indicate that no detectable re-solution of the TiC precipitates occurred as a result of the irradiation; and

(5) segregation of carbon to a void in the irradiated alloy was detected.

---

* Chang and Perlmutter[70] have shown that TiC precipitates do not thermally dissolve in Mo for temperatures less than approximately 1600 C.

Table 12

The composition of a neutron irradiated Mo-1.0 at.% Ti alloy determined with the atom-probe FIM.

REGION ANALYZED	NUMBER OF ATOMS DETECTED			CONCENTRATION (at. %)*	
	Mo	Ti	C	Ti	C
VOID NUMBER 1	742	3	0	0.4±0.2	<0.1
VOID NUMBER 2	8003	16	6	0.20±0.05	0.08±0.03
DEFECT FREE	10663	29	0	0.27±0.05	<0.01

* The ± values were calculated from the $\sqrt{N}/\Sigma N$ values where N is the number of atoms detected.

8.3 Discussion

The enhanced swelling of the alloy Mo-1.0 at.% Ti relative to pure Mo has been attributed primarily to an increase in the void density and to a lesser degree to an increase in the average diameter (or volume) of the voids in the alloy[68]. This suggests that both the nucleation and the growth rate of the voids is larger in the alloy than in pure Mo. The results presented in section 8.2 indicated that the enhanced swelling of the alloy cannot be attributed to segregation of Ti to the voids. Although a massive nonequilibrium segregation of Ti to the dislocations can probably be ruled out based on the absence of significant segregation to the voids, equilibrium segregation of Ti to dislocations remains a possibility. The small degree of carbon segregation which was detected may have been sufficient to change the sink properties of a void and thus affect the void growth rate*. In addition the carbon may have had an effect on the void nucleation rate.

* The diameter of the second void which was analyzed was estimated to be greater than 50 A based on the FIM image. If all of the detected carbon and titanium atoms were located on the surface of this void, the degree of surface coverage would have been less than 0.01 monolayer of carbon and 0.02 monolayer of titanium.

REFERENCES

1. E. W. Muller, J. A. Panitz and S. B. McLane, Rev. Sci. Instrum. 39, 83 (1968).

2. E. W. Muller and T. T. Tsong, Field Ion Microscopy (Elsevier, New York, 1969).

3. E. W. Muller, S. V. Krishnaswamy and S. B. McLane, Surface Sci. 23, 112 (1970).

4. E. W. Muller, S. B. McLane and J. A. Panitz, Surface Sci. 17, 430 (1969).

5. S. V. Krishnaswamy, S. B. McLane and E. W. Muller, J. Vac. Sci. Tech. 11, 899 (1974).

6. E. W. Muller and T. T. Tsong, in Prog. in Surface Sci. 4, p. 1-137 (Pergamon Press, New York, 1973).

7. E. W. Muller, Z. Physik 131, 136 (1951).

8. A. S. Berger, D. N. Seidman and R. W. Balluffi, Acta Met. 21, 123 (1973).

9. A. S. Berger, D. N. Seidman and R. W. Balluffi, Acta Met. 21, 137 (1973).

10. D. N. Seidman, K. L. Wilson and C. H. Nielsen, in Fundamental Aspects of Radiation Damage in Metals, p. 373-96 (National Technical Information Service, Springfield, VA, 1975).

11. K. M. Bowkett and D. A. Smith, Field Ion Microscopy, Chap. 5 (North Holland, Amsterdam, 1970).

12. K. M. Bowkett and D. A. Smith, Field Ion Microscopy, Chap. 6 (North Holland, Amsterdam, 1970).

13. S. S. Brenner and D. N. Seidman, Rad. Effects 24, 73 (1975).

14. S. S. Brenner and J. T. McKinney, Appl. Phys. Lett. 13, 29 (1968).

15. S. S. Brenner and J. T. McKinney, Surface Sci. 23, 88 (1970).

16. P. J. Turner, B. J. Regan and M. J. Southon, Surface Sci. 35, 336 (1973).

17. P. J. Turner, B. J. Regan and M. J. Southon, Vacuum 22, 443 (1972).

18. K. Kinosita, S. Nakamura and T. Kuroda, Japan J. Appl. Phys. 13, 1775 (1974).

19. T. M. Hall, A. Wagner, A. S. Berger and D. N. Seidman, Cornell University Materials Science Center Report No. 2357 (1975).

20. T. M. Hall, A. Wagner, A. S. Berger and D. N. Seidman, Scripta Met. 10, 485 (1976).

21. A. Wagner, T. M. Hall and D. N. Seidman, Rev. Sci. Instrum. 46, 1032 (1975).

22. J. Gallot, J. Sarrau and A. Bostel, Le Vide 179, 173 (1975).

23. H. O. Andren and H. Norden, 22nd International Field Emission Symposium, Georgia Institute of Technology (1975).

24. R. S. Chambers and G. Ehrlich, 22nd International Field Emission Symposium, Georgia Institute of Technology (1975).

25. R. J. Lewis and G. D. W. Smith, 22nd International Field Emission Symposium, Georgia Institute of Technology (1975).

26. A. J. Watts and B. Ralph, 22nd International Field Emission Symposium, Georgia Institute of Technology (1975).

27. E. Krautz, J. Ladurner and M. Leisch, 23rd International Field Emission Symposium, Pennsylvania State University (1976).

28. S. R. Goodman, S. S. Brenner and J. R. Low, Met. Trans. 4, 2363 (1973).

29. S. R. Goodman, S. S. Brenner and J. R. Low, Met. Trans. 4, 2371 (1973).

30. S. S. Brenner and S. R. Goodman, Scripta Met. 5, 865 (1971).

31. P. J. Turner and J. M. Papazian, Met. Sci. J. 7, 81 (1973).

32. A. Youle, P. J. Turner and B. Ralph, J. Microscopy 101, 1 (1973).

33. S. V. Krishnaswamy, S. B. McLane and E. W. Muller, Rev. Sci. Instrum. 45, 1049 (1974).

34. J. A. Panitz, CRC Critical Reviews in Solid State Physics, p. 153-79 (Chemical Rubber Company, Cleveland, 1975).

35. E. W. Muller and T. T. Tsong, Field Ion Microscopy, Chap. 2, (Elsevier, New York, 1969).

36. E. W. Muller, Phys. Rev. 102, 618 (1956).

37. A. S. Berger, Rev. Sci. Instrum. 44, 592 (1973).

38. W. B. Colson, J. McPherson and F. T. King, Rev. Sci. Instrum. 44, 1694 (1973).

39. F. Rosebury, Handbook of Electron Tube and Vacuum Techniques, (Addison Wesley, New York, 1965).

40. D. N. Seidman, R. M. Scanlan, D. L. Styris and J. W. Bohlen, J. Sci. Instrum. 2, 473 (1969).

41. A. T. Finkelstein, Rev. Sci. Instrum. 11, 94 (1940).

42. R. C. Bradley, Phys. Rev. 93, 719 (1954).

43. M. Abele and W. Meckbach, Rev. Sci. Instrum. 30, 335 (1959).

44. P. B. Bowden and D. G. Brandon, J. Sci. Instrum. 40, 213 (1963).

45. M. W. Thompson, Defects and Radiation Damage in Metals, p. 188-240, (Cambridge Press, London, 1969).

46. R. M. Scanlan, D. L. Styris and D. N. Seidman, Phil. Mag. 23, 1439 (1971).

47. R. M. Scanlan, D. L. Styris and D. N. Seidman, Phil. Mag. 23, 1459 (1971).

48. D. N. Seidman, J. Phys. F: Metal Phys. 3, 393 (1973).

49. D. N. Seidman, K. L. Wilson and C. H. Nielsen, Phys. Rev. Lett. 35, 1041 (1975).

50. K. L. Wilson and D. N. Seidman, Rad. Effects 27, 67 (1975).

51. J. T. Robinson, K. L. Wilson and D. N. Seidman, Phil. Mag. 27, 1417 (1973).

52. Available from the International Resistance Company (IRC).

53. S. S. Brenner and J. T. McKinney, Rev. Sci. Instrum. 43, 1264 (1972).

54. R. J. Lewis and G. D. W. Smith, 20th International Field Emission Symposium, Pennsylvania State University (1973).

55. E. W. Muller, S. V. Krishnaswamy and S. B. McLane, Rev. Sci. Instrum. 44, 84 (1973).

56. E. W. Muller and S. V. Krishnaswamy, Rev. Sci. Instrum. 45, 1053 (1974).

57. W. Meiling and F. Stary, Nanosecond Pulse Techniques, p. 219, (Gordon and Breach, New York, 1968).

58. C. A. Johnson, Rev. Sci. Instrum. 41, 1812 (1970).

59. J. A. Panitz, S. B. McLane and E. W. Muller, Rev. Sci. Instrum. 40, 1321 (1969).

60. S. V. Krishnaswamy and E. W. Muller, Rev. Sci. Instrum. 45, 1049 (1974).

61. B. J. Regan, P. J. Turner and M. J. Southon, J. Phys E: Sci. Instrum. 9, 187 (1976).

62. E. W. Muller, Ber. Bunsenges. Phys. Chem. 75, 979 (1971).

63. W. P. Poschenrieder, Int. J. Mass Spectrom. Ion Phys. 9, 357 (1972).

64. Handbook of Chemistry and Physics, (Chemical Rubber Co., Cleveland, 1967).

65. J. Moteff, V. K. Sikka and H. Jang, Physics of Irradiation Produced Voids, edited by R. S. Nelson, p. 181, (London, Her Majesty's Stationary Office, 1975).

66. J. Matolich, H. Nahm and J. Moteff, Scripta Met. 8, 837 (1974).

67. V. K. Sikka and J. Moteff, Met. Trans. 5, 1514 (1974).

68. F. W. Wiffen, p. 386, in reference 87.

69. Universal Cyclops Steel Corporation.

70. W. H. Chang and I. Perlmutter, High Temperature Materials, p. 347, (Interscience, New York, 1963).

71. B. L. Eyre, Proc. Discussion Meeting on Defects in Refractory Metals, edited by R. DeBatist, J. Nihoul and L. Stals, p. 311, (Mol, Belgium: SCK/CEN, 1972).

72. Climax Molybdenum Company.

73. E. E. Bloom, J. O. Stiegler, A. F. Rowcliffe and J. M. Leitnaker, Scripta Met. 10, 303 (1976).

74. W. G. Johnston, T. Lauritzen, J. H. Rosolowski and A. M. Turkalo, General Electric Report No. 76CRD019, (Schenectady, New York, 1976).

75. K. M. Bowkett and D. A. Smith, Field Ion Microscopy, Chap. 9, (American Elsevier, New York, 1970).

76. B. Ralph and D. G. Brandon, Phil. Mag. 8, 919 (1963).

77. T. Masumoto and R. Maddin, Mater. Sci. Eng. 19, 1 (1975).

78. J. L. Walter, F. Bacon and F. E. Luborsky, General Electric Report No. 76CRD027, (Schenectady, New York, 1976).

79. P. Rao and J. L. Walter, private communication (1976).

80. B. Leskovar, Physics Today 30 No. 11, 42 (1977).

81. M. Kaminsky, CRC Critical Reviews in Solid State Science 6, 433 (1976).

82. Radiation Effects on Solid Surfaces, edited by M. Kaminsky, (American Chemical Society, Washington, D. C., 1976).

83. Proc. of 2nd International Conference on Surface Effects in Controlled Fusion Devices, San Francisco (1976).

84. Surface Effects in Controlled Fusion, edited by H. Wiedersich, M. Kaminsky and K. M. Zwilsky, (North Holland, Amsterdam, 1974).

85. P. G. Shewmon, Science 173, 987 (1971).

86. Voids Formed by Irradiation of Reactor Materials, edited by S. F. Pugh, H. M. Loretto and D. I. R. Norris, (British Nuclear Energy Society, Reading, England, 1971).

87. Radiation Induced Voids in Metals, edited by J. W. Corbett and L. C. Ianniello, (AEC Symposium Series, CONF-710601, Albany, New York, 1971).

88. D. I. R. Norris, Rad. Eff. 14, 1 (1972).

89. D. I. R. Norris, Rad. Eff. 15, 1 (1972).

90. R. Bullough and R. S. Nelson, Physics in Technology 5, 1 (1974).

91. J. L. Katz and H. Wiedersich, J. Chem. Phys. 55, 1414 (1971).

92. J. L. Katz and H. Wiedersich, J. Nucl. Mater. 46, 41 (1972).

93. K. C. Russell, Acta Met. 19, 733 (1971).

94. H. Wiedersich, J. J. Burton and J. L. Katz, J. Nucl. Mater. 51, 287 (1974).

95. D. J. Reed, Rad. Effects 31, 129 (1977).

96. A. Normura and S. Kiyono, J. Phys. D: Appl. Phys. 8, 1551 (1975).

97. O. S. Oen and M. T. Robinson, Application of Ion Beams to Metals, edited by G. Carter, J. S. Colligon and W. A. Grant, p. 329 (Institute of Physics, London, England, 1976).

98. O. S. Oen and M. T. Robinson, Nucl. Instrum. Meth. 132, 647 (1976).

99. W. D. Wilson, L. G. Haggmark and J. P. Biersack, Phys. Rev. B 15, 2458 (1977).

100. A. Feurstein, S. Kalbitzer and H. Oetzmann, Phys. Lett. 51A, 165 (1975).

101. H. Oetzmann, A. Feurstein, H. Grahmann and S. Kalbitzer, Phys. Lett. 55A, 170 (1975).

102. H. Oetzmann, A. Feurstein, H. Grahmann and S. Kalbitzer, Proc. Int. Conf. on Ion Beam Surface Layer Analysis, edited by O. Meyer, G. Linker and F. Kappeler, p. 245, (Plenum Press, New York, 1976).

103. R. Behrisch, J. Bottiger, W. Eckstein, U. Littmark, J. Roth and B. M. U. Scherzer, Appl. Phys. Lett. 27, 199 (1975).

104. D. E. Rimmer and A. H. Cottrell, Phil. Mag. 2, 1345 (1957).

105. W. D. Wilson and R. A. Johnson, Interatomic Potentials and Simulation of Lattice Defects, edited by P. C. Gehlen, J. R. Beeler and R. I. Jaffee, p. 375, (Plenum Press, New York 1972).

106. W. D. Wilson, M. I. Baskes and C. L. Bisson, Phys. Rev. B 13, 2470, (1976).

107. W. D. Wilson and C. L. Bisson, Rad. Effects 19, 53 (1973).

108. M. W. Guinan and R. M. Stuart, ANS Transactions 21, 164 (1975).

109. E. V. Kornelsen, Rad. Effects 13, 227 (1972); E. V. Kornelsen, private communication (1977).

110. W. D. Wilson, Fundamental Aspects of Radiation Damage in Metals, edited by M. T. Robinson and F. W. Young, p. 1025, (CONF-751006, 1976).

111. W. D. Wilson and C. L. Bisson, Rad. Effects 22, 63 (1974).

112. J. A. DiCarlo and J. T. Stanley, Discussion Meeting on Defects in Refractory Metals, p. 13, (S.C.K./C.E.N., Mol Belgium, 1972).

113. L. G. Parratt, Probability and Experimental Errors in Science, (John Wiley and Sons, Inc., New York, 1961).

114. P. R. Bevington, Data Reduction and Error Analysis for the Physical Sciences, (McGraw Hill, Inc., New York, 1969).

115. L. J. Kieffer and G. H. Dunn, Rev. Mod. Phys. 38, 1 (1966).

116. E. W. Muller, S. B. McLane and J. A. Panitz, Surf. Sci. 17, 430 (1969).

117. E. W. Muller, S. V. Krishnaswamy and S. B. McLane, Phys. Rev. Lett. 31, 1282 (1973).

118. S. K. Allison, Rev. Mod. Phys. 30, 1137 (1958).

119. L. G. Haggmark, private communication (1977).

120. J. M. Walls, R. M. Boothby and H. N. Southworth, Surf. Sci. 61, 419 (1976).

121. J. M. Walls, A. D. Martin and H. N. Southworth, Surf. Sci. 50, 360 (1975).

122. J. M. Walls, H. N. Southworth and E. Braun, Vacuum 24, 471 (1974).

123. D. N. Seidman and K. H. Lie, Acta Met. 20, 1045 (1972).

124. R. Frauenfelder, J. Chem. Phys. 48, 3955 (1968).

125. R. Frauenfelder, J. Vac. Sci. Tech. 6, 388 (1968).

126. E. A. Aitken, H. C. Brassfield, P. K. Conn, E. C. Duderstadt and R. E. Fryxell, Trans. AIME 239, 1565 (1967).

127. G. E. Moore and F. C. Unterwald, J. Chem. Phys. 40, 2639 (1964).

128. L. N. Ryabchikov, Ukr. Fiz. Zh. 9, 293 (1964).

129. A. P. Zakharov, V. M. Sharapov and E. I. Evko, Fiz. Mek. Mater. 9, 29 (1973).

130. H. E. Schiott, Rad. Effects 6, 107 (1970).

131. S. V. Krishnaswamy, S. B. McLane and E. W. Muller, J. Vac. Sci. Tech. 13, 665 (1976).

132. J. Crank, The Mathematics of Diffusion, (Clarendon Press, Oxford, England, 1956).

133. C. Zener, Imperfections in Nearly Perfect Crystals, edited by W. Shockley, J. H. Hollomon, R. Maurer and F. Seitz, p. 289, (John Wiley and Sons, 1952).

134. R. Lowrie and A. M. Gomas, J. Appl. Phys. 38, 4505 (1967).

135. J. O. Steigler, p. 292, in reference 87.

136. L. Mansur, P. R. Okamoto, A. Taylor and Che-Yu Li, in Defects and Defect Clusters in BCC Metals and Their Alloys, edited by R. J. Arsenault, Nucl. Metall. 18, 509 (1973).

137. L. Mansur, P. R. Okamoto, A. Taylor and Che-Yu Li, Proc. 7th ASTM International Symposium on Radiation Effects on Structural Materials, (1974).

138. T. R. Anthony, p. 630, in reference 87.

139. P. R. Okamoto and H. Wiedersich, J. Nucl. Mater. 53, 336 (1974).

140. N. Q. Lam and R. A. Johnson, Phys. Rev. B 15, 1794 (1977).

141. P. R. Okamoto and S. D. Harkness, Trans. ANS 16, 70 (1973).

142. P. R. Okamoto, A. T. Santhanam, H. Wiedersich and A. Taylor, Nucl. Technol. 22, 45 (1974).

143. A. T. Santhanam, A. Taylor and S. D. Harkness, in Defects and Defect Clusters in BCC Metals and Their Alloys, edited by R. J. Arsenault, Nucl. Metall. 18, 302 (1973).

144. A. Barbu and A. J. Andell, Scripta Met. 9, 1233 (1975).

145. K. Farrell, J. Bentley and D. N. Braski, Scripta Met. 11, 243 (1977).

146. E. A. Kenik, Scripta Met. 10, 733 (1976).

147. J. Moteff, private communication (1977).

148. P. J. Birdseye, D. A. Smith and G. D. W. Smith, J. Phys. D: Appl. Phys. 7, 1642 (1974).

APPENDIX A

The following description of the function of APOS will follow the order of a typical operating session. The input and output statements from the computer are in capital letters, and the responses that have been typed in from the keyboard are underlined. Headings labeling the part of the program being used are double underlined. Comments are in lower case letters.

EXECUTIVE PROGRAM

RUN - starts APOS running in the EXECUTIVE program.

DATE = 9 APRIL 1950 - requests input of the date for labeling graphs.

IDENTIFICATION = TUNGSTEN 110 PLANE - identification for labeling graphs.

CLEAR HISTOGRAM? Y - response Y for yes clears the (m/n) histogram, N for no does not.

P,R,D,G, OR C? P - selects desired function of APOS as follows:

P - pulse tip and take data

R - read data from cassette tape

D - scan dictionary of (m/n)'s

G - graph data

C - compute calibration parameters

This concludes the function of the EXECUTIVE program. The response P on the last interrogation passes control to the subroutine PULSE.

PULSE SUBROUTINE

HISTOGRAM STORAGE RANGE IS 0 TO 200, BIN SIZE = 0.2 AMU OK? N

PICK LENGTH = 90 LENGTH = 100 PICK START = 5

HISTOGRAM STORAGE RANGE IS 0 to 100, BIN SIZE = 0.1 AMU OK? Y

This sequence of requests and responses has changed the histogram storage range from 0-200 to 0-100 amu and consequently has changed the bin size from 0.2 to 0.1 amu. The program has automatically converted the requested range to a range that will be compatible with the graph labeling procedure. Thus the requested length of 90 amu was changed to the standard length of 100 amu and the starting value of 5 amu was changed to 0 amu.

PRINT ERROR MESSAGES WHEN M/N TOO LARGE? Y

Whenever a calculated (m/n) is outside the histogram storage range the value of (m/n) will be printed on the CRT.

ALPHA = 1.0 LENGTH = 2000 TO = 56

NEW PARAMETERS? Y - requests if new values of the calibration parameters are desired.

ALPHA = 1.5

LENGTH IN MM = 2228

TO = 56

New calibration parameters are:

pulse factor $\alpha = 1.5$;

flight distance $d = 2228$ mm;

total delay time $t_o = 0.56$ μsec.

CLEAR HIST? N

NO FILES OPEN

OPEN A NEW FILE? Y

TYPE DRIVE AND FILE CT2:1

Since no cassette tape file was open for writing the data, the cassette on tape drive number 2 has been opened at file number 1.

PULSE? Y - Yes response branches to actual pulsing of the tip. (N response branches to RETURN TO EXECUTIVE? request, discussed below.)

HOW MANY PULSES? 1000

The computer now begins pulsing the tip 1000 times. As the FIM specimen is field evaporated the voltage is slowly increased by the operator to maintain a steady evaporation rate as monitored by the audio rate meter. After each pulse the computer reads the timer. If the TOF is an acceptable BCD number and is less than 90.00 μsec it is assumed to correspond to a true event and a voltage measurement by the A/D converter is initiated. The value of (m/n) for each TOF is calculated and the appropiate bin of the histogram is incremented by one. The TOF's are recorded on cassette tape preceded by the negative of the number of pulses applied to the specimen since the last event. If the voltages have changed since the last event they are also recorded on cassette tape preceded by a zero. Thus, when the tape is read back, a negative number is interpreted as a number of pulses and all positive numbers following it are interpreted as TOF's. The two numbers following a zero are interpreted as the dc and pulse voltages. The data

are written in blocks of fixed length (186 numbers) so that data can be read back in a consistent way.

130 ATOMS

1 RECORD - 130 events were recorded and one cassette tape record was filled.

HOW MANY PULSES? 0

RETURN TO EXECUTIVE? Y - Request for zero pulses passes control out of the pulsing mode into the branching request. A Y response causes return to the EXECUTIVE program. An N response would have caused return to the beginning of the PULSE subroutine.

CT2:1 IS STILL OPEN FOR WRITING

CLOSE IT? Y

CT2:1 HAS BEEN CLOSED AND CONTAINS 2 RECORDS

The cassette tape file can be left open when returning to the EXECUTIVE program, but has been closed since the data taking has been concluded.

CLEAR HISTOGRAM? N

P,R,D,G, OR C? G - Selects the graphing subroutine.

GRAPH SUBROUTINE

STORAGE RANGE 0 TO 100 AMU, BIN SIZE = 0.1 AMU. HISTOGRAM PLOTTING RANGE IS 0 TO 100 AMU OK? N

PICK LENGTH 4 LENGTH = 5 PICK START 59

HISTOGRAM PLOTTING RANGE IS 59 TO 64 AMU OK? Y

The horizontal range to be plotted has been selected to be between 59 and 64 amu. Note that the program

automatically restricts the selected range to a standard size within the storage range of the histogram.

MAX = 24 VERT RANGE = 30 OK? N

PICK VERT RANGE = 50

MAX = 24 VERT RANGE = 60 OK? Y

The program automatically picks a vertical range large enough for the maximum of the histogram over the selected (m/n) range. If the operator has chosen a larger range, it is converted to a standard size by the program.

IDENT = TUNGSTEN 110 PLANE OK? Y

At this point the CRT screen of the graphics terminal is cleared automatically and a histogram similar to those shown in section 5 is plotted. The operator then makes a hard copy of the histogram and clears the CRT screen.

RETURN TO EXECUTIVE? Y - A response of N would cause a return to the beginning of the GRAPH subroutine.

CLEAR HIST? Y

P,R,D,G, OR C? R - Read data from the cassette tape.

READ SUBROUTINE

DRIVE AND FILE TO BE READ CT2:1

CT2:1 OPENED FOR READING

FIRST RECORD = 0

LAST RECORD = 5 - The cassette tape on drive 2 has been opened to file 1. Records 0 to 5 will be read and analyzed.

EXCLUDE ANY DATA GROUPS? Y

EXCLUDE DATA IN GROUPS OF SIZE = (TERM. WITH NO. ≠ 1 TO 8)

? 8

? 0 Any TOF data which came in groups of 8 (i.e., all 8 counters in the digital timer contained true events) will be excluded. The 0 terminates the list because it is outside the range 1 to 8.

EXCLUDE DATA NUMBERS = (1 TO 8)

? 7

? 0 All data from the seventh counter will be ignored; the 0 terminates the list.

CREATE HIST (H), COMP PROFILE (P) OR BOTH (B) ? B

Select whether to create a histogram, a composition profile or both.

HISTOGRAM STORAGE RANGE IS 0 TO 100 AMU, BIN SIZE = 0.1 AMU OK? Y

CLEAR PRESENT HISTOGRAM Y

ALPHA = 1.5 LENGTH = 228 TO = 56

NEW PARAMETERS? N - The histogram information requested as in the PULSE subroutine

COMPO PROFILE INFO

Y AXIS M/N RANGES FROM 10 TO 20 AMU - The vertical axis of the composition profile will indicate the total number of events with (m/n) between 10 and 20 amu.

LENGTH OF Y AXIS = 3 (events) OK? Y

X AXIS M/N RANGES FROM 0 TO 100 AMU - The horizontal axis of the composition profile will indicate the total number of events with (m/n) between 0 and 100 amu.

LENGTH OF X AXIS = 200 (events) OK? Y

IDENT = TUNGSTEN 110 PLANE 10 TO 20 AMU VS 0 TO 100 AMU OK? Y

The computer now begins to read the tape and compute the histogram while simultaneously plotting the composition profile on the CRT. The computer then makes a hard copy of the composition profile and clears the CRT.

EOF AT RECORD 1 DATA 35

CT2:1 HAS BEEN CLOSED - When the program encounters an end of file (EOF) mark on the tape it notes the record and data numbers and then closes the file.

RETURN TO EXECUTIVE? Y

CLEAR HISTOGRAM? N

P,R,D,G, OR C? C

CALIBRATION SUBROUTINE

For the following example it will be assumed that the tungsten data (hypothetical) was taken at two sets of voltages. The data were then analyzed using the following (incorrect) calibration parameters: t_o = 0.50 μsec; α = 1.2; and d = 2200 mm. The $^{4}He^{+}$ peak and the $^{186}W^{+3}$ peak for the two sets of voltages were observed at the following (m/n):

	V_{dc}	V_{pulse}	$^{4}He^{+}$	$^{186}W^{+3}$
Case I	8000V	400V	4.19 amu	63.25 amu
Case II	8400V	200V	4.22 amu	63.71 amu

The first step in the calibration procedure is to work backward from the observed (m/n) values to obtain the equivalent TOF's.

COMPUTE TOF? Y

VDC = 8000 VPLSE = 400 ALPHA = 1.2 TO = 50 LENGTH = 2200

M/N = 4.19 TOF = 402.008 - (all times in tens of nanoseconds)

M/N = 63.25 TOF = 1417.65

M/N = 0 TOF W NEW PARAMETERS? Y

VDC = 8400 VPLSE = 200 ALPHA = 1.2 TO = 50 LENGTH = 2200

M/N = 4.22 TOF = 399.98

M/N = 63.71 TOF = 1409.85

M/N = 0 TOF W NEW PARAMETERS? N

Input (m/n) = 0 passes to branch statement allowing recomputation of TOF's with new parameters. Typing N causes the program to continue.

COMPUTE TO? Y - Compute t_o.

1ST M/N = 4 1ST TOF = 402.008

2ND M/N = 62 2ND TOF = 1417.65

TO = 56.1985

COMPUTE ALPHA? Y

1ST VDC = 8000 VPLSE = 400 TOF = 1417.7

2ND VDC = 8400 VPLSE = 200 TOF = 1409.85 TO = 56.2

ALPHA = 1.50338

COMPUTE LENGTH? Y

TO = 56.2 ALPHA = 1.5 VDC = 8000 VPLSE = 400

M = 186 N = 3 TOF = 1417.7

LENGTH = 2227.91

COMPUTE LENGTH WITH NEW PARAMETERS? N

This completes the actual calibration. The following computation of (m/n) serves as a check.

COMPUTE M/N? Y

VDC = 8000 VPLSE = 400 ALPHA = 1.5 TO = 56 LENGTH = 2228

TOF = 402.008 M/N = 4.00311

TOF = 1417.65 M/N = 61.9949

TOF = 0 M/N WITH NEW PARAMETERS? Y

VDC = 8400 VPLSE = 200 ALPHA = 1.5 TO = 56 LENGTH = 2228

TOF = 399.98 M/N = 4.00233

TOF = 1409.85 M/N = 61.994

TOF = 0 M/N WITH NEW PARAMETERS? N

Thus, the new calibration parameters t_o = 0.56μsec α = 1.5, and d = 2228mm give consistent results for the (m/n) values of $^{4}He^{+}$ and $^{186}W^{+3}$.

RETURN TO EXECUTIVE? Y

CLEAR HISTOGRAM? N

P, R, D, G, OR C? D

DICTIONARY SCANNING SUBROUTINE

TAPE FILE OF M/N DICT CT1:1

M/N RANGE 0 TO 8 - selected (m/n) range of interest is 0 to 8 amu

ALL ELEMENTS? N

INPUT ELEMENTS, INCLUDE BLANKS, SEPARATE WITH CARRIAGE RETURN, END WITH ZZ

? HE

? N

? ZZ

ELEMENTS ARE HE N

OK? Y Selected elements are helium and nitrogen. All others will be excluded.

M/N	ELEM	N	%	COMMENTS
2	HE-	+2	100	
4	HE-	+1	100	
4	HE-HE	+2	100	
4.7	N-	+3	99.6	
5	N-	+3	.4	
6	N-HE	+3	99.6	
6.3	N-HE	+3	.4	
7	N-	+2	99.6	
7.5	N-	+2	.4	
8	HE-HE	+1	100	

The first column contains the (m/n) value in amu, the second column contains the name(s) of the elements, the third column contains the charge state and the fourth column contains the percent natural abundance of the combination having that particular (m/n). The last column is for comments.

RETURN TO EXECUTIVE? Y

CLEAR HISTOGRAM? Y

P,R,D,G, OR C? _

APPENDIX B

This section describes a number of observations and techniques which were found to be useful in the operation of the atom probe.

1) Detection efficiency and random signals.

The following suggestions are designed to minimize the number of random output signals from the detector and maximize the detection efficiency of field-evaporated ions.

The background events observed in the (m/n) spectra are caused by random pulses produced at the Chevron ion detector. The major source of these random pulses in an atom probe employing a straight flight path is due to field-ionized gas atoms striking the detector. Even with a total gas pressure of $2 \cdot 10^{-10}$ torr the field-ionization current produced ~5 counts per second versus a typical dark current of 1 count per second. Thus the Chevron detector dark-current was a negligible source of background events in the (m/n) histogram compared to the field ionization current. Therefore in order to minimize random background events in the (m/n) histogram it was essential to operate the atom probe under UHV conditions. The field ionization of residual gas at 10^{-10} torr was conveniently used to determine if a specimen had failed during an atom probe analysis without the need to introduce any imaging gas or to remove the positive dc field and use electron field-emission. A small permanent magnet placed on the flight tube was used to deflect the field-ionized gas-beam. If a specimen had failed no change in the detector output count rate was observed when the magnet was placed on the flight tube.

When focusing the imaging gas onto the Chevron detector, the lens voltage was adjusted until a spot ~2mm in diameter was produced. The lens voltage was then increased by an amount equal to the pulse fraction times the pulse factor, i.e., the lens voltage was increased to $(1 + \alpha f)$ times the focused imaging gas voltage. In this way, the field-evaporated ions were focused onto the detector (maximizing detection efficiency) while the imaging gas-ions and the field-ionized residual gas were not focused (thus minimizing the background count rate). By making αf large (~0.2) the vast majority of the imaging gas-ions were so overfocused that they were not able to strike the Chevron detector thus dramatically decreasing the background noise typically seen in (m/n) histograms when the imaging gas is present.

If helium or hydrogen was used as the imaging gas a small permanent magnet placed on the flight tube was used to deflect the imaging gas beam, thus reducing background counts without significantly reducing the detection efficiency for the low (m/n) ratio field-evaporated ions.

Since there was always a neutral component to the imaging gas ion-beam it was never possible to completely eliminate background counts from the (m/n) histograms employing the aforementioned techniques. By using a magnet, the entire charged component of the beam was deflected so that it did not strike the detector. This yielded the minimum attainable background count rate which was a useful guidline when selecting the smallest possible αf value employed in the lens overfocusing method. Generally the ratio of neutral-to-charged beam was 10^{-3} during typical imaging conditions.

2) Improving mass resolution.

As the ratio of the pulse voltage to the dc voltage was decreased; i.e., as αf was decreased, the observed energy deficit tails in the (m/n) histogram decreased and thus the mass resolution increased (see section 3.5). A lower practical limit of ~0.02 for αf was found. Below this value the dc field-evaporation rate became comparable to the pulsed field-evaporation rate.

Increasing the flight-path length increased the mass resolution since the TOF measurement resolution improved and variations in the flight path length, for example when the ion passed through the focusing lens, became less significant. However, a practical upper limit on the flight path length was reached at ~2.2 meters due to deflection of the ion beam by the earth's magnetic field. For example, by simultaneously imaging in helium and neon, two distinct focused spots were seen at the Chevron detector for a flight path length of 2.222 meters. These spots were sufficiently far apart to indicate that a H^+ ion would strike the detector approximately $\frac{1}{2}$ detector diameter away from a W^{+3} ion. Clearly, a flight-path length much greater than 2 meters would have made it impossible to detect the entire mass range of 1 to 100 amu, unless extensive magnetic shielding were employed. The desirable method of aligning the specimen with the detector using field-emitted electrons was <u>not</u> possible; a 1 KeV electron has a circular path of radius ~1 meter due to the earth's magnetic field and thus the electrons can never reach the Chevron detector.

The fast electronics employed throughout the detection and timing

systems resulted in an effective detection dead time of ~22 nsec. In most cases adjacent (m/n) peaks were resolved since the TOF difference of the ions was greater than 22 nsec. However, with high voltages applied to the specimen, the difference in the TOF of a number of species is of the order of 20 nsec. Thus, based solely on TOF resolution, it would not be possible to distinguish them. For example, with a flight path lenght of ~2 meters and a total voltage of ~20 KV the difference in the TOF of $^{187}Re^{+3}$ and $^{186}W^{+3}$ is ~20 nsec. The most convenient solution was to employ specimens with small tip radii and hence low evaporation voltages when a high mass resolution was required (see section 5.2).

3) Controlling field-evaporation rates.

Controlling the field-evaporation rate of tungsten when both the imaging gas was present and nsec duration field-evaporation pulses were employed was extremely difficult. This effect may possibly be related to the large decrease in the field required to evaporate an atom when the imaging gas is present versus vacuum field evaporation. It was necessary to employ msec duration pulses when controlled dissections of a crystal were required when the imaging gas was present, for example when filming a pulse field-evaporation sequence.

This highly non-uniform field evaporation which occurred when nsec pulses were employed in the presence of the imaging gas may cause serious problems in quantitative atom-probe analyses (see section 6). In view of this fact, all atom-probe analyses presented in this work have been performed in the absence of an imaging gas.

Generally vacuum field-evaporation employing nsec pulses was found to be quite uniform and very controllable.

An audio ratemeter was interfaced to the detection and timing system. This ratemeter produced an audio signal (a click) whenever a field-evaporated ion struck the detector. By adjusting the voltage applied to the specimen a constant audible output from the ratemeter was obtained and thus a constant rate of field evaporation was maintained. The only exception noted thus far occurred in the field evaporation of the molybdenum (111) plane and was associated with the intrinsic mode of field evaporation of this particular plane of molybdenum. The ability to uniformly and controllably field evaporate an extensive volume of a specimen was essential for reliable quantitative atom-probe analyses as discussed in section 6.

4) Specimen to detector alignment.

The following procedure was developed to align the specimen with the detector. The dc voltage on the specimen was increased well above the best image voltage (BIV) to produce an out-of-focus image. The lens voltage was increased slowly and the specimen was positioned until a circular spot approximately 2 mm in diameter appeared on the Chevron detector. Because of the earth's magnetic field, different (m/n) ratio ions struck the Chevron detector at different positions. The correct spot positions for various imaging gas ions are schematically indicated in figure 77. It was essential that the dc voltage applied to the specimen was well above BIV so that prominent features in the FIM image were strongly blurred. If this was not done, often only the prominent features were actually aligned and focused with

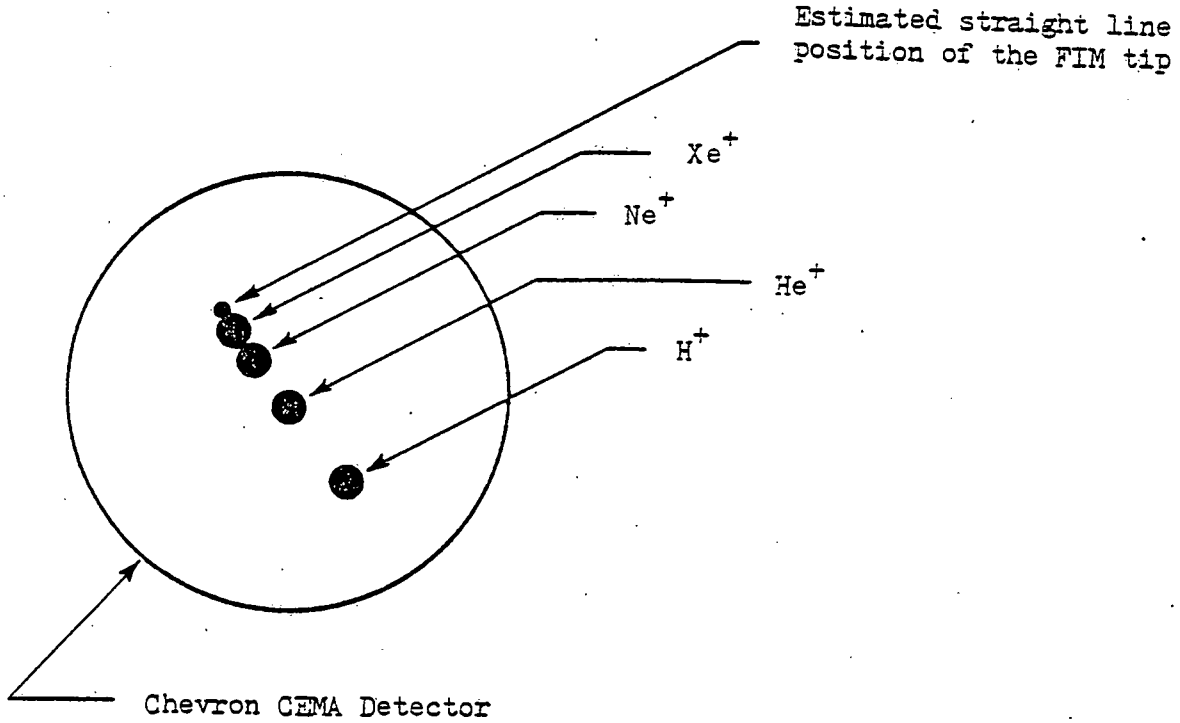

Figure 77. The experimentally observed position where various field ionized gas ions strike the detector is illustrated. As the (m/n) value of the ion increased, the gas ion spot approached the straight line position of the FIM tip. The conditions for this experiment were V_{dc} = 8000 V, d = 2222 mm and a tip-to-image intensification system distance of 400 mm.

the Chevron detector instead of the entire area beneath the probe hole. For example, at BIV the image of the edge of the (110) plane of W is much brighter than the center of the plane. If the specimen was not properly aligned and the lens was below the correct focusing voltage a bright line due to the edge of the (110) plane appeared at the chevron detector. This could have been easily mistaken for a focused point source with severe coma due to the lens system. The effect was particularly troublesome if an unusually bright atom present in the image was surrounded by darker atoms. This is illustrated in figure 78.

For each run the specimen and detector had to be realigned. It was often necessary to realign the specimen and the detector when either the specimen or the imaging system were moved. This was due to backlash in the goniometer and imaging system supports, and the fact that the specimen tip was rarely placed exactly at the intersection point of the two axes of rotation of the goniometer.

Fluctuations in room temperature of greater than 5 F generally caused a noticeable change in the alignment of the specimen with the detector. This was observed by noting the change in position of a spot on the Chevron detector produced by a well-focused beam of imaging gas-ions as the temperature of the room was varied.

5) Vacuum system.

The introduction of helium in to the FIM caused the release of other gases from the RGA, the ionization gauges and the ion gun. For a helium pressure of $1 \cdot 10^{-4}$ torr, CH_4 was released to a partial pressure of $\sim 10^{-9}$ torr from the ionization gauge and 10^{-9} to 10^{-8}

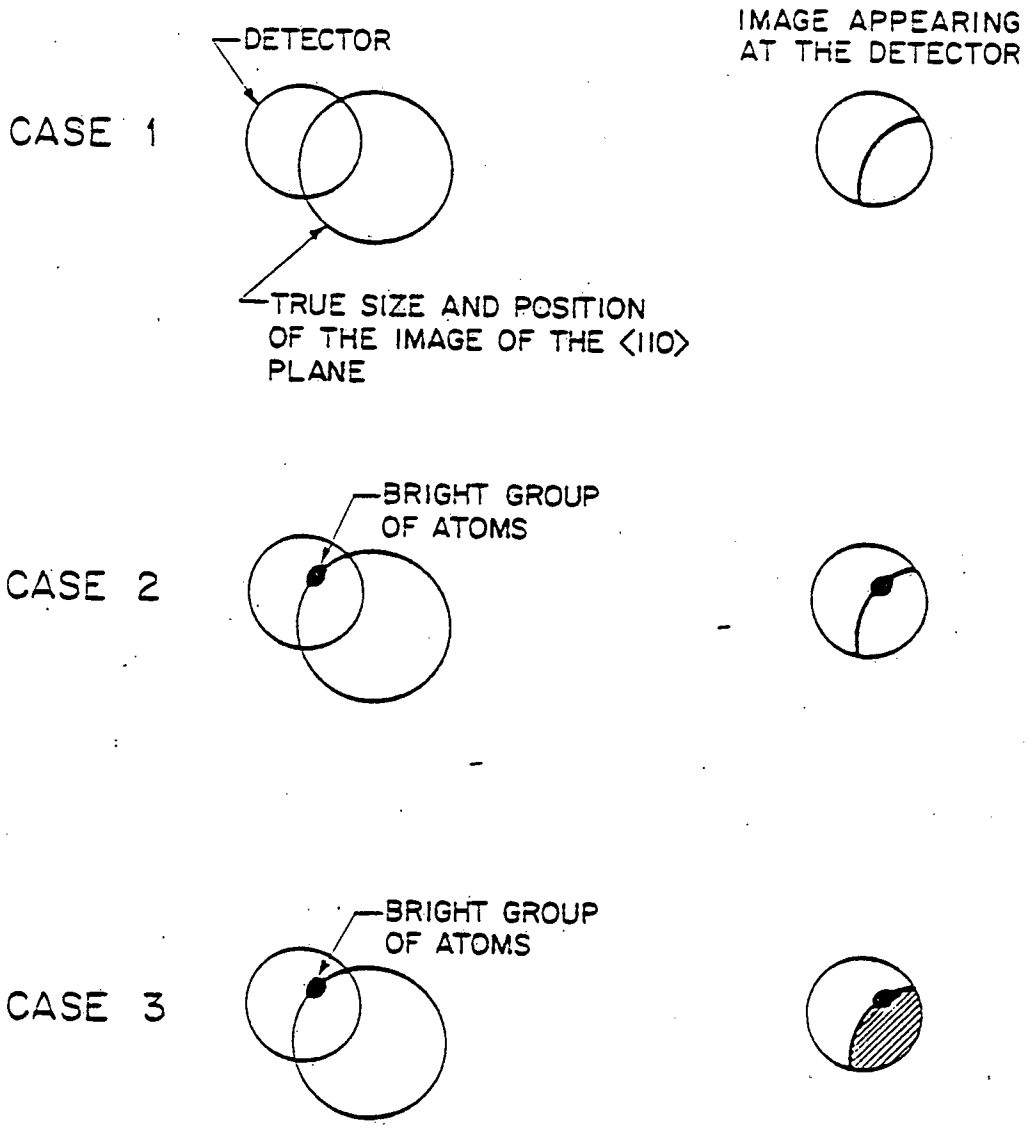

Figure 78. An illustration of problems associated with focusing the ion beam onto the detector. On the left hand side of the figure the true position and size of the image at the detector is indicated for a misaligned and underfocused tip. The right hand side illustrates the appearance at the Chevron ion detector for three cases. In cases 1 and 2 the tip is at BIV; note that the image at the detector can easily be mistaken as a focused point source with severe coma (particularly case 2). In case 3 the tip is well above BIV and the underfocused and misaligned condition of the tip is clearly indicated by the fact that the entire right hand side of the detector is illuminated.

torr from the ion gun, while CO was released from the RGA to a partial pressure of $\sim 10^{-10}$ torr. These partial pressures were measured under typical dynamical pumping conditions. By simply turning off all gauges etc. the production of these residual gases was eliminated, thus reducing the complexity of the (m/n) spectra.

The rate of removal of helium, introduced to a pressure of 10^{-4} torr, was increased if the RGA and ion gauges were not operated when the helium was present in the FIM. Apparently helium (ions) became trapped in the structual components of the RGA and/or ion gauge. The helium would then desorb slowly when pumping the helium from the FIM. This resulted in a higher ultimate partial pressure of helium. The ability to remove the helium gas introduced during a low-energy helium-ion irradiation to a partial pressure of 10^{-12} torr was essential in order to minimize the detection of background helium in the experiments performed concerning the range and mobility of helium in tungsten described in section 7.

The cold finger should not be baked above 160 C between runs. This procedure prevented excessive desorbtion of gases from the cold finger. The desorbed gas would reabsorb on the room temperature surfaces of the FIM and increase the ultimate pressure from $\sim 2 \cdot 10^{-10}$ to $\sim 10^{-9}$ torr. If the cold finger was baked above 160 C between runs, it was necessary to rebake the entire FIM to reattain the base pressure of $2 \cdot 10^{-10}$ torr.

6) Temperature control.

The most stable specimen temperatures were obtained by first precooling the cold finger and the specimen for one hour to the lowest

possible temperature (4.2K for the cold finger and 10K for the specimen) and then warming the specimen up to the desired temperature by decreasing the liquid helium flow rate. The apparent reason for this was that the radiation shields surrounding the cold finger and specimen took considerably longer to cool than either the cold finger or the specimen. Thus by accelerating the cooldown of the shields, the equilibrium shield temperature at the desired operating temperature was more quickly achieved. This eliminated the problem of a constant downward drift in the temperature of the specimen which otherwise occurred at a constant liquid-helium flow-rate.

The major heat input to the liquid helium was due to radiation from the outer jacket of the transfer tube. Since the temperature of the jacket of the transfer tube was coupled to the temperature of the room, small changes in room temperature caused significant changes in the specimen temperature. The best temperature stability I have been able to achieve was $\pm\frac{1}{2}\%$ of the specimen temperature over several hours.

In order to achieve the lowest possible specimen temperature with the minimum liquid-helium consumption it was necessary to chill the outer jacket of the transfer tube with liquid nitrogen or the cold helium exhaust gas. This technique reduced the liquid helium consumption rate at a specimen temperature of ~10 K (cold finger at 4.2 K) from ~1.7 liter to ~0.2 liter hr^{-1}.

7) Mass spectrometer artifacts.

When a specimen failed during the atom probe analysis, all eight timing chains in the digital timer were usually triggered. Thus when

a specimen failed the last eight TOF and hence the last eight (m/n) ratios were artifacts of the electronics and had to be discarded. This was found to be significant since these TOF were separated by ~40 nsec and usually produced eight peaks at or near H^+ in the (m/n) spectrum.

High-voltage breakdowns and numerous other sources of fast electrical noise usually triggered the digital timer. This resulted in unidentifiable peaks in the (m/n) spectra. In order to prevent artifacts in the (m/n) histograms all electrical noise which affects the operation of the digital timer must be eliminated, preferably at the source.

APPENDIX C

This section contains a description of the model employed to calculate the probability of observing a specific composition fluctuation in a random solid solution. The following quantities are defined:

N = total number of atoms detected;

n_i = total number of atoms of species i detected;

c_i = average measured concentration of species i;

a_i = number of atoms of species i detected in the composition fluctuation under analysis;

x = total number of atoms in the composition fluctuation under analysis.

Note that $x = \Sigma a_i$ and that $c_i = n_i/N$.

The probability (P) of detecting a cluster containing x atoms consisting of a_1 atoms of species 1, a_2 atoms of species 2, etc. in a random solid solution is;

$$P = \frac{x!}{\prod a_i!} \prod (c_i)^{a_i} . \qquad (C1)$$

An upper limit to the probability of detecting this cluster in a total sample of size N can be estimated as follows. The maximum number of possible locations in a composition profile in which this cluster of size x in a total sample of size N can occur is (N - x). Therefore the probability (P') of <u>not</u> detecting this cluster in a sample of size N is;

$$P' = (1 - P)^{N-x} . \qquad (C2)$$

The probability (Q) of detecting this cluster is 1 - P' and thus

$$Q = 1 - (1 - P)^{N-x}. \qquad (C3)$$

Since the factor (N - x) is the maximum number of locations for the cluster in the composition profile (i.e., all of the cluster locations are not independent measurements), Q represents an upper limit to the probability of detecting a specific composition fluctuation in a random solid solution. For small P, Q is given approximately by;

$$Q = (N - x)P. \qquad (C4)$$

For example, employing the average measured concentration for the components in LS1A listed in table 8 and equations C1 and C4, the probability of detecting the cluster listed in table 8 was calculated as follows:

$$P = \frac{14!\ (0.622)(0.162)^3(0.026)(0.018)^2(0.004)^2(0.017)^3(0.002)^2}{1!\ 3!\ 1!\ 2!\ 2!\ 3!\ 2!}$$

$$P \approx 2 \cdot 10^{-15}.$$

Since N was approximately equal to 5000, the upper limit on the probability (Q) of detecting the cluster was;

$$Q \approx (5000)(2 \cdot 10^{-15}) \approx 1 \cdot 10^{-11}.$$

APPENDIX D

This section contains a description of the model which was employed to estimate the systematic errors in the measurement of the mean range and standard deviation of the range due to the non-planar geometry of the FIM specimen.

The transverse straggling (Δy and Δz) is the standard deviation of the range profile in the directions perpendicular to the incident ion direction. For low energy helium ions incident on a heavy target such as tungsten, Δy and Δz are expected to be approximately equal to the range straggling (Δx)[98]. Due to the large transverse straggling, low energy helium ions incident on the (110) terraces adjacent to the central (110) plane of the W specimen were deposited within the volume analyzed by the atom probe as illustrated in Fig. 79. The model employed to estimate the magnitude of the error in the mean range and the standard deviation due to the non-planar geometry of the FIM specimen is described below.

The following quantities, illustrated in Fig. 79 were employed in the model:

r_a = radius of the cylindrical volume element analyzed by the atom probe;

R_t = radius of the FIM specimen in the region of the (110) pole;

d_{110} = interplanar spacing of the W (110) planes (2.2 A);

r_n = radius of the outer ledge of the n^{th} terrace;

A_n = area of the n^{th} terrace; i.e., $\pi(r_n^2 - r_{n-1}^2)$;

A_{110} = area of the topmost (110) plane; i.e., terrace number zero;

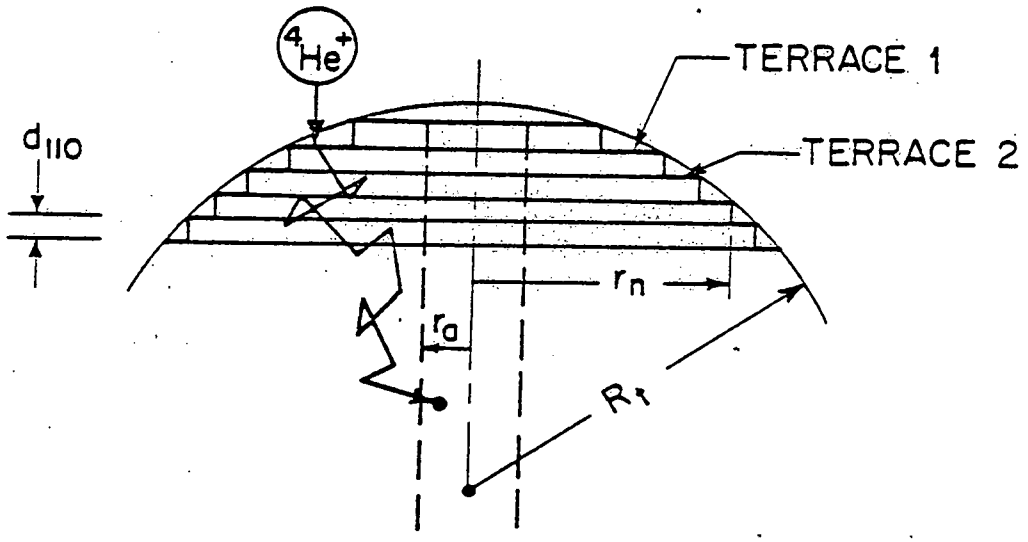

Figure 79. A schematic illustration of the FIM specimen showing a helium ion incident on terrace 1 and coming to rest within the volume analyzed by the atom probe.

$\bar{x}_m$ = measured mean range of the helium atoms detected in an irradiated specimen;

$\bar{x}_i$ = actual mean range of the helium atoms injected into the specimen during an irradiation.

The transverse straggling (Δy and Δz) was assumed to be equal to the measured Δx*. Helium ions incident on a terrace with $r_n \leq \Delta x + r_a$ were included in the number of helium atoms detected while helium ions incident on terraces with $r_n > \Delta x + r_a$ were excluded from the number of helium atoms deposited within the analyzed volume. The physical basis of this assumption is that the probability of depositing an incident helium ion at a transverse distance greater than Δx from the point of entry into the target is small. Since the fluence of helium ions was a constant on each (110) terrace, the total number of helium ions entering the n^{th} terrace was directly proportional to A_n. All ions incident on the n^{th} terrace, where $r_n \leq \Delta x + r_a$, were assumed to have been deposited uniformly in the directions perpendicular to the incident beam within the volume bounded by the outer ledge of the n^{th} terrace. For example, the ions incident on the topmost (110) plane were assumed to have been distributed uniformly in the transverse directions bounded by a radius $r_n \leq \Delta x + r_a$. The depth distribution of the ions incident on a particular terrace was equal to the true range profile referenced to that terrace. Thus the measured range

---

* Since the actual standard deviation was less than the measured standard deviation, this assumption yields an upper limit to the correction factor.

profile consisted of the superposition of (n) true range profiles (one for each of the n contributing terraces) and the profile due to the ions which entered the topmost (110) plane. Each of the (n) profiles was displaced from the profile due to the ions which entered the topmost (110) plane by a distance equal to nd_{110}. Thus the measured mean range ($\bar{x}_m$) is equal to;

$$\bar{x}_m = \frac{A_{110}(\bar{x}_i) + A_1(\bar{x}_i + d_{110}) + A_2(\bar{x}_i + 2d_{110}) + \cdots A_n(\bar{x}_i + nd_{110})}{A_{110} + A_1 + A_2 + \cdots A_n} . \quad (D1)$$

Therefore the error introduced into the measurement of the mean range is equal to $(\bar{x}_m - \bar{x}_i)$ and is given by the expression;

$$(\bar{x}_m - \bar{x}_i) = \frac{\Sigma\, jd_{110}A_j}{A_{110} + \Sigma\, A_j} \quad , \text{ for } j = 1 \text{ to } n. \quad (D2)$$

Based on the geometry of the specimen, the following expressions can be derived;

$$A_n = \pi\left[2R_t d_{110} + d_{110}^2(n^2 - 3n + 1)\right] ; \quad (D3)$$

$$A_{110} + A_1 + A_2 + \cdots A_n = \pi(2R_t nd_{110} + nd_{110}^2) ; \quad (D4)$$

$$r_n = \left[2R_t(n + 1)d_{110} - (n + 1)^2 d_{110}^2\right]^{\frac{1}{2}} \approx \left[2R_t(n + 1)d_{110}\right]^{\frac{1}{2}}. \quad (D5)$$

Employing equation D5 and the boundary condition that $r_n < \Delta x + r_a$ yields the following condition on n;

$$n \leq \frac{(\Delta x + r_a)^2}{2R_t d_{110}} - 1 . \quad (D6)$$

For all of the experimental results presented in section 7.4, $\Delta x \leq 42$ A, $r_a \leq 22$ A, and $R_t > 300$ A. Employing equation D6 and the

values of Δx, r_a, and R_t above, the maximum value of (n) was calculated to be equal to 2. Employing equations D2, D3, and D4, and the values of Δx, r_a, n, and R_t given above, the maximum value of $(\bar{x}_m - \bar{x}_i)$ was calculated to be approximately d_{110} or 2.2 A. Thus the measured mean range exceeded the actual mean range by at most 2.2 A due to the non-planar geometry of the FIM specimen.

The actual standard deviation of the range profile was calculated by noting that the measured range profile consisted of the superposition of three range profiles which were identical in shape and magnitude; i.e., approximately the same number of helium ions were contained in each profile. However each of the three profiles were displaced from one another by a distance d_{110} in the direction of the range measurement. The variance (S_b^2) of a distribution taken about a mean (b) is related to the variance (S_a^2) of the same distribution taken about a value (a) by the expression;

$$S_b^2 = S_a^2 - (a - b)^2 \qquad \text{(see reference 113).} \qquad \text{(D7)}$$

Therefore the variance of the actual range profile (S_i^2) is related to the measured variance (S_m^2) by the expression;

$$S_i^2 = S_m^2 - \frac{2}{3} d_{110}^2 \quad . \qquad \text{(D8)}$$

Since $d_{110}^2 \ll S_m^2$, the actual standard deviation (Δx_i) was essentially equal to the measured standard deviation (Δx_m).

A second source of systematic error in the measurement of the mean range and the standard deviation of the range was due to the presence of background helium as indicated in the control runs. The

equations which were employed to estimate these systematic errors are derived in this section.

The following quantities are defined:

N = total number of helium atoms detected in an irradiated specimen;

C = number of helium atoms detected in a control run;

$\bar{x}_c$ = measured mean depth of the helium atoms detected in a control run;

S_m^2 = measured variance taken about $\bar{x}_m$ of all of the helium atoms detected in an irradiated specimen;

S_c^2 = measured variance taken about $\bar{x}_c$ of the helium atoms detected in a control run;

S_i^2 = variance taken about $\bar{x}_i$ of the helium atoms injected into the specimen during an irradiation. This is the actual variance of the range profile and thus is the quantity which is desired.

The variance of the corresponding parent populations are denoted by σ^2 followed by the appropiate subscript. Note that the N helium atoms detected in an irradiated specimen consist of C background helium atoms plus (N - C) injected helium atoms.

The measured mean range ($\bar{x}_m$) is equal to the weighted average of $\bar{x}_i$ and $\bar{x}_c$ as shown below;

$$\bar{x}_m = \frac{(N - C)\bar{x}_i + C\bar{x}_c}{N} \quad . \tag{D9}$$

Therefore the actual mean range ($\bar{x}_i$) of the injected helium atoms is given by;

$$\bar{x}_i = \frac{\bar{x}_m}{(1 - \epsilon)} - \frac{\epsilon}{(1 - \epsilon)} \bar{x}_c \quad . \tag{D10}$$

where $\epsilon = C/N$

The error in the measured mean range is equal to;

$$(\bar{x}_m - \bar{x}_i) = \frac{\epsilon}{(1 - \epsilon)} (\bar{x}_c - \bar{x}_m). \tag{D11}$$

The measured variance (S_m^2) consists of the sum of the variance taken about $\bar{x}_m$ of the (N - C) helium atoms injected during the irradiation and the variance taken about $\bar{x}_m$ of the C background helium atoms. In order to illustrate this fact the following additional terms are defined:

x_m = measured depth from the initial surface of the FIM specimen of each of the helium atoms detected in an irradiated specimen;

x_i = depth of the injected helium atoms only;

x_c = depth of the background helium atoms detected during the run on an irradiated specimen.

Note that x_i and x_c are not directly measureable quantities. The measured variance is then given by;

$$S_m^2 = \frac{\Sigma(x_m - \bar{x}_m)^2}{N} = \frac{\Sigma(x_i - \bar{x}_m)^2 + \Sigma(x_c - \bar{x}_m)^2}{N}. \tag{D12}$$

Employing equation D7, the variance of the injected helium atoms taken about $\bar{x}_m$ is equal to $S_i^2 + (\bar{x}_i - \bar{x}_m)^2$. Thus the first summation in the right hand side of equation D12 is given by;

$$(N - C)[S_i^2 + (\bar{x}_i - \bar{x}_m)^2]. \tag{D13a}$$

Similarly the second summation in the right hand side of equation D12 is equal to;

$$C[S_c^2 + (\bar{x}_c - \bar{x}_m)^2]. \qquad \text{(D13b)}$$

Substituting these expressions into equation D12 and solving for S_i^2 yields;

$$S_i^2 = \frac{NS_m^2 - C[S_c^2 + (\bar{x}_c - \bar{x}_m)^2]}{(N - C)} - (\bar{x}_i - \bar{x}_m)^2 \qquad \text{(D14)}$$

Note that S_i^2 is the actual variance of the injected helium atoms. The only unknown quantity on the right hand side of equation D14 is S_c^2 where;

$$S_c^2 = \frac{\sum_1^C (x_c - \bar{x}_c)^2}{C} . \qquad \text{(D15)}$$

An experimental evaluation of S_c^2 requires an accurate measurement of the spatial distribution of the background helium. Due to the finite number of control runs, an accurate distribution was not determined. A reasonable estimate of S_c^2 can be obtained based on the following assumptions:

(1) the C helium atoms detected were randomly distributed in depth;

(2) the actual S_c^2 can be estimated by S_c^2 in the limit of a large number of helium atoms; i.e., as C approaches infinity. Then

$$S_c^2 = \frac{\int_0^{2x_c} (x - \bar{x}_c)dx}{\int_0^{2x_c} dx} = \frac{\bar{x}_c^2}{3} \qquad \text{(D16)}$$

The variance of the parent distribution is given by;

$$\sigma_i^2 = \frac{(N - C)}{(N - C - 1)} S_i^2 . \qquad \text{(D17)}$$

Employing equations D14, D16, and D17 the standard deviation of the parent range profile is given by;

$$\sigma_i = \left\{ \frac{NS_m^2 - C\left[\frac{\bar{x}_c^2}{3} + (\bar{x}_c - \bar{x}_m)^2\right] - (N - C)\cdot(\bar{x}_i - \bar{x}_m)^2}{(N - C - 1)} \right\}^{\frac{1}{2}} \qquad \text{(D18)}$$

Note that

$$S_m^2 = \frac{(N - C - 1)}{(N - C)} (\Delta x)^2 \quad \text{where } \Delta x \text{ is given in Table 11.} \qquad \text{(D19)}$$

A more convenient form of equation D18 for the direct calculation of σ_i from the experimental data is;

$$\sigma_i = \left[\frac{\Sigma(x_m - \bar{x}_i)^2}{(N - C - 1)} - \frac{C[4\bar{x}_c^2 - 6\bar{x}_i\bar{x}_c + 3\bar{x}_i^2]}{3(N - C - 1)} \right]^{\frac{1}{2}} \qquad \text{(D20)}$$

The expressions for estimating the error in the measured mean range and standard deviation (D11 and D18) are only exact in the limit as both N and C approach infinity. The validity of these expressions for small N and C was tested by employing a simulation technique (see section 4). Profiles were simulated based on the theoretical range profile of Haggmark et. al. The simulations were performed with N as a variable and ϵ fixed at 0.2; i.e., C = 0.2N. The mean range and standard deviation of the parent distribution; i.e., the theoretical profile, were compared with the corresponding quantities determined for the simulated profile before and after the correction for background helium was applied. By taking an ensemble of simulations, the corrected values of $\bar{x}$ and Δx were found to provide a better estimate of the values of $\bar{x}$ and Δx of the parent distribution than the measured

values of $\bar{x}$ and Δx in 65%, 75%, and 85% of the simulations for N = 25, 50, and 100 helium atoms respectively. Thus there was a high probability that the corrected $\bar{x}$ and Δx were better estimates of the true $\bar{x}$ and Δx for $N > 50$.